



Pedro Miguel Borges Lopes

FREE-SURFACE FLOW INTERFACE AND AIR-ENTRAINMENT MODELLING IN HYDRAULIC STRUCTURES

PhD Thesis in Civil Engineering, with specialization in Hydraulics, Water Resources and Environment,
supervised by Prof. Jorge Leandro and Prof. Rita F. Carvalho
and submitted to the Faculty of Sciences and Technology, University of Coimbra.

September, 2016



UNIVERSIDADE DE COIMBRA



FCTUC DEPARTAMENTO DE ENGENHARIA CIVIL
FACULDADE DE CIÊNCIAS E TECNOLOGIA
UNIVERSIDADE DE COIMBRA

Free-surface Flow Interface and Air-entrainment Modelling in Hydraulic Structures

Thesis Presented in partial fulfilment of the requirements for the Degree of Doctor of Philosophy in Civil Engineering in the scientific area of Hydraulic, Water Resources and Environment

Author

Pedro Miguel Borges Lopes

Supervised by

Jorge Eduardo Teixeira Leandro
M. Rita Fernandes de Carvalho

Coimbra, September, 2016

This thesis is dedicated to
my grandfather
Telmo de Lemos Lopes

Acknowledgements

I would like to express my sincere gratitude to the faculty and staff of the University of Coimbra and the researching centre MARE for hosting me during my Ph.D. A particular acknowledgement goes to my supervisors Dr. Jorge Leandro and Dr. Rita Fernandes de Carvalho for having given me the opportunity to stay in Coimbra to do my Ph.D and for having patiently guided me through it. Thanks also to Dr. James Shucksmith, Dr. Daniel Bung and Dr. Gavin Tabor for hosting me in their respective Universities during several months of my stays in Sheffield, Aachen and Exeter and for the invaluable help during the research.

I would like to express my gratitude to my friends and labmates: in Sheffield, Matteo; in Aachen, Lisa and Michael; in Exeter, Bernardas, Miriam, Recep and Shenan; and in Coimbra, Alex Almeida, João Marques, João Rocha, Nazmul, Ricardo Martins and Sílvia Carvalho, for their constant help and friendship. To all friends I have shared the house with, Anika, Danny, Felix, Gabriel, Scott and Thomas, my deepest thanks for welcoming me and making me feel a little closer to home. Also, thanks to Tânia and Courela that made it all the way from Portugal to come visit me wherever I was. And to all people I meet and I shared pieces of life during these years and have contributed to my success and happiness.

Finally, I would like to express my deepest gratitude to my parents Paulo and Cristina; my sister Joana; my grandparents Dolores and Agostinho, and my lovely wife Ana Gaudêncio. They became more than a family to me and without their support, this work would have not been possible.

Coimbra, September 2016

Pedro Lopes

Preamble

This work was funded by FCT (Portuguese Foundation for Science and Technology) through the Project UID/MAR/04292/2013 and Grant SFRH/BD/85783/2012, financed by MEC (Portuguese Ministry of Education and Science) and FSE (European Social Fund), under the programs POPH/QREN (2012-2013) (Human Potential Operational Programme from National Strategic Reference Framework) and POCH (2014-2016) (Human Capital Operational Programme) from Portugal2020.

An acknowledgement is owed to the following institutions that provided logistical and technical support during this Thesis:

- University of Coimbra
- MARE - Marine and Environmental Sciences Centre
- IMAR - Institute of Marine Research
- The University of Sheffield
- FH-Aachen - University of Applied Sciences
- College of Engineering, Mathematics and Physical Sciences (CEMPS) - University of Exeter

The numerical results here showed were performed on the Centaurus Cluster of the Laboratory for Advanced Computing of University of Coimbra, Portugal.

This work was accomplished using the Open Source CFD toolbox OpenFOAM®. OpenFOAM® is a registered trademark owned by OpenCFD® Limited (www.openfoam.com). OpenFOAM® is produced by OpenCFD® Limited – freely available and open source, licensed under the GNU General Public License.

This document was typeset with L^AT_EX 2_&. Mathematical symbols were realised using the *AMS*[®] packages for L^AT_EX provided by the American Mathematical Society. T_EX[®] and *AMS*[®] are registered trademarks of the American Mathematical Society (www.ams.org).

All other registered trademarks are property of their respective owners.

Financial Support:



Host Institutions:



Co-host Institutions:



The
University
Of
Sheffield.

FH AACHEN
UNIVERSITY OF APPLIED SCIENCES



Resumo

Quando a superfície livre se torna turbulenta e as instabilidades na interface entre o ar e a água são suficientemente grandes para quebrar as forças de tensão superficial, pode ocorrer emulsionamento de ar.

O estudo do emulsionamento de ar é de grande importância para a engenharia. São exemplos desses estudos a avaliação das perdas de energia e da altura mínima das paredes resultantes do dimensionamento de descarregadores de barragens, a previsão da perda / ganho de eficiência de drenagem em dispositivos de drenagem urbana pela presença de ar nas condutas, a simulação dos aspectos hidrodinâmicos resultantes da rebentação de ondas, ou a modelação dos processos de oxigenação de rios. No entanto, este fenômeno não pode ser resolvido usando apenas modelos baseados na técnica de Volume de fluido (VOF). O maior desafio reside na simulação da superfície livre, onde os modelos VOF comprovaram ser precisos, em conjunto com as pequenas flutuações da superfície livre (ordem de milímetros). Estas últimas tendem a ser menores do que o tamanho da malha de cálculo, e por isso não são detetáveis com modelos VOF, impedindo a correta simulação dos processos de formação de bolhas de ar, do seu transporte e das interações bolha / água.

O principal objetivo desta Tese é a simulação e análise das características fundamentais do escoamento com superfície livre em estruturas hidráulicas usando o modelo VOF presente no OpenFOAM®, para posteriormente melhorar a capacidade do “solver” original em simular o fenômeno de emulsionamento de ar.

A investigação apresentada nesta Tese começa por uma revisão da literatura onde são apresentados os principais métodos numéricos capazes de lidar com escoamentos ar / água com diferentes abordagens: escoamentos com superfície livre; escoamentos com fase continua e fase dispersa; escoamentos com superfície livre e uma fase dispersa; e principais conceitos sobre modelação do fenômeno de emulsionamento de ar. A par da realização de ensaios experimentais em sumidouros, caixas de visita e descarregadores em degraus, onde foram medidas a velocidade do escoamento, a posição da superfície livre e a concentração do ar, foram realizados vários testes numéricos com o objetivo de avaliar e melhorar a precisão e confiabilidade do “solver” *interFoam* do OpenFOAM®

relativamente ao comportamento hidrodinâmico do escoamento e a posição da superfície livre. Finalmente foi desenvolvido um novo “solver” capaz de avaliar a quantidade de ar gerada à superfície livre devido ao fenómeno de emulsionamento de ar, e de transportá-lo de acordo com o movimento do escoamento. Este “solver” utiliza um termo fonte para a deteção da quantidade de ar gerado por emulsionamento que foi, nesta Tese, tornado independente de quaisquer fatores de calibração.

As principais conclusões desta Tese mostram que o “solver” *interFoam* é capaz de resolver os processos hidrodinâmicos dos escoamentos em sumidouros e descarregadores em degraus e determinar a posição da superfície livre com grande robustez e precisão. Foi inclusivamente descrito um novo fenómeno de escoamento alternado no descarregador em degraus e produzida uma nova metodologia de deteção da superfície livre quando usado um modelo VOF. O novo modelo de emulsionamento de ar mostrou ser uma ferramenta eficaz na previsão da quantidade de ar formada à superfície livre e do seu transporte no seio da fase líquida do escoamento. Esta inclusão da fase dispersa permitiu a observação de um aumento da altura do escoamento no caso do descarregador de degraus e um incremento do coeficiente de drenagem no sumidouro. Foi também verificado que as velocidades encontradas na fase líquida não se alteraram significativamente com a presença de pequenas quantidades do ar.

Palavras-chave: Computação Dinâmica de fluidos (CFD), Emulsionamento de ar, Estruturas hidráulicas, OpenFOAM®, Superfície livre, Volume de Fluido (VOF)

Abstract

When the free-surface becomes turbulent and interface instabilities are large to disrupt the surface tension, a phenomena of air-entrainment or self-aeration is likely to occur.

Engineering concerns on the air-entrainment topic are vast. For instance the estimation of energy losses and the minimum walls height during the design stage of a spillway, the prediction of the loss / gain of efficiency in urban drainage elements due to air in pipes, the simulation of the hydrodynamic features of breaking waves, or even the simulation of river oxygenation in environmental engineering. However, this phenomena is far from being perfectly predicted using the common Volume-of-Fluid (VOF) models. The main challenge resides in simulation of the free-surface, in which the VOF models have proven to be accurate, together with the small fluctuations at the interface (order of millimetres). The smallest scales are likely to be smaller than the grid size, therefore not simulated by VOF models, but are still important in the simulation of bubble formation, their transport and iterations throughout the flow.

The aim of this Thesis is to replicate and analyse the free-surface flow characteristics in hydraulic structures using the VOF model present in the OpenFOAM[®], and further enhance the ability of the original solver to deal with the air-entrainment process.

The research presented in this Thesis starts by reviewing the literature on the most relevant numerical methods to deal with air-water flows in different approaches: free-surface flows, continuous-dispersed flows, free-surface flow with disperse phase and air-entrainment modelling. Physical experiences are performed in gullies, manholes and stepped spillways structures in order to acquire the flow velocities, free-surface position and air-concentration values. Further, several numerical tests in terms of accuracy and reliability of the *interFoam* solver, present in the OpenFOAM[®] toolbox, are performed to examine the flow hydrodynamics and free-surface position. Lastly, a new solver that computes the quantity of air generated at the free-surface and conveys that amount to the water body was developed and tested to the case of a stepped spillway and a gully. This solver uses a renewed air-entrainment source term that requires no calibration factor.

The main conclusions drawn are that *interFoam* solver returns a very robust and

reliable solution of flow dynamics and free-surface position when applied to cases as gullies and stepped spillways. An alternating skimming flow over the stepped spillways was described and a new methodology for free-surface detection when a VOF model is used was proposed. The new air-entrainment model proved to be an effective tool in the prediction of the quantity of air created at the free-surface and conveyed with the flow. The inclusion of dispersed air in the simulation contributed to the increment of flow depth in the stepped spillway and to a slight increase of drainage efficiency in case of the gully. The water velocities showed not to be affected by the presence of small quantities of dispersed air.

Keywords: Air-entrainment, Computational Fluid Dynamics (CFD), Free-surface, Hydraulic structures, OpenFOAM®, Volume-of-Fluid (VOF)

Table of Contents

Acknowledgements	iii
Preamble	v
Resumo	vii
Abstract	ix
Table of Contents	xi
Nomenclature	xvii
List of Figures	xxi
List of Tables	xxxi
List of Acronyms	xxxv
1 Introduction	1
1.1 Motivation	3
1.2 Aim and scope	5
1.3 Thesis structure	6
2 Literature Review	9
2.1 Methodologies for free-surface flows	11
2.1.1 Equations of motion	11
2.1.2 Turbulence modelling	11
2.1.3 Free-surface representation	13
2.1.3.1 Surface methods	13
2.1.3.2 Volume methods	15
2.2 Methodologies for continuous-dispersed two-phase flows	20

2.2.1	Two-fluid model	20
2.2.2	Algebraic Slip Mixture Model	22
2.2.3	Euler-Lagrange model	23
2.3	Hybrid formulations for two-fluid flows	24
2.4	Air-entrainment modelling	27
2.5	Experimental techniques and instrumentation for air-concentration measurements	31
2.5.1	Introduction	31
2.5.2	Intrusive devices	32
2.5.3	Non-intrusive techniques	33
3	Numerical and Experimental Investigation of a Gully Under Surcharge Conditions	35
3.1	Introduction	37
3.2	Experimental setup	38
3.3	Numerical simulations	39
3.4	Methodology	39
3.4.1	Experimental proceedings	39
3.4.2	Computational meshes	40
3.4.3	Boundary conditions	41
3.4.4	Computational simulations	41
3.5	Results	42
3.6	Discussion	44
3.7	Conclusions	48
4	Assessment of a VOF Model Ability to Reproduce the Efficiency of a Continuous Transverse Gully with Grate	49
4.1	Introduction	51
4.2	Experimental model	53
4.3	Numerical model	54
4.3.1	Mathematical formulation	54
4.3.2	Model description	55
4.3.3	Numerical mesh	56
4.3.4	Boundary conditions	56
4.3.5	Numerical approaches	58
4.4	Results	60
4.4.1	Influence of mesh refinement on inflows	60
4.4.2	Grate efficiency (numerical vs. experimental)	61

4.5	Discussion	63
4.5.1	Influence of mesh refinement on inflows	63
4.5.2	Grate efficiency (numerical vs. experimental)	63
4.6	Conclusions	65
5	Air-entrainment Characterization and Velocities Profiles in a Scaled Circular Manhole	67
5.1	Introduction	69
5.2	Experimental setup	69
5.3	Methodology	71
5.3.1	Acoustic Doppler Velocimeter measurements	71
5.3.2	Air-probe	72
5.4	Results	73
5.4.1	Mean velocities	73
5.4.2	Reynolds Stresses	74
5.4.2.1	Normal Stress	74
5.4.2.2	Shear Stress	74
5.4.3	Air profiles	74
5.5	Discussion	75
5.6	Conclusions	77
6	Numerical Procedure for Free-surface Detection Using a Volume-of-Fluid Model	79
6.1	Introduction	81
6.2	Numerical model	82
6.3	Experimental tests	85
6.4	Numerical procedure for free-surface detection	86
6.4.1	Flow depths at non-aerated flow region	86
6.4.2	Full numerical free-surface position	87
6.4.3	Top view of water depths	88
6.5	Discussion	91
6.5.1	Free-surface detection	91
6.5.2	Top view of water depths	93
6.6	Conclusions	93
7	Alternating Skimming Flow Over a Stepped Spillway	95
7.1	Introduction	97
7.2	Experimental tests	99

7.2.1	Experimental stepped spillway 0.5 m wide	99
7.2.2	Experimental stepped spillway 0.3 m wide	100
7.2.3	Ultrasonic sensor	100
7.2.4	High speed camera	101
7.3	Numerical model	102
7.3.1	Model equations	102
7.3.2	Computational domains, grid convergence study and model settings	104
7.3.3	Physical fluids properties, initial and boundary conditions	105
7.4	Methods to measure the free-surface	105
7.4.1	Free-surface measured with the ultrasonic sensor	105
7.4.2	Numerical procedure for free-surface detection	106
7.5	Model validation	106
7.6	Results	108
7.6.1	Flow stream-lines and flow pattern alternation	108
7.6.2	Flow properties	109
7.6.3	Turbulence statistics	110
7.7	Discussion	110
7.8	Conclusions	114
8	Explicit Calculation of Natural Aeration Using a Volume-of-Fluid Model	117
8.1	Introduction	119
8.2	Numerical model	121
8.2.1	General concepts	121
8.2.2	Bubble formation	123
8.2.3	Interface location	124
8.3	Results: example cases	125
8.3.1	2D Dam-break	125
8.3.2	3D vertical plunging jet	127
8.3.2.1	Radial velocity profiles	130
8.3.2.2	Free-surface detection and bubble formation	132
8.4	Conclusions	135
9	Flow Self-aeration Using a Sub-grid Volume-of-Fluid Model	137
9.1	Introduction	139
9.2	Mathematical formulation of the air-entrainment model	141
9.2.1	General concepts	141
9.2.1.1	Mean flow equations	141
9.2.1.2	VOF model	142

9.2.1.3	Turbulence model	143
9.2.2	Mass conservation of dispersed gas	143
9.2.3	Source of air at the free-surface	144
9.2.3.1	Volumetric source term	144
9.2.3.2	Free surface detection	146
9.2.3.3	Surface disturbances	146
9.2.4	Bubble breakup at free-surface	147
9.2.5	Two-fluid model closure	147
9.2.6	Solution procedure	148
9.3	Description of the experimental facility	148
9.4	Computational tests	150
9.5	Results	153
9.5.1	Free-surface detection	153
9.5.2	Influence of surface disturbances formulas and source of air	153
9.5.3	Air-concentration profiles	154
9.5.4	Flow velocity	157
9.6	Discussion	159
9.6.1	Free-surface detection	159
9.6.2	Surface disturbances, source of air and free-surface shape	159
9.6.3	Air-concentration and velocity profiles	160
9.7	Conclusions	162
10	Numerical and experimental study of the fundamental flow characteristics of a 3D gully box under drainage	163
10.1	Introduction	165
10.2	Experimental apparatus	167
10.3	Numerical model	168
10.3.1	General flow equations	168
10.3.2	Free-surface position	168
10.3.3	Turbulence closure	170
10.3.4	Sub-grid air-entrainment model	170
10.3.5	Mesh, initial and boundary conditions	171
10.3.6	Model discretisation and solution methods	172
10.4	Methodology	172
10.4.1	Experimental methodology	172
10.4.2	Numerical methodology	173
10.5	Results and Discussion	174

10.5.1 Steady-state achievement	174
10.5.2 Free-surface position	174
10.5.3 Velocity and turbulence	175
10.5.4 Time-averaging of air-concentration profiles	178
10.5.5 Discharge coefficients	180
10.6 Conclusions	182
11 Final Remarks	185
11.1 Conclusions	187
11.2 Research question	189
11.3 Future work	190
References	191
Appendix A Publications	213
Appendix B Workflow	217

Nomenclature

Roman letters

$\bar{\mathbf{u}}, \mathbf{U}$	mean velocity vector
\bar{u}, U	mean velocity
$\hat{\mathbf{g}}$	unit gravity vector
$\hat{\mathbf{n}}$	unit normal vector to the free-surface
\mathbf{f}, \mathbf{F}	volumetric force
\mathbf{f}_σ	volumetric surface tension force
\mathbf{g}	gravity vector
\mathbf{n}	normal vector to the free-surface
\mathbf{u}	velocity vector
\mathbf{x}	cartesian coordinates vector
u, v, w	component in x,y,z of velocity
a	surface disturbances
B	width in flow direction
C_α	binary coefficient to activate the compressive term
C_μ	constant for turbulence model
C_{air}	constant for air-entrainment model
D	diameter
E	efficiency
E_g	air-entrainment term
Fr	Froude number
g	gravity
H	drop height, height
h	water depth
h_c	critical water depth

I	turbulent intensity
i	slope
k	turbulent kinetic energy
L	characteristic length, length
l	step length, length scale
l'	turbulent length scale
p, P	total pressure
p^*	difference between total and hydrostatic pressure
Q	discharge
q	unit discharge
r	radius
Re	Reynolds number
s	step height
S_g	source term for air-entrainment
u	velocity
V	volume
w	step width or channel width
X, Y, Z	cartesian coordinates
x, y, z	cartesian coordinates

Greek letters

α	volume fraction
δ_{fs}	free-surface position indicator
Γ	difusivity
κ	interface curvature
τ	shear stress tensor
μ	dynamic viscosity
ν	kinematic viscosity
ϕ	general scalar property
ϕ_{ent}	interface thickness
ρ	density
σ	surface tension
ε	rate of energy dissipation
φ	slope

Subscripts

<i>a</i>	air
<i>b</i>	bubble
<i>c</i>	critical, compressive
<i>fk</i>	fluid <i>k</i>
<i>g</i>	gas phase, grate
<i>k</i>	phase indicator, $k = \{1, 2\}$
<i>l</i>	liquid phase
<i>m</i>	mixture
<i>P</i>	particle
<i>p</i>	secondary phase
<i>q</i>	primary phase
<i>t</i>	turbulent
<i>w</i>	water

List of Figures

Introduction	1
Literature Review	9
2.1 Surface methods to treat the interface: (a) Particles on interface method; (b) Height function method; and (c) LS method.	15
2.2 Volume methods to treat the interface: (a) Particles on fluid - MAC; and (b) Volume fraction method - VOF.	17
2.3 Volume fraction method SLIC: (a) Accurate distribution; (b) SLIC x-sweep; and (c) SLIC y-sweep. Adapted from (Ubbink, 1997).	17
2.4 Volume fraction method PLIC: (a) Accurate distribution; (b) PLIC; and (c) FLAIR. Adapted from (Ubbink, 1997).	18
2.5 Methodologies for continuous-dispersed two-phase flows: (a) Two-fluid model; (b) Algebraic Slip Mixture Model (ASMM); and (c) Euler-Lagrange. Black and blue arrows stands for the velocity of phase 1 (continuous) and phase 2 (dispersed) respectively. Red arrows are mixture velocities. Values on bottom-right corner of the cells are volume fraction values of phase 2. Adapted from (Rusche, 2002).	24
Numerical and Experimental Investigation of a Gully Under Surcharge Conditions	35
3.1 (a) Sketch of the experimental installation used for the study of the reverse flow [mm]. (b) Photograph of the experimental installation.	38
3.2 Points measured at the left (points 1 to 9) and right side of the gully (points 10 to 18).	40
3.3 3D view of mesh, grid detail and boundary conditions used in the numerical model OpenFOAM® for studying reverse flow in the gully.	41

3.4 Heights of the flow for different set of LES parameters (C_ε and C_k) using the simulation with 5 l/s at the inlet (Q5).	42
3.5 Average contour obtained with OpenFOAM® numerical model (—) compared with photographs in background and a Computational Vision Model (××) (Roque, 2011) for (a) Q4, (b) Q5 and (c) Q6.	43
3.6 (a) Total pressure (Pt) at the gully bottom in the centre profile. (b) Dynamic pressure (Pd) at the gully bottom in the centre profile.	43
3.7 (a) Flow heights in top of the gully. The triangles represent the maximum height of the jet (hJ), the squares represent the height at left side of the jet (hL), while the circles represents the height at right side (hR). The relations h-Q are shown in the figure. (b) Average total pressure (Pt) and average dynamic pressure (Pd) at gully bottom. The triangles represent the average pressure at the inlet (C), the squares represent the average pressure at left side of gully bottom (L), while the circles represents average pressure at right side of gully bottom (R). The relations Pt-Q and Pd-Q are shown in the figure.	44
3.8 Stream lines obtained with the numerical model in the middle longitudinal section of the gully. *Extrapolated discharges.	45
3.9 Velocity fields obtained with the numerical model in the middle longitudinal section of the gully. *Extrapolated discharges.	45
3.10 Sketch of centre point in the top of the gully and theta angle used for the study of the behaviour of the jet.	46
3.11 Velocities at directions x, y and z in the center point on the top of the gully for Q6.	46
3.12 FFT analysis for the theta angle and velocity Vz using Data Analysis Package using Q6.	46
3.13 (a) Histogram of frequencies of the theta angle. The 0 radians means the vector Vxy takes the positive direction of x-axis. This angle is illustrated schematically in the Fig. 3.10. (b) Histogram of frequencies for the velocity Vz in the centre point on top of the gully. This point is illustrated schematically in the Fig. 3.10.	47

Assessment of a VOF Model Ability to Reproduce the Efficiency of a Continuous Transverse Gully with Grate 49

4.1 Photographs of the experimental installation built at UPC Hydraulic Department: (a) rectangular platform with transverse grate downstream; (b) single grate type 2. Photographs by B. Russo.	53
--	----

4.2	Sketch of the experimental installation: (a) top view, (b) detail of grate and (c) cut B-B'. Units in millimetres.	55
4.3	Detail of the meshes used in this study: (a) Mesh 1 - homogeneous mesh with ranging spaces between 2 and 3 mm (b) Mesh2 – mesh refined at the channel bottom with cells 1 mm spaced.	57
4.4	Sketch of the simplified geometry of the grate, flow comes from the inflow boundary to the outflow. All the measures are in millimetres. The red point on the beginning of the grate hole identifies the axis origin.	57
4.5	Sketch of the process to calculate the coefficients C_1 and C_2 , used to calculated the corrected intercepted flow (CIF) using the numerical intercepted flow (NIF). Q_i , Q_{if} and Q_{out} are respectively the Inflow, Intercepted Flow and Outflow for one slot; Q_I , Q_{IF} and Q_{OUT} are respectively the Inflow, Intercepted Flow and Outflow for a group of slots.	59
4.6	3D image of free-surface average position over the slot and the correspondent choice of coefficients. For all the simulations, $i_x = 4\%$. Lw is the slot length occupied with water, L_s is the length of the grate slot.	60
4.7	Contour graph of RDE . q are the unit discharges and i_x the longitudinal slope of the channel.	61
4.8	Relative deviations between the numerical and the experimental efficiency.	62
4.9	Graph relating the efficiency with Froude number (F), flow depth (h) and width of the grate in the flow direction (B_g).	62

Air-entrainment Characterization and Velocities Profiles in a Scaled Circular Manhole

67

5.1	(a) Schematic representation of the experimental setup. Measures in [mm]. (b) Photograph of drainage surface. (c) Photograph of manhole and horizontal pipes for Conf1. (d) Photograph of manhole and horizontal pipes for Conf2.	70
5.2	Sketch of the manhole and the measured points with ADV Vectrino: (a) Lateral view, (b) Plane view.	72
5.3	Mean velocities at vertical profiles for: (a) Conf1, plane XZ; (b) Conf1, plane YZ; (c) Conf2, plane XZ; (d) Conf2, plane YZ.	73
5.4	3D stream-lines for (a) Conf1 and (b) Conf2.	74
5.5	Normal Stress $\langle uu \rangle$, $\langle vv \rangle$ and $\langle ww \rangle$ on plane XZ for (a) Conf1 and (b) Conf2.	75
5.6	Shear Stress $\langle uw \rangle$, $\langle uv \rangle$ and $\langle vw \rangle$ on plane XZ for (a) Conf1 and (b) Conf2.	76

5.7 Air concentration profiles at plane XZ (a-b) and plane XY (c-d).	76
--	----

Numerical Procedure for Free-surface Detection Using a Volume-of-Fluid Model	79
6.1 Scheme of stepped spillway, numerical model geometry, dimensions and mesh. Dimensions in meters.	84
6.2 Normalized water depth $h_w/h_{w,I}$ upstream of the inception point of aeration (where $X/X_I = 1.0$) for: experimental data from ultrasonic sensors; numerical $\alpha = 0.1$, $\alpha = 0.5$, $\alpha = 0.9$ and empirical expression of Meireles and Matos (2009).	87
6.3 Mean water levels measured experimentally with the central ultrasonic sensors at each step edge ($\bar{h}_{w,MicUS}$) and water levels calculated numerically by plotting the α isolines from 0.1 to 0.9 ($h_{w,N}$).	87
6.4 Values of numerical water volume fractions (α) that better match the mean flow depth measured with the ultrasonic sensors at each step edge from step 1 to 19 (o) and best-fit functions: $W\alpha(S)$ Eq. (6.8) (dashed-line) and $G\alpha(S)$ Eq. (6.9) (dash-long dash line). The contour lines on background image represent relative errors between the depth predicted by different α isolines and experimental data.	89
6.5 Mean water levels measured experimentally with the central ultrasonic sensors at each step edge ($\bar{h}_{w,MicUS}$) and water levels calculated numerically by applying Gumbel equation ($h_{w,Gumbel}$).	89
6.6 (a) Average flow depths measured with a set of three ultrasonic sensors ($\bar{h}_{w,MicUS}$) (sample rate: 200 Hz, acquisition time: 180 s) at each step edge from 1st to 19th step for $s = 0.06$ m, $w = 0.5$ m, $q = 0.07$ $m^2 s^{-1}$. The lateral ultrasonic sensors were distanced from spillway walls 80 mm. The circles identifies the influence areas of Microsonic Ultrasonic Sensor (MicUS). The pseudo-bottom corresponds to water level equal to zero. (b) Numerical free-surface level calculated with $\alpha = 0.1$. (c) Numerical free-surface level calculated with $\alpha = 0.5$. (d) Numerical free-surface level calculated with $\alpha = 0.7$	90
6.7 Numerical 2D average flow depths profile where α isoline is changing at every step edge according to Eq. (6.9).	90
Alternating Skimming Flow Over a Stepped Spillway	95

7.1	Experimental scheme of SSP05, numerical model geometry, dimensions and mesh. Dimensions in meters. The origin of system of coordinates XYZ is located at the end of the approaching channel, for which X is aligned with the pseudo-bottom. The system of coordinates xyz is used by the numerical model.	100
7.2	Photographs of the differences in flow patterns at (a) SSP05 and (b) SSP03. The photograph shown in (a) was slightly taken from above and as such some part of the water surface area is visible. Mean water level is marked in a dashed line. SK1 is a sub-regime of the skimming flow in which the mixing layer does not reach the end of the step. SK2 is a sub-regime where the recirculation vortex extend nearly over the step length interfering sometimes with the wake formation of the subsequent step.	101
7.3	Mean water levels measured experimentally with the Ultrasonic Sensor (US) at each step edge ($\bar{h}_{w,US}$) and water levels calculated numerically by plotting the $\alpha = 0.5$ and the limits of ± 0.4 ($h_{w,N}$). Data are taken from SSP05. . .	107
7.4	Bubble image velocimetry vs. numerical velocity profiles at step niches (SN) 6 to 13. Pearson (1986) (r^2) and Willmott (1981) (d) measures of fit are plotted on each graphic. $Z = 0$ refers to the pseudo-bottom level whereas Z_{max} is the free-surface level measured with the Ultrasonic sensors at each step edge ($\bar{h}_{w,US}$). Data are taken from SSP05.	108
7.5	Flow stream-lines and pressure on the steps calculated in SSP05.	109
7.6	Flow stream-lines and pressure on the steps calculated in SSP03.	110
7.7	Modelled averaged velocities of SSP05 at: (a) $Y = 0$ m and (b) $Y = Y_{max}/3$ [m] and of SSP03 at: (c) $Y = 0$ m and (d) $Y = Y_{max}/3$ [m]. X is the distance to the spillway crest and Z the vertical axis, perpendicular to the pseudo-bottom plane. U_{XZ} is the projection of the velocity vector on the plane XZ. The free-surface is represented by $\alpha = 0.5$. The contour lines delineate the velocity categories shown in the label.	111
7.8	Normalized velocity profiles at step niches from SN8 to SN13 in the two stepped spillways SSP03 and SSP05.	112
7.9	Flow velocities calculated at step 12 using: (a) Bubble Image Velocimetry (BIV), (b) numeric; and at step 13 using: (c) BIV, (d) numeric of SSP05. .	113
7.10	Modelled averaged turbulent kinetic energy at centre-line of stepped spillway: (a) SSP05 and (b) SSP03. X is the distance to the spillway crest and Z the vertical axis, perpendicular to the pseudo-bottom plane. The free-surface is represented by $\alpha = 0.5$. The contour lines delineate the categories shown in the label.	113

Explicit Calculation of Natural Aeration Using a Volume-of-Fluid Model 117

8.1	Free-surface with physical parameters used. Adapted from Ervine and Falvey (1987).	124
8.2	2D dam-break domain.	125
8.3	Dam-break process for the time steps $t = 0.1, 0.3, 0.7$ and 1.0s using the finest mesh (64×64 cells). Top images are photographs of the experiment, middle figures (a) show the function to detect the free-surface position (ϕ_{FS}) and bottom figures (b) show the bubble formation term (E_g) and its volume fraction on the cells ($E_{g,frac}$).	126
8.4	Mesh influence study of dam-break case at $t = 0.8\text{s}$. From the left to right the meshes are: 16×16 , 32×32 , 46×46 and 64×64 cells. Top figures (a) show the function to detect the free-surface position (ϕ_{FS}) and bottom figures (b) show the bubble formation term (E_g) and its volume fraction on the cells ($E_{g,frac}$).	126
8.5	Vertically-centred slice of the computational domain for the 3D circular plunging jet problem. The mesh presented corresponds to G0.00125 (Table 8.1).	128
8.6	Liquid velocity for pool depths (a) $x = 0.8d_1$ (m), (b) $x = 1.2d_1$ (m) and (c) $x = 2.0d_1$ (m). $U_1 = 3.5 \text{ m s}^{-1}$, $d_1 = 0.024 \text{ m}$ and $r_1 = 0.012 \text{ m}$	130
8.7	Liquid velocity profiles for some horizontal profiles along the pool depth ($x = 0.8d_1$ to $10.0d_1$). U_x is the velocity on the jet axis, x is the vertical direction and b the value of r where the velocity is half of the velocity on the jet axis. The profiles are compared with the solutions of (a) Wilcox and (b) Tollmien using mesh G0.0008	131
8.8	Temporal-averaged free-surface and air-cavity determined by: (a) keeping the finer mesh (G0.0008) and changing α value and (b) keeping $\alpha = 0.3$ and changing the mesh refinement. The x (m) axis is the vertical direction and r_1 (m) the jet radius at impact zone ($r_1 = 0.012 \text{ m}$).	132
8.9	2D centre-slice profiles of the free-surface and bubble formation term using the meshes: (a) G0.0008, (b) G0.00125, (c) G0.0025 and (d) G0.005. Isolines correspond to $\phi_{FS} = 0.1, 0.5$ and 0.9 . The axis x is the vertical direction and r_1 the jet radius at impact zone ($r_1 = 0.012 \text{ m}$).	134
8.10	Comparison between the value of free-surface wave amplitude (a) using (a) the formulation of Ma et al. (2011b) and (b) the concept proposed in this paper. The location of the free-surface is represented by $\alpha = 0.3$	134

Flow Self-aeration Using a Sub-grid Volume-of-Fluid Model**137**

9.1	Schematic representation of free-surface with definition of physical parameters.	145
9.2	Flow chart of the model. Light grey boxes are part of the standard <i>interFoam</i> solver. Dark grey boxes are additions to the code made in this work.	149
9.3	Scheme of the experimental installation.	150
9.4	Mesh convergence study: (a) X-velocity profiles placed above the 12th step edge; (b) Fine-grid M1 solution with discretisation error bars.	151
9.5	Detail of free-surface above steps 1 to 5 using (a) Volume-of-Fluid (VOF) equation (9.3) (test T1), (b) free-surface detection based on α_l values ($\delta_{fa,alpha}$) expressed by equation (9.15) (test T2) and (c) free-surface detection based on the gradient of α_l ($\delta_{fa,gradient}$), given by the algebraic equation (9.16) (test T3). Profiles taken at centre-channel.	153
9.6	Surface disturbances calculated along the stepped spillway for tests: T5 - surface disturbances calculated with a_3 , T7 - surface disturbances calculated with a_2 , and T8i/T9 - surface disturbances calculated with a_1 . Tests T5-i,ii,iii,iv applies respectively the calibration coefficient $C_{ent} = 0.01, 0.02, 0.05$ and 0.1. Test T9 differs from T8i by applying a limiter to S_g . Dots represent the surface disturbances calculated with the ultrasonic sensor.	154
9.7	Free-surface evolution delimited by $\alpha_l = 0.5$ for tests: T1 - no air model, T5i - surface disturbances calculated with a_3 and $C_{ent} = 0.1$, and T8i/T9 - surface disturbances calculated with a_1 . Test T9 differs from T8i by applying a limiter to S_g . Box plots represent the water depths measured with the ultrasonic sensor at each step edge, in which the whiskers represent the 2nd percentile and the 98th percentile. Profiles taken at centre-channel.	155
9.8	3D view of S_g term calculated at free-surface delimited by $\alpha_l = 0.5$ for tests: (a) T8i - simulation without limiter on S_g and (b) T9 - simulation with limiter on S_g	155
9.9	Air concentration profiles above step niche 12 for tests: T3 - Gas velocity $\bar{\mathbf{u}}_g = \bar{\mathbf{u}}_l$, T4 - two-way coupling model and gas velocity $\bar{\mathbf{u}}_g = \bar{\mathbf{u}}_l$, T5 - two-way coupling model and gas velocity $\bar{\mathbf{u}}_g = \bar{\mathbf{u}}_l + \bar{\mathbf{u}}_r$, and T6 - diffusivity term active. Profiles taken at centre-channel. Z=0 corresponds to pseudo-bottom level.	156
9.10	Sensibility test of air-concentration profile above step niche 12 for tests: (a) T5-i,ii,iii,iv - changing C_{air} constant in surface disturbances formula a_3 , and (b) T8-i,ii,iii,iv - changing bubble breakup factor at free-surface. Profiles taken at centre-channel. Z=0 corresponds to pseudo-bottom position.	156

9.11 Air-concentration profiles at odd Step Niches (SN) from 5 to 13 for tests: T1 - no air model, T8i - with air model, and T9 - with air model and limiters on S_g . Numerical results are plotted against experimental air-concentration profiles taken with air-concentration probe. Profiles taken at centre-channel. Z=0 corresponds to pseudo-bottom position.	157
9.12 X-velocity profiles at SN from 6 to 13 for tests: T1 - no air model, T8i - with air model, and T9 - with air model and limiters on S_g . Numerical results are plotted against data from BIV. Profiles taken at centre-channel. Z=0 corresponds to pseudo-bottom position.	158
Numerical and experimental study of the fundamental flow characteristics of a 3D gully box under drainage	163
10.1 Some examples of linking-elements: (a) grated inlet close to a side walk (Coimbra, Portugal), (b) curbside inlet (Coimbra, Portugal), (c) continuous grated inlets placed transversally to the street (Coimbra, Portugal), and (d) grated drop manhole in a park (Sheffield, United Kingdom). Photographs from author.	166
10.2 Steady-state convergence check for numerical simulations S1 (VOF), S2 (VOF + turbulence) and S3 (VOF + turbulence + air).	167
10.3 Numerical mesh and boundary conditions definition.	172
10.4 Steady-state convergence check for numerical simulations S1 (RANS + VOF), S2 (RANS + VOF + turbulence) and S3 (RANS + VOF + turbulence + air).	175
10.5 Free-surface position detected by $\alpha=0.1, 0.5$ and 0.9 at $y=0$ m for simulations: (a) S1 (RANS + VOF), (b) S2 (RANS + VOF + turbulence) and (c) S3 (RANS + VOF + turbulence + air). Dots mark the experimental free-surface position detected by the Computational Vision Model.	176
10.6 Time-averaged velocity fields at centre-plane of the gully: (a) measured with ADV, and simulations (b) S1 (RANS + VOF), (c) S2 (RANS + VOF + turbulence) and (d) S3 (RANS + VOF + turbulence + air). Blue area on top of ADV measurements indicate a zone where the signal correlation was low and no measurements were done.	177
10.7 Time-averaged turbulent kinetic energy profile at centre-plane of the gully: (a) measured with ADV, and (b) simulation S3 (similar results for S2) (RANS + VOF + turbulence + air).	177

10.8 Time-averaged air-concentration profiles (45-50s) using simulation S3, at positions (a) $y=0.1$ (back panel), (b) $y=0.04$, (c) $y=0$, (d) $y=-0.04$ and (e) $y=-0.1$ m (front panel). (f) Experimental observation.	178
10.9 Time-averaged air-concentration profiles interpolated over y-axis using simulation S3 in the time intervals: (a) 10-15 s, (b) 15-20 s, (c) 20-25 s, (d) 25-30 s, (e) 30-35 s, (f) 35-40 s, (g) 40-45 s and (h) 45-50 s. (i) Experimental observation.	179
10.10 Weir (C_w) and orifice (C_o) discharge coefficients for simulations S1, S2 and S3. Lines are the coefficients found by Martins et al. (2014). Asterisks (*) are simulations were the outlet boundary conditions characterises the experiments of Martins et al. (2014).	181
Final Remarks	185

List of Tables

Introduction	1
Literature Review	9
Numerical and Experimental Investigation of a Gully Under Surcharge Conditions	35
3.1 Summary of the discharge conditions performed in the experimental installation. Q – Flow at inlet (overflow), D – Internal diameter of pipe inlet, U – Velocity at inlet, Re – Reynolds Number, Fr – Froude Number.	39
3.2 Average Relative Errors (ARE) for numerical and experimental velocities at left (AREl) and at right (AREr) points of gully (see Fig. 3.2) for the five set of LES coefficients tested.	42
3.3 Sample Kolmogorov-Smirnov Test for the histograms presented in Fig. 3.13b.	46
Assessment of a VOF Model Ability to Reproduce the Efficiency of a Continuous Transverse Gully with Grate	49
4.1 Distribution of the applied correction coefficients (C_1) and (C_2), respectively described by (10) and (11). q are the unit discharges in $L/s/m$ and i_x the longitudinal slope of the channel in %. Note: * Simulations where the experimental efficiency is 1.	59
4.2 Relative deviations on the inflows (RDI) for the two meshed proposed – Mesh 1 and Mesh 2. q are the unit discharges and i_x the longitudinal slope of the channel.	60

4.3 Quantitative statistical coefficients to investigate the model accuracy. The coefficients relate the gully efficiency (experimental vs. numerical) for the range of flows from 16.67 to 66.67 $L/s/m$. d – Index of agreement; NSE – Nash-Sutcliffe Efficiency; $RMSD$ – Root Mean Square Deviation; $PBIAS$ – Percent Bias.	63
---	----

Air-entrainment Characterization and Velocities Profiles in a Scaled Circular Manhole 67

5.1 Experimental configurations. Q is the flow discharge, q is the unit flow discharge, h is the flow depth, U is the average velocity, Re is the Reynolds number ($Re=UD/\nu$) and Fr is the Froude number ($Fr=U/(gh_{surface})^{0.5}$)	71
---	----

Numerical Procedure for Free-surface Detection Using a Volume-of-Fluid Model 79

6.1 Constants used to fit the data marked with (o) on Fig. 6.4 to equations Eq. (6.8) and Eq. (6.9). The result of the measures of fit: Pearson's R-square (R2) (Pearson, 1986), Nash-Sutcliffe Efficiency (NSE) (Nash and Sutcliffe, 1970) and Index of agreement (d) (Willmott, 1981) are also presented.	88
6.2 Fit coefficients between the numerical flow depths calculated with Equation (6.9), $\alpha = 0.1$, $\alpha = 0.5$ and $\alpha = 0.7$ with experimental data at $Y = -0.17\text{ m}$, $Y = 0.0\text{ m}$, $Y = 0.17\text{ m}$ and global. The fit models are: R2 (Pearson, 1986), NSE (Nash and Sutcliffe, 1970) and d (Willmott, 1981). Color ■ highlights values higher than 0.8, color ■ highlights values higher than 0.5 and lower than 0.8, color ■ highlights values higher than 0.0 and lower than 0.5, and color ■ highlights values lower than 0.0.	91

Alternating Skimming Flow Over a Stepped Spillway 95

7.1 Model constants.	105
------------------------------	-----

Explicit Calculation of Natural Aeration Using a Volume-of-Fluid Model 117

8.1 Grid characteristics to demonstrate the mesh dependency. Zones $Z1$, $Z2$ and $Z3$ are represented in Fig. 8.5. *In this case, cells with 0.0008 m edges were placed just on the intersection between jet and pool.	129
---	-----

Flow Self-aeration Using a Sub-grid Volume-of-Fluid Model 137

9.1	Summary of tests and simulation settings used in this work. Gas velocity settings and Diffusivity are explained in §9.2.2. Model closure is explained in §9.2.5. Free-surface detection models (δ_{fs}) are described in §9.2.3.2. Surface disturbances formulas (a) are explained in §9.2.3.3. Bubble breakup settins are explained in §9.2.4. Limiters on S_g are presented in §9.2.3.	152
9.2	Accuracy of the tests T1, T8i and T9 in comparison to experimental air-concentration profiles measured with an air-concentration probe. NSE and Pearson- R^2 are used to quantitatively describe the accuracy of model outputs. An efficiency of 100% corresponds to a perfect match of modelled air-concentration profiles to the measured data. Bold numbers mark the best of NSE and R^2 for each step niche profile.	158
9.3	Accuracy of the tests T1, T8i and T9 in comparison to experimental velocity profiles measured using BIV technique. NSE and Pearson- R^2 are used to quantitatively describe the accuracy of model outputs. An efficiency of 100% corresponds to a perfect match of modelled velocity profiles to the measured data. Bold numbers mark the best of NSE and R^2 for each step niche profile.	159
Numerical and experimental study of the fundamental flow characteristics of a 3D gully box under drainage		163
10.1	Summary of simulation cases tested in this work.	174
Final Remarks		185

List of Acronyms

2D	Two-dimensional
3D	Three-dimensional
ADV	Acoustic Doppler Velocimeter
AIAD	Algebraic Interface Area Density
ARE	Average Relative Errors
ASM	Algebraic Stress Model
ASMM	Algebraic Slip Mixture Model
BC	Boundary Condition
BIV	Bubble Image Velocimetry
CAD	Computer-Aided Design
CICSAM	Compressive Interface Capturing Scheme for Arbitrary Meshes
CIF	Corrected Intercepted Flow
CFD	Computational Fluid Dynamics
CLSVOF	Combined Level-Set Volume-of-Fluid
COR	Correlation
CSF	Continuous Surface Force
d	Index of agreement
DAS	Donor-Acceptor Scheme
DD	Dual Drainage
DNS	Direct Numerical Simulation
FHWA	Federal Highway Administration
FFT	Fast Fourier Transforms

FLAIR	Flux Line-segment model for Advection and Interface Reconstruction
FAVOR	Fractional Area Volume Obstacle Representation
GCI	Global Convergence Index
GUI	Graphical User Interface
HRIC	High Resolution Interface Capturing
IPCC	International Panel to the Climate Changes
IPP	Image Processing Procedure
LES	Large-Eddy Simulation
LLS	Large-Length Scales
LS	Level-Set
MAC	Marker-And-Cell
MCLS	Mass-Conserving Level-Set
MicUS	Microsonic Ultrasonic Sensor
MLE	Multiple-Linking-Elements
MULES	Multidimensional Universal Limiter with Explicit Solution
MUSIG	Multiple Size Group
NIF	Numerical Intercepted Flow
NSE	Nash-Sutcliffe Efficiency
NVD	Normalised Variable Diagram
PBIAS	Percent-Bias
PDF	Probability Density Function
PISO	Pressure Implicit with Splitting of Operator
PIV	Particle Image Velocimetry
PLIC	Piecewise Linear Interface Calculation
R²	Pearson's R-square
RANS	Reynolds-Averaged Navier-Stokes
RAS	Reynolds-Averaged Simulation
RDE	Relative Deviation for Efficiency
RDI	Relative Deviation for Inflow

RMSD	Root-Mean-Square Deviation
RNG	Re-Normalisation Group
RSM	Reynolds Stress Model
SCADA	Supervision, Control And Data Acquisition
SGS	Sub-Grid Scale
SLS	Small-Length Scales
SLIC	Simple Line Interface Calculation
SN	Step Niches
SNR	Signal Noise Ratio
SST	Shear-stress transport
STL	STereoLithography
TKE	Turbulent Kinetic Energy
TVD	Total Variation Diminishing
UK	United Kingdom
UDS	Urban Drainage System
US	Ultrasonic Sensor
USACE	United States Army Corps of Engineers
VOF	Volume-of-Fluid
WES	Waterways Experiment Station

1

Introduction

1.1 Motivation

Air and water are constantly interacting in a very unstable and complex way throughout their interface. In case of air-water flows over hydraulic structures, the study of the air-water flows and their interactions allows the comprehension of the hydraulic performance of those structures, but also the anticipation of the effects caused by an eventual (un)desirable hydraulic phenomena. For instance, when the turbulence level at the air-water interface is large enough to overcome both surface tension and gravity forces, the air naturally starts entraining into the water, resulting in a phenomena commonly called air-entrainment or self-aeration.

The air-entrainment is a phenomenon that occurs in many environmental and engineering applications. Among other consequences, the air-entrainment phenomena is responsible for the increment of volume of the flow, changes in the density and the turbulent structure, an adequate supply of dissolved oxygen and carbon dioxide, and a positive play against pollution. First attempts to comprehend the air-entrainment can be traced back to the works of Straub and Anderson (1958) which described the self-aerated process of open-channel flows; Rajaratnam (1962) that described the aeration process of turbulent jets; Bormann (1968), Keller et al. (1974), and Wood (1991) that worked on self-aeration process on spillways; and Volkart (1980) which developed an investigation on the self-aerated flow process in steep and partially filled conduits of circular shape.

In hydraulic engineering, controlled aeration is often used to protect large spillways from cavitation damage (Falvey, 1980a,b; Kiger and Duncan, 2012; Bureau of Reclamation, 2015); to predict the water flow depth in the design stage of those structures (Falvey, 1980a); to increase the momentum, as the air within the boundary layer reduces the shear stress (Ackers and Priesley, 1985; Chanson, 1993); or to re-oxygenate the water flow, which contributes to the downstream river quality and the preservation of aerobic species (Chanson, 1997).

In urban drainage elements, air in storm-water pipes may get trapped and negatively affect the system (Pothof and Clemens, 2010) as in the failure of operation due to excess of air entrained at the pumps' inlet or at air valves (Lubbers and Clemens, 2005), producing energy losses in pressurized pipes (Lubbers and Clemens, 2006) or an associated capacity reduction in the passage from drop manholes to the pipes (Granata et al., 2014a).

In some industrial processes, the flow aeration is deliberately produced when jet impacts in the mass of water, generating high quantities of air bubbles in the water - the plunging jets. Plunging liquid jets can be found in the steel teeming process, waste-water treatment, roll-coating systems, oxygenation of chemical liquids, and plunging liquid jet bubble columns. Several experimental and theoretical studies have been conducted

on the complexity of air-entrainment phenomena in general plunging jets (Rajaratnam, 1962; McKeogh, 1978; Ervine et al., 1980; McKeogh and Ervine, 1981; Sene, 1988; Biñ, 1993; Evans et al., 1996; Chanson, 1997; Cummings and Chanson, 1997a,b; Chanson and Manasseh, 2003; Chanson et al., 2004; Kiger and Duncan, 2012).

Despite of the success of the experimental works, the numerical simulation of the flow self-aeration process is viewed as one of the most challenging subject under current investigation. The main challenge resides in simulation of the free-surface, in which the VOF models have proven to be accurate, together with the smaller scales of interface fluctuations (order of millimetres). The smallest scales are likely to be smaller than the grid size, therefore not simulated by VOF models, but are still important in the simulation of bubble formation, their transport and iterations throughout the flow.

In theory, Direct Numerical Simulation (DNS) could simulate all aspects of the entrainment process right down to the subsequent dynamics of the bubbles; however this would be incredibly time-consuming and, in some cases, the application of free-surface methods (as VOF) to dispersed phases could lead to a non-physical interpretation of bubbles or droplets (Cerne et al., 2001). Instead, for a realistic mesh resolution, the representation of the entrained air should be accomplished by the inclusion of an Eulerian dispersed phase model with a second set of equations representing the dynamics of the bubbles (Cerne et al., 2001; Moraga et al., 2008; Yan and Che, 2010; Hänsch et al., 2012; Wardle and Weller, 2013) and an analytical formula to simulate the transition between small- and large-scale gas phases at the interface (Hirt, 2003; Ma et al., 2010; Shi et al., 2010) or a sub-grid turbulence model (Lubin et al., 2006).

In the literature it is possible to find some codes adapted to simulate the air-entrainment. However, practically all of them are private or just reachable with the payment of costly commercial licences with several restrictions to get access to the source code. The OpenFOAM® Computational Fluid Dynamics (CFD) toolbox is a free, open-source software which besides offering several pre-build solvers and tools, gives the chance of freely change/adapt the code by any user programmer. Although no air-entrainment model has been implemented in OpenFOAM®, one of its strengths is the ability to study free-surface flows, achieved mainly through the VOF-based solver *interFoam* (Ubbink, 1997). This solver is further a good starting point for the development of an air-entrainment model.

This motivation lead to the research question that this Thesis intends to provide an insight on:

Is it possible to adapt a Three-dimensional (3D) CFD open-source model, which uses VOF method to detect the free-surface position, to compute the air-entrainment process in hydraulic structures?

1.2 Aim and scope

In order to provide an answer to the aforementioned research question, the Thesis is structured with regard to an aim and several objectives. The aim of this Thesis is to replicate and analyse the free-surface flow characteristics in hydraulic structures using the VOF model present in the OpenFOAM®, and further enhance the ability of the original solver to deal with the air-entrainment process. The goal is further divided into seven intermediate objectives:

- O1:** Review the literature regarding the main concepts to deal with air-water flows in the different scales: free-surface flows, disperse flows and air-entrainment concepts. A review of the experimental techniques used to measure the air-concentration values in air-water flows is also needed;
- O2:** Conduct experimental tests on three hydraulic structures - gully, manhole and stepped spillway, in order to emphasize some important flow features which can be both useful to characterise their efficiency and to validate further numerical aspects;
- O3:** Test to the capacities of the *interFoam* VOF-based model to describe the position of the free-surface, the flow physics and turbulent statistics, and applying it to the case of gullies and a stepped spillway;
- O4:** Develop a novel numerical procedure for free-surface detection using the Volume-of-fluid;
- O5:** Investigate the appearance and describe the flow physics of an unclassified alternating skimming flow regime when the spillway width was changed from 0.3 m to 0.5 m;
- O6:** Implement a source term for bubble rate at the free-surface that is independent of calibration factors, overcoming the main drawback of the current air-entrainment models; and investigate the influence of mesh refinement to the location of the aeration point;
- O7:** Implement and test a new solver developed in OpenFOAM® toolbox, capable of dealing with air-entrainment, to the case of a flow over a stepped spillway and a gully under drainage.

By achieving the aforementioned objectives, the work performed in this Thesis contributes with a new solver that is able to simulate the air-entrainment phenomena.

1.3 Thesis structure

The Thesis is divided into 11 Chapters. Chapters 1 and 2 cover the theoretical basis of this Thesis. Chapters 3 to 10 correspond to works submitted to international peer-reviewed journals and conferences. Chapter 11 draws the conclusions, answers the research question and suggests some topics for future research.

Chapter 1 (present Chapter) presents the motivation, the aim and scope and the structure of this Thesis.

Chapter 2 describes the theoretical fundamentals and literature review. The literature review starts by presenting the most common methodologies that can be used to simulate free-surface flows, continuous-dispersed flows and hybrid formulations for continuous-continuous-dispersed flows. A detailed review about the theory behind the air-entrainment modelling and the existent models are present afterwards. The Chapter closes with a short review of the experimental techniques to measure the air-concentration.

Chapter 3 presents the numerical and experimental investigation of a gully under surcharge conditions. This work is a test to the capacities of the *interFoam* VOF-based model to solve the flow physics in a gully and to verify its accuracy in the solution of the free-surface. The results of this work represent a step towards to the calibration and validation of the linking elements found in Dual Drainage (DD) models.

Chapter 4 investigates the ability of the *interFoam* VOF-based model in reproducing drainage efficiency of a continuous transverse gully with a grate, under different flow rates and slopes. In particular, the objective is to assess the numerical model's ability to predict the hydraulic efficiency of urban drainage elements.

Chapter 5 describes experimentally the recirculation processes inside a scaled manhole and contributes to the understanding of the hydraulic performance of the urban drainage systems. Mean velocity, turbulent statistics and air concentration profiles are used to demonstrate such characteristics.

Chapter 6 identifies a new numerical procedure to detect the free-surface using a VOF model. This work studies which isoline of water volume fraction should be used to better describe the free-surface position, depending on its characteristics. The different flow

regions of a skimming flow over a stepped spillway are identified using the flow depth measured with a single ultrasonic sensor.

Chapter 7 demonstrates the unequivocal existence of the alternating skimming flow regime when a 0.5 m wide stepped spillway is used, and describes the characteristics of this alternating skimming flow. This study is also from particular interest to the researchers as it shows that the centre-channel measurements may be insufficient for full regime definition for the given combination of flow rate and geometry. As future works in the stepped spillway will be based in this simulation, it is crucial to understand beforehand the basics of the flow physics in this structure as well as the applicability of the VOF model.

Chapter 8 investigates the capacities of a Volume-of-Fluid based model to detect the free-surface and predict the velocities inside the water phase, examining the effect of coarsening and refining the mesh on the prediction of the interface location. A reformulated explicit term for bubble formation that is independent of calibrating factors is proposed. This explicit term is included in the well validated *interFoam* VOF-based solver to accurately predict the interface position and used to solve the numerical and modelling aspects of the entrainment process for two canonical cases; the 2D dam break and 3D circular plunging jet cases. This study represents a starting point for the development of a VOF-based solver with a modelled closure to represent the entrained air.

Chapter 9 presents the novel air-entrainment model that can be applied in continuous air-water flows. To the existent VOF formulation from *interFoam* solver, used to detect the air/water interface, is added an advection-diffusion equation to simulate the dispersed bubble phase. The air generated at the free-surface is calculated according to the explicit source term for bubble formation proposed in Chap. 8. One-way coupling and two-way coupling versions of this model are tested. Results are obtained in terms of free-surface flow depths, air-concentration profiles and velocity fields and compared to experimental data acquired in a scaled stepped spillway model.

Chapter 10 applies the model developed in Chap. 9 to the case of a gully under drainage conditions. Experimental data is acquired in the same gully prototype as the one presented in Chap. 3. The air is detected in a sub-grid scale, generated by a source term and transported using a slip velocity formulation. Results are showed in terms of free-surface elevation, velocity profiles, turbulent kinetic energy, air-concentration profiles and discharge coefficients.

Chapter 11 draws conclusions of this Thesis and suggests some topics for future research.

2

Literature Review

2.1 Methodologies for free-surface flows

2.1.1 Equations of motion

The fluid motion is mathematically described by a set of equations expressing the conservation of mass and momentum, written in their conservative form as (Batchelor, 1967; Pope, 2000):

$$\frac{\partial \rho}{\partial t} + \nabla \cdot (\rho \mathbf{u}) = 0 \quad (2.1a)$$

$$\frac{\partial \rho \mathbf{u}}{\partial t} + \nabla \cdot (\rho \mathbf{u} \mathbf{u}) = \rho \mathbf{g} + \nabla \cdot \tau \quad (2.1b)$$

where ρ is the fluid density, \mathbf{u} is the three-dimensional velocity field, τ is the stress tensor, \mathbf{g} is the gravity acceleration vector and t the time. However, the system formed by Eq. (2.1a) and Eq. (2.1b) is indeterminate because the number of variables is greater than the number of equations. To solve that, a constitutive relation for Newtonian fluids should be considered by linearly relate the stresses with the rates of deformation (Jasak, 1996; Pope, 2000), the Newton's Law:

$$\nabla \cdot \tau = -\nabla \left(p + \frac{2}{3} \mu \nabla \cdot \mathbf{u} \right) + \nabla \cdot [\mu (\nabla \mathbf{u} + (\nabla \mathbf{u})^T)] \quad (2.2)$$

Applying the above equation to Eq. (2.1b) and assume an incompressible flow so that $\nabla \cdot \mathbf{u} = 0$, we write:

$$\nabla \cdot \mathbf{u} = 0 \quad (2.3a)$$

$$\frac{\partial \mathbf{u}}{\partial t} + \nabla \cdot (\mathbf{u} \mathbf{u}) = \mathbf{g} - \frac{1}{\rho} \nabla p + \nabla \cdot (\nu \nabla \mathbf{u}) \quad (2.3b)$$

where p is the pressure, $\nu = \mu/\rho$ the kinematic viscosity and μ the dynamic viscosity. These equations are known as 3D incompressible Navier-Stokes in their conservative form.

2.1.2 Turbulence modelling

Most fluid flows encountered in engineering practice are turbulent. Their study and understanding is “one of the most intriguing, frustrating and important problems in all of classical physics” (McDonough, 2007). As such, given the complexity of this topic and since the study of the turbulence effects in detail are not the intention of the Thesis, just

a brief description regarding the concepts that are going to be useful to this work are present in this section.

It is often referred that there is no universal description of the turbulence phenomena, however Richardson (1922)'s statement is likely to be one of the best:

*Big whorls have little whorls,
which feed on their velocity;
And little whorls have lesser whorls,
And so on to viscosity.*

This supports the theory stated by Kolmogorov (1962) that turbulence is composed by a large range of time and length scales, whose energy is transferred in a “cascade” system until it gets the complete dissipation (converted in thermal energy) on molecular scales. Therefore, when using numerical modelling, the complete description of turbulence comprehends the simulation of all these time and length scales.

In CFD, the effects of the turbulence are taken into account through the application of some numerical tools as such the phenomena can be computationally foreseeable. The first, DNS numerically integrates the governing equations over the entire rage of turbulent scales. This methodology is associated to a fine mesh and large computational effort, therefore just employable in cases of small domains and low Reynolds numbers.

The second approach is called Large-Eddy Simulation (LES) (Deardorff, 1970). As the name suggests, the effects of turbulence generated by the large eddies on the mean flow are the ones resolved by the governing equations, while small eddies are included on the solutions by means of a sub-grid scale model. To separate those two groups of eddies, LES uses a spatial filtering operation. The computational resources on terms of memory are still large.

The third approach, the Reynolds-Averaged Simulation (RAS) is a statistical based method, which is probably the most used in the current CFD simulations. In RAS methodology, the turbulent fluctuations appears in the equations of motion for the mean state as a correlation of velocity-component fluctuations according to Reynolds averaging technique (Launder and Spalding, 1974),

$$\phi(\mathbf{x}, t) = \bar{\phi}(\mathbf{x}, t) + \phi'(\mathbf{x}, t) \quad (2.4)$$

where $\phi'(\mathbf{x}, t)$ represents the fluctuation about the mean value $\bar{\phi}(\mathbf{x}, t)$. Applying the Reynolds averaging technique to the incompressible Navier-Stokes equations (2.3), the following form of the averaged equations, the incompressible Reynolds-Averaged

Navier-Stokes (RANS) equations, can be written as (Versteeg and Malalasekera, 2007):

$$\nabla \cdot \bar{\mathbf{u}} = 0 \quad (2.5a)$$

$$\frac{\partial \bar{\mathbf{u}}}{\partial t} + \nabla \cdot (\bar{\mathbf{u}} \bar{\mathbf{u}}) = \mathbf{g} - \frac{1}{\rho} \nabla p + \nabla \cdot (\nu \nabla \bar{\mathbf{u}}) + \overline{\mathbf{u}' \mathbf{u}'} \quad (2.5b)$$

where the term $\overline{\mathbf{u}' \mathbf{u}'}$ is called the Reynolds stress tensor (Jasak, 1996). Boussinesq (1877) postulated that momentum caused by turbulent eddies can be modelled with an eddy viscosity. In the Boussinesq approximation, the Reynolds stresses are linearly related to the velocity gradient in the form:

$$\overline{\mathbf{u}' \mathbf{u}'} = \nu_t [\nabla \mathbf{u} + (\nabla \mathbf{u})^T] + \frac{2}{3} k \mathbf{I} \quad (2.6)$$

where ν_t is the kinematic eddy viscosity, k the turbulent kinetic energy ($k = 0.5(\overline{\mathbf{u}' \cdot \mathbf{u}'})$) and \mathbf{I} the unit tensor. To calculate the variable ν_t , additional models containing extra transport equations are needed. The RAS models are classified in terms of the number of equations: zero-equation (e.g. Mixing length model), one-equation (e.g. Spalart-Allmaras model), two-equations (e.g. $k - \varepsilon$, $k - \omega$ models and Algebraic Stress Model (ASM)) and seven-equations (Reynolds Stress Model (RSM)). The most popular way is to express ν_t as a function of two equations, for k and its dissipation rate (ε) or the specific dissipation (ω), with several different formulations included in these families of models.

2.1.3 Free-surface representation

The meshes used in the numerical discretisation of the equations can be divided in static and dynamic meshes. In this section the two of the main methodologies used to predict the free surface in static meshes will be presented: surface methods and volume methods. More emphasis will be given to the volume methods, in particular to the VOF method.

2.1.3.1 Surface methods

The surface methods treat the free-surface either by a sharp interface, whose position is followed or tracked by marking it with special points, also known as marker points (Ubbink, 1997). Between those marker points, the free-surface is described by a polynomial function. The accuracy of the surface tracking methods depends strongly on the stability and precision of the interpolation method (Hyman, 1984). Within surface methods, the following are some of the most known methodologies (Ubbink, 1997):

a) Particles on interface method: This method was presented by Daly (1969) where the interface is tracked explicitly by a set of connected massless marker particles on a fixed grid (Figure 2.1a). In cases where the particles are distant from each other, the interface may not be well represented.

b) Height function method: In this method the interface is tracked introducing a height function that returns the distance of the point on the interface and the reference plane (Figure 2.1b). For closed interfaces such as bubbles or droplets, one defines a representative point inside the object and the radius at different angular positions is set as the distance function. The major difficulty of this method is that each coordinate of the reference plane is associated to only one interface value, that in case of breaking waves, results in a model failure.

c) Level-Set method: The Level-Set (LS) method was originally proposed by Osher and Sethian (1988) introducing a continuous function, known as a level set function, over all computational domain (Figure 2.1c). The function is positive in one fluid phase and negative in the other. The zero level ($\Phi = 0$) represents the exact position of the free-surface,

$$S(t) = \{x | \Phi(x, t) = 0\} \quad (2.7)$$

Given the superscript + or - that corresponds to a positive or negative distance of level Φ from the interface ($\Phi = 0$), the density ρ (similar for viscosity μ) can be expressed as:

$$\rho = \rho^- + H(\Phi)(\rho^+ - \rho^-) \quad (2.8)$$

where $H(\Phi)$ is the Heaviside step function. The interface is evolved by advecting the LS function in the flow field as if it were a material property,

$$\frac{\partial \Phi}{\partial t} + \mathbf{u} \cdot \nabla \Phi = 0. \quad (2.9)$$

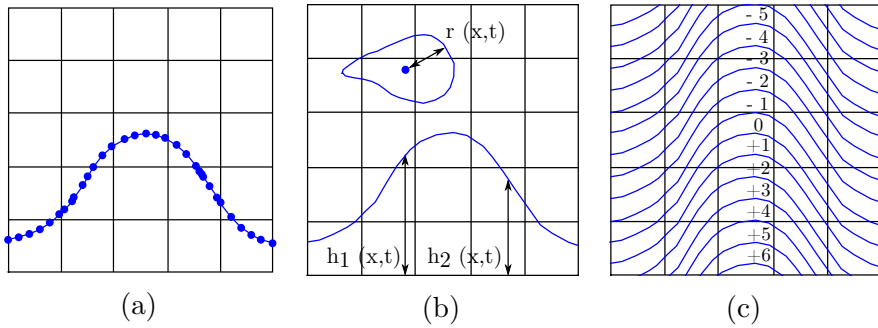


Figure 2.1: Surface methods to treat the interface: (a) Particles on interface method; (b) Height function method; and (c) LS method.

Advantages

- Surface methods define a sharp interface, which simplifies the analysis near the interface;
- Representation of the free-surface is independent of the representation of the flow field. Different resolutions can be assumed for both.

Disadvantages

- The volume of each fluid may not be conserved;
- More computationally expensive;
- They require user-intervention to handle topological changes, e.g. the merging of two interfaces.

2.1.3.2 Volume methods

In volume methods the entire domain is marked by massless particles, by an indicator function or even by a level-set function. Unlike the surface methods, in the volume methods the exact position of the interface is not known and, special techniques need to be applied to capture the interface as part of the solution algorithm (Ubbink, 1997). On the other hand, they can simply and accurately account for the interactions in smoothly varying interfaces (Hyman, 1984). Two important techniques have been developed: particles on fluid method and volume fraction methods.

a) Particles on fluid method: One of the earliest volume methods of particles on fluid for material interfaces is the Marker-And-Cell (MAC) method of Harlow and Welch

(1965). The location of fluid within the fixed grid is determined by a set of massless marker particles that move with the fluid. Cells full of marker particles are filled of fluid and cells with no marker particles are consequently empty. Hence, cells with marker particles which are adjacent to at least one empty cell, are interface cells (Figure 2.2a).

b) Volume fraction methods: The volume fraction methods are likely to be the most common methods to treat the free-surface. They present clear advantages regarding the MAC in matters of computational economy and storage, as only one variable is recorded (the volume fraction value), instead of the coordinates of the marked particles. All volume fraction methods use a scalar indicator function, also known by volume fraction function (α), that ranges from zero (no material) to one (completely filled with material) to distinguish the presence or not of phase fluid (Figure 2.2b). In this Thesis, special attention is given to the volume fraction method VOF because it is the basis of the solver used.

The popularity of the original VOF (Hirt and Nichols, 1981) and some of its extensions (Lemos, 1992; Ubbink, 1997; Carvalho, 2002) regard three key elements. The first element is the introduction of the advection equation to transport the volume fraction scalar,

$$\frac{\partial \alpha}{\partial t} + \nabla \cdot (\alpha \mathbf{u}) = 0. \quad (2.10)$$

Besides easy to implement, this equation has the advantage that the volume occupied by one fluid is not occupied by the other, thus the continuity is always verified. The second key element of VOF overcomes the main drawback of this method and contributed to the success of the methodology (Bombardelli et al., 2001). This is related to the way that advection equation is solved in order to avoid the smearing of the interface. If solving the advection equation [Eq. (2.10)] with lower order schemes, like the first order upwind method, smear the interface due to numerical diffusion, higher order schemes are unstable and result in numerical oscillations. Therefore, auxiliary methods are used to maintain the interface sharp (Rider and Kothe, 1997; Carvalho, 2002) and get a stable representation of the free-surface position. Those methods can be divided into four groups: by approximating the fluxes in a geometric way with (I) *geo-reconstruction schemes* or (II) by applying the *donor-acceptor scheme*; (III) by discretising the advection equation using *high-resolution schemes*, with or without (IV) adding an extra *compressive convection term*.

I) Geo-reconstruction schemes: The simplest type of geo-reconstruction method is the Simple Line Interface Calculation (SLIC) of Noh and Woodward (1976). It approximates the interface in each cell as piecewise constant, i.e. the interface is a line (or a

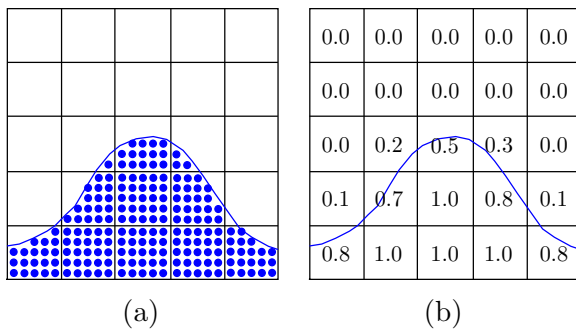


Figure 2.2: Volume methods to treat the interface: (a) Particles on fluid - MAC; and (b) Volume fraction method - VOF.

plane in 3D domain) parallel to one of the coordinate axes. In Two-dimensional (2D) cases this assumption results in two different situations: (1) the x-sweep, where the interface approximation uses the volume fraction values on the left and the right of the cell (Figure 2.3b) and (2) the y-sweep, which uses the values above and under the cell (Figure 2.3c). These methods are undesirable in most CFD codes due to their restrictions to rectangular cells and difficulties in extending to tree-dimensional meshes (Ubbink, 1997).

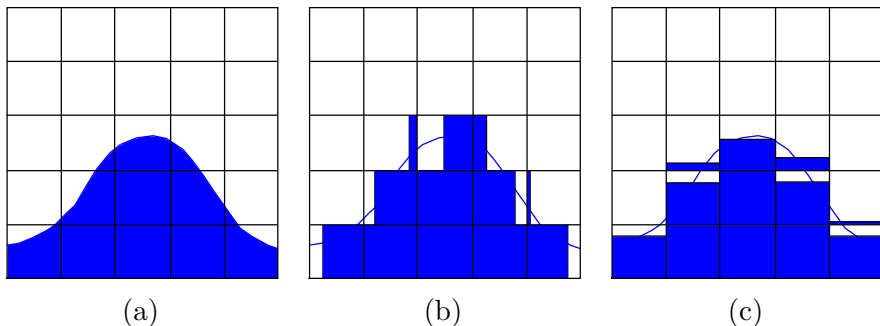


Figure 2.3: Volume fraction method SLIC: (a) Accurate distribution; (b) SLIC x-sweep; and (c) SLIC y-sweep. Adapted from (Ubbink, 1997).

The piecewise linear reconstruction or Piecewise Linear Interface Calculation (PLIC) methods are, in most cases, preferable. Original PLIC method (Youngs, 1984) (Figure 2.4b) assumes that the interface between two fluids has a linear slope within each cell, and uses this linear shape to calculate the advection of fluid through the cell faces. A different version, called Flux Line-segment model for Advection and Interface Reconstruction (FLAIR), uses line-segments instead of lines on the cells to calculate the fluxes (Ashgriz and Poo, 1991) (Figure 2.4c). More advanced geometric interface reconstruction use the least-square procedure (Pilliod and Puckett, 2004), splines (López et al., 2004) or a 2-steps reconstruction method (Roenby et al., 2016). The last, known as isoAdvector, was recently implemented in the OpenFOAM® and can be used in both 2D and 3D, structured and

unstructured meshes.

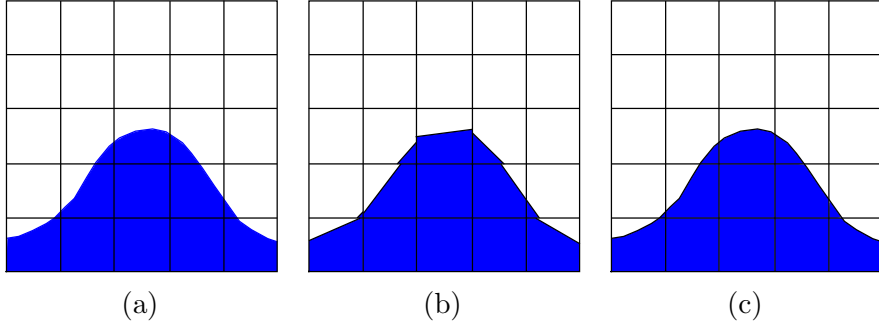


Figure 2.4: Volume fraction method PLIC: (a) Accurate distribution; (b) PLIC; and (c) FLAIR. Adapted from (Ubbink, 1997).

II) Donor-acceptor scheme: Donor-Acceptor Scheme (DAS) from Hirt and Nichols (1981) is a geometric method that uses the volume fraction value of the upwind/downwind cell (donor/acceptor cell) to predict the level of volume fraction transported through it during a time step. To ensure boundedness, the volume fraction value in the donor cell is used to adjust the level of fluid in the acceptor cell. A drawback with this formulation is that it changes any finite gradient to a step, giving an incorrect steepening on the interfaces that are aligned with the flow direction (Ubbink, 1997) and it does not preserve local boundedness (Ubbink and Issa, 1999).

III) High-resolution schemes: Another approach to preserve the interface resolution is to discretise the scalar transport equation for the volume fraction using a higher order schemes that prevent the smearing of the interface while guarantees bounded (i.e. between 0 and 1) volume fraction values. Some examples are Compressive Interface Capturing Scheme for Arbitrary Meshes (CICSAM) (Ubbink, 1997; Ubbink and Issa, 1999), High Resolution Interface Capturing (HRIC) (Muzaferija et al., 1998) and Multidimensional Universal Limiter with Explicit Solution (MULES) (OpenFOAM, 2014). These methods are preferable when the geometric schemes do not give satisfactory results, or when the flow calculation becomes unstable. CICSAM is a high-resolution differencing scheme based on the idea of the DAS using Normalised Variable Diagram (NVD) (Leonard, 1988). CICSAM scheme is formulated to switch between the more compressive Hyper-C scheme and less compressive Ultimate-QUICKEST scheme, where a weighting factor, based on the angle between the interface and the direction of motion, is introduced for the switching. This scheme is one of the available options present in ANSYS Fluent® code. Like CICSAM, HRIC scheme also relies on the NVD but it get rid of the dependence on the Courant

condition. HRIC is actually implemented in the STAR-CCM+® and, in a modified version, in ANSYS Fluent®. A very detailed comparison between CICSAM and HRIC can be found in (Waclawczyk and Koronowicz, 2008). Finally, MULES is a scheme developed by the OpenCFD® and implemented in OpenFOAM®. The fluxes are calculated using the first order upwind scheme when α is either 1 or 0 (away from the interface), and a second-order vanLeer's scheme in the interfacial zones (Deshpande et al., 2012). Another complementary and useful comparison about the different ways to treat the advection equation is presented by Gopala and van Wachem (2008).

IV) Compressive convection term: The compressive convection term is an “artificial” term that is added to VOF equation in order to sharp the interface. This method, although is used to keep the interface sharp even with first order schemes (Rusche, 2002; Weller, 2008), it can be used together with high resolution schemes. Unlike geo-reconstruction methods, this term is not as physically accurate, however it much simpler to implement and, most importantly, unlike PLIC is mass conservative. This method is currently implemented in the *interFoam* VOF solver from OpenFOAM®. Many other improvements have been done to this term to avoid some unphysical solution due to compression, as the works of Piro and Maki (2013) and Lee and Rhee (2015) which introduced the concepts of adaptive and dynamic interface compression methods to distinguish the necessity or not of the compressive term.

The third key element of the original VOF method is related to the introduction of a free-surface boundary condition. This is needed because the flow is only computed in water region. Air regions are considered as having negligible inertia and only capable of imposing a normal pressure on a liquid surface (Bombardelli et al., 2001). In other words, the free-surface boundary condition ensures continuity in the velocity (kinematic condition) and in the strain tensor (dynamic condition) (Carvalho, 2002). In more recent versions of VOF this free-surface boundary condition is not used. Instead, the flow is solved for both fluids introducing a variable density and viscosity which is calculated by a weighting the values for air and water according to the volume fraction scalar,

$$\rho = \rho_{water}\alpha + (1 - \alpha)\rho_{air} \quad (2.11a)$$

$$\mu = \mu_{water}\alpha + (1 - \alpha)\mu_{air} \quad (2.11b)$$

This approach is currently implemented in the several CFD codes as OpenFOAM® and ANSYS Fluent®.

Combined surface and volume methods are also a solution to get rid of the problem related to surface smearing. Sussman and Puckett (2000) proposed the method Combined Level-Set Volume-of-Fluid (CLSVOF), which combines the benefits of both VOF (mass conservation) and LS (interface sharpness). This coupling is achieved by advecting the interface using VOF, then calculating the interface normal through the LS method, and finally updating the physical properties from a smoothed Heaviside function. Mass-Conserving Level-Set (MCLS) method of Van der Pijl (2005) also linked the advantages of both VOF and LS, while the costly interface reconstruction step is discarded from the algorithm. Raees et al. (2011) evaluated the efficiency of MCLS against the VOF from OpenFOAM®. Albadawi et al. (2013) extended the CLSVOF model by introducing a LS field ϕ , so the interface is always defined by isoline $\phi = 0$. The new method improved the accuracy of the original VOF method when the surface tension influence is predominant.

Advantages

- Volume fraction methods use less memory. Only one value is saved for each computational cell;
- VOF method is a very robust method as long as a correct advection technique is applied.

Disadvantages

- The interface is unknown and the location of the interface is often represented by an indicator function;
- Some problems of interface smearing may occur.

2.2 Methodologies for continuous-dispersed two-phase flows

2.2.1 Two-fluid model

The Two-fluid or Eulerian model is the most elaborate two-phase approach. It solves $n = 2$ sets of mass conservation and momentum equations to describe each phase, and the phases are allowed to be continuously inter-penetrable, which means that volume fractions α_q and α_p for a control volume can be equal to any value between 0 and 1, depending on

the space occupied by phase q and phase p . Coupling is achieved through the pressure and interphase exchange forces as drag, lift or turbulent dispersion forces.

For incompressible fluids, the continuity equation for each phase k are given by (Ishii, 1975; Drew and Passman, 1998),

$$\frac{\partial \rho_k \alpha_k}{\partial t} + \nabla \cdot (\rho_k \mathbf{u}_k \alpha_k) = 0 \quad (2.12a)$$

$$\sum_{k=1}^n \alpha_k = 1 \quad (2.12b)$$

where the subscript k denotes the phase indicator, $k = 1$ for the continuous liquid phase and $k = 2$ for dispersed gas phase; α is the phase fraction, ρ the phase density and \mathbf{u} the phase velocity. The corresponding momentum equations for the two phases can be written as:

$$\frac{\partial \alpha_k \rho \mathbf{u}_k}{\partial t} + \nabla \cdot (\rho_k \alpha_k \mathbf{u}_k \mathbf{u}_k) = -\alpha_k \nabla p + \nabla \cdot (\alpha_k \tau_k) + \alpha_k \rho_k \mathbf{g} + \mathbf{F}_k \quad (2.13)$$

The tensor τ_k is the effective stress tensor and \mathbf{F}_k is the interfacial force, which explicitly contains the momentum exchanges between the two phases as drag force, lift force, virtual mass or turbulent dispersion force.

Advantages

- Phases are inter-penetrable and allowed to move at different velocities;
- This is a preferred method for bubbly flows or cases where the dispersed phase volume fraction is high ($> 10\%$) (Rusche, 2002);
- If accuracy is more important than computational effort, the two-fluid model is a better choice.

Disadvantages

- This model require more computer memory and disk space than Euler-Lagrange or ASMM model because it solves two sets of mass and momentum equations, each for continuous and dispersed phases;
- The complexity of Eulerian model can make it less computationally stable than remaining models.

2.2.2 Algebraic Slip Mixture Model

The ASMM, like the two-fluid model, considers that the different phases might inter-penetrated and move at different velocities. However, unlike two-fluid formulation, ASMM uses just one set of mass and momentum equations and does not need necessarily that one phase is dispersed - both can be continuous, like in free-surface flow models (e.g. VOF model). The mixture model can model n phases (continuous fluid or dispersed particles, bubbles or droplets) by solving the continuity and momentum equations for the mixture, the volume fraction equations for the secondary phases (p), and algebraic expressions for the relative velocities.

The continuity and momentum equations for the mixture can be obtained by weight summing the corresponding equations for each phase,

$$\frac{\partial \rho_m}{\partial t} + \nabla \cdot (\rho_m \mathbf{u}_m) = 0 \quad (2.14a)$$

$$\frac{\partial \rho_m \mathbf{u}_m}{\partial t} + \nabla \cdot (\rho_m \mathbf{u}_m \mathbf{u}_m) = -\nabla p + \nabla \cdot (\tau_m) + \rho_m \mathbf{g} + \mathbf{F} + \nabla \cdot \sum_{k=1}^n \alpha_k \rho_k \mathbf{u}_{dr,k} \mathbf{u}_{dr,k} \quad (2.14b)$$

where $\rho_m = \sum \alpha_k \rho_k$ is the mixture density, $\mathbf{u}_m = \sum (\alpha_k \rho_k \mathbf{u}_k) / \rho_k$ is the mass averaged mixture velocity, τ_m is the viscous stress tensor, \mathbf{g} is the gravity acceleration and α_k is the volume fraction of phase k . The velocity $\mathbf{u}_{dr,k}$ is the drift velocity for the secondary phase k .

Advantages

- Phases are inter-penetrable and allowed to move at different velocities using the concept of slip velocities;
- Less computational expensive than Two-fluid and Euler-Lagrange formulations because it solves just one set of mass and momentum equation for the mixture.

Disadvantages

- Due to the requirement of a strong coupling between the phases, ASMM is more suited for liquid-particle mixtures than for gas-particle mixtures;
- The accuracy of this model is highly dependent on the algebraic equation for the diffusion velocity (Verloop, 1995), i.e. the velocity of phase k relative to the centre of the mixture mass.

2.2.3 Euler-Lagrange model

In this method, a single set of equation solves the dynamics of the continuous phase, whereas the dispersed phase is represented by individual bubbles, droplets or particles, explicitly tracked by solving an individual equation of motion. The iteration between Euler and Lagrangian parts of the model is done through outer models for interfacial forces. From this relationship, three variants of Euler-Lagrangian approaches can emerge: one-way, two-way and four-way coupling.

When the dispersed second phase occupies a low volume fraction and particles size is very small, a one-way coupling model prevails between the two phases. In this model, the movement of the dispersed phase does not influence the dynamics of the continuous part. When the concentration of dispersed phase is higher, a two-way coupling model has to be implemented. The movement of dispersed particles has effects in the continuous phase and vice-versa. A four-way coupling model, beyond the interaction fluid-particles, it take into the account the momentum exchange in the interaction particle-particle.

Lagrangian tracking essentially applied the Newton's second law of motion to a particle to determine its position. Position and motion of each particle/gas bubble with mass \dot{m}_P can generally be calculated by:

$$\frac{dx_P}{dt} = \mathbf{u}_P \quad (2.15a)$$

$$\dot{m}_P \frac{d\mathbf{u}_P}{dt} = \sum \mathbf{F}_P \quad (2.15b)$$

In a two-way coupling, the source term for momentum transfer in momentum equation turns is given by:

$$\mathbf{F} = \mathbf{S}_P = \frac{1}{V_{cell}\Delta t} \sum_P \dot{m}_P ((\mathbf{u}_P)_{out} - (\mathbf{u}_P)_{in}) \quad (2.16)$$

where $\dot{m}_P((\mathbf{u}_P)_{out} - (\mathbf{u}_P)_{in})$ is the difference in particle momentum between the instant it enters and leaves a certain cell with volume V_{cell} . The force \mathbf{F}_P is subdivided in diverse individual interfacial and field forces, acting on the particle as: drag force, gravity buoyancy, virtual mass and Basset forces, etc.

Advantages

- Model allows quite naturally to represent additional dispersed phase properties, e.g. size, shape and temperature, as well as their effect on the continuous phase;
 - Each particle is fully tracked though the flow domain, retuning their exact position.

Disadvantages

- The computational effort is proportional to the number of particles, therefore it can be computationally expensive for high phase fractions;
 - For high dispersed phase volume-fractions ($> 10\%$), the increased coupling between the dispersed phase and the continuous phase can introduce numerical stability problems.

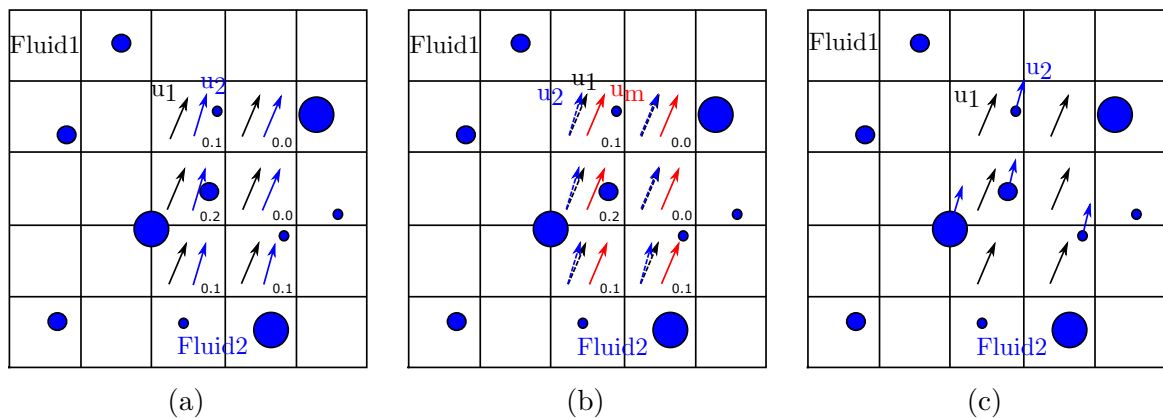


Figure 2.5: Methodologies for continuous-dispersed two-phase flows: (a) Two-fluid model; (b) ASMM; and (c) Euler-Lagrange. Black and blue arrows stands for the velocity of phase 1 (continuous) and phase 2 (dispersed) respectively. Red arrows are mixture velocities. Values on bottom-right corner of the cells are volume fraction values of phase 2. Adapted from (Rusche, 2002).

2.3 Hybrid formulations for two-fluid flows

The possible numerical solutions of free-surface (continuous - continuous phases) and continuous - dispersed flow phases were demonstrated in the sections §2.1 and §2.2 respectively. However, in the nature, most of the flows join the two aforementioned

approaches, as the case of a river flow, where at least two continuous phases and numerous examples of dispersed particles (bubbles, droplets, sediments, micro-particles of pollutants, etc.) are present. In theory, the interface capturing methods, such as VOF, could be used for a direct numerical simulation (i.e. DNS) of the continuous-dispersed flow, once accomplished the request of a mesh spacing $\approx 10 \times$ smaller than the smallest droplet or bubble found in the domain (Wardle and Weller, 2013); and yet finer mesh resolution in case of the simulation of bubble-bubble interaction or coalescence aspects. In practice, this size of mesh and the subsequent time steps needed to compute real multiphase turbulent flows, according to Courant limitations, are not feasible in the foreseeable future even with the expected expansion of the computer power. The two-fluid model is much more reliable, faster and physically correct in the simulation of dispersed flow than VOF if used to get a DNS solution of the bubbly phase. However, the equations of the two-fluid model are mathematically incorrect when trying to simulate a large interface (e.g. free-surface) due to the empirical closures (interfacial forces) applied in the averaged set of equations (Cerne et al., 2001).

In this sense, for this kind of complex turbulent flows with multiple continuous and dispersed phases, the solution goes through the coupling of an interface capturing method and a continuous-dispersed formulation in a single model. The interface capturing method would be used in order to solve the scales that are larger than the mesh resolution capacity (e.g. free-surface); whereas continuous-dispersed formulations are used to solve the physics of droplets in air and bubbles in water.

The initial idea of coupling an interface capturing method with the two-fluid formulation is attributed to Cerne et al. (2001). In zones where just one fluid is present or the interface is clearly defined, the RANS equations are solved together with VOF for interface tracking. In the reaming zones, the previous set of equations are turned into a two-fluid formulation to simulate the continuous-dispersed phases interaction. In a mathematical point of view, this blending system is not difficult to afford since the volume fraction scalar present in VOF used to track the free-surface has similar meaning as the phase fraction variable in two-fluid model. The main mathematical difference lies in the treatment of the velocities. In VOF the two phases share the same motion whereas in two-fluid formulation the phases are allowed to move at different velocities. When the fluids properties are moving from VOF model to the two-fluid, the velocities are keep the same, whereas, in reverse situation, the velocities are weighted-averaged in the phase fraction,

$$\begin{cases} \mathbf{u}_{1,\text{two-fluid}} = \mathbf{u}_{2,\text{two-fluid}} = \mathbf{u}_{\text{VOF}} & , \text{VOF to two-fluid model} \\ \mathbf{u}_{\text{VOF}} = \alpha \mathbf{u}_{1,\text{two-fluid}} + (1 - \alpha) \mathbf{u}_{2,\text{two-fluid}} & , \text{two-fluid to VOF model.} \end{cases} \quad (2.17)$$

The transition criterion between the two models is based on the local dispersion of the interface. Cells containing only one fluid are automatically solved with VOF model. However, if the gradient of the volume fraction scalar exceeds a certain threshold, then the VOF model is converted to a two-fluid model. Although this threshold value is user-changeable and a very simple way to switch between the two model, the accuracy of the model is strongly dependent on its magnitude. If the threshold is defined too high, the VOF model will be used in the majority of the domain, employing interface reconstruction every time that two phases are present, however, if too low, the VOF model is discarded and the phases are assumed as dispersed-continuous and inter-penetrable. Similar approaches to switch between the two formulations were proposed by Štrubelj et al. (2009) and Štrubelj and Tiselj (2011), that instead of choosing the minimum gradient to the interface, used the average of local volume fraction gradient; or by Wardle and Weller (2013), which based the transition criteria in the normalized magnitude of the gradient of the volume fraction.

Yan and Che (2010) introduced a promising unified solution framework by ensuring the automatic conservation of three fluid-phases, namely continuous water (phase 1) and continuous air phase (phase 2) and dispersed air (phase 3). A special treatment called “volume fraction redistribution” is used to deal with the cells containing both small and large length scale interfaces. The VOF model is activated if the continuous air phase fills completely the volume of the cell. In remaining cases, the two-phase model is used to solve the local characteristics of the remaining fluids (continuous water and dispersed air). The full system is controlled by the renewed volume conservation averaged-equation,

$$\alpha_2 \nabla \cdot \bar{\mathbf{u}}_2 + (1 - \alpha_2) \nabla \cdot (\alpha'_1 \bar{\mathbf{u}}_1 + \alpha'_3 \bar{\mathbf{u}}_3) = 0 \quad (2.18)$$

where $\alpha'_1 = \alpha_1 / (1 - \alpha_2)$ and $\alpha'_3 = \alpha_3 / (1 - \alpha_2)$ are partial volume fraction coefficients. As such, when α_2 is 1, the above equation is reduced to $\nabla \cdot \bar{\mathbf{u}}_2 = 0$, which corresponds to the solution of the interface tracking method. If α_2 is 0, then the continuity equation is turned into $\nabla \cdot (\alpha_1 \bar{\mathbf{u}}_1 + \alpha_3 \bar{\mathbf{u}}_3) = 0$, which is the continuity equation used in the two-fluid formulation. When the three phases are present, the authors decide to impose $\alpha_2 = 1$ as it cause less error in the zone away from the interface. The two momentum equations, one for the mixture of phase 1 and phase 2 and the other for the phase 3, have also suffered a special treatment in this model. The momentum exchange of the mixture has to be flexible according to the model formulation, by dividing it in two parts: the surface tension force when phase 2, and consequently phase 1, are present in the grid and the interfacial force, e.g. drag, lift, etc. when phase 2 is absent. The model was tested in the simulation of a flow containing both a large bubble and a swarm of small bubbles. One weakness of

this model is that the conservation of phase 1 and 3 cannot be guaranteed in the zone where all three phases coexist, which is the cost of considering the particularity of phase 2.

Hänsch et al. (2012) extended the inhomogeneous Multiple Size Group (MUSIG) presented in ANSYS CFX® by adding a continuous gas phase in order to solve simultaneously dispersed and continuous gas phases, and a continuous liquid phase. The transition between dispersed to continuous gas regions was assured by the “clustering method” that works as an additional interfacial force to two-fluid model framework. Closure models are switched when the local volume fraction of the continuous gas exceeds the critical value $\alpha = 0.3$ as done in the Algebraic Interface Area Density (AIAD) model (Höhne and Vallée, 2010). The solutions were verified qualitatively in the simulation of a plunging jet and a bubble column. More recent version of this model includes a sub-grid wave turbulence model to solve the smallest scales of turbulence across the interfaces (Hänsch et al., 2014). This is done with the inclusion of a new production term into the transport equation of turbulent kinetic energy of the liquid phase. The benefits of the implementation were qualitative showed in the simulation of the 2D dam break case.

Wardle and Weller (2013) introduced in OpenFOAM® v.2.2.1 a combination of an Eulerian multi-fluid framework with interphase tracking VOF method using a dynamic switching in the interface sharpening term. The solver was named in OpenFOAM® as *multiphaseEulerFoam*. The transition between the two models were based on the work of Cerne et al. (2001). Solver capability was tested in various examples including liquid1-liquid2-air simulations in which a sharp interface is maintained between each liquid and air, whereas liquid-liquid iterations were done using the dispersed phase formulation. Shonibare and Wardle (2015) extended this combined model to deal with variable bubble size using the reduced population balance method and applied it to a vertical plunging jet.

2.4 Air-entrainment modelling

Hybrid formulations of two-fluid and interface tracking methods (§2.3) have been successfully developed to take into account the coexistence in the same flow of continuous-continuous-dispersed phases. Main differences of such methods reside in the switching system between the two formulations. However, to study the air-entrainment process, it is necessary to introduce among, a robust and accurate sub-grid model that locates the point of aeration and the number of ingested air bubbles (Hirt, 2003; Moraga et al., 2008; Shi et al., 2010), a sub-grid scale turbulence model (Lubin et al., 2006; Hänsch et al., 2014; Witt et al., 2015), or a combination of both.

Hirt (2003) introduced in the TruVOF solver (embedded in the *FLOW-3D®*) a sub-grid air-entrainment model with two user-changeable options. The first option can be applied when the volume fraction of entrained air is low ($< 10\%$). In this case, the model uses a scalar variable to follow the motion of the air inside the water and the dynamics of the dispersed phase do not alter the water flow motion. The second alternative is more suitable for high volume fraction flows ($> 10\%$) and uses a variable density formulation to measure the influence of the dispersed air in the water phase. It introduces air in the domain and the flow suffer an increment of volume. The only possible escape of air is if it rises to the surface of the water.

The volume of air entrained per unit of time (V_g) at the water interface is explicitly calculated as,

$$V_g = C_{ent} A_s \sqrt{2 \frac{P_t - P_d}{\rho}} \quad (2.19)$$

where C_{ent} is the entrainment coefficient (the author suggest $C_{ent} = 0.5$ as initial guess) and A_s is the free-surface area at each cell. The air-entrainment term, and consequently the production of air, is activated whenever the perturbing component of turbulence $P_t = \rho k$, i.e. the turbulent kinetic energy, transcend the disturbance kinetic energy P_d . This stabilizing force is measured by the energy associated with a fluid element raised to a height (L_T) at the free-surface, plus the surface tension energy based on the curvature of L_t ,

$$P_d = \rho g_n L_T + \frac{\sigma}{L_T} \quad (2.20)$$

where,

$$L_T = C_\mu \sqrt{\frac{3}{2} \frac{k^{3/2}}{\varepsilon}} \quad (2.21)$$

with $C_\mu = 0.085$ for RNG $k-\varepsilon$ turbulence model. The term g_n is the gravity component normal to the free-surface and σ is the surface tension. To insure that the volume fraction of air does not exceed unity, which may cause numerical instabilities and plays no physical sense, the term for air-entrainment includes the factor of $(1 - \alpha_g)$, where α_g is the volume fraction of gaseous air. This factor, however, diminishes the amount of entrained air in the interfacial zone. In second model's option the inclusion of the variable density model is done by the equation,

$$\rho = (1 - \alpha_g)\rho_l + \alpha_g\rho_g \quad (2.22)$$

This model was validated in case of a plunging jet, vertical drop shaft, hydraulic jump in a conduit and a spillway (Hirt, 2003, 2012). The most sensitivity aspect of this model was found to be the level of turbulence chosen in case of a turbulent jet impinging in a pool of liquid. For the stepped spillway and the hydraulic jump, since the entrainment starts due to the turbulence at the free-surface, this aspect is not preponderant. However, the lack of an exhaustive validation and verification of this model has been outlined by some researchers. Valero and García-Bartual (2016) made an extensive calibration of the coefficients C_{ent} and σ , and showed that the model is highly dependent on the grid size used, beyond insufficiently accurate in the simulation of the air-concentration profile.

Lubin et al. (2006) simulated 3D plunging breaking waves by solving the Navier-Stokes equations, in air and water, coupled with a dynamic sub-grid scale turbulence model (LES). The model is used to describe accurately the air-entrainment process occurring when the waves break. This is an example that it is possible to use LES sub-grid turbulence models to cover the air-entrainment process, however due to the grid size used in this simulation ($\Delta x = \Delta y = \Delta z = 4 \times 10^{-4} \text{ m}$), the modelling is not always not practicable.

Moraga et al. (2008) proposed an air-entrainment model combining a Level-Set method with an Eulerian formulation, coupled with an injection algorithm for dispersed phase. The innovations of this model rely on the simulation of polydisperse flows where the bubbles' size is separated in different classes, and the inclusion of a bubble source term due to air-entrainment in a bubble size probability density function. The bubble source is activated when the downward liquid velocity is superior to 0.22 m/s at the free-surface region. Sensitivity analysis are performed to the parameters that compose this sub-grid model in a case of a breaking wave, among with an excellent correlation between accuracy and computational expense. The authors even suggested that a gain on the accuracy could be accomplished if the air entrainment region was influenced by the turbulence intensity and turbulent dissipation.

Ma et al. (2010) extended the previous work of Moraga et al. (2008), by replacing the source term for air-entrainment through the one implemented in Sene (1988), which is able to reproduce qualitatively the rate of air-entrainment for a vertical plunging jet. The source term become a function of the volumetric rate of air entrained per unit perimeter of the jet (q_A), the diameter of the jet at the impact zone (D_j), the volume of the liquid

phase where the air is entrained (V_S) and the characteristic bubble diameter (D_b),

$$E_g = \frac{6q_A D_j}{V_S D_b^3} \quad (2.23)$$

Based on the entrainment process described by Sene (1988) and Ervine and Falvey (1987), Ma et al. (2011b) reformulated the source term to deal with the turbulent kinetic energy at the free-surface and inward velocity,

$$E_g = C_{ent} \frac{f_E(D_b) \Delta D_b}{V_{avb}} \frac{\partial \mathbf{u}_{\hat{n}}}{\partial \hat{n}} \frac{k}{\phi_{ent} g} \quad (2.24)$$

where $f_E(D_b)$ is the Probability Density Function (PDF) of the source distribution as a function of bubble diameter (D_b). For the polydisperse model, ΔD_b is the width of the bubble diameter bin and $V_{avb} = \sum_{D_b} f_E(D_b) v_b \Delta D_b$ is the average bubble volume for the same bin in which v_b is the mean volume of a bubble having the diameter D_b . The applicability of this term has been proven in the simulation of several cases by means of changes in the air-entrainment coefficient, as like $C_{ent} = 0.02$ for the plunging jet case (Ma et al., 2011b), $C_{ent} = 11.8$ for the flow around the ship (Ma et al., 2011c) and $C_{ent} = 0.12$ for the hydraulic jump (Ma et al., 2011d). The dependence on this calibration factor is indeed the main drawback of this model as it can range in the order of 10^{-2} to 10^1 .

Shi et al. (2010) presented a 2-D polydisperse two-fluid bubbly flow model based on mixture theory. They formulated the breaking wave-induced air bubble entrainment term by connecting the shear production at the air–water interface ($P_r = \mu_t |\mathbf{S}|^2$) and the bubble number intensity with a certain bubble size spectra ($f_E(r_b)$). The source of bubble number per unit volume for bubble size i is given by:

$$E_{g,i} = C_{ent} P_r f_E(r_b) \Delta r_{b,i}, \quad P_r > P_{r0} \quad (2.25)$$

Unlike the model of Moraga et al. (2008) and all subsequent, in this model, the bubble advection velocity (\mathbf{u}_g) is simply calculated as sum of mean flow velocity and bubble-slip velocity,

$$\mathbf{u}_g = \mathbf{u}_m + \mathbf{k} w_s(r_b) \quad (2.26)$$

where \mathbf{k} is a vertical unit vector and $w_s(r_b)$ is the bubble-slip velocity, which is dependent to the bubble radius. The model was used to predict the air that entrains in a surf zone of a wave with patent under-prediction of the void fraction present at the beginning of breaking. The reason for this discrepancies, in author's perspective, is the absence of an algorithm that transport the air volume in the discrete phase to the continuous, and then,

the VOF model employed does not account for the entrainment of identifiable bubbles in the early stage of breaking.

Ma et al. (2011a) idealised a bubble entrainment source term for breaking waves by correlating it with the turbulence at the free-surface. It was assumed that the total energy required for bubble formation is linearly proportional to the turbulence dissipation rate (ε). The entrainment has assumed to take place in zones where the turbulence dissipation rate is greater than a critical value. The bubble creation rate was given by:

$$E_g = \alpha_l \frac{C_{ent}}{4\pi} \frac{\rho_l}{\sigma} r_b^{-2} \varepsilon \quad (2.27)$$

The velocity of the bubbly phase is calculated by means of the solution of the momentum equation, neglecting the temporal, advection and diffusion terms. This simplification allows the solution of the momentum equation in an explicit way. The entrainment coefficient was chosen as $C_{ent} = 0.18$. Through the comparisons with experimental data of a surf zone breaking wave test, it was demonstrated that the model describes bubble entrainment and void fraction evolution reasonably well. Some discrepancies in terms of void fractions were found in the simulation of the 2-D breaking wave phenomena, as the $k - \varepsilon$ turbulence model was not able to describe correctly the interactions between the dispersed and continuous phases, and consequently the correct aeration process.

Witt et al. (2015) simulated both 2D and 3D hydraulic jumps using an unsteady RANS, realizable $k - \varepsilon$ turbulence model, with a VOF treatment for the free-surface. No sub-grid model is used to inject air at the free-surface. The 2D void fractions were calculated with good accuracy in a zone closer to the free-surface, however the simulation tends to predict higher void fractions in the shear region near the toe of the jump. The 3D simulation of the hydraulic jump has solved the discrepancies found in the near toe region, but 20 s of the observed flow took 98 496 CPU hours, which is just feasible in a high-performance computer.

2.5 Experimental techniques and instrumentation for air-concentration measurements

2.5.1 Introduction

Air concentration is a vital parameter to characterise the presence of air in the flow. The air-concentration (C), sometimes called as void fraction, is defined as the portion of volume

occupied by gaseous the air (V_g) inside the air/water mixture ($V_g + V_l$), which can be generalised by the formula:

$$C = \frac{V_g}{V_g + V_l} \quad (2.28)$$

The interest on air measurement techniques experienced a significant progress on last decades, with the development and application of many techniques. An extensive review of some of those methods can be found in (Nagash, 1994; Matos et al., 2002; Chanson, 1997, 2002a, 2007). These reviews confirmed a significant progress on those techniques that solved main incapacities and drawbacks, displacing them in two main groups: intrusive and non-intrusive techniques. Intrusive devices are essentially rearranged Pitot tubes (mechanical systems), hot-film anemometry, resistive/conductive single/dual tip probes or double-tip fiber-optical probes. Non-intrusive techniques are still under development with many variants of image processing techniques, however special attention can be given to the BIV technique.

2.5.2 Intrusive devices

The first attempt to measure the air concentration was made by Lamb and Killen (1950). The authors measured the air-concentration by comparing the difference of electrical conductivity between the air-water mixture and the water alone. The results of this electrical method was compared with a mechanical structure for air-water mixture measurements previously developed by DeLapp (1947). The later consists in the continuous assemblage of an air-water mixture sample that is afterwards drawn off into a closed tank and from it determine the separation rate of the flow. Also Viparelli (1953) applied a conductive probe to calculate the air concentration profile in a 1:1 sloped flume and compare this technique with a modified Pitot tube structure. The Pitot tube was placed in the flow direction in order to syphon a sample of the mixture to an reservoir from which it is possible to measure the ratio air/water. He compared the results of this last mechanical process with a conductive probe and found that the last present always higher values of air concentration. Many other examples of the use of the rearranged Pitot tube can be found in literature as in (Matos, 1999) for the characterization of air concentration profiles on the steps edges of a stepped spillway, or in (Carvalho, 2002) using the modified Pitot to measure air concentration in the hydraulic jump. Although simple, this method only shows good results in a zone with low void fraction values and needs to know beforehand the flow direction which in strong hydraulic jumps or on the step cavities of the stepped spillway is not always possible.

Another methodology to measure the void fraction is the hot-film anemometry. It

has the advantage of barely being an intrusive device. Resch and Leutheusser (1972) and Resch et al. (1974) used hot-film anemometry coupled with conical probes to obtain instantaneous velocity (mean and fluctuations) and air content in the hydraulic jump. However, there are some difficulties in the signal interpretation and equipment calibration (Nagash, 1994).

Measurements of air concentration using resistive probes gain indeed more accuracy and reliability on the last decades as are from instance the air-concentration profiles acquired in hydraulic jumps in (Rajaratnam, 1962; Chanson and Brattberg, 2000; Chanson and Toombes, 2002; Chanson, 2007; Murzyn and Chanson, 2008), measurements in the aerated zone of a stepped spillway with different slopes and flow rates done in (Chanson, 1988; Afshar et al., 1994; Chanson, 1993, 2001, 2002b; Felder and Chanson, 2014) or measures of air concentration in a transversal section of a partially full pipe with high longitudinal slopes (Volkart, 1980). The main disadvantage of the standard probes, beyond being an intrusive technique is that the preferential direction of the flow needs to be known a priori. To overcome this difficulty, some prototype probes are being made. For instance, Borges et al. (2010) developed a new concept of conductivity probes combining three-holes pressure circuit and back-flushing. The probe can be set in two ways: (1) aligned with the flow so that the pressure in two symmetrically placed pressure holes is equal; or (2) collocated onto the flow and the different pressure values of the three holes, defines the angle between the probe and flow direction.

2.5.3 Non-intrusive techniques

Measurements of velocity profiles using the traditional Particle Image Velocimetry (PIV) technique fails in highly aerated flows due to the reflection of laser light in the surface of bubbles. In fact, PIV technique is limited to flows with no more than 10% air (Amador, 2005). Govender et al. (2002) used a technique similar to PIV with laser sheet to illuminate the aerated zone of a laboratory 2D breaking wave. Image cross-correlation techniques were applied to measure velocity profiles, turbulence intensity and water levels. Promising air-phase-averaged contours were acquired in this process, however due to the lack of a calibration scale, the air-profiles were plotted dimensionless.

Ryu et al. (2005) extended previous techniques and proposed the BIV technique that uses the bubble particles as trackers. The bubble velocity is measured by correlating the texture of the bubble images. This technique was applied in the measurement of mean velocity fields of plunging breaking wave impinging on structure.

Leandro et al. (2012) followed the work of Mossa and Tolve (1998), proposing an improved Image Processing Procedure (IPP) to measure the instantaneous and averaged

void fractions on hydraulic jump by analysing pixel intensity on images. This technique can provide measurement in different positions simultaneously, without any interference in the flow conditions. The results were compared with dual-tip conductivity probe measurements. Alike BIV, this approach is not able to measure the component along the axis perpendicularly to the camera image, thus the application in strongly 3D flows is compromised, since the image captured represents only a 2D plane.

3

Numerical and Experimental Investigation of a Gully Under Surcharge Conditions

Abstract: This paper deals with numerical and experimental investigation of a gully under exceptional situations after the sewer system becomes pressurized. These results are useful for the calibration and validation of the linking elements found in DD models. The experimental results were obtained in the Multiple-Linking-Elements (MLE) experimental installation that allows the simulation of full surcharge flow through a gully. The installation consists of an 8 m long and 0.5 m wide channel, fitted with a $0.6 \times 0.3 \times 0.3$ m gully with a 80mm diameter pipe inlet at the bottom. The numerical results were obtained using a three-dimensional structured mesh simulated in the OpenFOAM® toolbox. The results characterization focuses mainly on the jet area, whereby pressure-flow relations were derived for this specific gully. The good agreement found between numerical and experimental results, allowed the extrapolation to larger flow rates.

3.1 Introduction

During extreme rainfall events urban drainage systems may become pressurized, and the flow may surcharge through the gullies and manholes. This phenomenon is commonly called ‘reverse flow’ (Lopes et al., 2012). In extreme cases it may cause ‘urban geysers’ and sometimes the projection of the grate that covers the gully. To understand the hydraulics of drainage systems it is therefore important to characterize the hydraulic behaviour of each component of the sewer system. There are a large variety of models used to simulate the behaviour of flooding in cities. Among those, are the so called Coupled Urban Drainage Models or simply DD models (Leandro et al., 2009). Those are considered the best models to accurately simulate the flows which occur simultaneously on the surface and on the sewer systems. However, a fundamental weakness of DD models is the existence of few studies where the linking-elements (e.g. manholes or gullies) are actually calibrated. Experimental and numerical studies in manholes already exist; Guymer et al. (2005) presented some experimental results in surcharged manholes that explored the effects of diameter and surcharge on the solute transport. Stovin et al. (2008) and Bennett et al. (2011) used the previous experimental results to validate a 3D manhole CFD model.

Particular studies on gullies are fewer than of manholes, despite both having similar costs of experimental installations and computational efforts. The striking difference is the variability of the gullies geometry used in different countries which makes the efficient definition of a standard difficult. Gómez and Russo (2009) obtained experimental equations for the hydraulic efficiency of several continuous transverse grates used in Spain. Carvalho et al. (2011) used a 2DV in-house numerical model to study some Portuguese gullies in drainage conditions and more recently in reverse conditions (Carvalho et al., 2012). Romagnoli et al. (2013) studied experimentally the reverse flow in the MLE experiment. Galambos (2012) and Djordjević et al. (2013) presented experimental and numerical investigations using 3D CFD model to investigate the hydraulic performance of United Kingdom (UK) gullies during drainage and surcharge conditions. Other studies on Portuguese gullies using 3D numerical model OpenFOAM® are performed in (Martins et al., 2012; Lopes et al., 2012). The work presented intends to be a step forwards in understanding the hydraulic behaviour of the Portuguese gullies in reverse conditions, which can be useful for the calibration of linking elements in DD models. The experimental installation MLE constructed at the Laboratory of Hydraulics and Water Resources of University of Coimbra is able to simulate flows in the range of 2 to 6 l/s at the inlet. The numerical results are obtained using the OpenFOAM® open-source toolbox. The paper starts by presenting the experimental installation and numerical model used, followed by the methodology used for comparing the numerical and experimental studies developed

for verifying the accuracy of the numerical model, particularly in the area close to the jet. The paper then presents the extrapolation to larger discharge rates by using the calibrated numerical model while the behaviour of the flow inside the gully box is analysed.

3.2 Experimental setup

The physical tests were carried out in an existent full scale experimental gully inside a multi-purpose channel at the Hydraulic Laboratory of University of Coimbra where the channel flow, the pumps regime and the valves are electronically controlled by a Supervision, Control And Data Acquisition (SCADA) system. The experimental facility is composed by an acrylic platform with 1% slope, 8 m long and 0.5 m wide and an acrylic gully box with dimensions 0.6 m long 0.3 m deep and 0.3 m wide (Fig. 3.1). In order to simulate the surcharge conditions, the gully bottom is connected to a small reservoir by a 0.08 m internal diameter PVC opaque pipe. The water level in this reservoir can provide the control of the static pressure and the verification of the steady state flow. The experiment downstream outlet is a free outfall. This structure can be used to replicate a range of discharges from 2 to 6 l/s.

The photographs of the flow were taken using digital Sony Alpha DSLR-A350 camera with 14.2 MP with a lens DT18-70 mm F3.5-5.6. The camera was supported by a tripod during all the experiments fixed in a specific place. To provide the bubbles illumination, a reflector Photoflex SilverDome NXT with 1000W light was used. The instantaneous velocity data set were collected using a Nortek AS® 10MHz Acoustic Doppler Velocimeter (ADV).

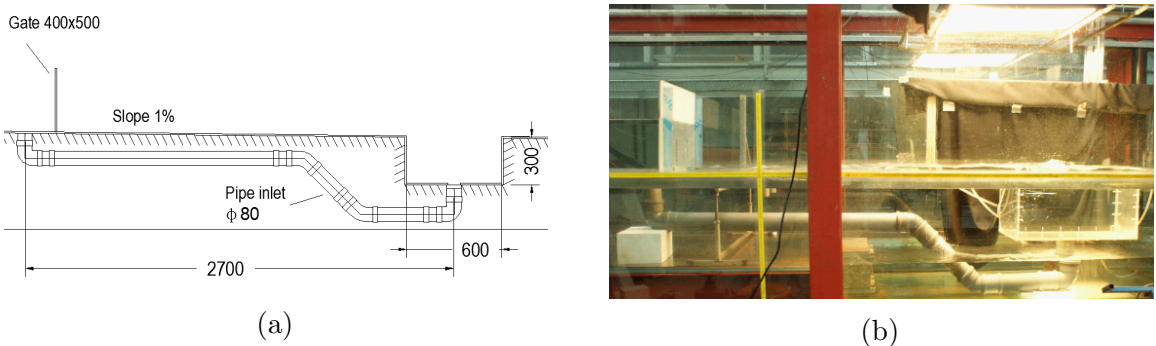


Figure 3.1: (a) Sketch of the experimental installation used for the study of the reverse flow [mm]. (b) Photograph of the experimental installation.

3.3 Numerical simulations

Solutions are obtained using OpenFOAM® v1.7.1 with the solver *interFoam* (Ubbink, 1997) and Pressure Implicit with Splitting of Operator (PISO) (Issa, 1985) used for interactive computation of unsteady incompressible flows. The solver *interFoam* is able to reproduce the multiphase flows with VOF method (Hirt and Nichols, 1981) where a transport equation is able to determine the relative volume fraction of the two phases (“alpha1” in OpenFOAM® nomenclature) in each computational cell.

The Smagorinsky LES model (Smagorinsky, 1963) was used. It can reproduce similar results with less computational effort than DNS, solving only the large scales of turbulence and approximate the smalls ones using simplified methods, similar to RANS, the Sub-Grid Scale (SGS) models. In this model, the eddy-viscosity (μ_t or μ_{SGS}) is modelled using a constant C_s relatable with the constants C_ε and C_k . The pre-defined values in OpenFOAM® are $C_\varepsilon = 1.05$, $C_k = 0.07$ and $C_s = 0.13$ (Damián and Nigro, 2010).

3.4 Methodology

3.4.1 Experimental proceedings

Three different tests were carried out with sewer discharges of 4, 5 and 6 l/s. These flows are controlled upstream by the SCADA system and through the heights in the reservoir. Nevertheless, as these discharges were near the low limit range for SCADA, they were confirmed by the volumetric method. Table 3.1 summarize the tests name (Q_x), flow rates (Q), internal diameter of the pipe inlet (D), averaged velocity at the inlet (U), Reynolds numbers (Re) and Froude numbers (Fr).

Table 3.1: Summary of the discharge conditions performed in the experimental installation. Q – Flow at inlet (overflow), D – Internal diameter of pipe inlet, U – Velocity at inlet, Re – Reynolds Number, Fr – Froude Number.

	Q (l/s)	D (m)	U (m/s)	Re (-)	Fr (-)
Q4	4	0.08	0.796	6.37×10^4	0.90
Q5	5	0.08	0.995	7.96×10^4	1.12
Q6	6	0.08	1.194	9.55×10^4	1.35

Each flow was filmed and photographed 10 times and the most representative photograph was chosen to compare visually with the numerical results. Furthermore a

Computational Vision Model in Simulink™ developed by Roque (2011) was used to find the average contour for the free surface using the entire film. This model is based in image treatment and segmentation techniques to find at each instant the two largest lines within the domain for a given spatial threshold. One of those lines represents the channel bottom and the other the free surface. The distance between the midpoints of those lines is the flow depth. The acquisition rate used in the model was set to 30 fps. Measurements of the velocity of the jet were obtained using an ADV probe. The low ADV correlations obtained inside the jet prevented the use of such points, therefore, only the points in the vicinity of the jet were used. In total, 19 points were measured in two vertical lines with 0.03 m spacing (Fig. 3.2). The frequency and sampling period were set to 1 Hz and 180 s respectively.

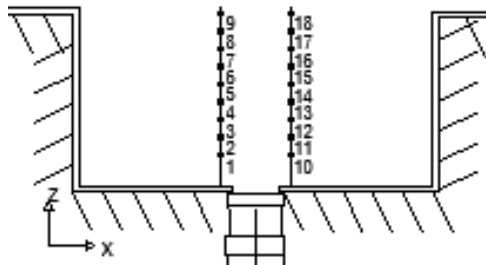


Figure 3.2: Points measured at the left (points 1 to 9) and right side of the gully (points 10 to 18).

3.4.2 Computational meshes

To accurately replicate the physical experiment, some adjustments were made in the mesh. A previous study from the Authors showed good results with the application of a sudden enlargement and a curve at the gully inlet to reproduce the head losses in the pipe and the real trajectory of the velocity vectors at the inlet, respectively (Fig. 3.3) (Lopes et al., 2012). The mesh used is regular and non-regular with grid spacing between 0.01 m and 0.04 m, making a total of 278 855 points. The finer mesh is applied to the gully box whereas the coarser mesh is applied to the main channel when the vortex characterizations are not so important. The mesh was generated using the blockMesh utility available in the OpenFOAM® toolbox. This kind of mesh is harder to generate comparatively to the use of Computer-Aided Design (CAD) software's (e.g. SALOME platform or GMSH), but the well-structured grid contribute efficiently to the control of the grid space and for the decreasing of the computational time-step.

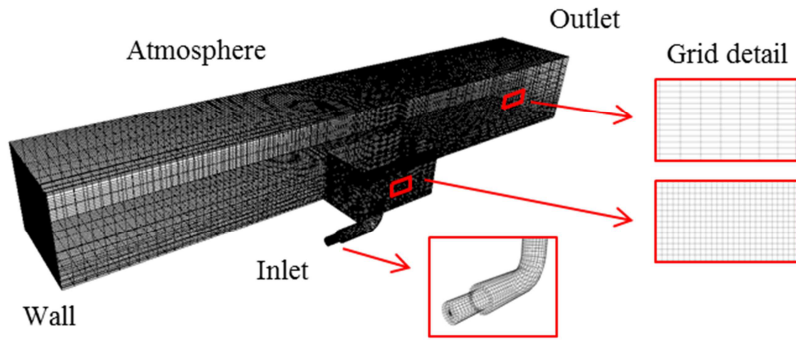


Figure 3.3: 3D view of mesh, grid detail and boundary conditions used in the numerical model OpenFOAM® for studying reverse flow in the gully.

3.4.3 Boundary conditions

Four types of boundary conditions were used in the model. The parametrisations and characteristics depending on their functional propose: The inlet (end of pipe) only allows flow in at a fixed velocity; the outlet is a boundary where the fluids exits the domain (right side of the channel), where the relative pressure is fixed to 0; in the atmosphere the air can make exchanges with the outside and the relative pressure is set to 0 and the wall have the condition of no slip and therefore the velocity is set to 0. When one parameter is stipulated the other boundary parameters are calculated by OpenFOAM®.

3.4.4 Computational simulations

All the numerical results were obtained after 15 seconds of simulation. The Authors experience in similar structures and computational simulations showed that 10 or 15 seconds of simulation were sufficient to reach the steady state (Carvalho et al., 2012; Martins et al., 2012; Lopes et al., 2012). The average results obtained are related to the last 5 seconds of simulation.

The computational simulations were performed using turbulence closure. The Smagorinsky LES model was chosen because it shows good consistency comparatively to experimental results (Gong and Tanner, 2009). The two parameters C_ε and C_k need however to be adjusted to each case (Damián and Nigro, 2010). Several values were tested around the standard values proposed in OpenFOAM® Toolbox, $C_\varepsilon = 1.05$ and $C_k = 0.07$ for the simulation Q5. In total, five simulations with different combinations were computed (C1 to C5). The Average Relative Errors (ARE) between numerical and experimental results for the velocity near the centre of the gully are showed in Table 3.2 and errors around 30% were found. However, these errors are acceptable in the vicinity of jets because of the large

temporal variation of the velocity profile as attested by other authors (Hussein et al., 1994). Nevertheless the selection of the parameters $C_\varepsilon = 1.05$ and $C_k = 0.07$ (combination C3) was based on the ARE (Table 3.2). Figure 3.4 shows the experimental and the numerical data for flow heights above the gully.

Table 3.2: Average Relative Errors (ARE) for numerical and experimental velocities at left (AREl) and at right (AREr) points of gully (see Fig. 3.2) for the five set of LES coefficients tested.

	C_ε	C_k	AREl	AREr	ARE
C1	1.05	0.07	35%	30%	33%
C2	1.05	0.055	35%	42%	38%
C3	1.05	0.03	31%	27%	29%
C4	1.15	0.07	41%	21%	31%
C5	1.25	0.07	25%	37%	31%

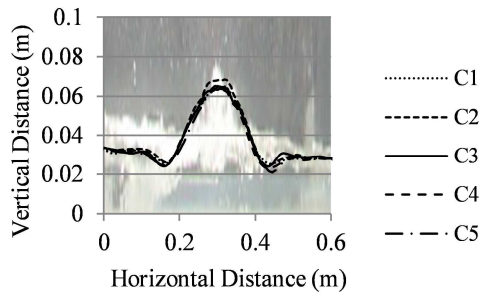


Figure 3.4: Heights of the flow for different set of LES parameters (C_ε and C_k) using the simulation with 5 l/s at the inlet (Q5).

3.5 Results

Figure 3.5 shows the numerical average contour in the central section of the gully. The computational simulations are compared with the representative photograph of each flow and the average contour of the jet extracted from the Computational Vision Model (Roque, 2011).

After calibration of the jet through the experimental photographs, new numerical simulations are computed for flows with 8 and 10 l/s at the inlet (those simulations are symbolized with *). Figure 3.6a and Figure 3.6b show respectively the total pressure (Pt) and dynamic pressure (Pd) at gully bottom in the center profile of the gully for the simulations Q4, Q5, Q6, Q8 and Q10 l/s. The total pressure is the sum of static pressure with dynamic pressure (Pt=P+Pd).

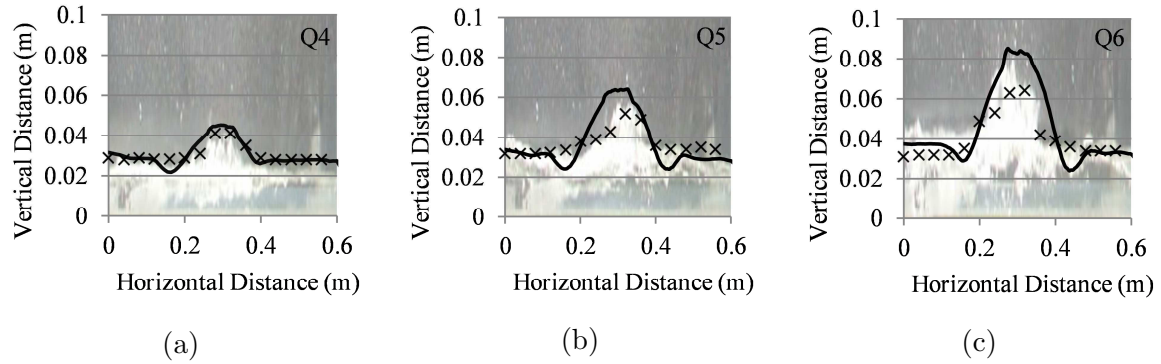


Figure 3.5: Average contour obtained with OpenFOAM® numerical model (—) compared with photographs in background and a Computational Vision Model (××) (Roque, 2011) for (a) Q4, (b) Q5 and (c) Q6.

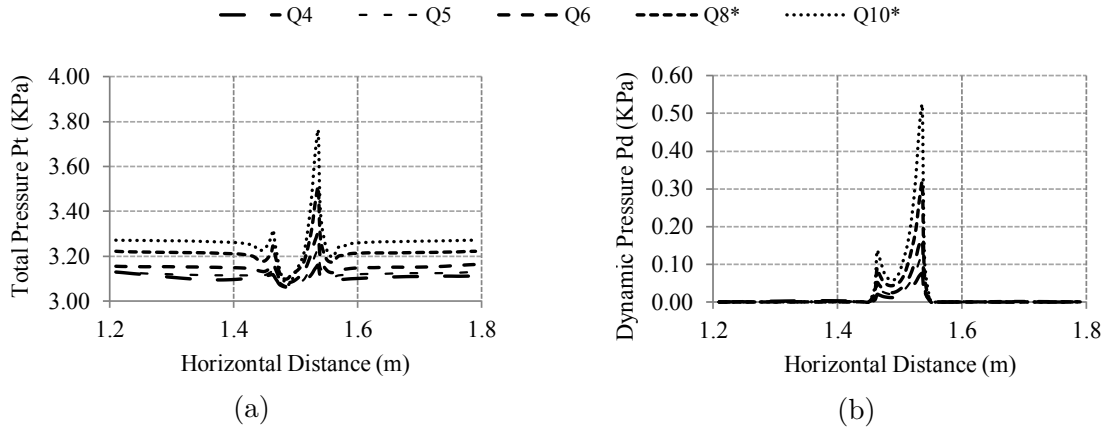


Figure 3.6: (a) Total pressure (P_t) at the gully bottom in the centre profile. (b) Dynamic pressure (P_d) at the gully bottom in the centre profile.

Figure 3.7a shows the maximum heights of the jet (h_J) and the flow depths at the left (h_L) and the right side (h_R) of the gully. Figure 3.7b shows the average total pressure (P_t) and average dynamic pressure (P_d) at gully bottom in the centre (C), left (L) and right side (R) of the gully. The adjustments to the best trend lines are made herein and the relations for h -Q (flow height – sewer overflow), P_t -Q (total pressure – sewer overflow) and P_d -Q (dynamic pressure – sewer overflow) are shown.

Figure 3.8 shows the average stream lines of the gully in the middle longitudinal section. Figure 3.9 shows the average velocity fields in the middle longitudinal section of the gully obtained from the numerical model using a grey scale in the range 0 to 3.3 m/s.

Figure 3.11 represents the temporal velocities in a point centred in the top of the gully (Fig. 3.10) for the simulation Q6. Analogous behaviour was found for the remaining simulations. For the sake of simplicity they are not presented in this paper. Figure 3.12 shows the application of Fast Fourier Transforms (FFT) to the theta angle and the vector

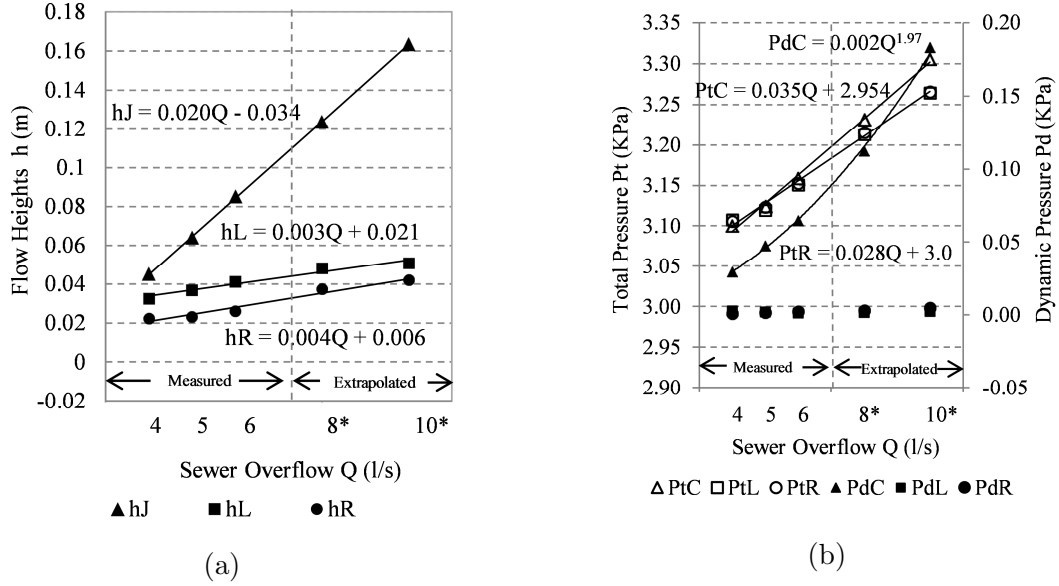


Figure 3.7: (a) Flow heights in top of the gully. The triangles represent the maximum height of the jet (hJ), the squares represent the height at left side of the jet (hL), while the circles represents the height at right side (hR). The relations $h-Q$ are shown in the figure. (b) Average total pressure (Pt) and average dynamic pressure (Pd) at gully bottom. The triangles represent the average pressure at the inlet (C), the squares represent the average pressure at left side of gully bottom (L), while the circles represents average pressure at right side of gully bottom (R). The relations $Pt-Q$ and $Pd-Q$ are shown in the figure.

V_z for the simulation Q6. The FFT is used to obtain the dominant frequency of the signals or periodic structures in time series data.

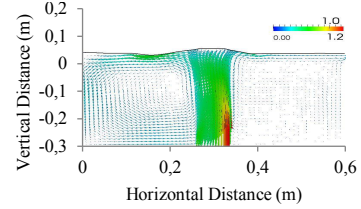
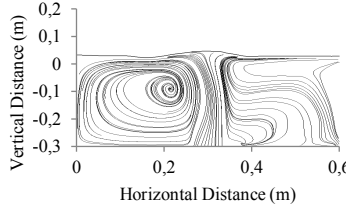
Figure 3.13a represents a histogram of frequencies for the direction of the vector V_{xy} through a theta angle (in radians), schematically represented in Fig. 3.10. If the direction of the vector V_{xy} is the same of x-axis, the theta angle is equal to zero and evolves anti-clock-wise. The adjustment of maximum V_z to a linear equation was done herein. Figure 3.13b shows a histogram of frequencies of vector V_z in the centre point in top of gully.

Table 3.3 shows the adjustment to a normal distribution of the V_z histogram using the Sample Kolmogorov-Smirnov (K-S) Test. In this test assuming the null hypothesis the data is better adjusted by a Gaussian distribution.

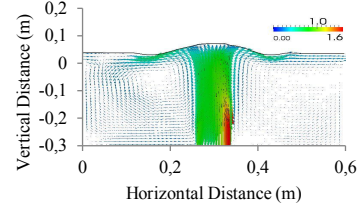
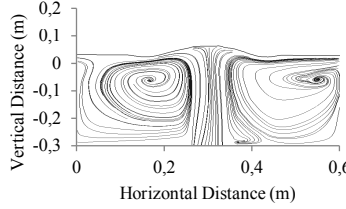
3.6 Discussion

The comparisons of the flow heights in the numerical and the experimental simulations are in good agreement. Figure 3.5 shows coherent results between numerical average

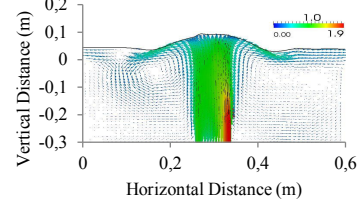
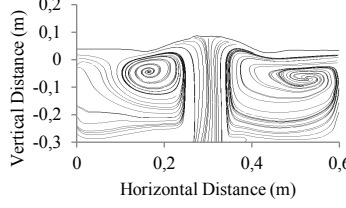
(a) Q4



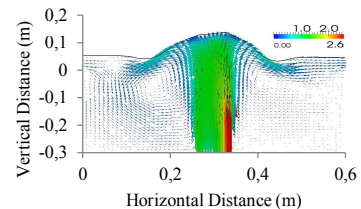
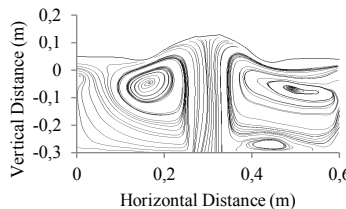
(b) Q5



(c) Q6



(d) Q8*



(e) Q10*

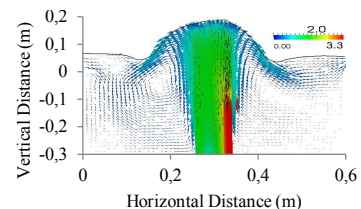
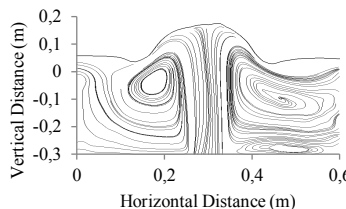


Figure 3.8: Stream lines obtained with the numerical model in the middle longitudinal section of the gully.
*Extrapolated discharges.

Figure 3.9: Velocity fields obtained with the numerical model in the middle longitudinal section of the gully.
*Extrapolated discharges.

contours, photographs of the experiments, and the free-surface contours captured with the Computational Vision Model.

Figure 3.6a shows the pressure at the gully bottom in the centre profile. The minimum pressure corresponds to the centre of the jet although the maximum values are near the side walls. At the gully sides the total pressure is almost constant and approximately equal

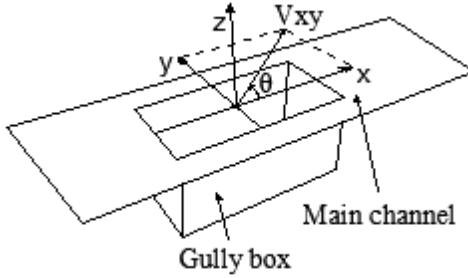


Figure 3.10: Sketch of centre point in the top of the gully and theta angle used for the study of the behaviour of the jet.

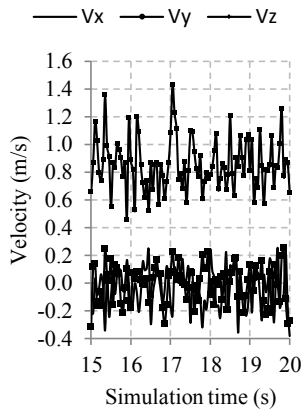


Figure 3.11: Velocities at directions x, y and z in the center point on the top of the gully for Q6.

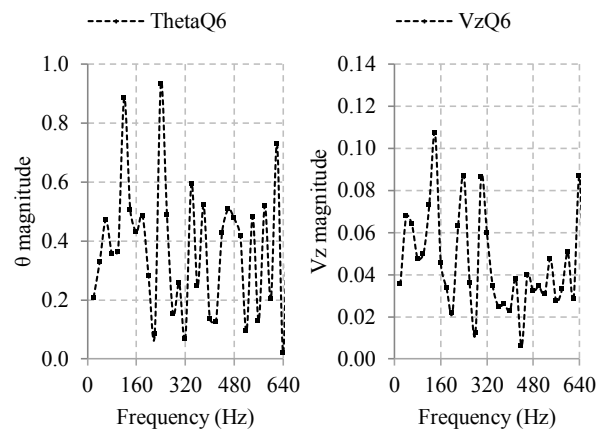


Figure 3.12: FFT analysis for the theta angle and velocity Vz using Data Analysis Package using Q6.

Table 3.3: Sample Kolmogorov-Smirnov Test for the histograms presented in Fig. 3.13b.

	FVzQ4	FVzQ5	FVzQ6	FVzQ8*	FVzQ10*
Mean (μ)	0.405	0.629	0.854	1.229	1.578
Std Deviation (σ)	0.130	0.182	0.188	0.235	0.281
p-value of K-S test	0.837	0.616	0.138	0.694	0.861
95% Confidence min.	0.150	0.272	0.486	1.148	1.481
95% Confidence max.	0.659	0.985	1.222	1.309	1.674

to the hydrostatic pressure. The dynamic pressure, showed in Fig. 3.6b is almost null near the bottom wall, affected by the lower velocities of the gully eddies, and their contribution to the total pressure can be neglected. Nevertheless, at the inlet, the contribution of the dynamic pressure for the total pressure should be considered. The asymmetry of the jet could be explained by the influence of the pipe curve used in the experiments and eddies'

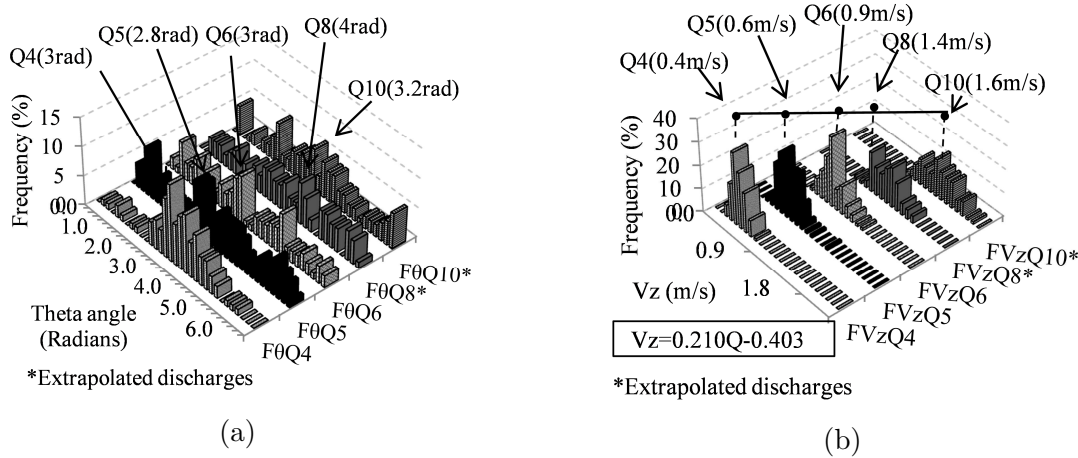


Figure 3.13: (a) Histogram of frequencies of the theta angle. The 0 radians means the vector V_{xy} takes the positive direction of x-axis. This angle is illustrated schematically in the Fig. 3.10. (b) Histogram of frequencies for the velocity V_z in the centre point on top of the gully. This point is illustrated schematically in the Fig. 3.10.

position.

Relations h-Q are presented in Fig. 3.7a whereas relations P-Q and Pd-Q are presented in Fig. 3.7b. The relations h-Q can be approximated using linear equation, while the relations P-Q and Pd-Q use linear and power law adjustment. The average total pressure at left and right side of the gully is coincident and governed with the same equation ($PR=PL$). The average dynamic pressure (Pd) in both sides of the jet are near zero, hence the adjustment to trend line was discarded.

The numerical stream lines and vector fields are showed in Fig. 3.8 and Fig. 3.9, respectively. The surcharge flow is characterized by a strong jet in the centre and two large eddies in both sides of the gully. The increasing of the sewer overflow decreases the size of the eddy presented in the left side of the gully and increases the eddy presented on the right side. Three different situations can be defined: 1) for discharge smaller than 4 l/s, the left vortex occupies all the left side of the gully while on the right side, the vortex is negligible; 2) for discharge between 5 and 6 l/s, one vortex appear near the right wall, while on the left side the vortex size decreases and changing the direction of the jet; 3) for discharge greater than 8 l/s the vortex on the right side takes all the right domain and the left side vortex is closer to the jet.

The FFT analysis shows the existence of a dominant frequency of approximately 240Hz and 100Hz for the theta angle and for the Vz, respectively. The theta angle frequency (Fig. 3.10) shows a maximum value between 2.8 and 4 radians for the five numerical simulations tested (Fig. 3.13a), i.e. in the negative direction of x-axis. This result is more visible for lower discharge and could be explained by the influence of the large eddy in the

left side of the jet. The decrease of the left eddy size also decreases the influence on the jet and therefore a greater variability of frequencies is found.

For the velocity Vz case, the maximum value increases with the discharge (Fig. 3.13b). A linear equation that connects the maximum values of velocity is found and can be used to extrapolate for larger discharges. The adjustment to a normal distribution was done for the Vz histogram with good results and the 95% confidence interval around the mean values is showed in the Table 3.3. After analysing the confidence intervals, the extreme values of confidence interval for Q8 and Q10 are closer to the average value than Q4 and Q5. This could indicate less uncertainty in the average values obtained with large discharge, however here we have no experimental data.

3.7 Conclusions

This paper presented numerical and experimental results of surcharge flow in a Gully, especially focussing on the jet characterization and the height it reaches above the gully. The average contour and jet heights were defined for three experimental and five numerical simulations. Average velocities and streamlines at the centre profile of gully were also presented.

The following conclusions were obtained:

- as expected, the height above the gully reached with the jet increases with the increasing of the sewer overflow;
- two eddies at the gully box were found for the tested discharges, one at each side of the jet;
- the jet shows one preferential direction for the negative x-axis sharpest for lower discharges;
- the three relations h-Q, three relations P-Q and the relation Pd-Q presented can be used to calibrate the linking elements in Drainage Models.

Future studies could be looking into the gully under normal drainage conditions and analysis of other gully structures.

4

Assessment of a VOF Model Ability to Reproduce the Efficiency of a Continuous Transverse Gully with Grate

Abstract: This paper deals with the numerical investigation of the drainage efficiency of a continuous transverse gully with grate's slots aligned in the flow direction and compared with experimental data sets. The gully efficiency attained with a 3D numerical model is compared and validated against experimentally data. The numerical simulations are performed using a computational fluid dynamics VOF solver. Different slopes, from 0 to 10% and a wide range of drainage flows, from 6.67 to 66.67 L/s/m are simulated. The linear relation between Froude number and efficiency of the gully is in agreement to the one experimentally obtained.

4.1 Introduction

The complete and safe drainage in a flooding situation, caused by extreme rainfall events is one of the most challenging concerns for hydraulic engineers in urban areas, especially since a large part of cities are covered with impermeable areas. To drain such flows, efficient Urban Drainage System (UDS) needs to be designed giving special attention to gullies and manholes. These elements, also known as “linking elements”, contribute to the drainage of the flow from surface to the underground pipe systems. Theoretical and numerical studies on linking elements efficiency are from imperative importance to create constitutive relations between the underground and surface systems, and with them, calibrate urban drainage models (Djordjević et al., 2005; Leandro et al., 2009, 2016).

In areas where it is possible to define one point where the major part the flow drains to (e.g. in curves along streets, sidewalks or gardens), the gullies are typically efficient structures, capturing part of the flow from the surface to the sewer systems. Gullies’ inlet is normally rectangular and placed at the same level as the pavement, covered, in the most of the cases, by a grate which can have different sizes and shapes. In some countries, gullies are replaced by drop sewer manholes covered with a resistant grate, and placed on streets following the same rules as for the gullies.

The current design guidelines for United States of America gullies are based upon a report published by Federal Highway Administration (FHWA) with topics about efficiency and size requirements (FHWA, 1984, 2001). In Portugal, urban drainage elements design follows the by-law RGSPPDADAR (1995) which contains general rules to implement gullies but nothing related to their efficiency. Occasionally, the hydraulic performance and efficiency of gullies can be found in some catalogues of grates manufacturers (e.g. NFCO (1998)). Given this worldwide diversity of grate inlets and implementation, detailed studies are needed.

Efficiency studies of several grate types and curb inlets have been conducted by WEF & ASCE (1992), Spaliviero and May (1998), Comport and Thornton (2009), Russo and Gómez (2011) and Comport et al. (2012). The efficiency of Portuguese gullies was numerically studied by Carvalho et al. (2011) using a 2D VOF/Fractional Area Volume Obstacle Representation (FAVOR) model. The latter study was further extended by Martins et al. (2014) with 3D numerical simulations using the OpenFOAM® and the *interFoam* solver. The Authors compared water depths through the gully and the discharge coefficients for a large set of flow rates. In case of drop manholes, the studies are mainly focused on their efficiency, performance, shape and energy dissipation (Carvalho et al., 2012; Rubinato et al., 2013; Granata et al., 2014b).

When underground pipes get pressurized, the flow can emerge to the surface through

the gullies and manholes forming a jet. Romagnoli et al. (2013) used an ADV to measure the flow behaviour and the turbulent structure of the flow under reverse conditions in Portuguese gullies. Lopes et al. (2015b) and Leandro et al. (2014b) furthered the study of Portuguese gullies and found numerical relations between the flow from the ground pipe system and the height of the jet, and characterized the 2D vertical velocity profile inside a gully using the *interFoam* solver within OpenFOAM®. Vertical frequency and preferential direction of the jet at the surface were also studied. An experimental and numerical study in a typical United Kingdom gully under surcharge was made by Djordjević et al. (2013) to replicate the interactions between the surface flow and the ground drainage systems.

In large paved areas, such as squares, airports or high sloping roads, the common gullies inlets are ineffective to capture all the amount of rainfall water. In such cases, the continuous longitudinal transverse gullies represent a widely accepted solution, since the main design concern is on the positioning of the grate in the direction perpendicular to the flow. Due to the lack of tests in transverse gullies and their efficiency in different conditions, Gómez and Russo (2009) studied experimentally four types of grates, found typically in Spain and differing in the alignment and distribution of the slots, under different longitudinal slopes and five approaching flows. They formulated four linear relations, one for each grate type, which link the hydraulic efficiency to some particular flow conditions (Froude number and water depth) and the grate length. The study was further extended by Russo et al. (2013) with the formulation of empirical expressions to relate grate hydraulic performance to flow parameters and grate geometry.

The advances of the last decades in CFD allow the prediction of the flow in some components of the UDS and the evaluation of the different design factors for an efficient project and operation (Jarman et al., 2008; Tabor, 2010; Bennett et al., 2011; Djordjević et al., 2013). The freeware and open-source OpenFOAM® is one of these CFD packages. Special attention is given to the solver *interFoam* due to its capability to deal with free-surface flow with arbitrary configurations.

In this paper we aim to investigate the ability of the *interFoam* VOF model in reproducing drainage efficiency of a continuous transverse gully with a grate, under different flow rates and slopes. In particular we aim to assess the numerical model's ability to predict the hydraulic efficiency of urban drainage elements. Section §4.2 describes the experimental installation and procedure. The numerical mesh and the numerical model are presented in section §4.3, along with the simulations performed, the different meshes tested, the boundary conditions of the numerical model and the numerical simplifications. Section §4.4 compares and validates the grate efficiency obtained numerically with the experimental datasets, further discussed in Section §4.5. Finally, Section §4.6 summarizes and concludes the work.

4.2 Experimental model

The experiments were performed in the laboratory of Hydraulic Department of Technical University of Catalonia using the same installation described in (Gómez and Russo, 2009). It consists of a 1 : 1 scale model of a 1.5 m wide and 5 m long rectangular surface and a transversal grate placed downstream (Fig. 4.1a). The platform is able to simulate lanes with transversal slope up to 4% and longitudinal slope up to 14% and a wide set of flow rates from 20 to 200 L/s. A motorized slide valve regulates the flow discharged to the model and an electromagnetic flow meter measures the flow rates with an accuracy of 1 L/s. Upstream of the platform, the flow passes through a tank to dissipate the energy, providing horizontal flow conditions to surface water. The flow intercepted by the gully is conveyed to a V-notch triangular weir and the flow measurement is carried out through a limnimeter with an accuracy of 0.1 mm. Flow depths on the platform are visually obtained by reading a thin graduated scale.

The transverse grate used in this study is a composition of three single grates type 2 (Fig. 4.1b). This work comprises forty combinations of eight different longitudinal slopes $i_x = 0, 0.5, 1, 2, 4, 6, 8, 10\%$ and five unit inflows $q = 6.67, 16.67, 33.33, 50.00, 66.67 \text{ L/s/m}$. The transversal slope is $i_y = 0\%$.

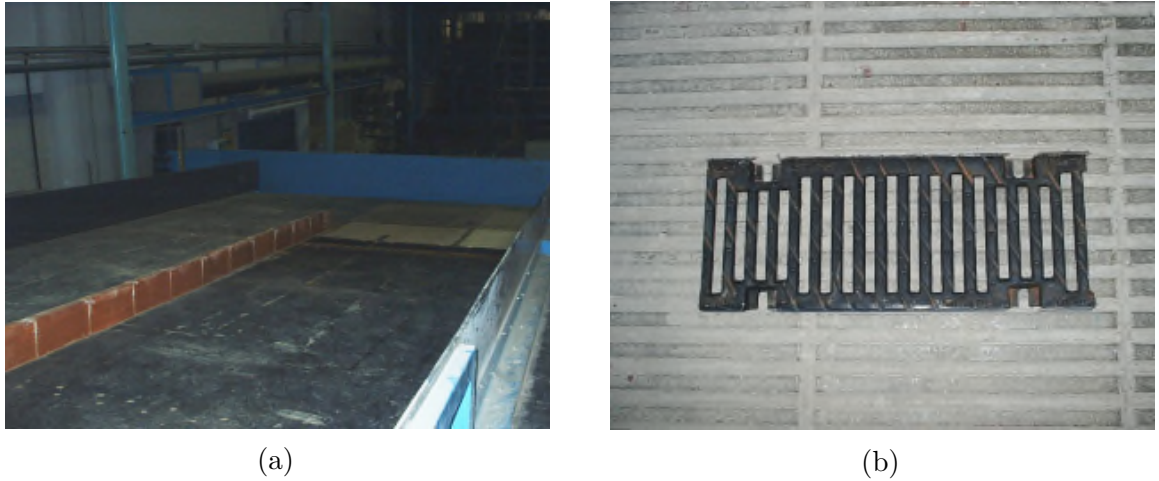


Figure 4.1: Photographs of the experimental installation built at UPC Hydraulic Department: (a) rectangular platform with transverse grate downstream; (b) single grate type 2. Photographs by B. Russo.

4.3 Numerical model

4.3.1 Mathematical formulation

The numerical simulations are performed using the solver *interFoam* within the free-ware and open-source CFD OpenFOAM® v.2.1.0. The mass and momentum equations are solved for isothermal, incompressible and immiscible two phase flows, written in their conservative form:

$$\nabla \cdot \mathbf{U} = 0 \quad (4.1)$$

$$\frac{\partial \rho \mathbf{u}}{\partial t} + \nabla \cdot (\rho \mathbf{u} \mathbf{u}) = -\nabla p^* - \mathbf{g} \cdot \mathbf{x} \nabla \rho + \nabla \cdot (\mu \nabla \mathbf{u}) + (\nabla \mathbf{u}) \cdot \nabla \mu + \mathbf{f}_\sigma \quad (4.2)$$

where ρ and μ are the fluid density and viscosity, \mathbf{g} the gravitational acceleration, \mathbf{u} the fluid velocity vector, \mathbf{f}_σ the volumetric surface tension force, τ the viscous stress tensor and $\nabla \cdot \tau$ viscous stress term, defined as follows:

$$\nabla \cdot \tau = \nabla \cdot [\mu(\nabla \mathbf{u} + (\nabla \mathbf{u})^T)] = \nabla \cdot (\mu \nabla \mathbf{u}) + (\nabla \mathbf{u}) \cdot \nabla \mu \quad (4.3)$$

The modified pressure p^* is adopted by removing the hydrostatic pressure from the total pressure (P). This is advantageous for the specification of pressure at the boundaries (Rusche, 2002).

$$\nabla P = \nabla p^* + \rho \mathbf{g} + \mathbf{g} \cdot \mathbf{x} \nabla p \quad (4.4)$$

The *interFoam* uses the VOF technique, first developed by Hirt and Nichols (1981), to follow and capture the interface between two different fluids by using a transport/advection equation. The transport-advection equation is given by Eq. (4.5); the last term is the compressive term (Weller, 2008; Berberović et al., 2009) which is used here to mitigate the effects of numerical diffusion and to keep the gas-liquid interface sharp rather than using interface reconstitution schemes. This term uses the compressive velocity (\mathbf{u}_c).

$$\frac{\partial \alpha}{\partial t} + \nabla \cdot (\alpha \mathbf{u}) + \nabla \cdot [\mathbf{u}_c \alpha (1 - \alpha)] = 0 \quad (4.5)$$

Each cell of the domain is attributed an α value, ranging from 0 to 1 depending on which portion of cell is occupied by fluid 1. Giving to fluid 1 the physical characteristics of water and to fluid 2, the physical characteristics of air, it means that cells with α equal to 1 only have water whereas cells with α equal 0 only have air and therefore, cells with intermediate values are interface cells (or free-surface cells) (Ubbink, 1997). The physical properties of the mixture are defined as a weighted average of the physical properties of

the two fluids denoted by subscripts 1 and 2, on the fraction occupied on each cell:

$$\rho = \alpha \rho_{f1} + (1 - \alpha) \rho_{f2} \quad (4.6)$$

$$\mu = \alpha\mu_{f1} + (1 - \alpha)\mu_{f2} \quad (4.7)$$

The volumetric surface force function is explicitly estimated by the Continuum Surface Force model developed by Brackbill et al. (1991) which is also function of the volume fraction:

$$\mathbf{f} = \sigma \kappa \nabla \alpha \quad (4.8)$$

After discretisation in space and time domains, PISO algorithm (Issa, 1985) is used for the pressure-velocity coupling.

4.3.2 Model description

Figure 4.2 shows the full domain experimentally studied by Gómez and Russo (2009) for the continuous grate with slots parallel to the longitudinal flow direction. The different inflows are included in the simulations by an input of uniform velocity and flow depths, whereas the different slopes are carried out numerically changing the direction of the gravity vector.

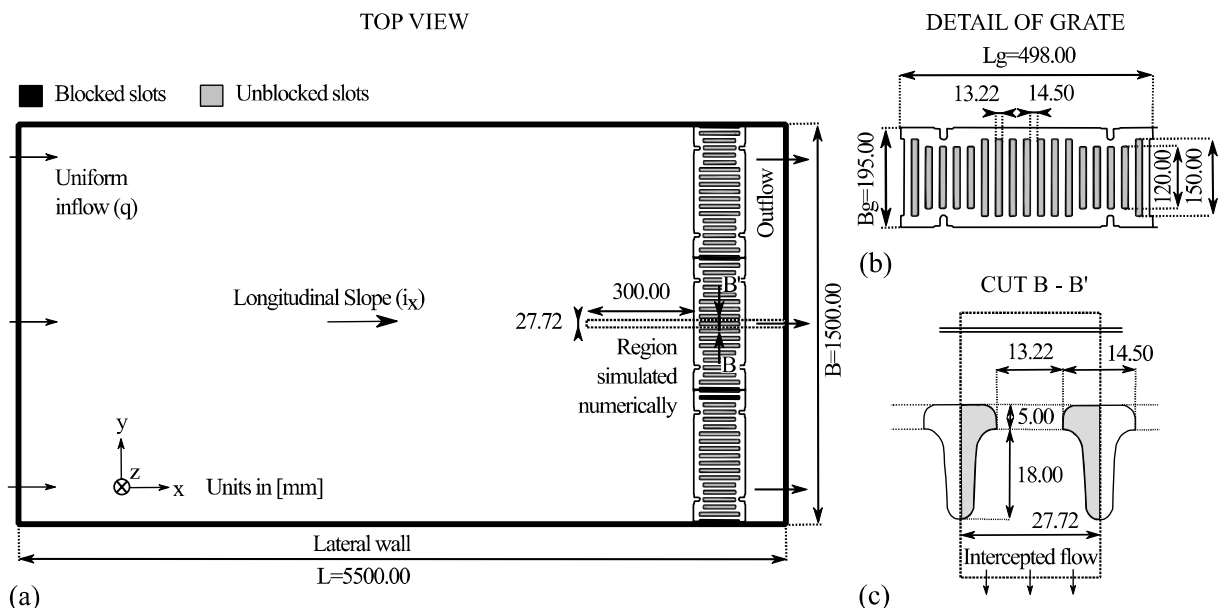


Figure 4.2: Sketch of the experimental installation: (a) top view, (b) detail of grate and (c) cut B-B'. Units in millimetres.

Earlier work on modelling gullies (Carvalho et al., 2012; Lopes et al., 2015b) proved

that setting the *interFoam* to laminar characteristics can provide accurate results with fast convergence. The laminar model solves the mass and momentum equations together with the advection equation for α without any turbulence approach. To achieve a quick convergence to the steady state flow, the domain is initially filled by water up to a height corresponding to the expected flow depth. The steady state is achieved after 5 s of simulation, time in which the volume of water in the domain becomes constant. The results presented are a further average of 5 s to 6 s of simulation. The simulation time step starts at 5×10^{-5} s and it is progressively increased to values which do not allow the Courant number to exceed the pre-fixed value of 0.5. Each simulation is carried out in parallel over 3 sub-domains using two Quad-Core processors of the Centaurus Cluster, installed on the Laboratory for Advanced Computing of the University of Coimbra. The 3 sub-domains are vertically divided in the longitudinal direction of the mesh.

4.3.3 Numerical mesh

A 3D section of the grate is built using the open-source Salome v.6.4.0 software (Salome, 2011). In this study two different meshes are used: Mesh 1) is built with the NETGEN tetrahedral algorithm with edges ranging from 2 to 3 mm, making a total of 42 772 cells (Fig. 4.3a); and Mesh 2) refined both closer to the channel bottom and on the gully inlet (Fig. 4.3b). This refinement limits the edges to lengths lower than 1 mm, resulting in a total of 94 215 cells. It should be noted, that the simulation of the full domain (i.e. the whole grate) is challenging because of the mesh generation and the added computational cost due to the large number of cells required. Our earlier work on this study, showed that in order to assure a good representation of the flow field, the mesh near to the grate slots needs to be as small as 1 mm. This value is in-line with other researchers work on gullies (Djordjević et al., 2013) that also used such fine meshes to model urban drainage devices. Extrapolating this edge size to the full domain, the total number of cells can quickly rise to approximately 45 million of cells. In order to reduce the number of cells in the domain, this study simplifies the grate geometry to one grate slot with 27.72 mm width and assures its representativeness by recognizing the symmetry planes between slots and applying proper boundary conditions.

4.3.4 Boundary conditions

Five types of Boundary Condition (BC) are included in the simulations (Fig. 4.4). The Inflow BC allows to specify the flow entering to the channel. Due to the wide quantity of simulations performed with different inflow conditions (flow depth and velocity), the inflow is defined according to flow field conditions using a dynamic BC – extension *swak4Foam*.

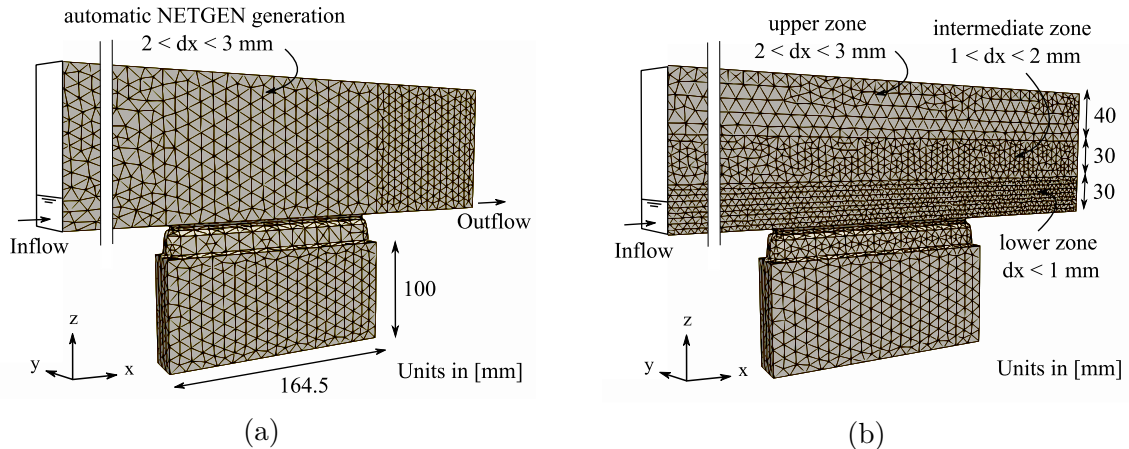


Figure 4.3: Detail of the meshes used in this study: (a) Mesh 1 - homogeneous mesh with ranging spaces between 2 and 3 mm (b) Mesh2 – mesh refined at the channel bottom with cells 1 mm spaced.

Two Outflows are defined, one on the channel platform and other on the bottom. The Atmosphere BC allows the air to leave and to enter in the domain and is defined on the top of the domain. The total pressure on both Outflow and Atmosphere BC is set to zero. The Wall BC, which represents the bottom of the channel and the grate walls, is set to slip-BC. The lateral walls are Symmetry Planes to assume the continuity of the domain.

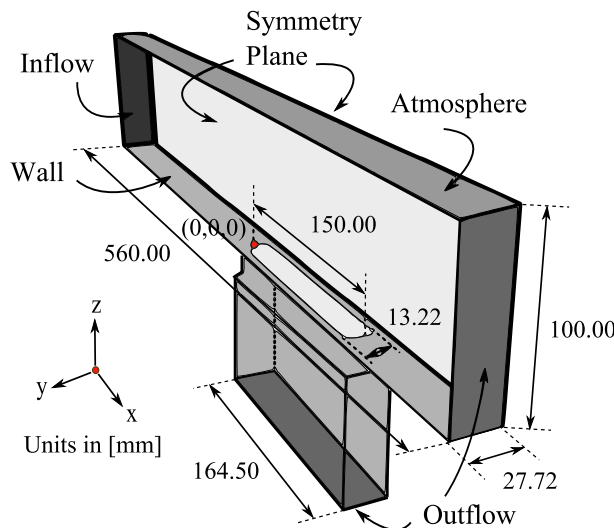


Figure 4.4: Sketch of the simplified geometry of the grate, flow comes from the inflow boundary to the outflow. All the measures are in millimetres. The red point on the beginning of the grate hole identifies the axis origin.

4.3.5 Numerical approaches

The complete grate, i.e. the 3 groups of grate type 2, exhibit non homogeneous characteristics along the y direction (Fig. 4.2). Some grate slots are completely blocked with concrete (marked in the Fig. 4.2 in black colour) whilst others feature different lengths (marked in Fig. 4.2 with grey colour). In a homogeneous grate, i.e. if all the grate slots had the same dimensions, the single grate slot could numerically replicate the efficiency of the complete grate. However, in a non-homogeneous grate, using the 150 mm length slot as representative of the real grate could lead to an overestimation of the grate efficiency, due to an increased inlet area and therefore intercepted flow. To overcome this issue, the total intercepted flow is calculated as a function of the uncovered area used for drainage by the use of correction coefficients implemented on the Numerical Intercepted Flow (NIF), based on area proportionality, resulting in a Corrected Intercepted Flow (CIF), Eq. (4.9).

$$CIF = \beta \times NIF \quad (4.9)$$

where β is a coefficient that takes into account the obstructed area, which can take either the value of coefficient C_1 , or C_2 or a multiplication of C_1 and C_2 , as shown in Fig. 4.5. The reasoning behind the C coefficients will now be explained. Q_i , Q_{if} and Q_{out} are the inflow, intercepted flow and outflow for just one slot, respectively and Q_I and Q_{IF} are the inflow and intercepted flow for the group of five slots, respectively. Coefficient C_1 takes into account the blocked slots. When one slot is blocked, Q_{IF} is calculated as five times the C_1 , times the Q_{if} , where C_1 is given by the number of uncovered slots, divided by the total number of slots. In this case, the Q_{IF} (or CIF) becomes equal to four times the Q_{if} . Coefficient C_2 takes into account the lower drainage efficiency of the shorter slots (i.e. with 120 mm length). If two slots are 0.5 shorter in length, Q_{IF} (or CIF) is calculated as $5 \times C_2 \times Q_{if}$, where C_2 is equal to three slots with length L_s , plus two slots with $0.5 \times L_s$, divided by the simulated five slots with length L_s . In this study, coefficients C_1 and C_2 are:

$$C_1 = \frac{\text{N. on unblocked slots in the complete grate}}{\text{Total of slots in 1.5m}} = \frac{50}{55.5} = 0.9009 \quad (4.10)$$

$$C_2 = \frac{\text{Length of 120mm slots} + \text{Length of 150mm slots}}{\text{Length simulated numerically}} = \frac{6 \times 120 + 11 \times 150}{17 \times 150} = 0.9294 \quad (4.11)$$

C_1 is always applied to the numerical intercepted flow unless the experimental efficiency of the grate is 100%. C_2 is applied if during the numerical simulations $L_w/L_s > 4/5$ (i.e. 120 mm/150 mm), where L_w is the slot length occupied with water (Fig. 4.6). Ideally both coefficients should be verified numerically by running the complete grate, however the

computational time required to do so, and the existence of real data upon the coefficients could be validated deemed the test-and-try process as preferable solution. Table 4.1 summarizes the distribution of the coefficients in simulations and Fig. 4.6 presents the 3D average free-surface position for simulations with $i_x = 4\%$ and the corresponding coefficients to be employed in each case.

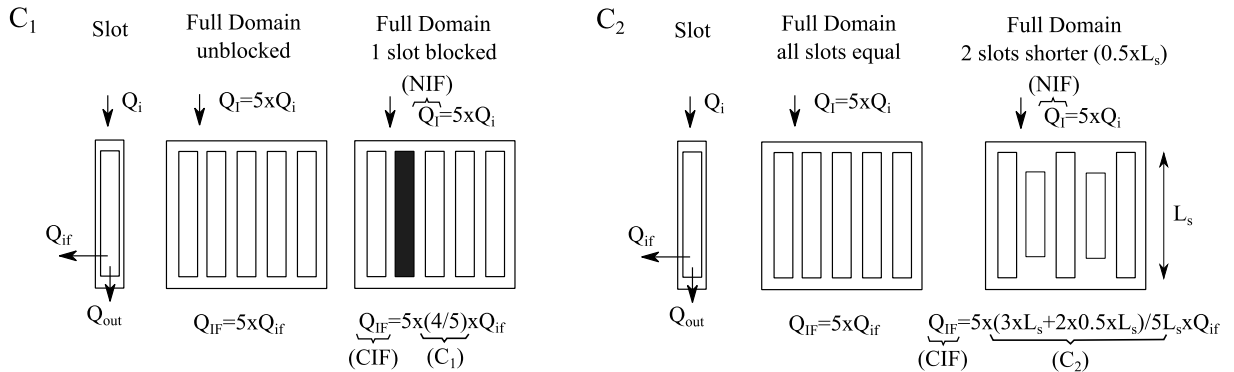


Figure 4.5: Sketch of the process to calculate the coefficients C_1 and C_2 , used to calculate the corrected intercepted flow (CIF) using the numerical intercepted flow (NIF). Q_i , Q_{if} and Q_{out} are respectively the Inflow, Intercepted Flow and Outflow for one slot; Q_I , Q_{IF} and Q_{OUT} are respectively the Inflow, Intercepted Flow and Outflow for a group of slots.

Table 4.1: Distribution of the applied correction coefficients (C_1) and (C_2), respectively described by (10) and (11). q are the unit discharges in $L/s/m$ and i_x the longitudinal slope of the channel in %. Note: * Simulations where the experimental efficiency is 1.

i_x (%)	q ($L/s/m$)				
	6.67	16.67	33.33	50.00	66.67
10.0	*	C_1	C_1	$C_1 \times C_2$	$C_1 \times C_2$
8.0	*	C_1	C_1	$C_1 \times C_2$	$C_1 \times C_2$
6.0	*	C_1	C_1	$C_1 \times C_2$	$C_1 \times C_2$
4.0	*	C_1	C_1	$C_1 \times C_2$	$C_1 \times C_2$
2.0	*	C_1	C_1	$C_1 \times C_2$	$C_1 \times C_2$
1.0	*	C_1	C_1	$C_1 \times C_2$	$C_1 \times C_2$
0.5	*	*	C_1	C_1	$C_1 \times C_2$
0.0	*	*	C_1	C_1	$C_1 \times C_2$

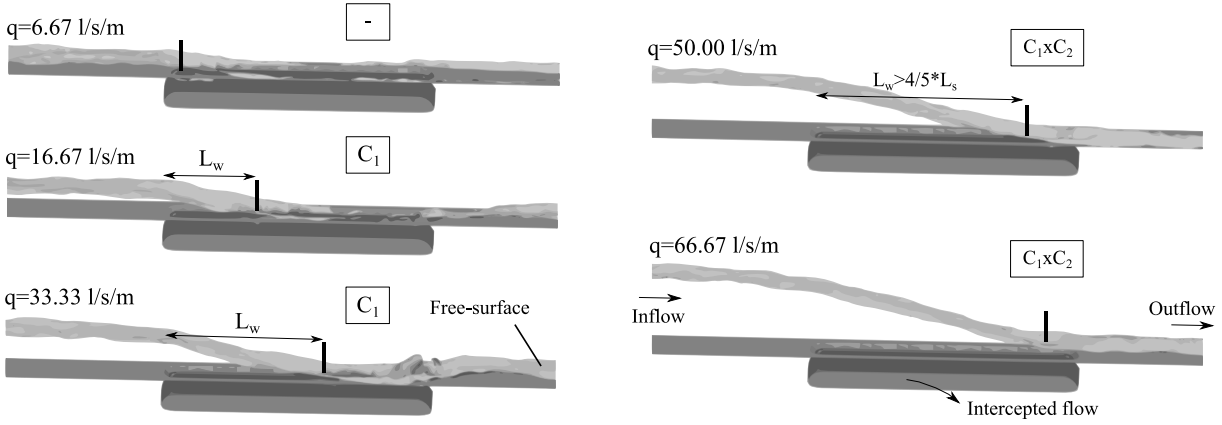


Figure 4.6: 3D image of free-surface average position over the slot and the correspondent choice of coefficients. For all the simulations, $i_x = 4\%$. L_w is the slot length occupied with water, L_s is the length of the grate slot.

4.4 Results

4.4.1 Influence of mesh refinement on inflows

The inflow values acquired with Mesh 1 and Mesh 2 are assessed against the inflows imposed on the model, i.e. experimental inflows. Table 4.2 presents the relative deviations between the numerical and experimental inflows for the entire set of drainage flows and the highest slopes ($> 2\%$). The Relative Deviation for Inflow (RDI) is calculated through Eq. (4.12).

$$RDI(\%) = \frac{\text{Exp. inflow} - \text{Num. inflow}}{\text{Exp. inflow}} \quad (4.12)$$

Table 4.2: Relative deviations on the inflows (RDI) for the two meshed proposed – Mesh 1 and Mesh 2. q are the unit discharges and i_x the longitudinal slope of the channel.

i_x (%)	Mesh 1					Mesh 2					
	q (L/s/m)					q (L/s/m)					
	6.67	16.67	33.33	50.00	66.67		6.67	16.67	33.33	50.00	66.67
10.0	22.22	37.78	16.67	3.70	1.67	0.00	0.00	1.11	0.00	0.56	
8.0	38.89	13.33	7.78	6.67	0.00	0.00	0.00	0.00	0.74	0.00	
6.0	16.67	11.11	7.78	0.74	2.78	0.00	0.00	1.11	0.00	0.56	
4.0	22.22	6.67	8.89	2.96	0.56	0.00	2.22	0.00	0.00	1.67	
2.0	22.22	13.33	5.56	1.48	0.00	0.00	0.00	0.74	2.22		

4.4.2 Grate efficiency (numerical vs. experimental)

Figure 4.7 shows the contour graph of the relative deviations between the numerical and experimental efficiencies of the grate for the complete set of simulations using Mesh 2. The Relative Deviation for Efficiency (RDE) is calculated in a similar way as RDI, but instead Experimental and Numerical Inflows, the variables are Experimental and Numerical Efficiencies.

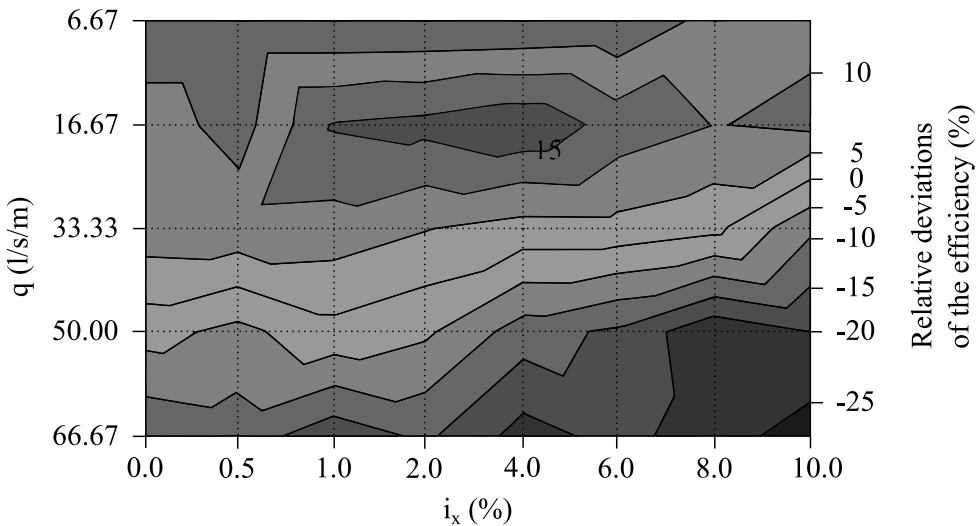


Figure 4.7: Contour graph of RDE . q are the unit discharges and i_x the longitudinal slope of the channel.

Figure 4.8 presents the numerical efficiency plotted against the experimental values. Limits of $\pm 10\%$, -28% (maximum negative) and $+19\%$ (maximum positive) errors are added to the graph.

Gómez and Russo (2009) related the efficiency (E) to hydraulic and dimensional parameters such as the Froude number (F), the width of the grate in the flow direction (B_g) (in our case $B_g = 195 mm$) and the flow depth upstream of the grate (h). The procedure is shown in Fig. 4.9. The R^2 correlation coefficient of the more adequate linear trend line, adapted to the experimental results ($ExpR^2$) is presented as well in Fig. 4.9. The $NumR^2$ coefficient is the correlation between the experimental trend line and the numerical data. The simulations with $6.67 L/s$ are discarded from the graphic due to the constant efficiency equal to 1. This disposal was also adopted in the study of Gómez and Russo (2009).

Table 4.3 presents four quantitative statistical coefficients used to verify the accuracy of the numerical model. The numerical efficiency is tested against the experimental for the flows from 16.67 to $66.67 L/s/m$. The d , developed by Willmott (1981), measures the degree of model prediction error and varies between 0 and 1. Value 1 indicates the perfect

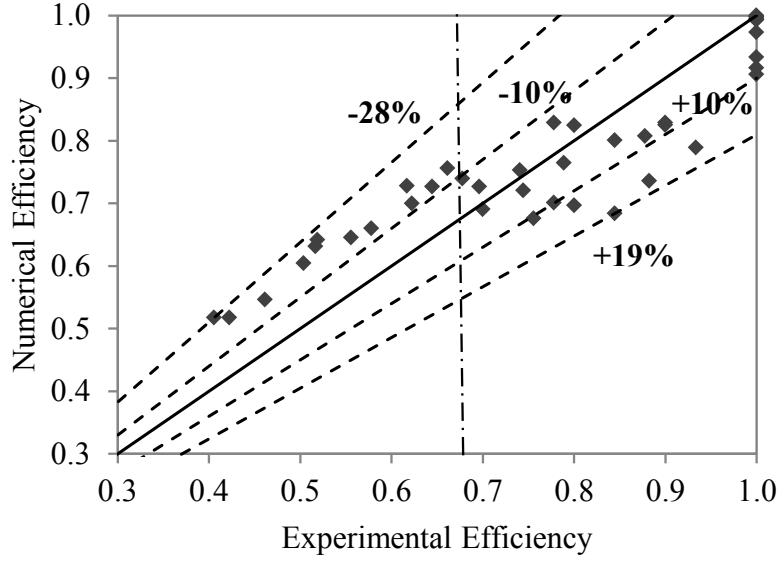
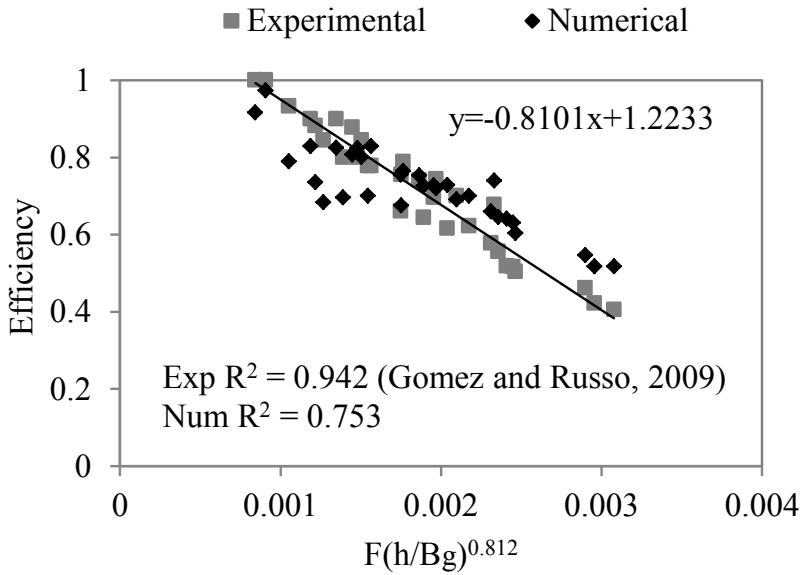


Figure 4.8: Relative deviations between the numerical and the experimental efficiency.

Figure 4.9: Graph relating the efficiency with Froude number (F), flow depth (h) and width of the grate in the flow direction (B_g).

agreement between the observed and predicted values. The NSE coefficient (Nash and Sutcliffe, 1970) ranges between $-\infty$ and 1 and reaches the optimal value when $NSE = 1$. Values between 0 and 1 are viewed as good levels of performance whereas values lower than 0 indicate unacceptable performance. The Root-Mean-Square Deviation (RMSD)

presents good agreement when the residuals are closer to zero. The Percent-Bias (PBIAS) indicates, in percentage, the average tendency of the simulated values to be larger or smaller than observed ones (Gupta et al., 1999). Positive values indicate overestimation, whereas negative values indicate underestimation. The optimal value is 0.

Table 4.3: Quantitative statistical coefficients to investigate the model accuracy. The coefficients relate the gully efficiency (experimental vs. numerical) for the range of flows from 16.67 to 66.67 $L/s/m$. d – Index of agreement; NSE – Nash-Sutcliffe Efficiency; $RMSD$ – Root Mean Square Deviation; $PBIAS$ – Percent Bias.

Coefficient	Obtained value	Optimal value
d	0.887	1
NSE	0.712	1
$RMSD$	0.087	0
$PBIAS$	-0.909	0

4.5 Discussion

4.5.1 Influence of mesh refinement on inflows

Analysis of Table 4.2 shows that for Mesh 1, in the lowest flows ($q = 6.67 L/s/m$), RDIs assume values higher than 15%. This high discrepancy can be attributed to the lack of cells in the bottom of the channel, and consequently the vertical velocity profiles either the turbulent boundary layer are not accurately modelled. For the highest flow ($q = 50.00$ and $q = 66.67 L/s/m$), the relative deviations are not too high, assuming values that do not exceed 7%. Using a second mesh generation, refined near the channel bottom with cells not larger than 1 mm (Mesh 2), the RDIs are far better than in Mesh 1. The values are now lower than 2% both for the highest and lower values of flow rates. This result shows that the refinement near to the bottom of the channel highly influences the accuracy of the data included on the model and consequently the results obtained.

4.5.2 Grate efficiency (numerical vs. experimental)

Figure 4.7 shows that RDEs are much more sensible to the inflow than to the slope conditions, although the global RDE increases slightly with the increment of both variables. The maximum positive RDE value occur for the intermediate slope, $i_x = 4\%$ and for a relative small inflow, $q = 16.67 L/s/m$ ($RDE = +19\%$) whereas the maximum negative RDE occurs for the maximum slope, $i_x = 10\%$ and the maximum inflow, $q = 66.67 L/s/m$.

($RDE = -28\%$). It can be concluded that the *interFoam* model is more efficient in the medium range inflows (about $q = 33.33 \text{ L/s/m}$) and medium-small slopes (which we define as $\leq 2\%$) than in the range of high and low flow rates and high slopes where the errors magnitude can be greater than $\pm 10\%$. Similar conclusion was obtained by Martins et al. (2014) on the simulation of a gully under normal drainage. For small flow rates, the *interFoam* model misrepresented the flow dropping from the surface into the gully, by producing a falling jet attached to the side wall, instead of producing a free-fall jet profile. It is likely that the same should occur in other drop structures as manholes, weirs or orifices.

Equation (4.12) can help clarify the reason for RDEs larger than 10%. According to Eq. (4.12), a negative RDE value means that the numerical efficiency is higher than the experimental (efficiency is overpredicted) whereas positive RDE value represent the opposite (efficiency is underpredicted). For lower discharges the outflow jet remains attached to the upstream wall of the gully box, misrepresenting the jet profile and the existing void fraction which should be observed between the upstream wall and the outflow jet. This phenomenon decreases the velocity of the jet and the amount of flow intercepted by the gully, thus resulting in the underprediction of the gully efficiency and the positive RDEs. For highest discharges the jet is detached from the wall and the numerical simulation improves; nonetheless, in this case a 3D vortex appears between the wall and the outflow jet which increases both jet velocity and the amount of flow intercepted and overpredicts the efficiency of the gully (negative RDEs). Nonetheless it should be emphasized that these discrepancies are mostly found in the regions of extreme values (both inflows and slopes). For the intermediate inflow ranges and medium-small slopes ($\leq 2\%$), which represent most of the drainage inlet in real urban systems, show a good numerical accuracy and the *interFoam* gully model can be employed for assessing its efficiency.

Figure 4.8 displays experimental efficiencies against the numerical efficiencies. The perfect agreement between those values is represented by the continuous line and relative deviations are represented with dashed lines. Although the limits of good accuracy for the numerical model are not generally defined, because it depends on the detail we want to resolve, in CFD simulations of UDS and for most engineering purposes it is usual to consider a good numerical performance for simulations were the relative deviations from the real data fall below $\pm 10\%$ (Begum et al., 2011). As such Fig. 4.8 shows the $\pm 10\%$ limits and the maximum and minimum error lines. 60% of the simulations fall within the limits $\pm 10\%$. 30% are found in the zone limited by the -10% and -28% lines, and 10% are found in the zone limited with the lines $RDE = +10\%$ and $+19\%$. Therefore it is suggested that the *interFoam* model must be carefully applied for continuous grate

whenever the efficiency falls below 0.68 (limit marked with dot-slash vertical line).

Figure 4.9 shows the relations between the Froude number, depth and grate length with the efficiency both for experimental and numerical data. The $NumR^2$ is very similar to the one obtained with the experimental data, showing that the expression established by Gómez and Russo (2009) for this type of continuous grate with bars parallel to the flow direction is similar to the one obtained applying the *interFoam* model. The statistical coefficients shown on Table 3 support the previous conclusion. The numerical efficiency (predicted) obtained is similar to the experimental one (observed). For all the tests simulated, the obtained coefficients are similar to the optimal value of the test (Moriasi et al., 2007).

4.6 Conclusions

This article presents the assessment of the ability of a VOF model to reproduce the efficiency of a continuous transverse gully with grate with bars parallel to the flow direction. The validation of the VOF model was done by comparing with experimental real-scale data. The study focuses on its hydraulic efficiency which is the basis for the comparison and validation. In total, forty combinations of flow rates and slopes were tested. Two different meshes were generated with the Salome-Platform software to represent the geometry of the grate inlet with different refinements. The refinement of the mesh near to the channel bottom was shown to be preponderant to achieve the good accuracy of the numerical model, especially for shallow waters.

The relative deviations between the numerical and experimental data were calculated in relation to the flow rates and the various slopes. It was concluded that the numerical model is much more efficient in medium-high efficiencies range, which are mostly found in urban drainage systems. A linear relation was found between the flow Froude number and the efficiency of the grate. The R^2 values found were similar to the experimental relations achieved in (Gómez and Russo, 2009).

This study showed that the *interFoam* VOF solver can provide results similar to the ones obtained using experimental facilities, rendering the use of the numerical model a useful alternative to laboratory testing in the efficiency prediction of this and other types of gullies with grate.

5

Air-entrainment Characterization and Velocities Profiles in a Scaled Circular Manhole

Abstract: Manholes are one of the most common element of UDS linking the surface (streets, sidewalks, gardens) to the ground network pipes. During exceedance flow events these elements act to transfer flow between surface and subsurface systems. To understand the performance of UDS detailed studies on flow behaviour within these structures is required. To date the influence on air entrainment on flow in circular manholes has not been widely explored. This study intends to describe the recirculation processes inside the manhole using the mean velocity profiles acquired experimentally with an ADV Vectrino and the respective turbulence analysis. The air concentration inside the manhole is also measured with an in-house resistive dual-tip probe. Two scenarios are tested: (1) simultaneously flow from the surface to the manhole and flow on the subsurface system pipes and (2) flow only from the surface to the manhole.

5.1 Introduction

According to the International Panel to the Climate Changes (IPCC) (IPCC, 2012), climate change is expected to lead to an increase in the frequency and magnitude of “extreme events” (Young, 2002), such as floods. One way to mitigate the flood impacts is to understand the flow behaviour inside the linking elements of the UDS, such as manholes and gullies, and use this understanding to improve design. Improved knowledge of the behaviour of such elements can also be crucial to develop internal boundary conditions in the Dual Drainage numerical models (Leandro et al., 2009).

Several experimental studies about the flow behaviour inside the gullies and its efficiency can be found on the literature (Djordjević et al., 2013; Lopes et al., 2015b; Páscoa et al., 2013; Romagnoli et al., 2013; Russo et al., 2013). Fewer descriptive studies exist specifically related to manholes (Guymer et al., 2005; Stovin et al., 2008). The air on the UDS is also another important subject of study. The air besides changes to the properties of the flow, such as the water-air mixture density and compressibility and consequently the turbulent structure of the flow, has a significant role in the reduction of the hydraulic capacity of the UDS. The full implications of the air entering the urban drainage system are at present unknown.

This work aims to experimentally describe the turbulence and the air inside one circular manhole under steady flow conditions during surface to subsurface flow exchange. The turbulence is characterized by quantification of the temporally averaged velocity and Reynolds stresses. The air profiles are described by the mean air concentration. One ADV is used to measure the velocity inside the manhole, while the presence of the air is detected by one in-house resistive dual-tip probe. Both instruments are intrusive but these techniques are irreducible ways to characterize the flows.

5.2 Experimental setup

The experimental setup is constructed in the Water Laboratory of the Department of Civil and Structural Engineering of the University of Sheffield (Fig. 5.1). It consists in a scaled model of an urban drainage system, which connects the surface ($4\text{ m} \times 8.2\text{ m}$) with 1% slope in longitudinal direction to two horizontal, acrylic pipes underneath (inner diameter $D=75\text{ mm}$). Linking the surface to the pipes has one circular acrylic manhole with $D=240\text{ mm}$ diameter and 480 mm height. The flows from the inlet surface, pipe inlet, and pipe outlet are controlled and monitored by independent valves and flowmeters. The water level in the manhole is either controlled by one pressure transducer previously calibrated and verified *in situ* by a graduated ruler with the zero coincident to the bottom

of the manhole.

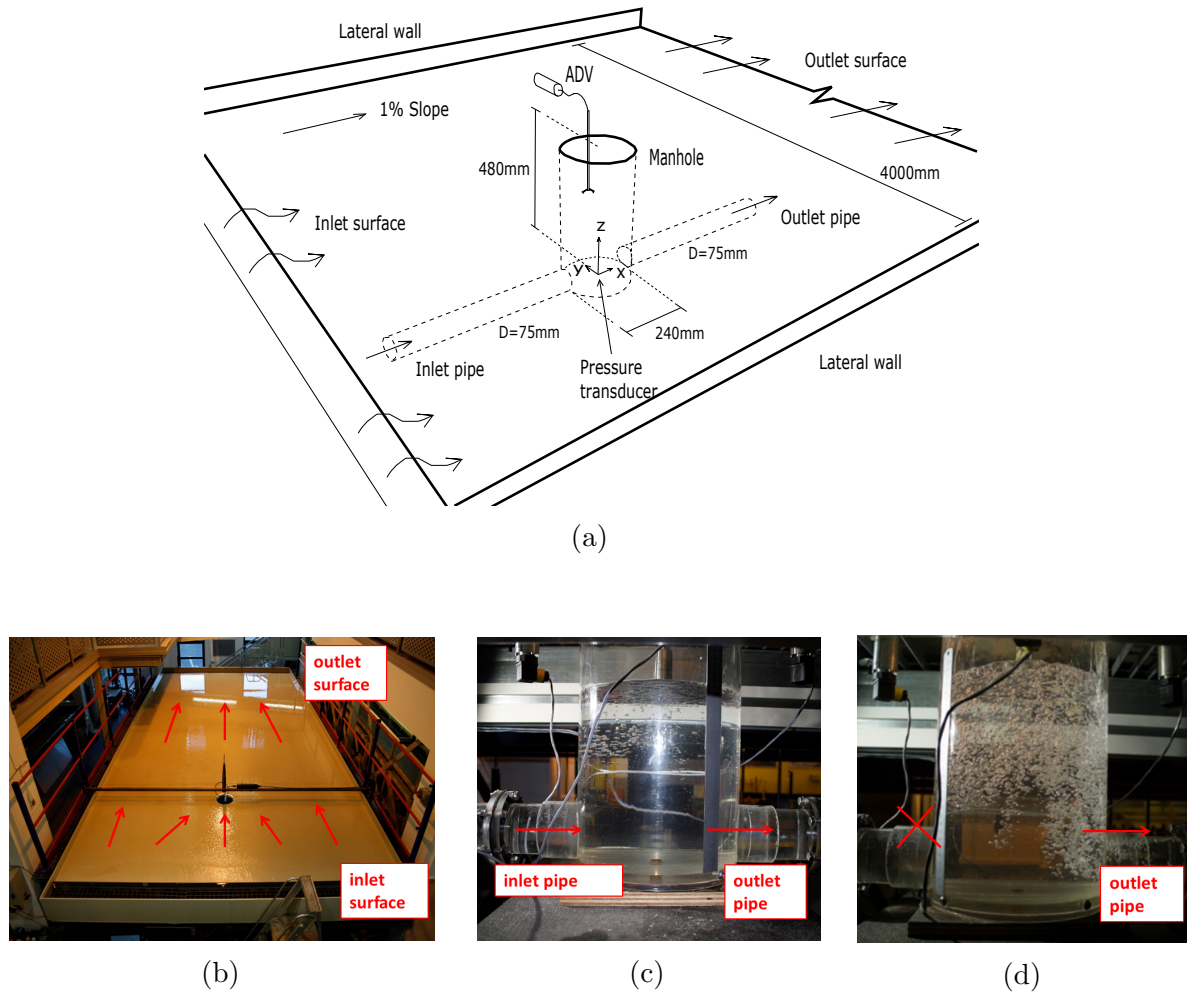


Figure 5.1: (a) Schematic representation of the experimental setup. Measures in [mm]. (b) Photograph of drainage surface. (c) Photograph of manhole and horizontal pipes for Conf1. (d) Photograph of manhole and horizontal pipes for Conf2.

Two different steady flow configurations are tested: Conf1 - flow from the surface plus flow from the inlet pipe, and Conf2 - only flow from the inlet surface. Table 5.1 resumes the characteristics of each configuration.

Table 5.1: Experimental configurations. Q is the flow discharge, q is the unit flow discharge, h is the flow depth, U is the average velocity, Re is the Reynolds number ($Re=UD/\nu$) and Fr is the Froude number ($Fr=U/(gh_{surface})^{0.5}$)

		Conf1	Conf2
Surface flow	q ($l/s/m$)	1.066	2.496
	h (mm)	9.626	13.468
	U (m/s)	0.111	0.236
	Fr (-)	0.360	0.734
Inlet pipe	Q (l/s)	0.379	0
	U (m/s)	0.086	0
	Re (-)	6.411×10^3	0
Outlet pipe	Q (l/s)	1.303	2.060
	U (m/s)	0.295	0.466
	Re (-)	2.203×10^4	3.484×10^4
Manhole	h (mm)	240	280

5.3 Methodology

5.3.1 Acoustic Doppler Velocimeter measurements

An ADV, Nortek Vectrino Downlooking 10 MHz with flexible cable is used to record the water velocity in time in several points of the manhole. The Vectrino uses the Doppler technology to measure four velocity components: u , v , w_1 and w_2 , where w_1 and w_2 are independent measurements of the vertical velocity ($w = (w_1 + w_2)/2$) in a sampling volume located 50 mm below the probe sensors. The sampling volume in these experiments is a cylinder of 6 mm diameter and 15 mm height. The sampling rate of the ADV is adjustable from 1 Hz to 200 Hz (Plus firmware) and the velocity range can be set to ± 0.01 , ± 0.1 , ± 0.3 , ± 1 , ± 2 or ± 4 m/s . The sampling time used is 300 s (total of 15 000 samples at 50 Hz) and the nominal velocity range is set to 1 m/s (vertical velocity range = 0.54 m/s and horizontal velocity range = 1.88 m/s) to avoid the phase wrapping (Romagnoli et al., 2013).

The water velocity signal is recorded at different points of the manhole, schematically represented on Fig. 5.2. Vertically, the measured points are spaced 20 mm, while horizontally they are radially distanced 40 mm.

The data obtained by the ADV is post-processed with the free-ware software WinADV version 2.031 (Wahl, 2000). The post-processing treatment include the removal of spikes using the phase-space threshold method proposed by Goring and Nikora (2002), further

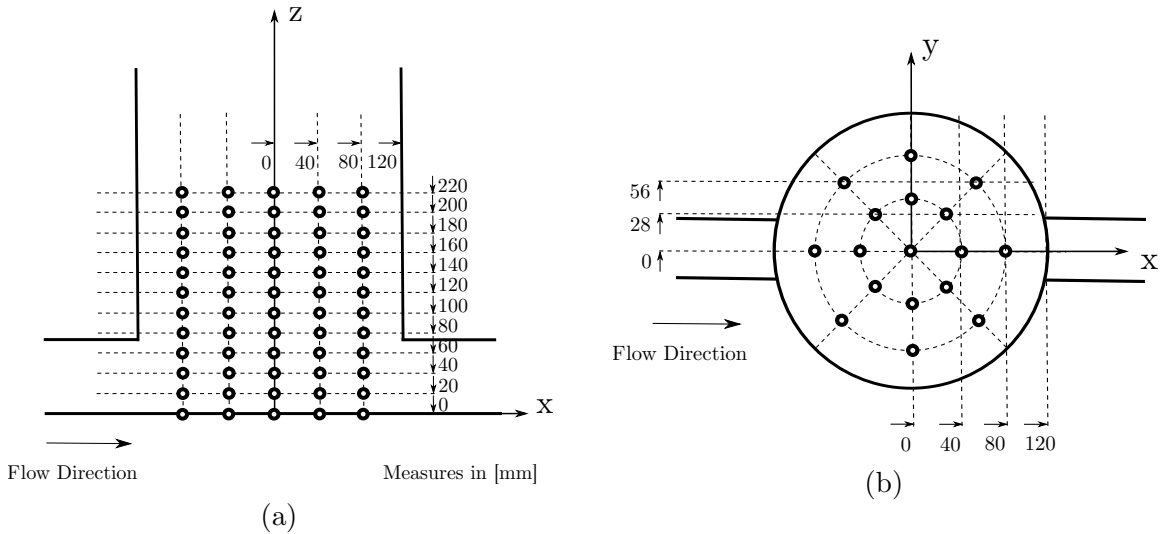


Figure 5.2: Sketch of the manhole and the measured points with ADV Vectrino: (a) Lateral view, (b) Plane view.

modified by Wahl (2003); the elimination of values in the data series with a Signal Noise Ratio (SNR) lower than 15 db; and the exclusion of values with lower correlation values. For the turbulent analysis, many ADV manufacturers and Authors usually recommends deleting samples with correlations below the 70% since the SNR is higher (Wahl, 2000).

5.3.2 Air-probe

A dual-tip conductivity probe (or simply air-probe in this document) is used to measure the air-concentration inside the manhole. The principle behind the air-probe is the different conductivity of each phase - air and water, which is detected by the needle measuring low and high voltage. This principle allows concluding when the probe is in the presence of water or air. The advantage of the dual-tip probe is that besides allowing the measurement of the void fraction, it also measures the velocity of the bubbles by correlating the time periods in the two needles. The needles are made by two concentric electrodes with outer diameter of 1 mm and internal electrode of 0.3 mm and distanced in flow direction by 5.8 mm. The points measured with the air-probe are identical to those measured with the ADV (Fig. 5.2) adding one new circle of points with radius 100 mm, to capture the air that enters on the fluid closer to the walls of the manhole. The data obtained by the air-probe is acquired at 1 000 Hz during 3 minutes by an Graphical User Interface (GUI)-MatLAB software.

5.4 Results

5.4.1 Mean velocities

Figure 5.3a and Fig. 5.3c show the mean velocities obtained by ADV measurements in the plane XZ of the manhole for both configurations tested where the outlet pipe is situated at the right side of the figures.

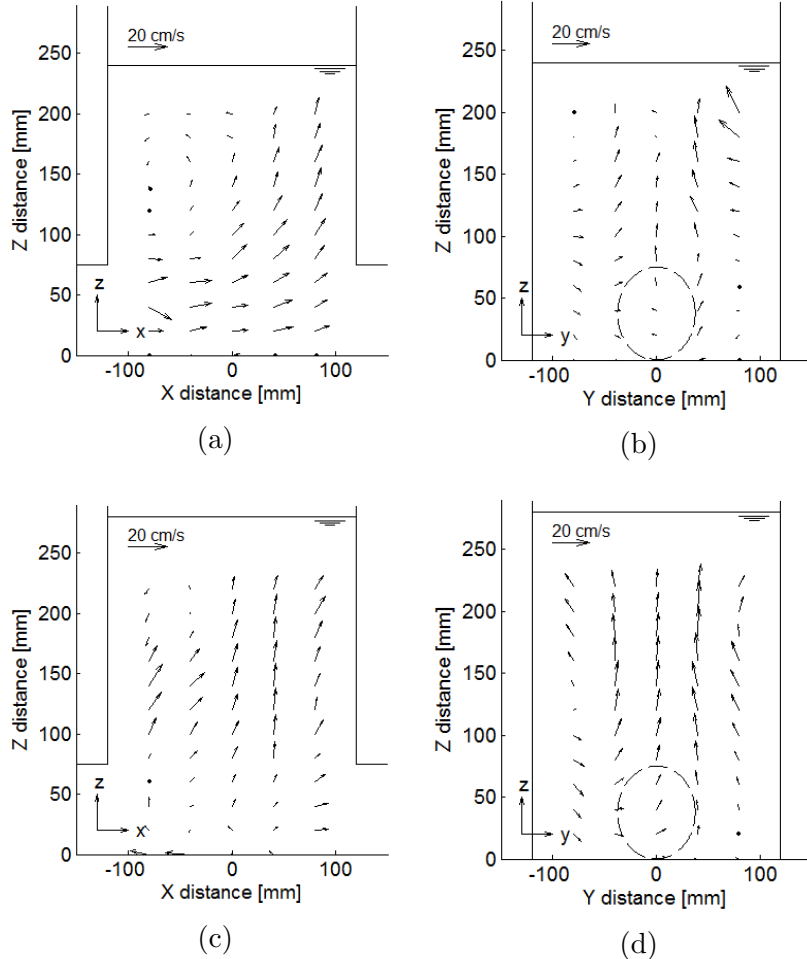


Figure 5.3: Mean velocities at vertical profiles for: (a) Conf1, plane XZ; (b) Conf1, plane YZ; (c) Conf2, plane XZ; (d) Conf2, plane YZ.

Figure 5.4 shows the mean stream-lines for the two configurations tested. Figure 5.4a shows the 3D vortexes on the top of the manhole, characteristic of Conf1.

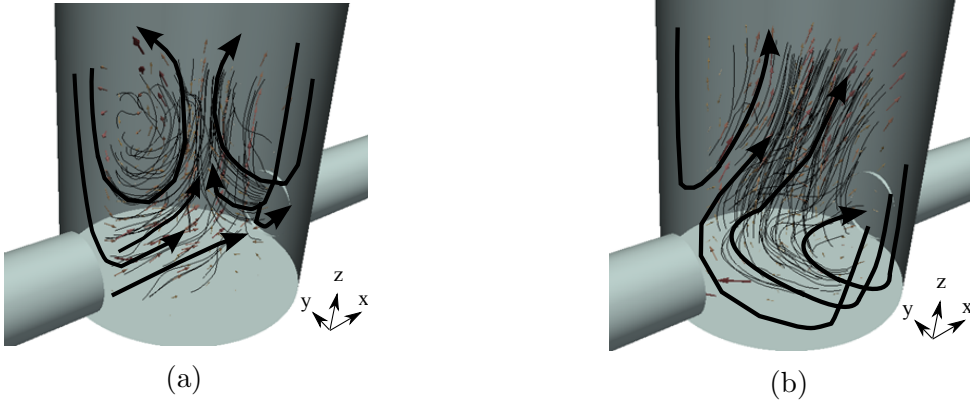


Figure 5.4: 3D stream-lines for (a) Conf1 and (b) Conf2.

5.4.2 Reynolds Stresses

The Reynolds stress tensor $\langle u_i u_j \rangle$, where u_i and u_j represents the components i and j of the velocity, is the contribution of the turbulent motion to the mean stress tensor. The diagonal components of the matrix are the normal stress whereas the non-diagonal components are the shear stress.

5.4.2.1 Normal Stress

Figure 5.5 shows the normal stress distribution in the manhole $\langle uu \rangle$, $\langle vv \rangle$ and $\langle ww \rangle$ for Conf1 and Conf2 (Fig. 5.5a and Fig. 5.5b respectively). The plots showed profiles of XZ planes where the outlet pipe is situated at the right side of the figures. The vectors plotted are the mean velocities.

5.4.2.2 Shear Stress

The shear stress components play an important role on the theory of mean momentum transfer. Figure 5.6 shows the shear stress distribution in the manhole $\langle uw \rangle$, $\langle uv \rangle$ and $\langle vw \rangle$ for the Conf1 and Conf2 (Fig. 5.6a and Fig. 5.6b respectively). The profiles showed are plots of XZ planes where the outlet pipe is situated at the right side of the figures. The vectors plotted are the mean velocities.

5.4.3 Air profiles

The air entrainment was studied only for the Conf2. Figure 5.7 shows the average air-concentration profile in the XZ plane. Figure 5.7c shows the average air-concentration profile at one XY plane ($Z=80\text{ mm}$). Figure 5.7b and Fig. 5.7d are side and plan view photographs of the flow respectively.

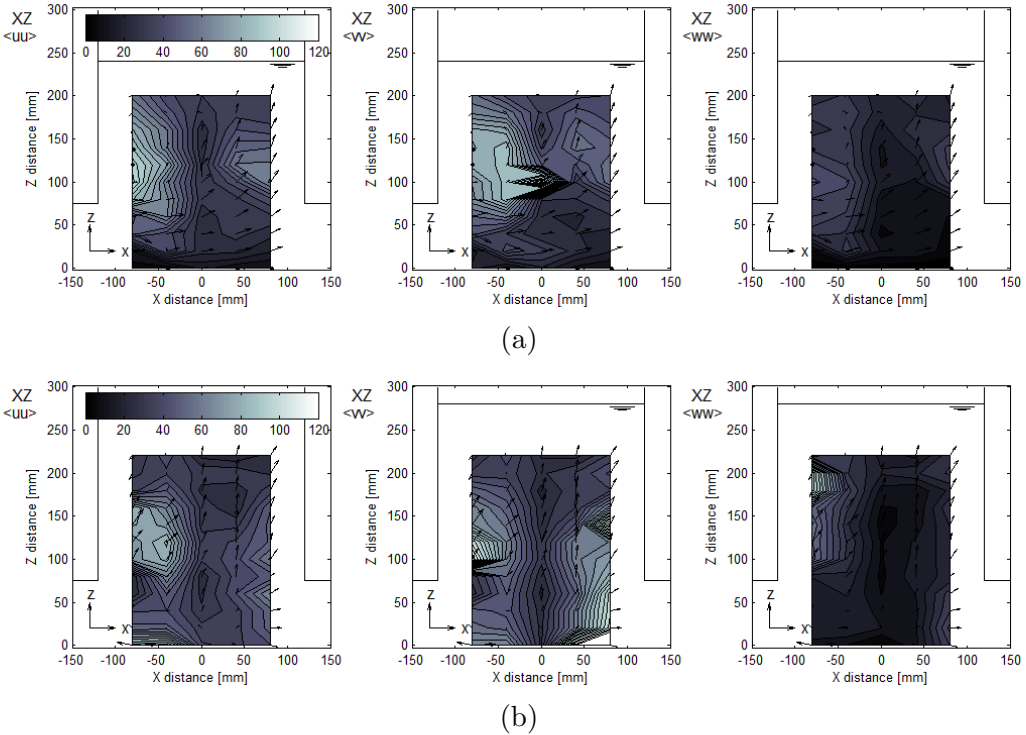


Figure 5.5: Normal Stress $\langle uu \rangle$, $\langle vv \rangle$ and $\langle ww \rangle$ on plane XZ for (a) Conf1 and (b) Conf2.

5.5 Discussion

Conf1 (Fig. 5.3a) exhibits a recirculation vortex near to the top left side of the profile, showing that the preferential flow direction is from the inlet pipe to the surface. The flow from the surface enters the water body with the manhole close to the manhole walls. These points could not be directly measured with the ADV due the presence of air bubbles and lower signal correlation values. The highest velocities on Conf1 are due to the influence of the pipe inlet flow. Conf2 (Fig. 5.3c) is characterized by a strong column of flow rising on the centre of the manhole, further creating a small vortex on the left side of the profile. In the plane YZ (Fig. 5.3b and Fig. 5.3d), the flow pattern is identical for both configurations, characterized by a vertical flux from the bottom to the top in the centre profile of the manhole. At the top of Plane YZ for Conf1 it can be viewed the continuation of the vortex created on the plane XZ. From Fig. 5.4b it is elucidative that part of the flow rises on the centre profile of the manhole and other part goes directly to the outlet pipe.

Analysing Fig. 5.5, it can be seen that for both configurations the highest values of normal stresses are at the left side of the profiles and above the pipe inlet. For the Conf1 the lower values are on the centreline and on the bottom of the manhole. For Conf2 the

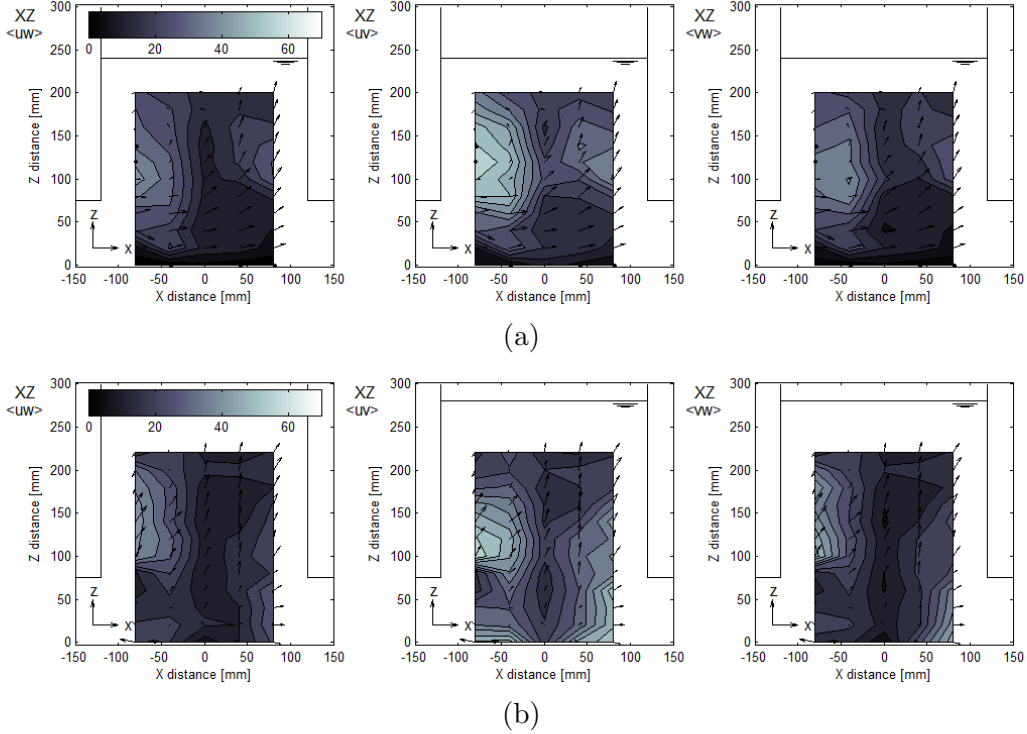


Figure 5.6: Shear Stress $\langle uw \rangle$, $\langle uv \rangle$ and $\langle vw \rangle$ on plane XZ for (a) Conf1 and (b) Conf2.

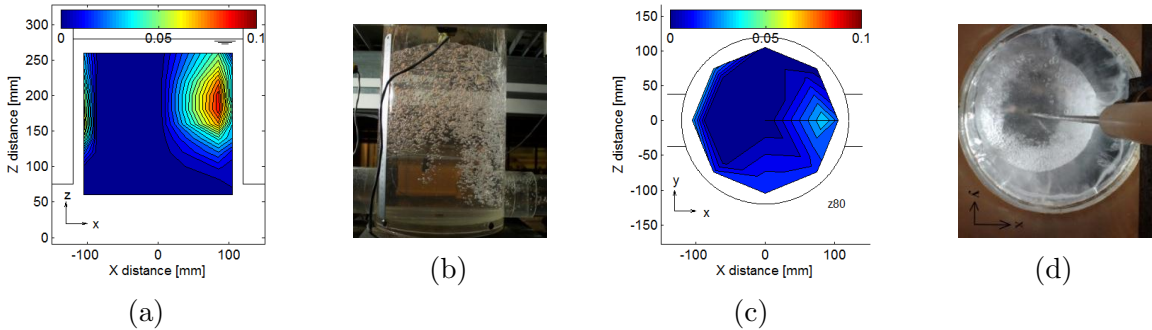


Figure 5.7: Air concentration profiles at plane XZ (a-b) and plane XY (c-d).

lower values are on the centreline of the profiles showed. The normal stresses in the zone above the pipe inlet are always higher than in the zone in front of it. This suggests that even if the flow from the pipe is nil, the presence of the pipe decreases the Reynolds stresses and prevents the occurrence of the vortexes.

The shear stresses in Fig. 5.6 are lower than the normal stresses presented in Fig. 5.5. For the Conf1 it can be visualized that the highest values of shear stress are at the top of the connection between the manhole and the pipe inlet due the creation of a three-dimensional vortex or a recirculation zone within the flow. Contrary to what might be expected, the

$\langle uv \rangle$ shear stress is higher than $\langle uw \rangle$, showing that the momentum transfer is more intense on the plane XY than on plane XZ. The shear stress distribution for Conf2 differs slightly from that observed in Conf1. The main difference is related to the shear stress found on the bottom of the manhole and downstream of the manhole, best observed in Fig. 5.6b- $\langle uv \rangle$. The water that transfers into the manhole from the surface reaches the bottom of the manhole via the manhole's walls. This process transports large quantities of bubbles to the bottom.

Regarding air concentration profiles on Fig. 5.7 and as previously mentioned, the surface flow enters in the manhole by flowing down the manhole walls causing the influx of a large quantity of bubbles. At the left side of Fig. 5.7a and Fig. 5.7b the bubbles vanish a small distance ($\approx 180\text{ mm}$ from the surface) above the entrance of the inflow pipe whereas at right side the bubbles penetrate to $Z=70\text{ mm}$. The highest air density is observed downstream of the manhole at $Z=200\text{ mm}$ and this air penetrates deep until reaching the entrance of the outlet pipe. The non-uniformity of the air concentration on the plan view can be explained by the non-homogeneity of the flow depth at the inlet surface causing a flow more intense on the left side of the manhole.

5.6 Conclusions

The study describes experimentally the flow pattern and the air entrainment inside a scaled manhole. Two study cases are explored, one simulating flow entering the manhole both from an inflow pipe and via surface flow and other with flow only from the surface. The main findings of the research are summarised as:

- The presence of the pipe inlet, influences the flow pattern inside the manhole even if the flow is nil;
- At upstream of the circular manhole surges always a recirculation vortex, and its dimension increases when exists flow from the pipe inlet;
- In both configurations, the flow descends through the walls of the manhole and rises through the centreline;
- The air-concentration has a non-homogeneous profile. The highest concentrations are at downstream of the manhole, 100 mm below the free-surface in the scaled model studied.
- Presence of surface flow entrains a significant amount of air within the urban drainage system. The air penetrates deep enough into the manhole to enter the piped urban

drainage system. In a real system the degree of air entering the system will be a function of the surface flow and manhole depth. The full implications of the air entering the urban drainage system are at present unknown and warrant further research.

6

Numerical Procedure for Free-surface Detection Using a Volume-of-Fluid Model

Abstract: During the stage design of a stepped spillway is fundamental the prediction of the maximum water depth for wall height definition. Many experimental and numerical studies were made in this subject, however the combination of both in order to enhance aspects about free-surface characteristics and their numerical prediction are still uncovered. The captured free-surface from a VOF based model is compared with flow depths measured with three ultrasonic sensors in a stepped spillway. A numerical procedure to predict the free-surface is developed and validated using both the top view and lateral profile of water depths. Relative errors between numerical and experimental free-surfaces are calculated along with this procedure.

6.1 Introduction

Air-water flows over stepped spillways were fundamentally subject of investigation in laboratory since the late 1980s. Most flow discharges correspond to the skimming flow regime, characterized by a coherent stream skimming over the steps and forming recirculation zones of air-water mixture on step cavities. Three distinct zones of flow over the stepped spillway can be reported: (1) an upstream zone, characterized by a smooth and glassy free surface and a non-aerated flow region over the steps; (2) an intermediate zone initiated by the surface inception point, i.e. the point where the turbulent boundary layer reaches the free surface and the air starts gradually entering on the water body; and (3) a downstream zone, characterized by a rapidly flow region, where the flow depths, velocities and air concentration profiles reach an equilibrium, also denominated as uniform flow region. The last is initiated by the pseudo-bottom inception point, i.e. the point where the air-water mixture reaches the pseudo-bottom channel. The upstream and intermediate zones are known together as aerated flow region.

Most numerical and experimental studies on stepped spillways are focused on flow depths predictions in the uniform flow region, due to its crucial importance on the design stage of walls height. Based on theoretical and empirical data, Chanson (2001) presented formulas to calculate the flow depths on the non-aerated of a stepped spillway, based on the position of the inception point. Flow depths on a United States Army Corps of Engineers (USACE)-Waterways Experiment Station (WES) standard model stepped spillway were measured experimentally by Boes and Hager (2003) in the uniform flow region and numerically by Bombardelli et al. (2010) in the non-aerated part. A 2D dynamic mesh model was used by Tabbara et al. (2005) to predict the free-surface shape over a USACE-WES stepped spillway. The free-surface was assumed as a boundary of the model that returned a qualitatively consistent solution to the experiments. Simões et al. (2013) presented an experimental study about the shape of mean surface profiles, position of inception point and water depth at the inception point in a pressurized intake stepped spillway. The flow depths were attained with a displacement of ultrasonic sensors. The same technique was used by Bung (2013) to describe the experimental free-surface wave's frequency and amplitude, as well as the uniform flow depth in a zone far downstream of the inception point for a smooth invert stepped spillway. Despite such findings towards the statement of flow depths over a stepped spillway, all aforementioned studies were performed on the centre-channel, assuming no influence from the walls, whereas the numerical free-surface is generally represented in VOF models by a water volume fraction of 0.5. Furthermore, be sure on this volume fraction value has significant importance to detect the free-surface position and thickness when modelling bubble entrainment or

breakup in a sub-grid air-entrainment model (Moraga et al., 2008).

In this work we develop a numerical procedure to detect the free-surface within a VOF model. Next section (§6.2) describes the equations behind the numerical model, the computational domain and mesh, the model constants and the numerical procedures. The experimental facilities and equipments are presented in Section §6.3. Section §6.4 introduces the new numerical procedure to study the free-surface elevation. The results of this process and model results are showed in Section §6.4 and argued in Section §6.5. Last Section (§6.6) presents the conclusions of this work.

6.2 Numerical model

The stepped spillway model is solved with a set of Navier-Stokes equations, together with VOF technique to capture the free-surface and Shear-stress transport (SST) $k - \omega$ turbulence model closure. Interface capturing models such as the VOF model (implemented in the OpenFOAM® v.2.3.0 toolkit as *interFoam*) represent the dynamics of the two phases in terms of a shared velocity and pressure field governed by a single set of Navier-Stokes equations. The location of the two-fluids interface is captured using a indicator function. For a system of isothermal, incompressible and immiscible two-phase flow, the averaged equations for conservation of mass and momentum are written in their conservative form by:

$$\nabla \cdot \mathbf{U} = 0 \quad (6.1)$$

$$\frac{\partial \rho \mathbf{U}}{\partial t} + \nabla \cdot (\rho \mathbf{U} \mathbf{U}) = -\nabla p^* - \mathbf{g} \cdot \mathbf{x} \nabla \rho + \nabla \cdot (\mu \nabla \mathbf{U}) + (\nabla \mathbf{U}) \cdot \nabla \mu + \mathbf{f}_\sigma \quad (6.2)$$

where ρ ($kg\ m^{-3}$) is the weighted averaged local density between the two fluids, \mathbf{g} ($m\ s^{-2}$) is the gravitational acceleration, \mathbf{U} ($m\ s^{-1}$) is the velocity vector, p^* is the pressure, calculated by removing the hydrostatic pressure from the total pressure, $\nabla \cdot (\mu \nabla \mathbf{U}) + (\nabla \mathbf{U}) \cdot \nabla \mu$ is the decomposition of shear stress tensor, μ ($Kg\ m^{-1}s^{-2}$) is the dynamic viscosity and \mathbf{f}_σ ($kg\ m^{-2}s^{-2}$) is the volumetric surface tension force.

Together with the previous equations, *interFoam* uses the VOF technique (Hirt and Nichols, 1981) to capture the interface between two fluids by solving a transport/advection equation (Eq. (6.3)).

$$\frac{\partial \alpha}{\partial t} + \nabla \cdot (\alpha \mathbf{U}) + \nabla \cdot [\mathbf{U}_c \alpha (1 - \alpha)] = 0 \quad (6.3)$$

At each cell of the domain is defined an alpha (α) value representing a volume fraction of fluid 1 ($f1$) in a cell and ranging from 0 to 1 (Carvalho et al., 2008; Ubbink, 1997).

In case of air-water flow, the fluid 1 is normally associated to the water, and the water surface (free-surface) is therefore represented by cells where α is within the interval $[0,1]$. The present model includes a numerical artifice of interfacial compression (3rd term of Eq. (6.3)) to keep the interface confined to a small number of cells (Weller, 2008; Berberović et al., 2009). The factor $\alpha(1 - \alpha)$ ensures that compressive term is calculated just at interfacial cells of the domain whereas a compressive velocity (Eq. (6.4)) acts as a velocity perpendicular to the interface as follows:

$$\mathbf{U}_c = C_\alpha |\mathbf{U}| \frac{\nabla \alpha}{|\nabla \alpha|} \quad (6.4)$$

C_α is a binary coefficient that activates ($C_\alpha = 1$) or neglects ($C_\alpha = 0$) the compressive velocity and consequently the interface compression term. The gradient of the volume fraction divided by modulus of its gradient returns the direction of the normal to the interface.

The volumetric surface force function is explicitly estimated by the Continuous Surface Force (CSF) model (Eq. (6.5)) developed by Brackbill et al. (1991) where σ ($kg\ s^{-2}$) is the surface tension and κ (m^{-1}) is the surface curvature calculated through $\kappa = \nabla \cdot (\nabla \alpha / |\nabla \alpha|)$.

$$\mathbf{f}_\sigma \approx \sigma \kappa \nabla \alpha \quad (6.5)$$

Turbulent variables were calculated with the SST $k - \omega$ model (Menter, 1993) which combines the best of two RANS formulations: it takes advantage of the accuracy and robustness of $k - \omega$ model in the near-wall zone, whereas the free-stream region, i.e. the outer part of the boundary layer, is simulated with a high-Reynolds-number formulation of $k - \epsilon$ model. This means that $k - \omega$ calculates the turbulence generated by vortexes on the steps of the spillway, whilst the turbulence on the zone above the pseudo-bottom is predicted by the $k - \epsilon$ model. A simplified form of SST $k - \omega$ model can be written as:

$$\frac{\partial(\rho k)}{\partial t} + \nabla \cdot (\rho k \mathbf{U}) = \nabla \cdot [\Gamma_k \nabla k] + G_k - Y_k \quad (6.6)$$

$$\frac{\partial(\rho \omega)}{\partial t} + \nabla \cdot (\rho \omega \mathbf{U}) = \nabla \cdot [\Gamma_\omega \nabla \omega] + G_\omega - Y_\omega + D_\omega \quad (6.7)$$

where Γ_k and Γ_ω represent the effective diffusivity of k and ω . G_k is the generation of turbulence kinetic energy due to the mean velocity gradients and G_ω the production of ω , whereas Y_k and Y_ω are their respective dissipation. D_ω is the cross-diffusion term that results from the transformation of $k - \epsilon$ theory into $k - \omega$ model.

The domain used in this work follows dimensions showed in Fig. 6.1. Three uniform and structured meshes (M1, M2 and M3) are applied in order to simulate the flow over

stepped spillway and to perform a grid convergence test. M1, M2 and M3 have cells with $0.005 \times 0.005 \times 0.005 m^3$, $0.007 \times 0.007 \times 0.007 m^3$ and $0.01 \times 0.01 \times 0.01 m^3$, generating a total of 6 528, 2 754 and 816 thousands volumes within the domain. Richardson extrapolation, following Celik et al. (2008) procedure was performed over 30 points along the vertical velocity profile placed on top of 12th step edge for the three meshes proposed. The Global Convergence Index (GCI), which measures the percentage of convergence for the finer mesh to a mesh independent solution is $GCI_{M1} = 5\%$, value that proves a good level of accuracy on results from M1, but also the unneccessariness of a even finer mesh considering the small gain of accuracy, by weighing on the computational speed. The maximum discretisation uncertainty is found at the point closest to the bottom wall due to large velocity gradients. On the free-stream flow the uncertainty on the maximum velocity is 0.23%, i.e. a difference of $0.0059 ms^{-1}$ between M1 and the optimal solution.

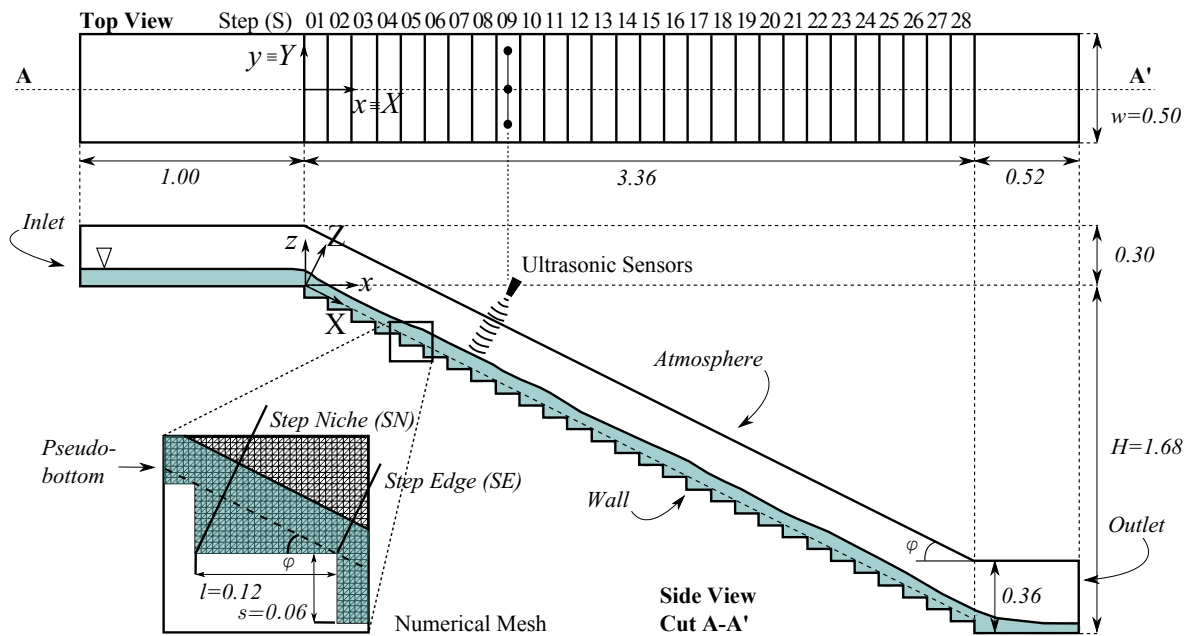


Figure 6.1: Scheme of stepped spillway, numerical model geometry, dimensions and mesh. Dimensions in meters.

Four BC are imposed to the model. Inlet-BC has a Dirichlet-BC for volume fraction (α) and velocity. Outlet-BC allows the water and air to leave the domain by setting the normal derivative of α and U as zero (Newman-BC) and pressure as hydrostatic. Atmosphere-BC allows mass changes for air phase. Slip condition is imposed for U in Wall-BC. Wall functions are used for turbulent statistics.

Fluids physical properties corresponds to those at $15^\circ C$ and surface tension is defined to $0.072 kg s^{-2}$. Maximum Courant number and maximum Courant number for α are

both set to 0.5. A steady-state solution is achieved after 24 s of simulation in a average time step of 0.00033 s. This state is identified from the criteria that the residuals of k , ε and p , and the volume fraction on the domain were kept constant in time. The clock time needed to compute 25 s using mesh M1 was 345 087 s (approx. 4 days in a continuous run) in a cluster with 16 processors (2 nodes of 2 quad-core processors @ 2.40GHz) and 24GB RAM memory. The averaged values from the last 1 s of simulation time with a writing step of 0.05 s are used to plot the results.

6.3 Experimental tests

Experimental data is acquired in a stepped spillways physical model built at the Hydraulic Engineering Section Laboratory of FH Aachen - University of Applied Sciences. The water runs in a closed circuit of water composed by two reservoirs. The flow rate is controlled by a butterfly valve and measured by an inductive flow meter. Inside the head tank, placed upstream of spillway, is installed a plastic grid to harmonise the flow and reduce the turbulence at inlet. Between the head tank and the first step exists an approaching channel of 1 m length that guarantees a hydrostatic pressure distribution. The spillway model is composed by 28 steps (S1 to S28) with 0.12 m length \times 0.06 m high \times 0.50 m width, resulting in a total drop height $H = 1.68$ m (Fig. 6.1). The slope is constant and equal to $\varphi = 26.6^\circ$. The unit water discharge is defined to $q_w = 0.07 \text{ } m^2 s^{-1}$, which returns a critical water depth at stepped spillway crest of $h_c = 0.08$ m ($h_c/s = 1.3$). The structural designs here used and flow conditions originate a skimming flow regime with a surface inception point at the 5th step edge, visually detected through the appearance of free-surface fluctuations.

Three mic+130/IU/TC MicUS (operating range: 200 to 1300 mm, resolution: 0.18 mm) are used to measure the flow depths over the stepped spillway from step edge 1 to step edge 19 during 180 s at 200 Hz. The central sensor is located in the centre-line of the spillway whereas the external sensors are distanced 80 mm from the side-walls. This distance is defined in order to avoid the signal being reflected on the walls or collide with another sensor's signal. Vertically, the ultrasonic sensors are exactly 461 mm above the pseudo bottom of the spillway. They are placed in a row, perpendicularly to the flow direction. To discard errors that might occur from the reflection of the signals on ejected droplets, in the raw data set, the signal is filtered to a smooth data using the same filtering process proposed by Bung (2013): the outlier values are discarded from the raw sample by setting a double threshold, defined as being the mean value \pm three times the standard deviation.

6.4 Numerical procedure for free-surface detection

On the basis of VOF method, every cell that has a value of α within the interval 0 to 1 is a free-surface cell. Although this theory works fine on a smooth and laminar free-surface, in a turbulent flow the free-surface is highly irregular and its averaged shape may not be so accurate. The numerical free-surface may spread over a large number of cells, and although many authors use $\alpha = 0.5$ (Albadawi et al., 2013; Lopes et al., 2015b; Turan et al., 2007; Witt et al., 2015) as first guess for free-surface position, in fact, all the remaining isolines or isosurfaces (in case of 2D or 3D simulations) are feasible of being correct. The procedure presented herein relates the step number with the α value through the comparison of the correct flow depth measured with MicUS, following the next 2 stages:

1. In the first stage, the time-averaged flow depths measured with central ultrasonic sensor are used to trace a longitudinal free-surface profile. After, confidence intervals are added to the mean in order to reflect the amplitude of free-surface fluctuation. Isolines of numerical water volume fractions values are used for comparison.
2. In the second stage, for each step edge, it is saved the value of water volume fraction that better fits the experimental free-surface level. This choice is here based upon the smallest relative errors. The selected values of water volume fraction are then fit to a continuous function that is chosen over a global optimization of three measures of fit: R² (Pearson, 1986), NSE (Nash and Sutcliffe, 1970) and d (Willmott, 1981). Since each measures of fit has best-fit result as 1, the global fit must be 3.

Results

6.4.1 Flow depths at non-aerated flow region

Meireles and Matos (2009) proposed an normalized expression that relates the distance to the spillway crest (X), normalized with the the distance of the inception point to the crest (X_I) with the flow depth (h_w), normalized with the water depth at inception point ($h_{w,I}$). This expression is deduced for $1.09 < h_c/s < 2.85$ and $\varphi < 30.0^\circ$. Figure 6.2 shows the normalized water depth ($h_w/h_{w,I}$) measured with the ultrasonic sensors and the numeric isolines of $\alpha = 0.1$, $\alpha = 0.5$ and $\alpha = 0.9$ and compare them with the solution of Meireles and Matos (2009).

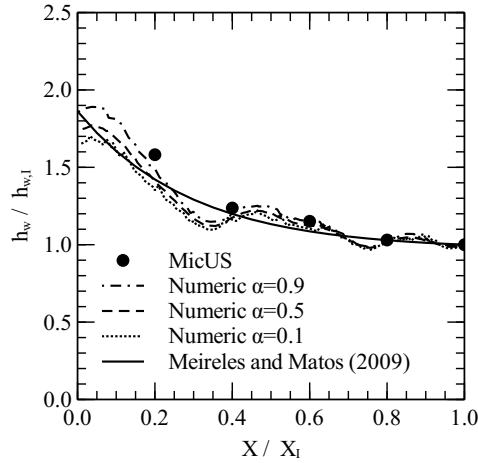


Figure 6.2: Normalized water depth $h_w / h_{w,I}$ upstream of the inception point of aeration (where $X / X_I = 1.0$) for: experimental data from ultrasonic sensors; numerical $\alpha = 0.1$, $\alpha = 0.5$, $\alpha = 0.9$ and empirical expression of Meireles and Matos (2009).

6.4.2 Full numerical free-surface position

Stage 1 Figure 6.3 shows the mean water levels measured with the central ultrasonic sensor at step edges from step 1 to 19 ($\bar{h}_{w,MicUS}$). Confidence intervals of 90% for the mean are added to the graphic. The water surface position represented by α isolines ranging from 0.1 to 0.9 are also represented on the figure ($h_{w,N}$).

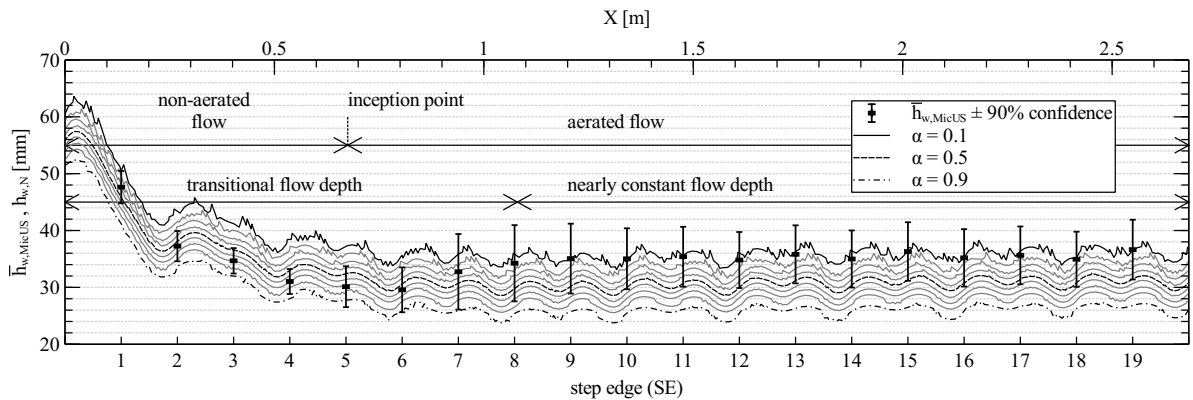


Figure 6.3: Mean water levels measured experimentally with the central ultrasonic sensors at each step edge ($\bar{h}_{w,MicUS}$) and water levels calculated numerically by plotting the α isolines from 0.1 to 0.9 ($h_{w,N}$).

Stage 2 Figure 6.4 registers with circles (\circ) the values of α that have smaller relative errors to the real free-surface elevation at each step edge. A visual analysis of the resultant

distribution allowed to select, from the large variety of linear functions existent on the literature, two that can apparently fit this specific data - Weibull (Weibull, 1951) and Gumbel (Gumbel, 1935) distributions. These, despite being used for statistical problems, their applicability is extensible to represent extreme value functions. The final form of $W\alpha(S)$ and $G\alpha(S)$ functions are written under the Eq. (6.8) and Eq. (6.9), where constants β and η are known as shape and scale parameters, while λ and b are new constants used to adjust the distributions to present case. Table 6.1 presents the optimal constants that result from the application of three measures of fit.

$$W\alpha(S) = \frac{\beta}{\eta} \left(\frac{S}{\eta} \right)^{\beta-1} e^{-(S/\eta)^\beta} \lambda + b \quad (6.8)$$

$$G\alpha(S) = \frac{1}{\beta} e^{(S-\eta)/\beta} e^{-e^{(S-\eta)/\beta}} \lambda + b \quad (6.9)$$

Table 6.1: Constants used to fit the data marked with (o) on Fig. 6.4 to equations Eq. (6.8) and Eq. (6.9). The result of the measures of fit: R2 (Pearson, 1986), NSE (Nash and Sutcliffe, 1970) and d (Willmott, 1981) are also presented.

	Equation constants				fit coefficients			
	β	η	λ	b	R ²	NSE	d	global fit
$W\alpha(S)$ (Eq. (6.8))	2.242	4.692	3.331	0.112	0.980	0.961	0.990	2.932 (out of 3)
$G\alpha(S)$ (Eq. (6.9))	2.268	4.273	3.920	0.116	0.992	0.984	0.996	2.973 (out of 3)

Figure 6.5 shows the numerical flow depths along the stepped spillway by the application of Gumbel equation with coefficients found in Table 6.1.

6.4.3 Top view of water depths

Figure 6.6 illustrates the top profile for time-averaged flow depths along the stepped spillway. Figure 6.6a shows the flow depths measured with the MicUS. Each circle represents the area of water surface that was measured by the MicUS. Figures 6.6b-d represent the numerical averaged free-surface level calculated on the same points as showed on experimental profile by changing the value of cell water volume fraction for $\alpha = 0.1$, $\alpha = 0.5$ and $\alpha = 0.7$, respectively. The circles are smaller in this case because numerically, it is possible to give the exact flow depth at the chosen coordinates.

Figure 6.7 presents the top numerical flow depths profile, where α isoline is changing at every step edge according to Eq. (6.9) and the constants in Table 6.1. In the Y direction of

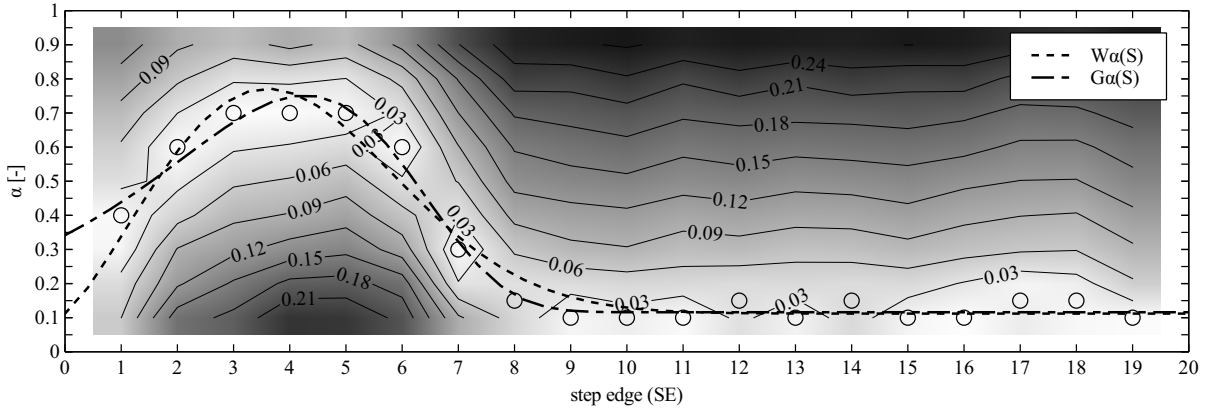


Figure 6.4: Values of numerical water volume fractions (α) that better match the mean flow depth measured with the ultrasonic sensors at each step edge from step 1 to 19 (\circ) and best-fit functions: $W\alpha(S)$ Eq. (6.8) (dashed-line) and $G\alpha(S)$ Eq. (6.9) (dash-long dash line). The contour lines on background image represent relative errors between the depth predicted by different α isolines and experimental data.

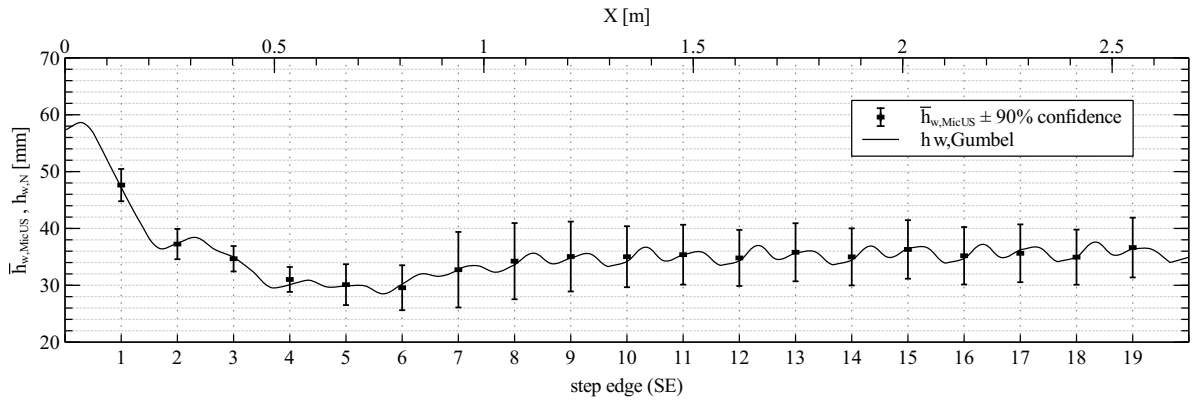


Figure 6.5: Mean water levels measured experimentally with the central ultrasonic sensors at each step edge ($\bar{h}_{w,MicUS}$) and water levels calculated numerically by applying Gumbel equation ($h_{w,Gumbel}$).

the stepped spillway the points are placed at $Y = -2Y_{max}/3$, $Y = 0.0$, $Y = 2Y_{max}/3$ (m).

Table 6.2 shows the results of adjustment of the free-surface levels generated with the experimental data with the numerical free-surface achieved with $\alpha = 0.1$, $\alpha = 0.5$, $\alpha = 0.7$ and the application of Eq. (6.9). The adjustment is measured with the application of three measures of fit: R2 (Pearson, 1986), NSE (Nash and Sutcliffe, 1970) and d (Willmott, 1981). Data is compared at $Y = -2Y_{max}/3 = -0.17$ m, $Y = 0.0$ m, $Y = 2Y_{max}/3 = 0.17$ m and over all the free-surface (global).

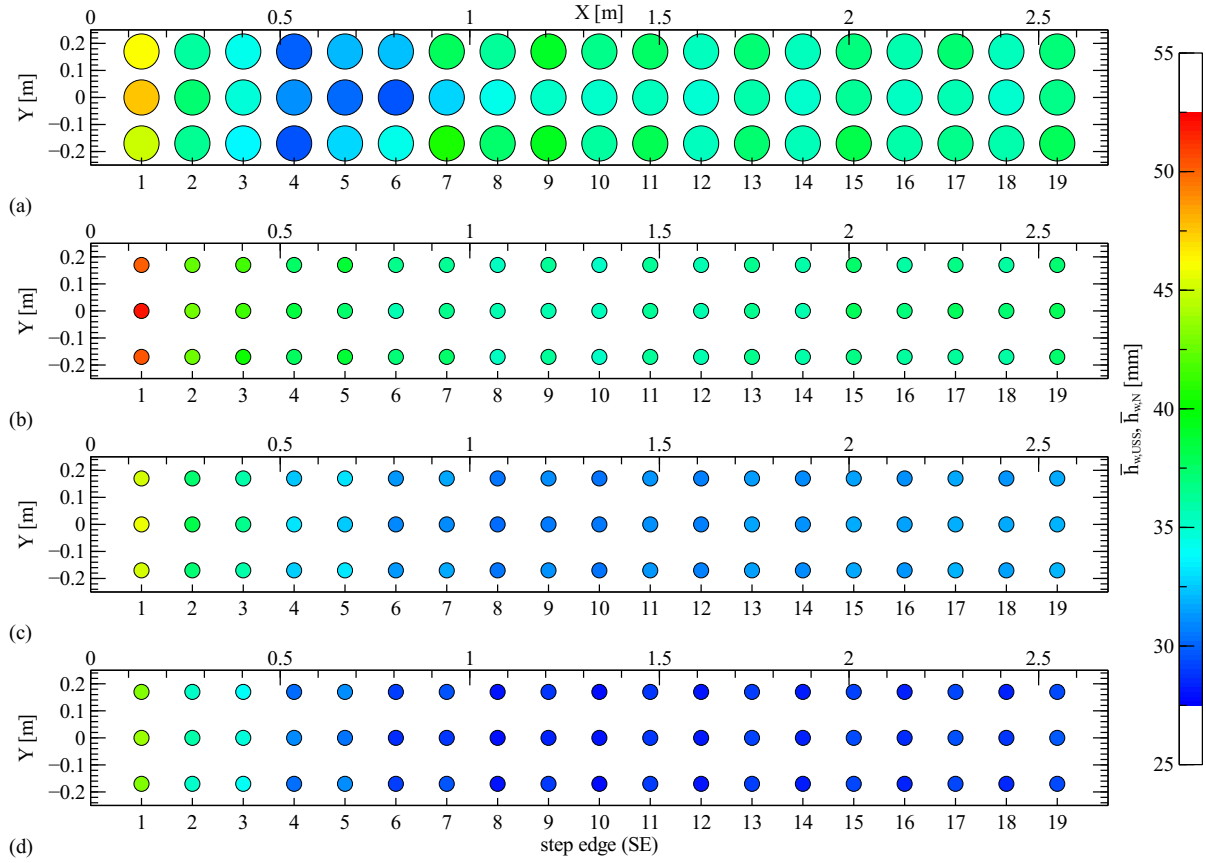


Figure 6.6: (a) Average flow depths measured with a set of three ultrasonic sensors ($\bar{h}_{w,MicUS}$) (sample rate: 200 Hz, acquisition time: 180 s) at each step edge from 1st to 19th step for $s = 0.06 \text{ m}$, $w = 0.5 \text{ m}$, $q = 0.07 \text{ m}^2 \text{s}^{-1}$. The lateral ultrasonic sensors were distanced from spillway walls 80 mm. The circles identifies the influence areas of MicUS. The pseudo-bottom corresponds to water level equal to zero. (b) Numerical free-surface level calculated with $\alpha = 0.1$. (c) Numerical free-surface level calculated with $\alpha = 0.5$. (d) Numerical free-surface level calculated with $\alpha = 0.7$.

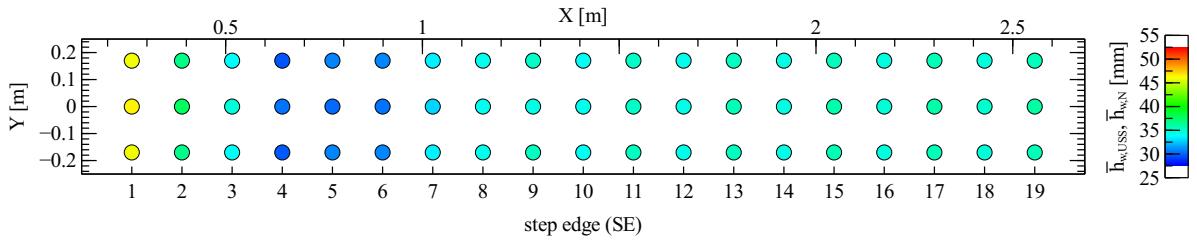


Figure 6.7: Numerical 2D average flow depths profile where α is isoline is changing at every step edge according to Eq. (6.9).

Table 6.2: Fit coefficients between the numerical flow depths calculated with Equation (6.9), $\alpha = 0.1$, $\alpha = 0.5$ and $\alpha = 0.7$ with experimental data at $Y = -0.17\text{ m}$, $Y = 0.0\text{ m}$, $Y = 0.17\text{ m}$ and global. The fit models are: R2 (Pearson, 1986), NSE (Nash and Sutcliffe, 1970) and d (Willmott, 1981). Color ■ highlights values higher than 0.8, color ■ highlights values higher than 0.5 and lower than 0.8, color ■ highlights values higher than 0.0 and lower than 0.5, and color ■ highlights values lower than 0.0.

Y (m)	Equation (6.9)			$\alpha = 0.1$			$\alpha = 0.5$			$\alpha = 0.7$		
	R ²	NSE	d	R ²	NSE	d	R ²	NSE	d	R ²	NSE	d
-0.17	0.835	■ 0.302	0.849	0.454	-0.378	0.663	0.444	■ -1.791	0.544	0.439	-4.429	0.425
0.00	0.993	■ 0.977	0.994	0.784	-0.133	0.775	0.748	0.051	0.776	0.732	-1.302	0.602
0.17	0.931	■ 0.633	0.915	0.526	-0.275	■ -2.280	0.554	■ -1.230	0.601	0.542	■ -3.510	0.461
global	0.905	■ 0.682	0.921	0.586	-0.206	0.721	0.581	■ -0.826	0.643	0.569	0.735	0.499

6.5 Discussion

6.5.1 Free-surface detection

Figure 6.2 shows that the normalized water depth ($h_w/h_{w,I}$) measured with the ultrasonic sensors and the numeric isoline of $\alpha = 0.1$, 0.5 and 0.9 are in general good agreement with the solution of Meireles and Matos (2009), particularly for the zone closer to the inception point, i.e. where $X/X_I = 1.0$. This result is from particular interest to prove the accuracy of our model in the laminar zone of the flow and to show that, in this zone, the range of water volume fraction isolines are giving a self-similar shape.

Averaged flow depths measured with MicUS in Fig. 6.3 shows that before reaching the inception point, the flow depth is decreasing indicating an accelerated flow regime. The confidence interval is small, meaning that the free-surface does not suffer much variations in time, as indeed was expected for a smooth and laminar free-surface. In this case, the free-surface waves amplitude do not spread over more than 5 mm, unlike the further steps where the wave's amplitude are about 10 mm. Flow depth increases from step 5 to 8 from which it becomes constant and roughly equal to 35 mm. To this distance is commonly called as transition length of free-surface. This emphasizes the theory that the air entrained at step 5 creates a bulk of flow, quantitatively described with an average flow depth increasing of about 4 mm (depth at step 8 less the depth at step 5). This development in free-surface wave structure, starting on spillway crest and ending on the aeration point, is similar to that described in the work of Simões et al. (2013). From step 8 to 19th, the potential energy generated with the decrease of flow depth was eventually fully released and the flow reaches a nearly equilibrium of its properties due to the fact that both mean flow depth and wave's amplitude are kept nearly constant. Note that the flow is uniformly and fully aerated just after step 19th.

Figure 6.3 also shows that many water volume fraction isolines are within the confidence interval of experimental water depths, which is a result of the good accuracy of this numerical model on interface detection. However, it is impossible to define a single isoline for α that reproduce the overall shape of the free-surface. Two situations can be easily observed: (1) Until reaching the 8th step edge, the characteristics of turbulence, with the development of a boundary layer; velocities, that increase with distance to the spillway crest; and the flow aeration, that starts on the centre-channel after step 5, are constantly changing from one step to another. The flow depths are therefore function of too many variables and the water depths measured with the MicUS are a combination of α 's isolines on the interval of 0.1 to 0.7. (2) After the 8th step edge, the $\alpha = 0.1$ isoline is generally coincident to the values of water depths measured by the ultrasonic sensors. The averaged relative errors between the numerical free-surface and experimental are shown in background of Fig. 6.4. In the zone where the free-surface is laminar, i.e. all steps before step edge 5, isoline $\alpha = 0.7$ presents an averaged relative error of 2% to experimental. Between step edge 5 and 8, the aeration is under development and numerical free-surface is given by a change of water volume fraction values between 0.7 and 0.1. The errors here can reach $\approx 20\%$ if using $\alpha = 0.1$ to calculate the water depth in step edge 5. In the aerated zone with stable flow depth (after step edge 8), the best α isoline is kept constant to 0.1 (averaged relative error of 2%). This finding is indeed in line with works of Cain and Wood (1981), Wood et al. (1983) and Chanson (1988) where the concept of free-surface is associated to an elevation of air-concentration equal to 90%, i.e. 10% of water or numerically $\alpha = 0.1$.

The interval of smallest relative errors is used to fit an overall equation based on the Weibull and Gumbel distribution following the form of Eq. (6.8) and Eq. (6.9), and the coefficients in the Table 6.1. Both functions pass on the white zone of Fig. 6.3 and have similar shape, although a most noticeable difference can be found on the first step. The value of the global fit coefficient for Eq. (6.9) is in better agreement (2.973 out of 3) than for Eq. (6.8), however, both are accurate in the relation step number versus volume fraction. The highest values registered in Gumbel function for water volume fraction, $\alpha = 0.75$, were found slightly before the aeration point, where the free-surface level assumes its lower level. The minimum values of α are located along the aeration zone with constant water depth ($\alpha = 0.12$).

The water level position calculated through the application of Gumbel equation is shown in substantially good agreement against experimental in Fig. 6.5. Interesting to visualize that the free-surface waves on the aeration zone remained intact after this process of calibration. Although these Gumbel or Weibull equations may just be representative of this case of study, this process for free-surface detection is generally designed for future applications.

6.5.2 Top view of water depths

Figure 6.6a shows the experimental free-surface elevation. On its basis we can notice that the top view of free-surface elevation has his lowest level across the steps 4 to 6. It is known that the inception point at the centre-line for this specific flow rate and spillway characteristics occurs on the 5th step edge, that is clearly visible through the low flow depth registered. However the inception point or aeration point does not start here, but instead, close to the walls of the 4th step edge, situation that was not reported in previous works, probably by the lack of studies of the flow behaviour close to the spillway walls. This finding was also verified during the experiments through the appearance of a small number bubbles on the 4th step cavity and a white free-surface front. When the flow passes by 6th step edge, the depth is kept roughly constant with no much difference noticed between the depth at centre-line and side walls. Figs. 6.6b-d show respectively the numerical free-surface elevation using $\alpha = 0.1$, $\alpha = 0.5$ and $\alpha = 0.7$.

Fig. 6.7 the top numerical free-surface based on the values of α from $W\alpha(S)$ equation (Eq. (6.9)). This type of free-surface representation, i.e. the combination of the various α values to represent one single and general free-surface is not a common situation in CFD, however is clearly visible that the free-surface represented in Fig. 6.7 is much closer to the experimental, rather than using a overall fixed value for α . The same can be concluded on Table 6.2 where the application of Eq. (6.9) shows a better agreement to the experimental than using solely $\alpha = 0.1$, $\alpha = 0.5$ or $\alpha = 0.7$.

6.6 Conclusions

This work presents a numerical procedure for free-surface detection. Flow depth measurements were conducted at each step edge of a stepped spillway using three ultrasonic sensors disposed transversally to the flow direction were. A 3D numerical model of the stepped spillway based on a single set of Navier-Stokes equations together with VOF equation to capture the free-surface position and SST $k - \omega$ for turbulence closure is made. Flow water depths are compared with experiments. The following conclusions can be retrieved from the work:

- There is no global α isoline that predicts the overall shape of free-surface, contrary to what is assumed when using a constant $\alpha = 0.5$. Instead of it, $\alpha = 0.7$ should be assumed in the non-aerated zone (relative errors with experimental of 2%) and $\alpha = 0.1$ when the flow is fully aerated (relative errors with experimental of 2%). The general concept that $\alpha = 0.5$ represents the free-surface can be adopted just if the free-surface is non aerated and assuming errors of around 5 to 8%.

- The procedure for numerical free-surface detection outputs a step number versus volume fraction (α) value based on two extreme values functions: Gumbel and Weibull. The adjustment of those functions was optimized in order to get the smallest deviations between numerical and experimental flow depths measurements. A general equation for step versus volume fraction was produced with good agreement for this specific case of study and its applicability revealed better results than using solely one α isosurface. The process represents a step forward for the creation of a future global relation that is independent of geometric characteristics of the stepped spillway or flow rate.
- Experimental measurements of flow depths using the central ultrasonic sensor allowed the definition of the different flow regions over a stepped spillway. An upstream zone characterized by a smooth and laminar free-surface identified by small confidence intervals to the mean value of flow water depths. The flow water depth decreases until reaches its minimum at step 5, where the air starts entraining on the water. When values of flow water depths becomes constant, i.e. after step edge 8, the flow is fully aerated and the air-water mixture volume does not increase substantially.

7

Alternating Skimming Flow Over a Stepped Spillway

Abstract: *The study of stepped spillways in laboratory scales has been essentially focused on two separated sub-regimes within skimming flow. In this paper we investigate the appearance of an unclassified alternating skimming flow regime in a 0.5 m wide stepped spillway which does not fit on these earlier definitions, and which does not occur in a 0.3 m wide spillway. Our aim is to explain the genesis of this unclassified flow which is visualised in the physical stepped spillway, by using 3D numerical modelling. Flow depths and velocities are measured using an ultrasonic sensor and Bubble Image Velocimetry in the wider flume (0.5 m). The numerical model is validated with the experimental data from the 0.5 m wide spillway. After validation, the channel width of the same numerical model is reduced to 0.3 m wide spillway in order to characterize (compare) the case without (with) alternating skimming flow. Both cases are solved using Reynolds-Averaged Navier-Stokes equations together with the VOF technique and SST $k - \omega$ turbulence model. The experimental results reveal that the alternating skimming flow regime is characterised by an evident seesaw pattern of flow properties over consecutive steps. In turn, the numerical modelling clarified that this seesaw pattern is due to the presence of a complex system of cross waves along the spillway. These cross waves are also responsible for a mass and momentum exchange in the transversal direction and for the formation of the alternating skimming flow in the spillway.*

7.1 Introduction

Numerous experimental studies of current stepped spillways designs have been performed mainly since the 80's (Hager and Pfister, 2013) to study the high complex flow structure, concerning air-concentrations, velocities and energy losses. The flow over a stepped spillway is usually divided in three regimes, depending on the flow rate and its structural geometry: nappe, transition and skimming flow.

The skimming flow occurs in most steep structures and high flow discharges. In skimming flow, the water skims over a pseudo-bottom that connects all the step edges. At the upstream, the surface is smooth and glassy and a boundary layer is developing from the bottom inlet in direction to the free-surface. It is commonly believed that when this boundary reaches the free-surface, the natural turbulence induces the self-aeration of the flow, forming the so-called inception point of aeration. More recently, Valero and Bung (2016) pointed out the effects of air flow to the self-aeration process. Further downstream the flow reaches an equilibrium of its properties.

For stepped chutes with moderate and flat slopes ($\varphi \leq 25^\circ - 30^\circ$), Chanson (2002b) and Ohtsu et al. (2004) proposed two sub-regimes SK1 and SK2 for the skimming flow regime. The observed patterns can be described as follows. In the sub-regime SK1 the mixing layer does not reach the end of the step. A wake zone is formed downstream of each step edge with a recirculation vortex underneath. The free-surface is undulant and in extreme cases, partially parallel to the step tread. In SK2, the wake and the recirculation vortex extend nearly over the step length interfering sometimes with the wake formation of the subsequent step. The free-surface is roughly parallel to the pseudo-bottom and does not suffer much the influence of this sub-regime.

The latter sub-regimes may form an alternating skimming flow when a combination of flow nature and/or dimensional characteristics of the stepped spillway are convened. Such feature of skimming flows was previously described by Yasuda and Chanson (2003) and Felder and Chanson (2009) through the definition of an oscillating seesaw pattern between alternate step edges on a $\varphi = 21.8^\circ$ stepped spillway. This seesaw was observed in terms of the maximum bubble count rate, depth-averaged void fraction, characteristic depth and interfacial velocity (Yasuda and Chanson, 2003) on top of consecutive step edges. However, and to the authors' knowledge, detailed numerical/experimental studies about this phenomena do not exist.

In laboratory investigations, researchers have focused their work on the steps located downstream of the inception point of air concentration for a skimming flow regime, assessing variables such as air concentration (Chanson, 1988, 1993; Chanson and Toombes, 2002; Gonzalez et al., 2008; Leandro et al., 2014a), flow depths (Bung, 2013; Pegram et al.,

1999; Simões et al., 2013) velocity distributions (Amador et al., 2004; Cain and Wood, 1981; Boes and Hager, 2003; Rice and Kadavy, 1996) and pressure on the steps (Amador, 2005; Gomes, 2006); and air-concentrations, velocities and energy dissipation in a SK1 regime (Gonzalez, 2005; Gonzalez et al., 2006). In spite of such works, only few studies were focused on non-aerated zone (Bombardelli et al., 2010; Carvalho and Amador, 2009; Meireles and Matos, 2009) and at the inception point (Hunt and Kadavy, 2013; Meireles et al., 2012; Pfister and Hager, 2011; Valero and García-Bartual, 2016).

Application of numerical modelling of stepped spillway flows were mainly limited to the non-aerated flow region. Cheng et al. (2006) adopted a mixture model with a Re-Normalisation Group (RNG) $k-\varepsilon$ turbulent model to analyse velocity distribution and pressure profiles on step cavities in aerated zone as well as a qualitative study about air concentration over the entire stepped spillway. Carvalho and Amador (2009) used a numerical model based on 2D VOF to solve the water characteristics of the non-aerated flow region and get velocities and turbulent intensities as well as descriptions of cavitation phenomena and shear layer shape were also presented. Same model, this time with RNG $k-\varepsilon$ closure was used by Carvalho and Martins (2009) to study the hydraulic jumps formed on the steps. Bombardelli et al. (2010) focused their work on the non-aerated part of the stepped spillway. Water velocities, free-surface elevation and characteristics of the development of the boundary layer were solved numerically using the TruVOF solver from FLOW-3D® together with two turbulent models: $k-\varepsilon$ and RNG $k-\varepsilon$. Kositgittiwong et al. (2012) analysed the accuracy of five turbulence models in a simulation of a stepped spillway. The authors found that $k-\omega$ models are suited to the near-wall zone whereas Realizable $k-\varepsilon$ performs better in the upper zone of the flow. Nikseresht et al. (2013) used VOF and mixture models, together with various turbulence closures to simulate a two-phase turbulent flow over a stepped spillway. Comparisons in terms of energy dissipation rate and velocity for the numerical simulations with experiments were presented in the work. Nonetheless, most experimental and numerical studies are solely focused on the centre-line of the stepped spillway and under a skimming flow regime assuming that it is representative of the flow near the walls (Hager, 1992).

In this work we investigate the transition of an alternating skimming flow regime to an homogeneous SK1 regime when the spillway width is changed from 0.5 m (SSP05) to 0.3 m (SSP03). The alternating skimming flow regime is defined by the alternated presence of SK1 and SK2 sub-regimes in two consecutive steps. Section §7.2 presents the two experimental facilities where these two distinct regimes were observed, and the equipment used to measure the flow depths and velocities in SSP05 flume. Section §7.3 describes the equations behind the numerical model used, along with the two computational domains (SSP03 and SSP05), numerical constants and procedures. Section §7.4 introduces the

experimental and numerical methods to study the free-surface elevation. Section §7.5 presents the numerical validation of the SSP05 model according to the experimental data acquired. Section §7.6 presents the results necessary for the comparison between the validated SSP05 model with the SSP03 model. The presence of the alternating skimming flow regime is discussed in Section §7.7. Section §7.8 summarises the main findings of this work.

7.2 Experimental tests

7.2.1 Experimental stepped spillway 0.5 m wide

Experimental data are acquired in a 0.5 m wide stepped spillways physical model built at the Hydraulic Engineering Section Laboratory of FH Aachen - University of Applied Sciences. The water is pumped from an underground tank to a head reservoir positioned upstream of the spillway structure and then returned to the downer tank in a closed circuit of water. The flow rate is controlled by a butterfly valve and measured by an inductive flow meter. Inside the head tank a plastic grid is installed to harmonise the flow and reduce the turbulence at the inlet. Between the reservoir and the first step exists an approaching channel of 1 m length. The spillway model has 28 steps with dimensions $0.12 \times 0.06 \times 0.50$ m (step length \times height \times width ($l \times s \times w$)), resulting in a total drop height (H) of 1.68 m (Fig. 7.1).

The chute angle is constant and equal to $\varphi = 26.6^\circ$. The unit water discharge is defined to $q_w = 0.07 \text{ m}^2 \text{s}^{-1}$ which returns a critical water depth of $h_c = 0.08 \text{ m}$ ($h_c/s = 1.3$). The structural designs here used and flow conditions originate a skimming flow regime with a surface inception point at the 5th step edge, verified by the observation of white water front and surface fluctuations. The uniform flow region starts after 19th step edge or $H_u = 1.097 \text{ m}$ according to Bung (2011a). The flow condition is at the lower end of the skimming flow regime and hence some features of the unstable transition flow regime may still be present (Felder and Chanson, 2011a,b). Ideally one should test also for further flow conditions. In any case the present study already shows beyond any doubt the presence of the alternating skimming flow. Future work will look into defining the range of occurrence of this regime.

Since gravity and inertia are important in the stepped chutes, the present study is based upon the Froude similitude. However, true dynamic similarity may not be completely achieved due to scale effects. Chanson (2002b) recommends model scales between 1/1 and 1/10 to achieve true similarity of air-entrainment and avoid significant scale effects. Pfister and Chanson (2012) refer to a minimum Reynold number of 2 to 3×10^5 or a minimum

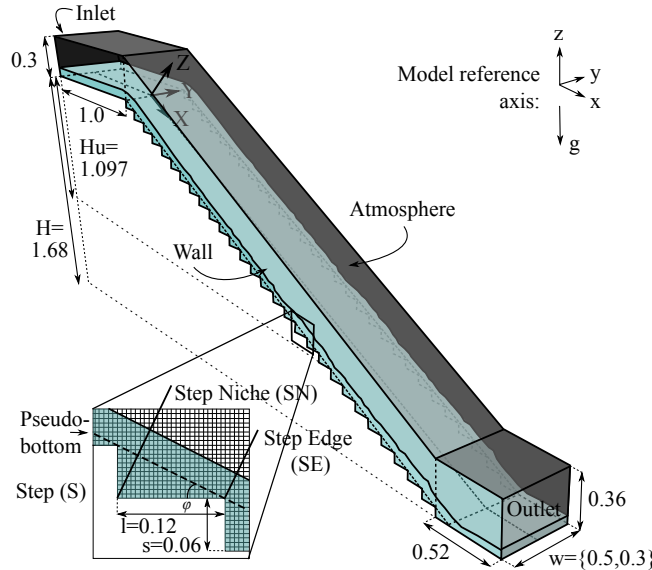


Figure 7.1: Experimental scheme of SSP05, numerical model geometry, dimensions and mesh. Dimensions in meters. The origin of system of coordinates XYZ is located at the end of the approaching channel, for which X is aligned with the pseudo-bottom. The system of coordinates xyz is used by the numerical model.

Webber number of 140 to consider also surface tension effects. These conditions are also met in (Bung, 2011a). Figure 7.2a shows the presence of an alternating skimming flow in the SSP05 structure.

7.2.2 Experimental stepped spillway 0.3 m wide

The 0.3 m wide stepped spillways physical model was built at the University of Wuppertal. SSP03 structure is narrower than SSP05 and had 39 steps of $0.12 \times 0.06 \times 0.30$ m, forming a total drop height of 2.34 m. Water was pumped into an open head tanks and then conveyed through an approaching channel with a length of 1 m where small tubes at the inlet reduced the flow turbulence. A more complete description of SSP03 can be found in the work of Bung (2011a). This structure was used for flow visualisation and no measurements were made. Figure 7.2b show the presence of a SK1 regime in the SSP03 structure.

7.2.3 Ultrasonic sensor

The free-surface elevation over the SSP05 stepped spillway was measured experimentally with an US placed at channel centre-line. A Microsonic mic+130/IU/TC US sensor (operating range: 200 to 1300 mm, resolution: 0.18 mm) is moved from step edge 1 to step

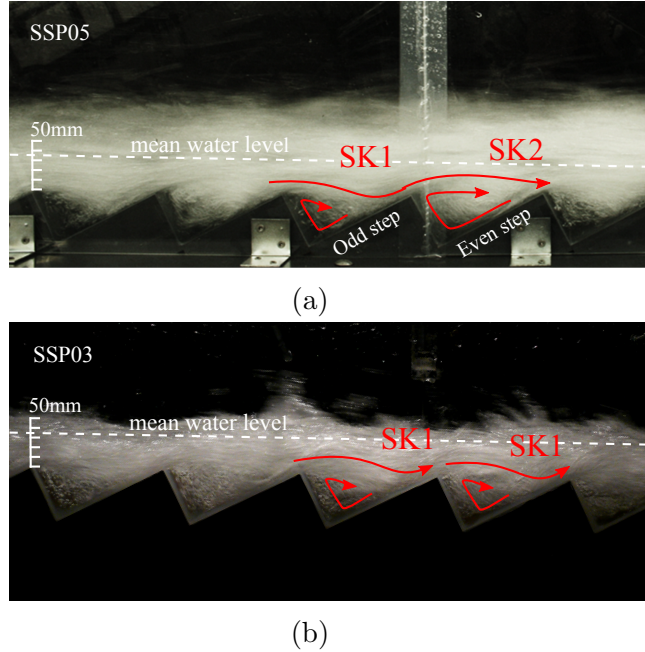


Figure 7.2: Photographs of the differences in flow patterns at (a) SSP05 and (b) SSP03. The photograph shown in (a) was slightly taken from above and as such some part of the water surface area is visible. Mean water level is marked in a dashed line. SK1 is a sub-regime of the skimming flow in which the mixing layer does not reach the end of the step. SK2 is a sub-regime where the recirculation vortex extend nearly over the step length interfering sometimes with the wake formation of the subsequent step.

edge 19 (the step edge location is exemplified in Fig. 7.1). During the experiments, the US is exactly 461 mm above the pseudo bottom of the spillway to avoid being outside of the operating range. Data are sampled during 180 s at 200 Hz. The longitudinal movement of the sensor is attained using an ISEL LES4 engine (maximum length: 2990 mm, accuracy: 0.1 mm), starting on the first step edge and sequentially moved by ≈ 135 mm (distance between two subsequent step edges in flow direction). The maximum length of this engine corresponds to the distance of the spillway crest to step edge 19 which constrains the range of measurements.

7.2.4 High speed camera

Numerical flow velocities close to the wall are validated using BIV (Bung, 2011b). The flow field from step 6 to 13 of SSP05 is individually captured with a high-resolution high-speed camera (HSC) Phantom Miro M120 (sample rate: 700 fps, resolution: 1920×1200 px) equipped with Nikon 50mm f/1.4D AF Lens. The camera is positioned 0.6 m away from the spillway front wall. In order to enhance the contrast, the backside wall of the flume is made of black PVC. The front wall is transparent, allowing the lateral visualization of the

flow. Each step is illuminated with the same light intensity, achieved by the sequential displacement of two white halogen spotlights on the top of the spillway. Due to RAM limitations, at 700 fps and under the maximum resolution, the maximum acquisition time is 1 s. In order to ensure a sharp image, before each measurement the pump is switched off and the lens are focused to a printed target, positioned 2-5 mm inside the acrylic wall.

BIV technique is applied to this work in order to obtain the flow velocity field close to the side walls. The bubbles are used as tracers and illuminated by halogen spotlights. Some loss of accuracy must be taken into account, because bubbles can leave focused planes and distort the resulting velocity field (Leandro et al., 2014a). The BIV calculation in this study is done with the commercial LaVision DaVis 8 software. After some tests about software performance and accuracy, a simple cross-correlation (i.e. frame1×frame2, frame2×frame3, [...]) analysis of an interrogation window size of 96×96 px with 75 % overlap is chosen. The velocity is an average from the 1 s measurement as this time period shown to be sufficient to get accurate results with errors below 3% (Leandro et al., 2014a). Also, according to Felder and Chanson (2015b), for sub-sample durations between 1 and 45 s, the maximum cross-correlation coefficient did not change significantly and decreased for smaller sub-sample durations.

7.3 Numerical model

7.3.1 Model equations

The two stepped spillways models are solved with a set of Navier-Stokes equations, together with SST k- ω turbulence closure and VOF technique to detect the free-surface. Interface capturing models such as the VOF model (implemented in the OpenFOAM® v.2.3.0 toolkit as *interFoam*) represent the dynamics of the two phases in terms of a single velocity field and pressure field governed by a single set of Navier-Stokes equations. For a system of isothermal, incompressible and immiscible two-phase flow, the averaged-equations for mass conservation and momentum are written in their conservative form as:

$$\nabla \cdot \bar{\mathbf{u}} = 0 \quad (7.1)$$

$$\frac{\partial \rho \bar{\mathbf{u}}}{\partial t} + \nabla \cdot (\rho \bar{\mathbf{u}} \bar{\mathbf{u}}) = -\nabla p^* - \mathbf{g} \cdot \mathbf{x} \nabla \rho + \nabla \cdot (\mu \nabla \bar{\mathbf{u}}) + (\nabla \bar{\mathbf{u}}) \cdot \nabla \mu + \mathbf{f} \quad (7.2)$$

where ρ [kg m⁻³] is the fluid local density, \mathbf{g} [m s⁻²] the gravitational acceleration, $\mathbf{x} = \{x, y, z\}$ are the Cartesian coordinates (Fig. 7.1), $\bar{\mathbf{u}}$ [m s⁻¹] the velocity vector, $\nabla \cdot (\mu \nabla \bar{\mathbf{u}}) + (\nabla \bar{\mathbf{u}}) \cdot \nabla \mu$ the decomposition of shear stress tensor, μ [Kg m⁻¹s⁻²] the dynamic viscosity and \mathbf{f} [kg m⁻²s⁻²] the volumetric surface tension force. A modified

pressure p^* is adopted by removing the hydrostatic pressure from the total pressure (p). It is also important to note that the velocity vector $\bar{\mathbf{u}}$ represents the shared velocity of the two fluids, i.e. $\bar{\mathbf{u}} = \bar{\mathbf{u}}_{f1} = \bar{\mathbf{u}}_{f2}$, rather than in mixture models where $\bar{\mathbf{u}}_{fk}, k = \{1, 2\}$ can assume different magnitudes at fluids interface.

Together with the previous equations, the solver uses the VOF technique, firstly developed by Hirt and Nichols (1981), to capture the interface between two fluids by solving a transport/advection equation [Eq. (7.3)].

$$\frac{\partial \alpha}{\partial t} + \nabla \cdot (\alpha \bar{\mathbf{u}}) + \nabla \cdot [\bar{\mathbf{u}}_c \alpha (1 - \alpha)] = 0 \quad (7.3)$$

Basically, at each cell of the domain an alpha (α) value is defined representing a fraction of volume of fluid in a cell and ranging from 0 to 1 (Carvalho et al., 2008; Ubbink, 1997). Cells completely filled with fluid 1 ($f1$) will get $\alpha = 1$ and cells filled with fluid 2 ($f2$), a value $\alpha = 0$, and the physical properties of the two-fluid mixture are therefore a weighted average of two fluids properties based on the ratio of the two fluids volume. The interface, or free-surface in case of air-water flows, is represented by the jump of alpha values from 0 to 1, where a compressive term is used to confine the interface into a small region of the domain (last term on [Eq. (7.3)]) (Berberović et al., 2009). The sub-term $\alpha(1 - \alpha)$ ensures that the compressive term is calculated just at the interfacial cells of the domain, whereas the compressive velocity ($\bar{\mathbf{u}}_c$) Eq. (7.4), that acts as a velocity perpendicular to the interface, keeps the interface sharp. C_α is a binary coefficient that activates ($C_\alpha = 1$) or neglects ($C_\alpha = 0$) the interface compressive term.

$$\bar{\mathbf{u}}_c = C_\alpha |\bar{\mathbf{u}}| \frac{\nabla \alpha}{|\nabla \alpha|} \quad (7.4)$$

The volumetric surface force function (\mathbf{f}) is explicitly estimated by the CSF model developed by Brackbill et al. (1991).

Although the RSM is the most accurate way to calculate the turbulence in stepped spillway as shown by Nikseresht et al. (2013), simulations using RNG $k-\varepsilon$, realizable $k-\varepsilon$ or SST $k-\omega$ can be also applied with less computational effort and much simpler boundary conditions (Bombardelli et al., 2010; Kositgittiwong et al., 2012; Rahimzadeh et al., 2012). The turbulence closure used in the present study is the SST $k-\omega$, introduced by Menter (1993), which combines the best of two RANS formulations: it takes advantage of the accuracy and robustness of $k-\omega$ model in the near-wall zone, whereas the free-stream region, i.e. the outer part of the boundary layer, is simulated with a high-Reynolds-number formulation of $k-\varepsilon$ model. This means that $k-\omega$ calculates the turbulence generated by vortexes on the steps of the spillway, whilst the turbulence on the zone above the pseudo-bottom is predicted by the $k-\varepsilon$ model. A simplified form of SST $k-\omega$ model can be written

as:

$$\frac{\partial(\rho k)}{\partial t} + \nabla \cdot (\rho k \bar{\mathbf{u}}) = \nabla \cdot [\Gamma_k \nabla k] + G_k - Y_k \quad (7.5)$$

$$\frac{\partial(\rho \omega)}{\partial t} + \nabla \cdot (\rho \omega \bar{\mathbf{u}}) = \nabla \cdot [\Gamma_\omega \nabla \omega] + G_\omega - Y_\omega + D_\omega \quad (7.6)$$

where Γ_k and Γ_ω represent the effective diffusivity of k and ω . G_k is the generation of turbulence kinetic energy due to the mean velocity gradients and G_ω the production of ω , whereas Y_k and Y_ω are their respective dissipation. D_ω is the cross-diffusion term that results from the transformation of k- ε theory into k- ω model.

7.3.2 Computational domains, grid convergence study and model settings

The model applies two different computational domains for each experimental setup (i.e. 0.3 and 0.5 m wide channel). SSP05 is a stepped spillway identical to the experimentally studied (Fig. 7.1) with 0.5 m wide steps and where we found the presence of an alternated flow pattern over adjacent steps (Fig. 7.2a). SSP03 is instead a 0.3 m wide channel were this alternation is not visible (Fig. 7.2b).

For SSP05, three uniform structured grids (N1, N2, N3) of $0.005 \times 0.005 \times 0.005 \text{ m}^3$, $0.007 \times 0.007 \times 0.007 \text{ m}^3$ and $0.01 \times 0.01 \times 0.01 \text{ m}^3$ are used in this work to perform a grid convergence study. The meshes are created using snappyHexMesh tool from OpenFOAM®, based on a STereoLithography (STL) file created in SALOME v.6.4.0 software (Salome, 2011). N1 has 6 528 000 cells, N2 has 2 754 000 cells and N3 has 816 000 cells. Richardson extrapolation, following Celik et al. (2008) procedure was performed over 30 points along the X-velocity profile placed above the 12th step edge. The local order of accuracy p ranges from 1.6 to 13.0 with a global average of 4.6. Oscillatory convergence occurs at 23% of the 30 points. The maximum discretisation uncertainty is 28% at the point closest to the bottom wall, which corresponds to 0.25 ms^{-1} , whereas on the free-stream flow the uncertainty on the maximum velocity is 0.23% (0.0059 ms^{-1}). Large uncertainties close to the walls are due to the large velocity gradients. The GCI, which measures the percentage of convergence of the finer mesh to an mesh independent solution is $\text{GCI}_{\text{N}1} = 5\%$, value that shows a large confidence on the results for N1.

The steady-state solution is achieved after 24 s of simulation in an average time step of 0.00033 s. This state is identified from the criteria that the residuals of k , ε and p , and the volume fraction on the domain were kept constant in time. Using N1 grid, the clock time needed to compute 25 s was 345 087 s (approx. 4 days in a continuous run) in a

cluster with 16 processors (2 nodes of 2 quad-core processors @ 2.40GHz) and 24GB RAM. The averaged values from the last 1 s of simulation time with a writing step of 0.05 s are used to plot the results.

7.3.3 Physical fluids properties, initial and boundary conditions

The physical properties of the two fluids and model constants are summarized in Table 7.1.

Table 7.1: Model constants.

Parameter	f_1 = water ($15^\circ C$)	f_2 = air ($15^\circ C$)	model
ρ [$kg\ m^3$]	998.78	1.225	-
ν [$m^2\ s^{-1}$]	1.1094e-06	1.4657e-05	-
σ [$kg\ s^{-2}$]	-	-	0.072

The initial condition of the simulation assures a 0.1 m deep water flow over all the structure with $u_x = 0.7\ ms^{-1}$. The *inlet* boundary condition fixes the value for \bar{u} as $u_x = 0.7\ ms^{-1}$, α as 1 and sets gradient zero for p^* . The *atmosphere* just allows the air to leave the domain by setting \bar{u} as dependent of the total pressure. The *wall* boundaries sets gradient zero for α , p equal to hydrostatic pressure and zero velocity for \bar{u} (i.e. non-slip condition). At *outlet* all the variables have zero gradient.

7.4 Methods to measure the free-surface

7.4.1 Free-surface measured with the ultrasonic sensor

The use of ultrasonic sensors to measure flow depths is a quite reliable method even in aerated flows (Wang and Chanson, 2015; Felder and Chanson, 2014), but care has to be taken during operation. The main issue is that the acoustic signal can be affected by the presence of surface waves or ejection of droplets from the air-water mixture and the signal may not be reflected back to the same sensor, either by the reflection in a very disturbed surface or droplets, or by the impact in the lateral walls. In this work, the lateral walls are outside the signal operation volume, therefore to discard remaining errors from the raw data set, the signal is filtered to a smooth data using the same filtering process proposed by Bung (2013). The outlier values are discarded from the raw sample by setting a double threshold, defined as being the mean value \pm three times the standard deviation. This process proved being efficient in the spikes removal without interpose the quality of the data.

7.4.2 Numerical procedure for free-surface detection

On the basis of VOF method, every cell that has a value of α within the interval 0 to 1 is a free-surface cell. Although this theory works fine on a smooth and laminar free-surface, in a turbulent flow, the free-surface is highly irregular and its averaged shape may not represent the free-surface accurately. The numerical free-surface may spread over a large number of cells, and although it is common to use $\alpha = 0.5$ as first guess for free-surface position (Albadawi et al., 2013; Lopes et al., 2015b; Witt et al., 2015), all remaining isolines or isosurfaces (in case of 2D or 3D simulations) are likely to be correct.

7.5 Model validation

The numerical model is validated with experimental measurements of flow depths and velocity profiles calculated with BIV. It should be noted that validation of the numerical model may also include other feature of skimming flows on stepped spillways, e.g. the air-water flow characteristics. However, air-water properties are not the focus of this work. Furthermore, VOF model cannot be used to simulate entrapped air. Future work of the Authors will look at this feature by using more advanced numerical models (Lopes et al., 2016b).

Figure 7.3 shows the mean water levels measured with the US at step edges from step 1 to 19 ($\bar{h}_{w,US}$). Confidence intervals of 90% to the mean are added to the graphic. The numeric water surface position represented by $\alpha = 0.5$ isoline, varied by ± 0.4 is also represented in the figure ($h_{w,N}$). The top limit is representative of $\alpha = 0.1$ and the bottom limit is $\alpha = 0.9$. The stable flow depth beginning is defined when the depth variation between adjacent steps becomes less than 1 mm.

Figure 7.4 shows the comparison of BIV velocity profiles to numerical at step niches from 6 to 13. Numerical velocity profiles are determined 0.005 m away from the lateral wall, i.e. the value of velocity on the first cell face, which matches with the distance between the focused target and the flume wall (consult sec. 7.2.4). Pearson (1986) (r^2) and Willmott (1981) (d) measures of fit are used to evaluate the accuracy of the model. Both coefficients range from 0 to 1, where unity indicates perfect match.

The US data in Fig. 7.3 shows that flow depth increases from step 5 to 8, becoming constant and roughly equal to 35 mm. Before step 5, the US confidence interval is small, meaning that the free-surface does not suffer much variations in time, as indeed was expected for a smooth and laminar free-surface. From step 8 to 19, the flow reaches a nearly equilibrium of air-entrainment due to the fact that both mean flow depth and wave's amplitude are kept nearly constant. The isoline of $\alpha = 0.5$ reproduces quite well

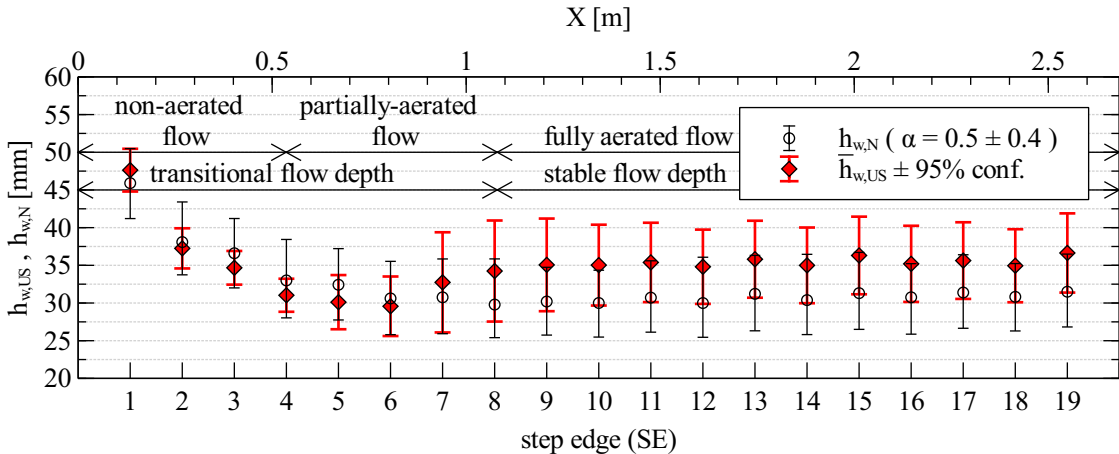


Figure 7.3: Mean water levels measured experimentally with the US at each step edge ($\bar{h}_{w,US}$) and water levels calculated numerically by plotting the $\alpha = 0.5$ and the limits of ± 0.4 ($h_{w,N}$). Data are taken from SSP05.

the zone where the flow is non-aerated or partially-aerated, i.e. $\bar{h}_{w,US} \approx h_{w,N}$ before step edge 6. The averaged relative error is 5%. When high quantity of air enters the water body (after step edge 8), the $\bar{h}_{w,US}$ is no longer represented by $\alpha = 0.5$ but instead by $\alpha = 0.1$. The averaged relative error between $\alpha = 0.1$ isoline and the experimental flow depth from step 8 to 19 is 3%. This finding is in line with previous works: Bung (2013) shows that, for an identical setup, the time-averaged free-surface of an air-water mixture measured with a similar US corresponds to an elevation with air-concentration equal to 90% (same as 10% of water or $\alpha = 0.1$). However, although the quantity of air present at each step influences the correct α isoline, the overall measurements of water depths made with the US are within the limits of the numerical free-surface thickness, which supports the good applicability of the model and hence validates the numerical solution for flow depths. An evident seesaw pattern in terms of flow water depth can be seen after the step 10. Such pattern was observed before for some ranges of slopes and step heights (Chanson and Toombes, 2002; Felder and Chanson, 2009). This work aims to go one step further by using numerical modelling to explain the alternating pattern.

When BIV is used to validate the numerical model, some loss of accuracy has to be taken into account specially when the step cavity is not fully aerated, or on the free-stream flow region where the air bubbles are sometimes indistinguishable, as happens on SN6 and SN8 respectively. However, numerical velocity profiles at step niches show quite good agreement when compared with BIV calculation as measures of fit are higher than 0.972. The model reliability in terms of velocity fields is proven here.

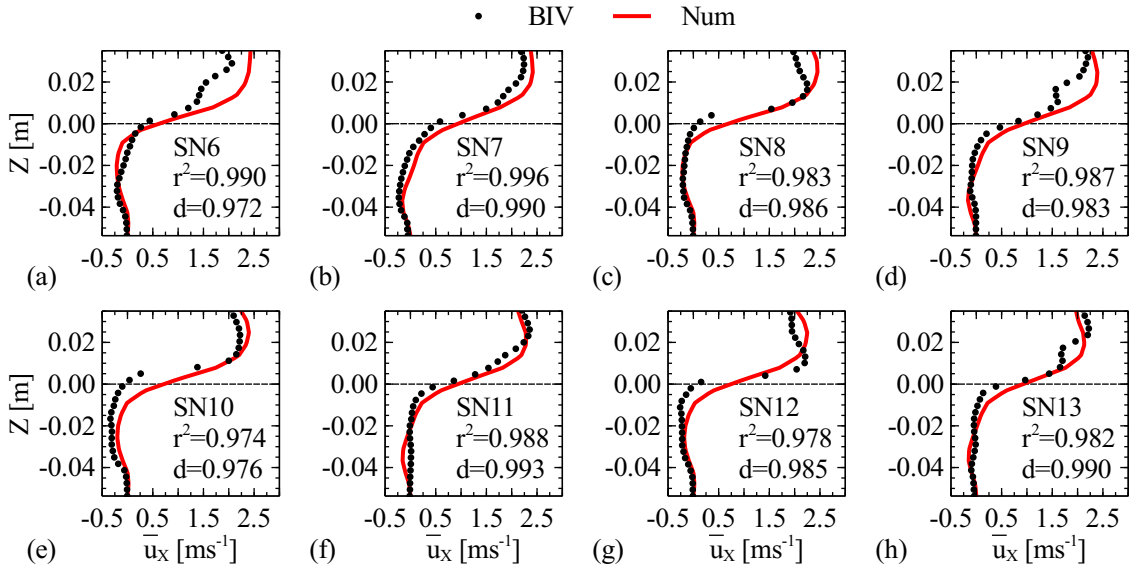


Figure 7.4: Bubble image velocimetry vs. numerical velocity profiles at step niches (SN) 6 to 13. Pearson (1986) (r^2) and Willmott (1981) (d) measures of fit are plotted on each graphic. $Z = 0$ refers to the pseudo-bottom level whereas Z_{max} is the free-surface level measured with the Ultrasonic sensors at each step edge ($\bar{h}_{w,US}$). Data are taken from SSP05.

7.6 Results

7.6.1 Flow stream-lines and flow pattern alternation

The analysis of the flow pattern alternation is made between steps 12 and 13. Although the steps 12 and 13 are not in the uniform flow region, the free-surface is quasi-stable (Fig. 7.3) and the observed flow pattern does not change in the subsequent pair steps. This section shows a 3D view of the flow stream-lines. Figure 7.5 presents the stream-lines (in light grey) over step 12 and 13 of SSP05, calculated by placing a seeding line 1 mm above the respective step edge. This seeding line shows the trajectory of 50 massless particles of fluid (100 particles/m) that are passing through the line. Figure 7.6 presents the stream-lines over step 12 and 13 of SSP03, calculated by placing a seeding line 1 mm above the respective step edge. The proportion of seeding are the same as in Fig. 7.5, 100 particles/m which results in a total of 30 particles uniformly distributed in the channel width (represented in light grey). At the step treads and risers are plotted the pressure values. Particles trajectories presented in Fig. 7.5 and Fig. 7.6 are drawn according to what can be visualised from the stream-lines traced. The short rolls zones meet all volume within two consecutive SK2 regimes with a SK1 regime in between.

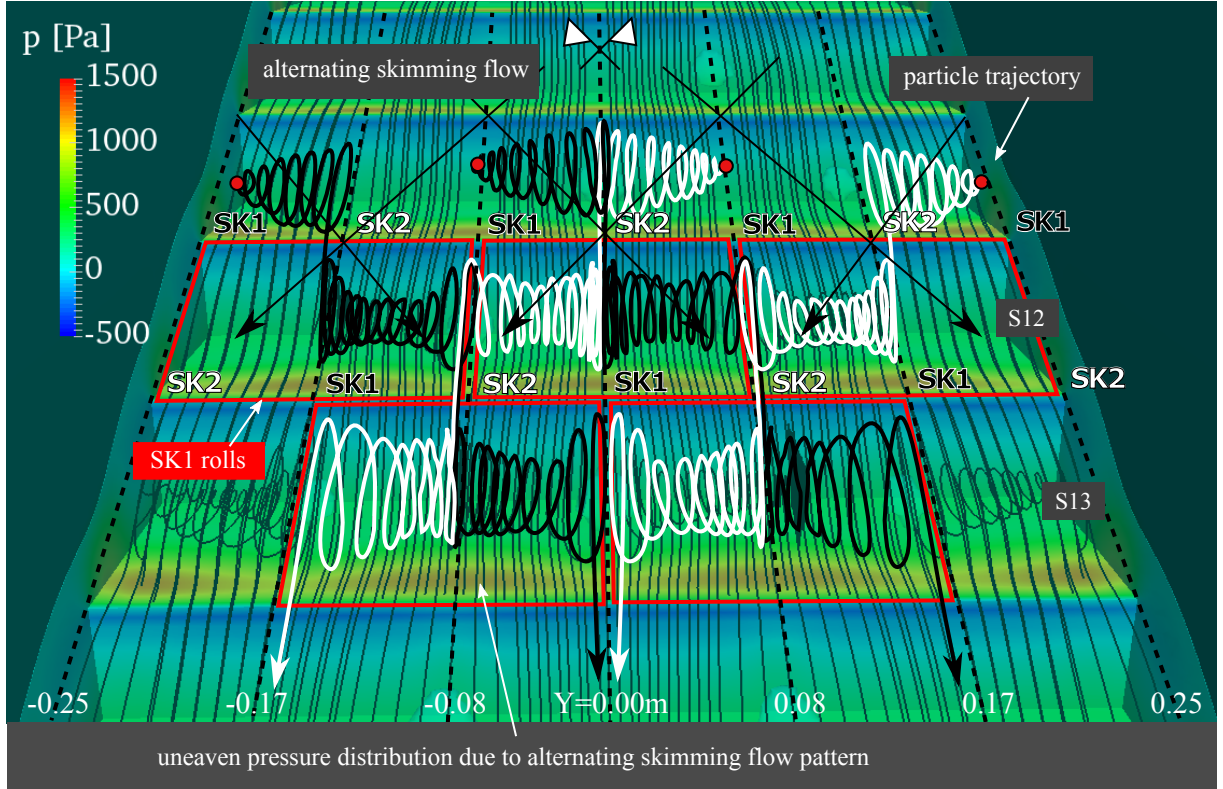


Figure 7.5: Flow stream-lines and pressure on the steps calculated in SSP05.

7.6.2 Flow properties

This section shows the longitudinal flow velocity on the stepped spillway, i.e. plane XZ. Figure 7.7a-b presents a comparison of modelled velocities at $Y = 0 \text{ m}$ (i.e. the centre-line) and $Y = Y_{max}/3 \text{ [m]}$ ($Y = 0.08 \text{ m}$) on SSP05, whereas Figures 7.7c-d show a comparison of modelled velocities at $Y = 0 \text{ m}$ and $Y = Y_{max}/3 \text{ [m]}$ ($Y = 0.05 \text{ m}$) on SSP03. The velocities here presented are the projection of U on the plane XZ. The contour lines delineate the velocity categories shown in the label.

Figure 7.8 shows the modelled averaged velocities of SSP03 and of SSP05 at $Y = 0 \text{ m}$ in the step niches from 8 to 13. The horizontal axis is normalized with the velocity at the free-surface whereas the vertical axis is normalized with the numerical water flow depth given by $\alpha = 0.1$.

Figure 7.9 presents the result of the application of BIV technique and numerical stream-lines on step 12 (Fig. 7.9a and Fig. 7.9b) and step 13 (Fig. 7.9c and Fig. 7.9d).

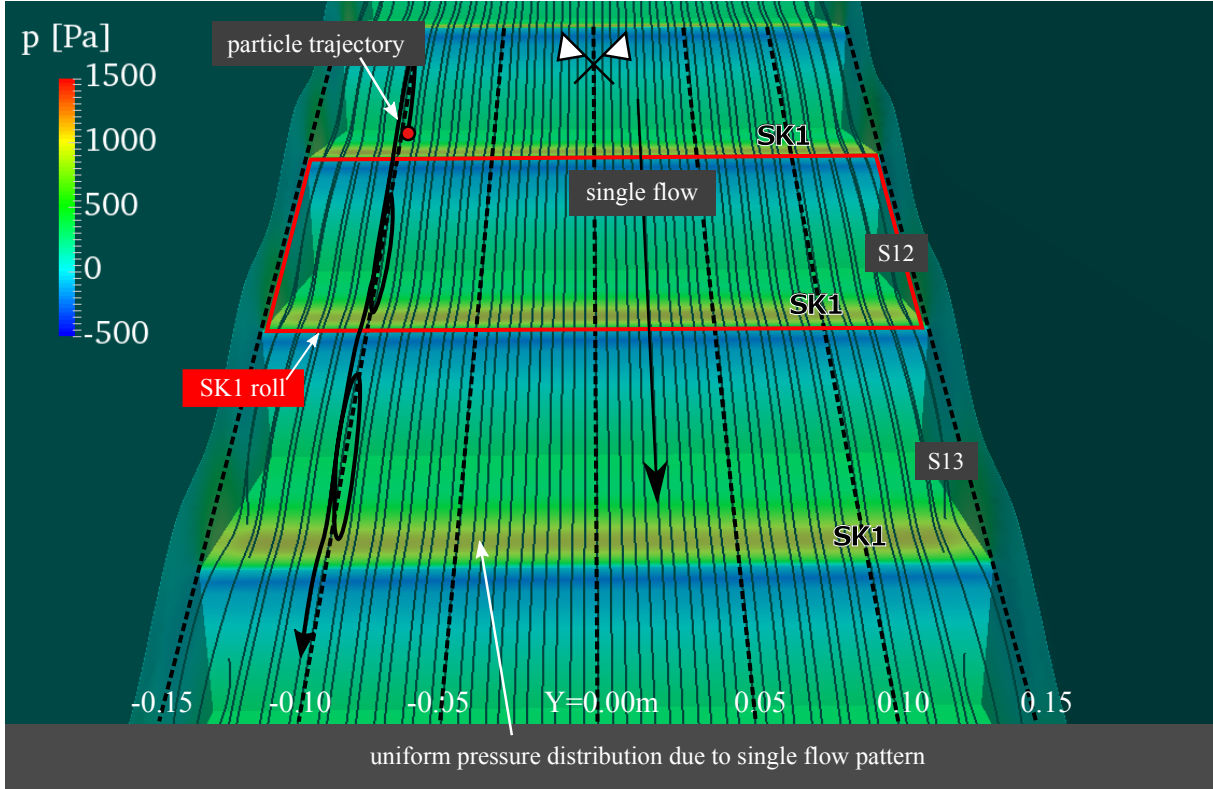


Figure 7.6: Flow stream-lines and pressure on the steps calculated in SSP03.

7.6.3 Turbulence statistics

The turbulent kinetic energy $k = 1/2\langle u_i u_i \rangle$, where u_i is the i component of fluctuating velocity, characterises the energy in the fluctuating velocity field. Figure 7.10 shows the numerical turbulent kinetic energy for the two stepped spillway installations at $Y = 0$ m. The contour lines delineate the categories shown in the label.

7.7 Discussion

Figures 7.5 and 7.6 show the flow stream-lines on steps 12 and 13 for SSP05 and SSP03. The figures clearly indicate that in the wider stepped spillway (SSP05) a different flow pattern emerges, either looking longitudinally or transversely, induced by widening the spillway from 0.3 m to 0.5 m. Looking just for the centre-channel plane, the high pressures present in the S12 tread ($p \approx 1500$ Pa) indicate the presence of a roll smaller than step length. The mixing layer does not reach the end of the step, which is a typical description of a SK1 regime. In the S13 tread, the pressure is lower ($p \approx 1000$ Pa). The roll does not collide with the step but occupies all cavity, indicating the presence of SK2 regime. This description shows that the water that leaves S12 in the centre-channel jumps all over the

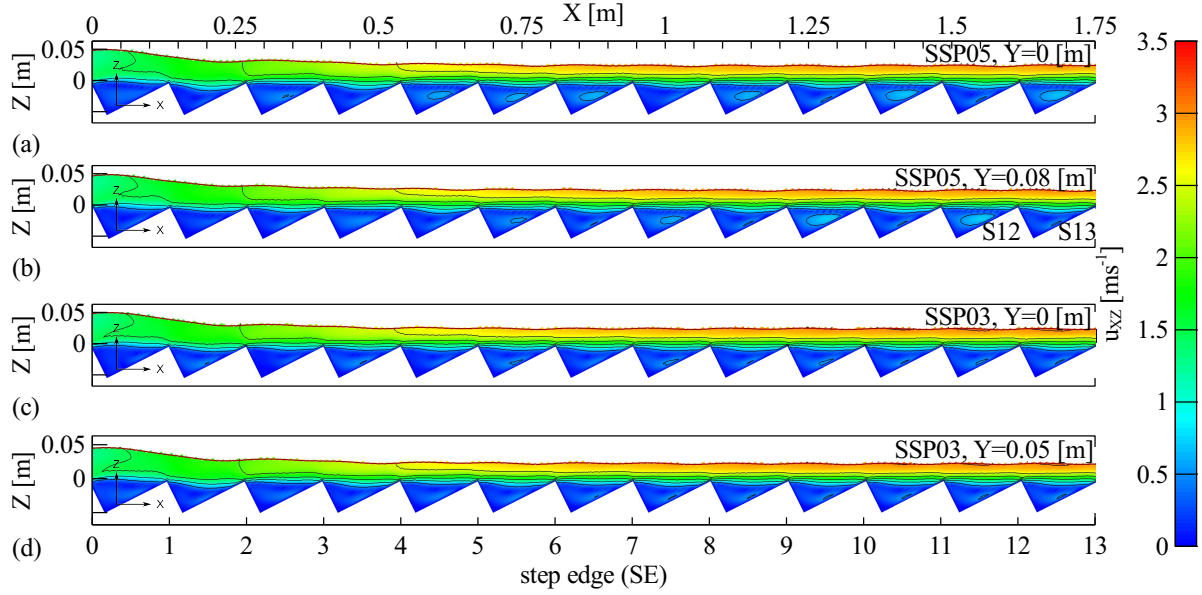


Figure 7.7: Modelled averaged velocities of SSP05 at: (a) $Y = 0 \text{ m}$ and (b) $Y = Y_{\max}/3 \text{ [m]}$ and of SSP03 at: (c) $Y = 0 \text{ m}$ and (d) $Y = Y_{\max}/3 \text{ [m]}$. X is the distance to the spillway crest and Z the vertical axis, perpendicular to the pseudo-bottom plane. U_{XZ} is the projection of the velocity vector on the plane XZ . The free-surface is represented by $\alpha = 0.5$. The contour lines delineate the velocity categories shown in the label.

S13, colliding ahead in S14. This flow pattern has a wave length of two step cavities as described in (Felder and Chanson, 2009).

In a wider view of step 12 of SSP05 (Fig. 7.5) it is possible to observe three SK1 rolls in the transversal direction of the spillway which rotate short than step length. On step 13, the pattern is diverted, and we can now notice two SK1 rolls centred on the spillway width, plus two halves that are starting/ending on the walls. Each roll is limited transversally by a SK2 regime.

Another interesting issue is that the flow pattern observed on the centre-line of the stepped spillway ($Y = 0 \text{ m}$) is replicated at $Y = \pm 2Y_{\max}/3 \text{ [m]}$ ($Y \approx \pm 0.17 \text{ m}$), whereas the longitudinal flow pattern at $Y = \pm Y_{\max}/3 \text{ [m]}$ ($Y \approx \pm 0.08 \text{ m}$) is reproduced close to the stepped spillway walls. A transversal mass and momentum exchange is visible in the wider spillway. For any of the four particles highlighted in Fig. 7.5, is it possible to see that their path starts in the centre of the roll (inside the step cavity), from where they keep rolling until collide with another particle that travels in the opposite direction. In the collision points (intersections), the flow depth is increased by a SK2 regime whilst in the non-intersections, a SK1 regime form a trough in the water surface. The particles do not change their direction until reach the opposite wall, place where they reflect to start a new cycle. As the SK2 is preceded by SK1 in the longitudinal direction, this phenomena is the

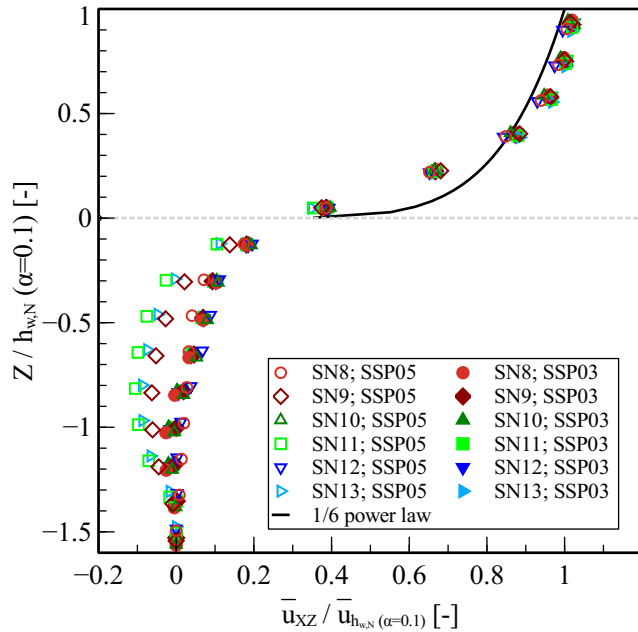


Figure 7.8: Normalized velocity profiles at step niches from SN8 to SN13 in the two stepped spillways SSP03 and SSP05.

reason for the seesaw pattern visible in Fig. 7.3 and referenced in (Felder and Chanson, 2009).

At SSP03 (Fig. 7.6), the flow is uniformly distributed on the transversal direction of the flume and the stream-lines parallel to the spillway walls. A single flow pattern equivalent to SK1 is found all over the structure. The roll on the steps is always shorter than the step length.

Figure 7.7a and Fig. 7.7b show the velocity distribution the centre-plane of SSP05 and distanced 0.08 m from the centre ($Y = Y_{max}/3 [m]$). Figure 7.7c and Fig. 7.7d show the velocity distribution in the centre-plane of SSP03 and distanced 0.05 m from the centre ($Y = Y_{max}/3 [m]$). From a general point of view, it can be noticed that the velocity at the free-surface is increasing with the distance to the spillway crest, which is in line with previous research works (Bombardelli et al., 2010). At SSP05 and $Y = 0 m$ it can be observed a large vortex that occupies the entire step cavity on the steps 11 and 13. This represents a SK2 regime. At steps 10 and 12 the flow does not skim over the steps, but instead, it collides with the step tread creating a jump of water ahead forming a SK1 regime. At SSP05 and $Y = 0.08 m$, the flow regimes permutes and SK2 appears now on the even steps whereas SK1 occurs on odd steps. This last alternation system is also visible close to the side walls as shown in Fig. 7.9. The profiles measured at SSP03 do not show this alternating skimming flow pattern, neither longitudinally nor transversely (Fig. 7.7c-d). A regime SK1 found over the entire SSP03 structure is equivalent to the

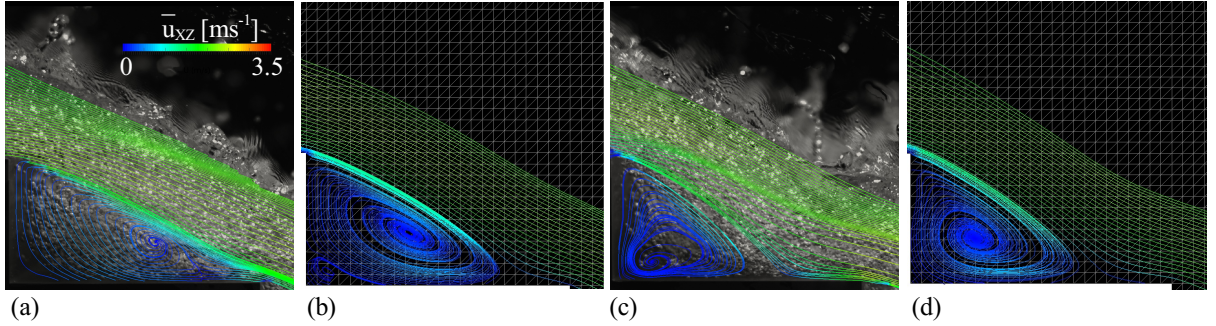


Figure 7.9: Flow velocities calculated at step 12 using: (a) BIV, (b) numeric; and at step 13 using: (c) BIV, (d) numeric of SSP05.

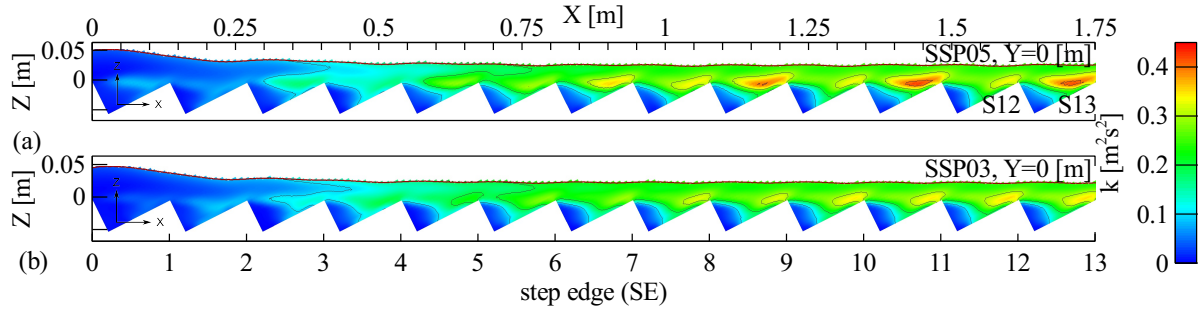


Figure 7.10: Modelled averaged turbulent kinetic energy at centre-line of stepped spillway: (a) SSP05 and (b) SSP03. X is the distance to the spillway crest and Z the vertical axis, perpendicular to the pseudo-bottom plane. The free-surface is represented by $\alpha = 0.5$. The contour lines delineate the categories shown in the label.

SK1 found in SSP05.

Felder and Chanson (2015a) showed a close agreement of several air-water flow properties for stepped spillways with different channel widths on top of the step edges. However, as can be seen in Fig. 7.8, most differences are found in the cavity of step niche and not on the free-stream flow. The velocity profile on top of the pseudo-bottom does not change substantially with the increase of channel width.

The turbulent kinetic energy (k) is mostly generated in the steps and in other parts of the flow through the velocity gradients. Numerical profiles show an increasing of k with distance to the spillway crest, which is in fact a result of the development of the boundary layer. At the first step, it is clear that the higher values of k are found at the step cavity and step edge. The higher value of k increases in direction to the free-surface reaching at the 5th step edge (self-aeration point) a value of $0.2 \text{ m}^2\text{s}^{-2}$. After the 7th step edge the value of k becomes roughly equal to $0.225 \text{ m}^2\text{s}^{-2}$, which is slightly higher than in step 5.

The velocity gradient is one of the most important reason for the high values of k . The occurrence of a SK2 regime on odd steps of SSP05 explains why the values of turbulent

kinetic energy are so high close to the step edges ($\approx 0.45 \text{ m}^2\text{s}^{-2}$). The water flow collides strongly on the end of the step and the vortex formed beneath is generated due to the transference of the energy from the free-stream flow. The vortex occupy all cavity and higher velocities are found when compared to SK1 regime (Fig. 7.7a). On even steps, the water has less momentum and collides on the base of the step. The slight peak of energy is due to the wake formed in the end of the step. Like velocity, the turbulent energy found on even steps of SSP05 is comparable to the pattern in SSP03. Different values of integral turbulent time and length scales were also found by (Felder and Chanson, 2015a) in the stream region of the flow for different channel widths.

7.8 Conclusions

In this work we investigated an alternating skimming flow regime (SK1 and SK2). The regime was observed when the spillway width was changed from 0.3 m to 0.5 m . The 0.5 m wide stepped spillway (SSP05) shows an alternated flow pattern which was not visible on a 0.3 m wide stepped spillway (SSP03). In the latter, the flow remained uniform along the longitudinal and transversal direction of the spillway. Both spillway numerical models were solved with a set of Navier-Stokes equations, together with SST k- ω turbulence model closure and VOF technique to detect the free-surface. The SSP05 model was validated using the free-surface elevation that was measured experimentally with an US. Numerical flow velocities close to the wall were validated using BIV.

The following conclusions can be retrieved from this work:

- The numerical model allowed to describe and explain the appearance of an unclassified alternating skimming flow pattern present in the SSP05 spillway;
- The alternating skimming flow observed in the wider spillway - SSP05 is characterised by (1) a SK1 regime at the even steps and a SK2 regime at odd steps at channel centre-line ($Y = 0 \text{ m}$), and (2) a flow pattern alternation lagged in one step near the side walls and $Y = Y_{max}/3 \text{ [m]}$. At SSP03 the flow regime is uniform at each step and followed a SK1 regime;
- The presence of the seesaw pattern of water depths was explained by the presence of a complex system of cross waves along the spillway. The water depth is higher in the intersection of these cross waves, and lower outside those intersections. This repetitive process lead to the formation of consecutive SK2 and SK1 regimes, and consequently to the seesaw pattern of flow properties, which had been observed in experimental installations (Yasuda and Chanson, 2003; Felder and Chanson, 2009);

- The presence of an alternating skimming flow is more evident at step cavities than in the free-stream flow (Fig. 7.8). In fact, the air-water flow properties measured on top of the pseudo-bottom and on top of step edges do not change deeply with the presence of the alternating skimming flow or with the channel width, as shown by Felder and Chanson (2015a);
- The experimental measurements of the flow depth showed an evident water volume increment after the 5th step, where the inception point occurred. The lowest water level value happened on step edge 5 at the centre-plane. Despite the uniform flow regime starting after the 12th step edge, the flow depth after the 8th step was nearly constant;
- The use of *interFoam* VOF solver together with SST k- ω turbulence approach from OpenFOAM® allowed the representation of the main vortex features of the flow field in the aerated and non-aerated flow region.

8

Explicit Calculation of Natural Aeration Using a Volume-of-Fluid Model

Abstract: Accurate prediction of the air-entrainment process in air-water two-phase turbulent flows is one of the most computationally challenging subjects under current investigation in hydraulic engineering. An ideal numerical model for air-entrainment needs to be accurate and fast in the definition of a macroscopic interface and simultaneously precise enough to take into account the formation of bubbles through the free-surface, their transport and their natural interactions: bubble-bubble and bubble-fluid. The problem is made more complex by the strong coupling between mesh and solution exhibited by interface capturing schemes which are commonly used for such problems. This paper examines numerical and modelling aspects of the entrainment process for two canonical cases; the 2D dam break and 3D circular plunging jet cases. We start by investigating the capacities of a VOF based model to detect the free-surface and predict the velocities inside the water phase, examining the effect of coarsening and refining the mesh on the prediction of the interface location. A reformulated explicit term is used to detect bubble formation and air-entrainment at the free-surface, without the need of a calibration process and adapted to run together with VOF models. The results obtained with this new approach are further compared with similar cases in the literature in terms of bubble formation and free-surface wave's amplitude. The correct definition of the free-surface was found to be strongly dependent on the mesh refinement in a way that has very significant implications for the development of air-entrainment modelling.

8.1 Introduction

Air-entrainment occurs in most turbulent free-surface flows in nature resulting in a dispersed two-phase flow below the surface with a complex turbulent mixture structure, where compressibility and density are important physical properties affecting the air-entrainment and transport characteristics. The accurate prediction of air-entrainment is a very ambitious goal for most CFD. The air-water interface is very unstable and the length scales of turbulence range from those influenced by the bubbles and surface tension (order from microns to millimetres) to those of the mean flow (order of meters). The simulations should be able to work on a coarse grid in order to simulate the mean flow behaviour, the free-surface position and all the similar Large-Length Scales (LLS), whilst at the same time being sufficiently detailed to model the transport of the bubbles of gas within the flowing fluid and simulate important phenomena as bubble formation, breakup, coalescence and collision, which take place on Small-Length Scales (SLS).

In CFD, VOF (Hirt and Nichols, 1981) and LS (Sethian, 1998) based models are typically used to capture the interface between two fluids, solving a single set of Navier-Stokes equations representing both air and water, together with an indicator function propagated by an advection equation. These interface models are widely used for many free-surface flows with macroscopic interfaces and LLS systems, as in vertical plunging jets (Kendil et al., 2010; Maiwald and Schwarze, 2011; Qu et al., 2011). Direct Numerical Simulations could simulate all aspects of the entrainment process right down to the subsequent dynamics of the bubbles; however this would be incredibly time-consuming and, in some cases, the application of VOF method to dispersed phases could lead to a non-physical interpretation of bubbles or droplets (Cerne et al., 2001). Instead, for a realistic mesh resolution the representation of the entrained air (SLS system) can be accomplished by the inclusion of an Eulerian dispersed phase model with a second set of equations representing the dynamics of the bubbles. Different approaches that follow this idea can be found in the literature. The model of Cerne et al. (2001) blends the VOF interface tracking with a two-fluid model formulation (Drew and Passman, 1998). In this model, in zones where the phase separation are clear and where just one fluid is present, the two-fluid model is switched off and a single set of Navier-Stokes equations together with the VOF method is solved instead. A criterion based on the local dispersion of the interface is used to switch between the two formulations, however, the accuracy of the results has exhibit a strong dependence on the value of this threshold which goes against the essence of a blending model. To overcome the dependency of the dispersion threshold, Yan and Che (2010) introduced a unified solution framework for coupling VOF with a two-fluid model. The idea was to blend the two formulations ensuring the conservation

of all three phases; i.e. when the LLS of air are present (phase2), the interface tracking model is activated; then when the LLS are absent from the cell, the two-phase model is used to solve for the local characteristics of the fluids (phase1 for water and phase3 for bubbles). The model shown to be efficient for the simulation of a rising bubble and a swarm of bubbles in a vertical pipe. However, volume fraction conservation when the three phases are present is not guaranteed, with particular losses occurring for phase2. Wardle and Weller (2013) introduced in OpenFOAM® a hybrid formulation based on the combination of an Eulerian multifluid framework (to solve the SLS) with an interface capturing method using VOF (to solve the LLS), along with a switching function based on the work of Cerne et al. (2001). Shonibare and Wardle (2015) extended this hybrid model to deal with variable bubble size using the reduced population balance method and applied it to a vertical plunging jet. A similar conceptual approach to the last was implemented by Marschall and Hinrichsen (2013) in OpenFOAM® for solely two-phase flows. Hänsch et al. (2012) extended the inhomogeneous MUSIG-approach by adding a continuous gas phase in order to solve simultaneously in the same domain, dispersed and continuous gas phases. The transition between the two was modelled by the "clustering method" that utilises an additional interfacial force applied to the Eulerian multifluid framework. The solutions were verified for the case of plunging jets. Yet another type of subgrid models combine an interface model (VOF/LS) with the two-phase flow formulation by including a source term to detect the air formation at the free-surface (Hirt, 2003; Ma et al., 2010, 2011b). Source terms at the interface relate the rate of bubble formation to surface flow properties such as local turbulence and the size of interface waves.

A typical experiment in which air-entrainment has been observed and extensively studied is the plunging jet (Abramovic, 1963; Baylar and Emiroglu, 2014; Biń, 1993; Chanson, 1997; Chanson et al., 2004; Kiger and Duncan, 2012; Rajaratnam, 1976; Sene, 1988). Plunging jets are efficient mechanisms to dissipate energy, and in doing so produce and transport significant quantities of bubbles through the body of the water. Practical examples of plunging jets include dam spillways and plunge pool stilling basins, wastewater treatment, oxygenation of bioreactors and river re-oxygenation. Air-entrainment in the pool depends upon the jet impact, the physical properties of air and water, the jet diameter, the free falling distance between the jet and the pool, and the jet turbulence. At the intersection point of the jet and the water, free-surface instabilities are the reason for air-entrainment when the jet impact velocity exceeds a characteristic velocity or onset velocity (Chanson, 1997). Slightly above the onset velocity, the air entrains in the form of individual bubbles and small pockets. At the impact point, the free-surface is observed to assume a shape which balances the forces between both sides of the interface. With increased liquid velocity at the jet impact zone, the local stress is increased, and small

cavities are formed and pulled below the free surface. Deeper into the pool, these cavities decrease in radius but continue balancing the surface forces. A critical condition is reached where either (a) a steady balance of forces can no longer be maintained or (b) the inferior end of the cavity or the free-surface is disrupted by disturbances at the free jet stream and/or on the pool. The result is the sequential generation of small bubbles or air pockets below the free surface. In this case, the rate of air-entrainment is very small and challenging to measure with common intrusive probes. At higher jet velocities, a substantial air pocket or sheath is formed at the periphery of the jet below the free surface; this air pocket is unstable and its breakup forms the entrained air bubbles which are then the subject of transport within the body of the water (Biñ, 1993).

This paper proposes a reformulated explicit term for bubble formation that is independent of calibrating factors by using a renewed formula for surface wave's amplitude. The explicit term was included in the well validated *interFoam* VOF solver from the OpenFOAM® toolkit to accurately predict the interface position (Leandro et al., 2014b; Lopes, 2013; Lopes et al., 2015b). An interface location coefficient is necessary for this coupling. This study represents a starting point for the development of a VOF-based model with a modelled closure to represent the entrained air. Section §8.2 develops the equations behind the numerical model along with the interface location technique and the air-entrainment term. Section §8.3 presents the results and their discussion for two canonical test cases; a 2D dam break case and a 3D plunging jet. Finally, section §8.4 presents conclusions.

8.2 Numerical model

8.2.1 General concepts

Interface capturing models such as the VOF model (implemented in the OpenFOAM® toolkit as *interFoam*) represent the free-surface dynamics of the two phases in terms of single phase-weighted velocity and pressure fields, governed by a single set of mass and momentum equations. For a system of isothermal, incompressible and immiscible two-phase flow, the Reynolds averaged equations for mass conservation and momentum are written in their conservative form:

$$\nabla \cdot \mathbf{U} = 0 \quad (8.1)$$

$$\frac{\partial \rho \mathbf{U}}{\partial t} + \nabla \cdot (\rho \mathbf{U} \mathbf{U}) = -\nabla p^* + \mathbf{g} \cdot \mathbf{x} \nabla \rho + \nabla \cdot \boldsymbol{\tau} + \mathbf{f} \quad (8.2)$$

where ρ ($kg\ m^{-3}$) is the fluid local density, \mathbf{g} ($m\ s^{-2}$) the gravitational acceleration,

\mathbf{U} ($m\ s^{-1}$) the velocity vector, $\boldsymbol{\tau}$ (Pa) the shear stress tensor, p^* (Pa) a modified pressure adopted by removing the hydrostatic pressure ($\rho g \cdot \mathbf{x}$) from the total pressure and \mathbf{f} ($kg\ m^{-2}s^{-2}$) the volumetric surface tension force. It is important to note that in interface capturing models, the velocity vector \mathbf{U} acts as a shared velocity of the two fluids, i.e. $\mathbf{U} = \mathbf{U}_{f1} = \mathbf{U}_{f2}$, rather than in mixture models where $\mathbf{U}_{fk}, k = \{1, 2\}$ can assume different magnitudes.

The decomposition of the viscous stress term is given by the Stokes's stress constitutive equation [Eq. (8.3)] where μ ($kg\ m^{-1}s^{-2}$) is the dynamic viscosity.

$$\nabla \cdot \boldsymbol{\tau} = \nabla \cdot [\mu(\nabla \mathbf{U} + (\nabla \mathbf{U})^T)] = \nabla \cdot (\mu \nabla \mathbf{U}) + (\nabla \mathbf{U}) \cdot \nabla \mu \quad (8.3)$$

Together with the previous equations, *interFoam* uses the VOF technique (Hirt and Nichols, 1981) to capture the interface between the two fluids by solving a transport/advection equation [Eq. (8.4)]. Basically, at each cell of the domain we define an alpha (α) value representing the fraction of the volume of the fluid in that cell (Carvalho et al., 2008; Ubbink, 1997). Cells completely filled with fluid 1 ($f1$) will be represented by $\alpha = 1$ and cells filled with fluid 2 ($f2$), by a value $\alpha = 0$. The interface is localised to the cells where α is intermediate between these two values. The advection equation also includes an interfacial compressive term to confine this interface region into as small a region of space as possible (the last term on the l.h.s. of Eq. (8.4)) (Berberović et al., 2009; Weller, 2008), rather than using interface reconstruction schemes (Rider and Kothe, 1997).

$$\frac{\partial \alpha}{\partial t} + \nabla \cdot (\alpha \mathbf{U}) + \nabla \cdot [\mathbf{U}_c \alpha (1 - \alpha)] = 0 \quad (8.4)$$

The term $\alpha(1 - \alpha)$ ensures that the compressive term is calculated just at the interfacial cells of the domain, while C_α is a binary coefficient that activates ($C_\alpha = 1$) or deactivates ($C_\alpha = 0$) the interface sharpening term. The source term also includes the compressive velocity (\mathbf{U}_c) that acts as a velocity perpendicular to the interface and is written as:

$$\mathbf{U}_c = C_\alpha |\mathbf{U}| \frac{\nabla \alpha}{|\nabla \alpha|} \quad (8.5)$$

It is worth emphasising that the interface is merely being localised within the volume of space for which $0 < \alpha < 1$. For simplicity it is often taken that the interface is represented in post-processing by the isosurface $\alpha = 0.5$, but strictly speaking this is simply an assumption, one which we wish to explore in the present work.

When α assumes values between 0 and 1, the physical properties of the two-fluid mixture are defined as a weighted average of two fluid properties:

$$\rho = \alpha \rho_{f1} + (1 - \alpha) \rho_{f2} \quad (8.6)$$

$$\mu = \alpha \mu_{f1} + (1 - \alpha) \mu_{f2} \quad (8.7)$$

The volumetric surface force function is explicitly estimated by the CSF model [Eq. (8.8)] developed by Brackbill et al. (1991) where σ ($kg\ s^{-2}$) is the surface tension and κ (m^{-1}) is the surface curvature calculated as $\kappa = \nabla \cdot (\nabla \alpha / |\nabla \alpha|)$.

$$\mathbf{f} = \sigma \kappa \nabla \alpha \quad (8.8)$$

The turbulent kinetic energy (k) and rate of energy dissipation (ε) are calculated using the realizable $k - \varepsilon$ turbulence model, with the effective dynamic viscosity (μ) being given by a sum of molecular viscosity (ν) and turbulent viscosity (ν_t) ($\mu = \rho(\nu_t + \nu)$). The choice of the realizable $k - \varepsilon$ is based on its known ability to accurately predict the spreading rate of both planar and round jets (Fluent Inc., 2006; Yeoh and Tu, 2010). This turbulent model is also superior to the standard $k - \varepsilon$ model for the simulation of flows involving rotation, boundary layers under strong pressure gradients, separation and recirculation. The realizable $k - \varepsilon$ also requires less computational time than RNG $k - \varepsilon$ which was derived to deal with the swirl effect on turbulence (Fluent Inc., 2006).

8.2.2 Bubble formation

The air-entrainment process is described by the inclusion of a function E_g ($m^{-3}s^{-1}$) which describes the rate of bubble generation at the free-surface. It is calculated at the end of each time-step and does not change any convergence process within the standard solver. The formulation of this variable follows closely the work of Ma et al. (2011b), who represent it as:

$$E_g = \left\langle \frac{\partial \mathbf{U}_n}{\partial n} \right\rangle \frac{a}{\phi_{ent} V_g} \quad (8.9)$$

where \mathbf{U}_n is the normal velocity component to the free-surface, a (m) is the amplitude of the cavities formed at the free-surface (Fig. 8.1), V_g (m^3) is the volume of a sphere calculated assuming an averaged bubble diameter and ϕ_{ent} (m) is the interface thickness, given by $\phi_{ent} = 0.05L$, where L (m) is a characteristic linear dimension (equal to the pipe diameter for pipe flow or the hydraulic diameter when dealing with river systems). The symbols $\langle \rangle$ are used to turn the normal derivative zero if its value is less than zero:

$$\langle f(x) \rangle = \begin{cases} f(x) & , f(x) > 0 \\ 0 & , f(x) \leq 0 \end{cases} \quad (8.10)$$

A rough way to predict the volume fraction occupied by the bubble phase at each cell can be done by $E_{g,frac} = E_g V_g \Delta t$, where Δt (s) is the computational time step. This neglects the advection and diffusion terms of the void fraction conservation and transport at the free-surface, however, when the velocities are small, it can provide a good first impression of void fraction magnitude.

In this work and according to Ervine and Falvey (1987), the amplitude of the surface disturbances (a) is considered as having the same order of magnitude as the radius of the turbulent eddies at the free-surface (l'). From here, we obtain:

$$a = l'/2 = C_\mu^{3/4} \frac{k^{3/2}}{2\varepsilon} \quad (8.11)$$

where C_μ is a turbulence model constant which in the $k - \varepsilon$ model theory assumes the value 0.09 (Pope, 2000; Versteeg and Malalasekera, 1995). Similar criteria is used by Hirt (2003) to calculate surface disturbances at free-surface in the CFD commercial code Flow-3D®. In the model of Ma et al. (2011b), the amplitude of the surface disturbances (a) is calculated as $a = C_{ent} k/g$, where C_{ent} is a constant that needs to be calibrated for each case.

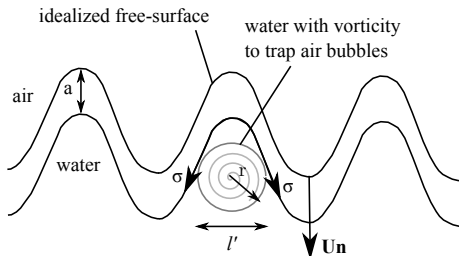


Figure 8.1: Free-surface with physical parameters used. Adapted from Ervine and Falvey (1987).

8.2.3 Interface location

The location of the air-entrainment in our VOF model does not follow the same criteria as in work from Ma et al. (2011b) (which uses LS methods). In LS, the interface can either be located by assuming a certain threshold for interface thickness, or by limiting the velocity to some threshold value. However, in VOF models, the interfacial structure can only be detected by the change of volume fraction or by its gradient, as for example in the

the algebraic equation formulated by Hänsch et al. (2012). In this work, E_g is calculated using a similar criterion as used for the compressive term, i.e. by multiplying the last by the function $\phi_{FS} = 4\alpha(1 - \alpha)$. This will work as a masking function, which returns 0 when calculated in cells away from the free-surface and 1 at the interface. From the fact that this coefficient uses α to detect the free-surface, it is fairly essential keep the interface confined to a small number of cells possible, and from this we see the need of a mesh dependence study.

8.3 Results: example cases

8.3.1 2D Dam-break

The example presented here is the benchmarking 2D dam-break case without obstacle. This case is used by many other authors to show the capabilities of free-surface models and of interest for this work as it can exhibit several possible zones of natural aeration of the flow and the interface location. A static water column is initially held against the left wall by a vertical gate as shown in Fig. 8.2. On removing the gate, the water column collapses and the resulting slosh hits the right wall before returning in the form of a small propagating wave.

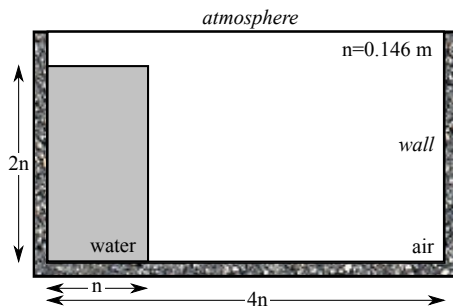


Figure 8.2: 2D dam-break domain.

Numerical simulations are performed in four different meshes: 16×16 , 32×32 , 46×46 and 64×64 cells. The fluid properties were chosen to represent the physical values of water and air at 15°C . Surface tension is set to 0.072 kg s^{-2} , the averaged bubble radius (r_b) is 0.002 m and $\phi_{ent} = 0.05n = 0.0071 \text{ m}$, where n stands for the water column width (Fig. 8.2). The domain is bounded by walls with the exception of the top one that represents the atmosphere. The pressure at the walls is given by Neumann BC, whilst the velocity is set to no-slip (Dirichet-BC).

Figure 8.3 presents snapshots of the free-surface position for $t = 0.1, 0.3, 0.7$ and 1.0 s for finer mesh. Figure 8.3a shows the ϕ_{FS} function and Fig. 8.3b the values of the terms

E_g and $E_{g,frac}$. Figure 8.4 demonstrates the influence of changing the mesh size on the free-surface position for $t = 0.8 s$. Again, Fig. 8.4a shows the ϕ_{FS} function and Fig. 8.4b the values of the terms E_g and $E_{g,frac}$.

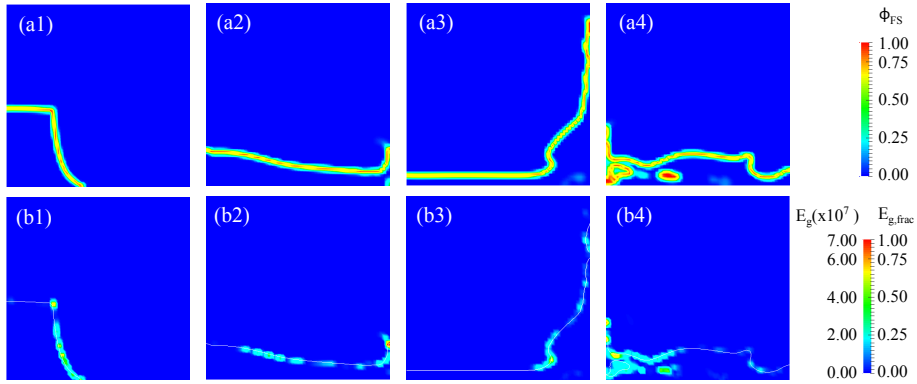


Figure 8.3: Dam-break process for the time steps $t = 0.1, 0.3, 0.7$ and $1.0s$ using the finest mesh (64×64 cells). Top images are photographs of the experiment, middle figures (a) show the function to detect the free-surface position (ϕ_{FS}) and bottom figures (b) show the bubble formation term (E_g) and its volume fraction on the cells ($E_{g,frac}$).

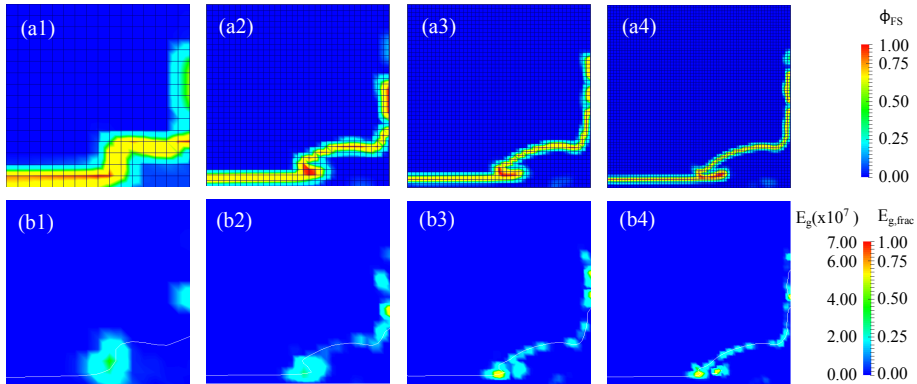


Figure 8.4: Mesh influence study of dam-break case at $t = 0.8s$. From the left to right the meshes are: 16×16 , 32×32 , 46×46 and 64×64 cells. Top figures (a) show the function to detect the free-surface position (ϕ_{FS}) and bottom figures (b) show the bubble formation term (E_g) and its volume fraction on the cells ($E_{g,frac}$).

The function used to detect the free-surface has demonstrated excellent accuracy throughout the simulation time even when a large cavity is formed inside the fluid (Fig. 8.3a4). One second after the collapse of the water column (Fig. 8.3b1), due to the friction with the bottom wall, air is forced to enter from the bottom, where the term E_g assumes high values. High values of air-entrainment can also be seen in the zone where the water collides with the right wall (Fig. 8.3b2) and on its way back in the area where a small cavity of the breaking wave is formed (Fig. 8.3b3). The mesh influence study show

a large difference between meshes 16×16 and 32×32 cells both for ϕ_{FS} and E_g values. The free-surface in the last three finer meshes have a similar shape, whereas the maximum values of E_g are on the order of 4×10^7 in the mesh with 32×32 cells (Fig. 8.4b2) and of the order of 5×10^7 for 46×46 and 64×64 cells (Fig. 8.4b3 and Fig. 8.4b4). This shows that, even with the decreasing of the mesh size, the values of E_g are quasi mesh independent, although its spacial location is sensible to the grid size.

8.3.2 3D vertical plunging jet

The **ed!** (**ed!**) computational domain represents a part of the experimental apparatus used by Chanson and Manasseh (2003), schematically represented in Fig. 8.5. This experimental work provides extensive data on void fraction and bubble count rate inside the water, which despite not being relevant in this work, will be useful to compare the results when a full air-entrainment model is completed. The simulation of a 3D domain rather than a 2D domain allows us to better represent all the flow structures across the interface which are manifestly 3D structures. Also, comparisons to the 3D model of Ma et al. (2010) in terms of E_g values and later for void fractions can be done clearly and without constraints (note that Ma et al. (2010) applied their model to the same case in their study).

A plunging jet of clean water is ejected from a $d_0 = 0.025\text{ m}$ diameter nozzle, into a pool of stationary water. The distance between the water surface and the nozzle is constant and equal to $x_1 - x_0 = 0.1\text{ m}$. The impact velocity of the jet at the pool is $U_1 = 3.5\text{ m s}^{-1}$. Velocity profiles are obtained at different horizontal planes from $0.8d_1\text{ (m)}$ to $10.0d_1\text{ (m)}$ below the initial pool free-surface, where d_1 is the jet diameter at the impact zone ($d_1 \approx 0.024\text{ m}$) and r_1 the jet radius ($r_1 \approx 0.012\text{ m}$). To investigate the impact of mesh resolution on the solution, three different grids with different mesh resolutions were generated and their characteristics summarized in Table 8.1. In order to decrease the computational time, instead of using spatially uniform meshes, three zones with different grid sizes are created as defined in Fig. 8.5.

The initial conditions are set as represented in Fig. 8.5. The pool is filled with stationary water ($U = 0\text{ m s}^{-1}$) to a constant depth. A cylindrical column of water with a fixed inlet velocity is used to represent the jet. In order to get fast convergence of the solution and computational stability the air velocity in the vicinity of the jet is set equal to the jet velocity. Four different BC are used in this simulation as shown in Fig. 8.5. The velocity at the *inlet* is calculated based on the jet impact velocity using Bernoulli's principle, $U_0 = \sqrt{U_1^2 - 2g(x_1 - x_0)} = 3.21\text{ m s}^{-1}$. The *atmosphere* just allows the air to leave the domain by setting U as dependent on pressure with total pressure set as zero. The *lateral* boundaries have Neumann-BC for α, p equal to hydrostatic pressure and

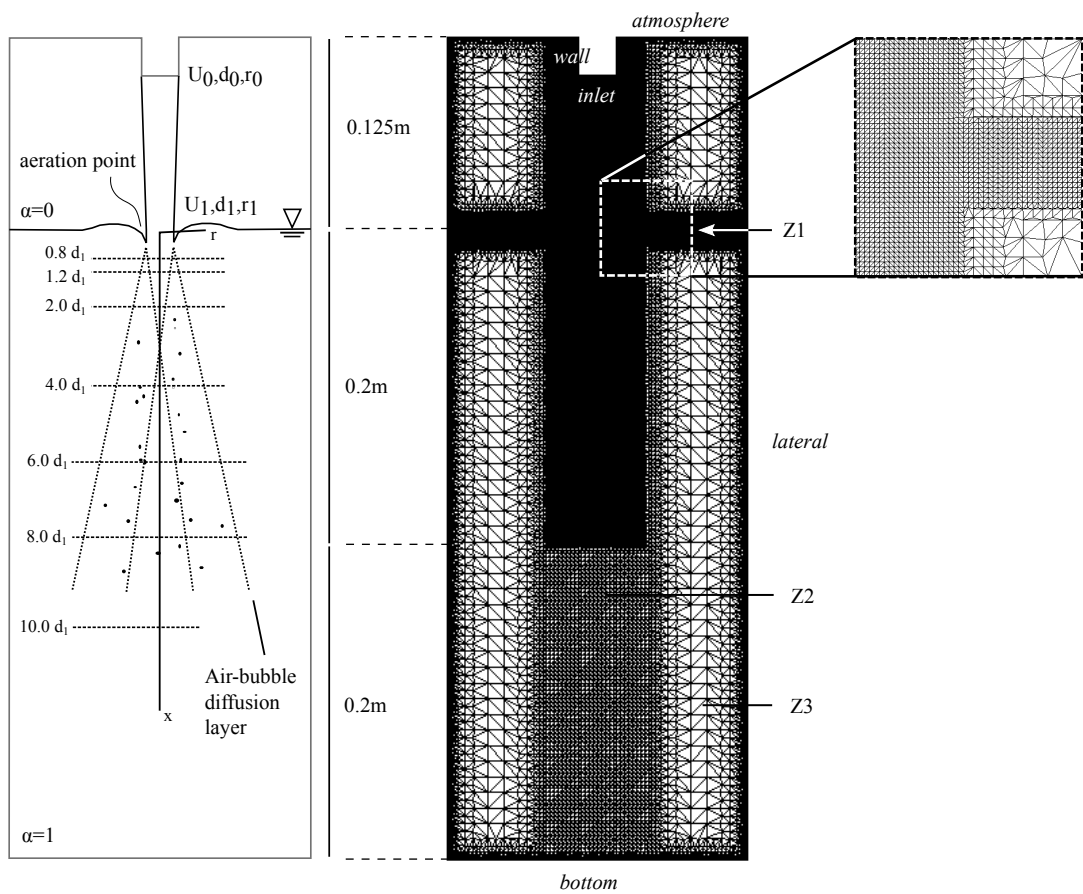


Figure 8.5: Vertically-centred slice of the computational domain for the 3D circular plunging jet problem. The mesh presented corresponds to G0.00125 (Table 8.1).

Table 8.1: Grid characteristics to demonstrate the mesh dependency. Zones $Z1$, $Z2$ and $Z3$ are represented in Fig. 8.5. *In this case, cells with 0.0008 m edges were placed just on the intersection between jet and pool.

	cell length, Δx (m)			N.Cells	N.Proc.	Time (s)
	jet and surface ($Z1$)	centre-bottom ($Z2$)	lateral ($Z3$)			
Coarse grid ($G0.005$)	0.005	0.005	0.005	84 192	16	1 963
Medium grid ($G0.0025$)	0.0025	0.0025	0.005	521 124	16	39 891
Fine grid ($G0.00125$)	0.00125	0.0025	0.005	2 104 460	16	281 073
Finnest grid ($G0.0008$)	0.0008 - 0.00125*	0.0025	0.005	2 458 835	32	284 242

non-slip Dirichet-BC for U . For the *bottom* boundary the hydrostatic pressure is set to $\rho f_1 g(x_{bottom} - x_1) = 3915.2\text{ Pa}$ and Neumann-BC are used for the remaining variables. In order to verify the correct application of these boundary condition, we simulated with the coarser mesh the full experimental domain and verified that the results in terms of U , p and α in the zone close to the jet agreed with those calculated on the smaller domain.

The k , ε and ν_t variables at the *inlet* are calculated by:

$$k_0 = \frac{3}{2}(U_0 I_0)^2 = 0.000235\text{ }m^2 s^{-2} \quad (8.12)$$

$$\varepsilon_0 = C_\mu \frac{k_0^{3/2}}{l_0} = 0.000371\text{ }m^2 s^{-3} \quad (8.13)$$

$$\nu_{t,0} = C_\mu \frac{k_0^2}{\varepsilon_0} = 1.3416 \times 10^{-5}\text{ }m^2 s^{-1} \quad (8.14)$$

where U_0 (m s^{-1}) is the mean flow velocity at jet inlet; I_0 (%) the turbulent intensity at jet inlet, set as 0.39 % (value from the experiment of Chanson and Manasseh (2003)) and l_0 (m) the length scale at jet inlet, in this study calculated as $l_0 = 0.035 d_0$ (m). On the remaining boundaries k_0 , ε_0 and $\nu_{t,0}$ are defined as Dirichlet-BC. The fluid properties were chosen based on the physical values of water and air at 15°C. Surface tension is set to 0.072 kg s^{-2} , bubble radius (r_b) is 0.00175 m and $\phi_{ent} = 0.0012\text{ m}$. The simulation ran with the extra term activated from the beginning. A steady-state solution was acquired

after 6500 time iterations with an averaging time step of 0.0001 s for the simulation with coarser mesh, which gives a final time of about 0.65 s . This state was identified from the criteria that the residuals of k , ε and p , and the volume fraction on the domain were constant in time. The averaged values from the last 0.1 s were used to plot the results. Maximum Courant number and maximum Courant for α are both defined to 0.5.

8.3.2.1 Radial velocity profiles

The liquid velocity plays a key role in the transport of bubbles into the fluid. This therefore represents a good variable with which we can validate the solution and demonstrate grid independence. In order to prove this, in this section, the computed radial distribution of liquid velocity is presented. Figure 8.6 shows the dimensionless radial velocity profiles (U/U_1) on the pool depths of $x = 0.8d_1$, $1.2d_1$ and $2.0d_1$ for the four meshes presented. These three profiles were chosen here because these were the positions where Chanson and Manasseh (2003) measured experimentally the air concentration profiles.

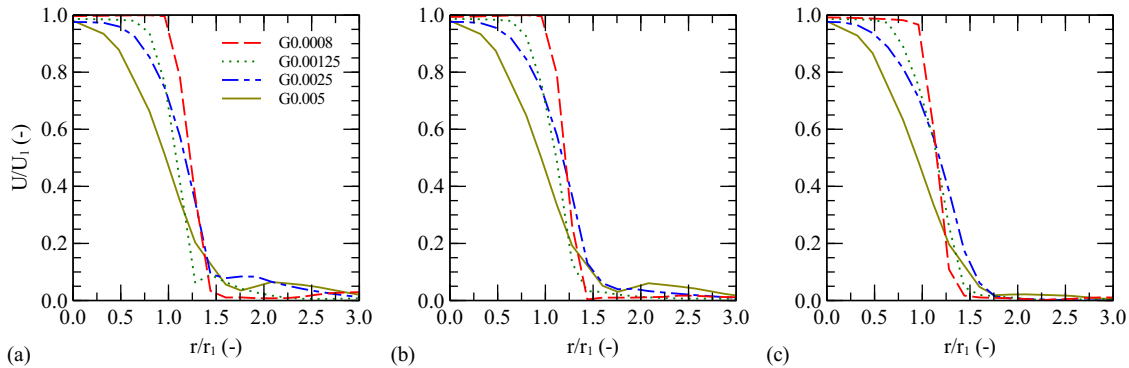


Figure 8.6: Liquid velocity for pool depths (a) $x = 0.8d_1\text{ (m)}$, (b) $x = 1.2d_1\text{ (m)}$ and (c) $x = 2.0d_1\text{ (m)}$. $U_1 = 3.5\text{ m s}^{-1}$, $d_1 = 0.024\text{ m}$ and $r_1 = 0.012\text{ m}$.

From the data in Fig. 8.6, it can be seen that the velocity has the maximum value at the jet centreline and tends to zero away from the centre. For a free jet in air, the greater the distance from the jet inlet, the lower and wider the velocity profile becomes, eventually assuming the universal shape of a Gaussian curve (McKeogh and Irvine, 1981). However, for a jet impacting a pool it is also known that the profiles closer to jet impact zone are affected by the abrupt decreasing of the velocity from its maximum value to zero. This situation is clearly visible in the results of the finer mesh (Fig. 8.6). The velocity on the jet axis was equal to 3.5 m s^{-1} ($U/U_1 = 1.0$), and this value remained constant until a distance equal to the radius of the jet. After reaching a distance of $1.0r/r_1$, the velocity passed from this maximum to roughly zero in about $0.25r/r_1$. On the coarser meshes, numerical viscosity smooths the profile; the axis velocity remains correct and the

curves tends to zero velocity at similar values of $r/r_1 \approx 1.5$, but the shape of the curve between these extremes is significantly affected, with a smoother shape for the coarser meshes indicating a reduction of velocity inside the jet ($r/r_1 < 1.0$). On the finest mesh the jet flow remains as a plug flow and the variation in velocity is restricted to the air region around it. From these results we can also assume that we reach a mesh independent solution for the grid with $\Delta x = 0.0008 \text{ m}$.

More interesting results are obtained when the profiles are plotted in a different dimensionless form. In a developed flow region the curve must present an self-similar shape in all the sections and it can be compared with the solutions of Wilcox (Wilcox, 1993)(Fig. 8.7a) and Tollmien (Abramovic, 1963; Rajaratnam, 1976)(Fig. 8.7b). On both, the local velocity U is divided by the velocity on the jet axis U_x . The radial distance r is rendered dimensionless by dividing it by the vertical distance x for Wilcox profile and by dividing r by b for Tollmien solution, where b represents the value of r where the velocity is half of the velocity on the jet axis. Note that in a developing flow region $U_x = U_1$.

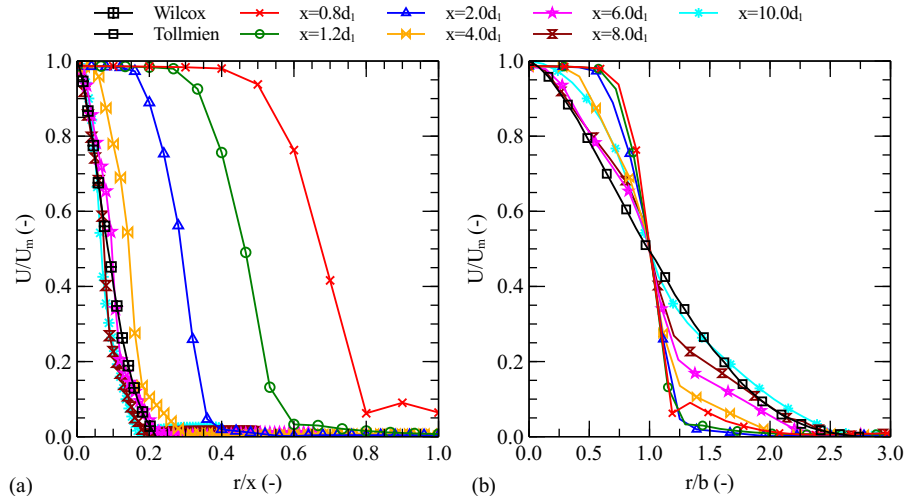


Figure 8.7: Liquid velocity profiles for some horizontal profiles along the pool depth ($x = 0.8d_1$ to $10.0d_1$). U_x is the velocity on the jet axis, x is the vertical direction and b the value of r where the velocity is half of the velocity on the jet axis. The profiles are compared with the solutions of (a) Wilcox and (b) Tollmien using mesh G0.0008

Figure 8.7 presents the fluid velocity profiles for horizontal profiles at distances $x = 0.8d_1$ to $x = 10.0d_1$ from the beginning of jet impact zone and the comparison with the solutions of Wilcox and Tollmien using mesh G0.0008. Since these solutions were derived to predict the velocities in the fully developed flow region (Abramovic, 1963), we must keep in mind that they will not necessarily correctly predict the flow at the jet beginning, and this is indeed what we find. From the analysis of Fig. 8.7a and Fig. 8.7b it can be noted that the

profiles are converging to a self-similar solution, however, the first three profiles are quite a long way away from the fully developed solution, indicating that those are within the developing flow region and can not be used as a comparison. The true convergence and self-similarity was achieved slightly after $4.0d_1$, as is better shown in Fig. 8.7a. The profile at $x = 10.0d_1$ is shown not to converge on the approximation to the Tollmien solution at distances to the axis of the jet lower than $1.0r/b$ (Fig. 8.7b). At this depth the mesh is coarser and consequently the results are less accurate. The velocities plotted at profiles $x = 0.8d_1$ to $8.0d_1$ were evaluated in the refinement zone $Z1 - Z2$, whereas $10.0d_1$ were evaluated further down in the zone just covered by the refinement $Z2$ (Fig. 8.1).

8.3.2.2 Free-surface detection and bubble formation

The dependence of the free-surface location on the α value and on the mesh refinement is shown in Fig. 8.8. Figure 8.8a shows the variation of the free-surface shape with α values on the finest mesh ($G0.0008$). Figure 8.8b shows the free-surface for different meshes keeping the value of alpha constant to 0.3.

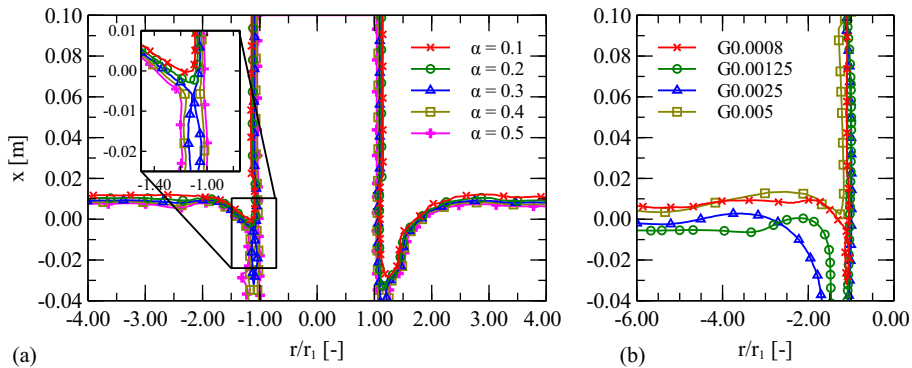


Figure 8.8: Temporal-averaged free-surface and air-cavity determined by: (a) keeping the finer mesh ($G0.0008$) and changing α value and (b) keeping $\alpha = 0.3$ and changing the mesh refinement. The x (m) axis is the vertical direction and r_1 (m) the jet radius at impact zone ($r_1 = 0.012$ m).

In a VOF simulation, the value of α that correctly represents the interface is not clearly defined; the interface is instead captured in the values between 0 and 1. Although some authors use a value of 0.5, the appropriate value should be subject of an analysis depending on the case under consideration. The α isosurface is strongly influenced by turbulence at the free-surface and by what value of α we wish to consider as a threshold for the interface. Figure 8.8 shows the temporally averaged shape of the free-surface and the air cavity for various values of α . The overall shape of the free-surface (Fig. 8.8a) seems insensitive to the value of α used, however the cavity shape increases substantially in volume with

increasing values of α . In fact, the interface fluctuations are higher in the air-cavities of the jet than in the remaining free-surface, making the value of α much more important in those regions.

Figure 8.8b presents the shape of the interface for the different levels of mesh refinement. The lack of cells in the coarser mesh produces a smoother connection between the pool free-surface and the jet, and neglects the creation of air cavities. In the other hand, the medium and fine mesh are able to generate and detect the cavities, however due to the lack of mesh resolution to calculate correctly the forces acting on the interface, the air cavity may not be formed correctly and closed, although we can see on the fine grid a smaller gap between the jet and the surface. At the end, the finest mesh has sufficient resolution to generate and close the cavities.

The effect of changing the mesh resolution is highly significant for the overall modelling of the entrainment process. As mentioned in the introduction, the whole entrainment process could be simulated by resolving the free-surface all the way to the scale of the entrained bubbles, however doing so would be phenomenally expensive and inappropriate for an engineering simulation. A more cost-effective approach would be to model the large scale shape of the free-surface on a relatively coarse mesh, with modelled entrainment into an Eulerian two-fluid model representing the statistical propagation of subgrid scale entrained bubbles. Technically speaking, for the Eulerian two-fluid model to work the bubble size should be substantially smaller than the cell size; however since the process of air-entrainment is a continuous one which is having to be truncated at some intermediate scale, it is likely that this constraint is being violated at some point.

The function E_g , representing the number of bubbles formed at the free-surface, is also presented in this section. Figure 8.9 shows the time-averaged values of E_g for the four meshes used and the free-surface position, delimited by ϕ_{FS} isolines of 0.1, 0.5 and 0.9. As mentioned before, a sharp interface is very important in order not to spread the E_g term over a large number of cells. In the first instance, observing Fig. 8.9, just the meshes $G0.0008$ and $G0.00125$ show E_g values calculated at the intersection of the jet with the pool, which is indeed the position where bubble formation was observed experimentally. However, our concern is also about the accuracy of E_g , and in these terms, $G0.0008$ mesh generates closest values when compared with the work of Ma et al. (2011b) and a more precise location of the zone of aeration – it can be noticed the generation of bubbles exactly inside of the air cavity, whereas in remaining meshes, E_g is spread all over the free-surface.

Figure 8.10 shows the comparison between the values of free-surface wave amplitude (a) using (a) the formulation of Ma et al. (2011b) and (b) the concept proposed in the current paper. Around the jet impact zone and inside the air cavity, the values are reasonably similar in both cases ($a \approx 0.001\text{ m}$). These places, out of all the area occupied by the

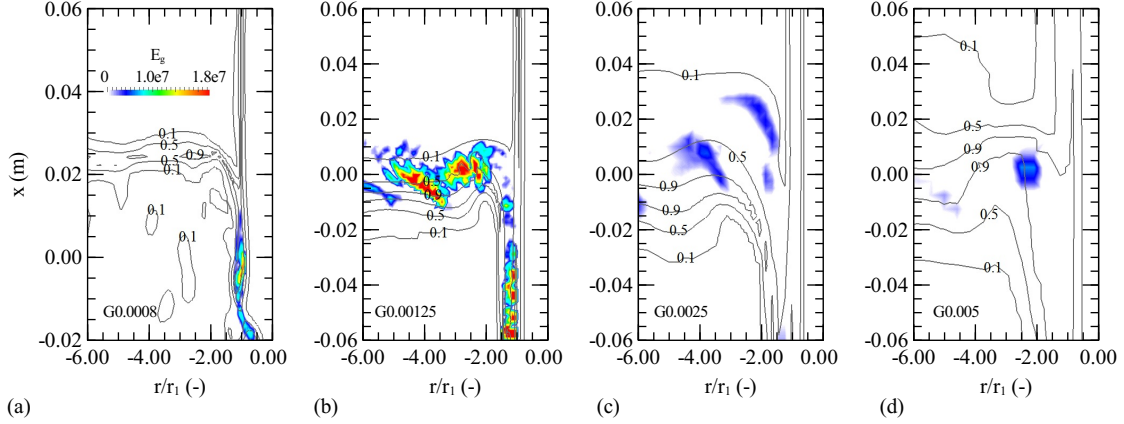


Figure 8.9: 2D centre-slice profiles of the free-surface and bubble formation term using the meshes: (a) $G0.0008$, (b) $G0.00125$, (c) $G0.0025$ and (d) $G0.005$. Isolines correspond to $\phi_{FS} = 0.1, 0.5$ and 0.9 . The axis x is the vertical direction and r_1 the jet radius at impact zone ($r_1 = 0.012\text{ m}$).

free-surface, are exactly the zones where the comparison should be made. The differences found at the centre of the jet has no importance for the calculation of E_g term and can be ignored.

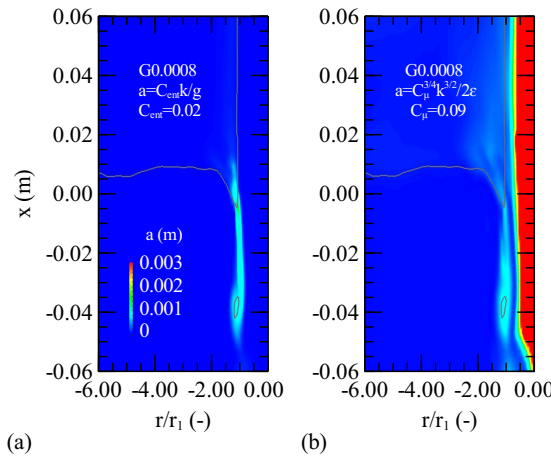


Figure 8.10: Comparison between the value of free-surface wave amplitude (a) using (a) the formulation of Ma et al. (2011b) and (b) the concept proposed in this paper. The location of the free-surface is represented by $\alpha = 0.3$.

8.4 Conclusions

The present work attempts to numerically simulate air entrainment in two canonical cases; a 2D dam break and 3D circular plunging jet using CFD. We investigate the interplay of numerical factors such as mesh resolution with the modelling processes of surface capturing and entrainment modelling. The VOF interface model as implemented in the code *interFoam* from the open-source OpenFOAM® toolkit was used to reproduce the interface between the water and air. In addition, an explicit term for air-entrainment detection was adapted to run with VOF models without a need of a calibration process. This was done by implementing a factor for free-surface detection and new concept of surface wave's amplitude based on the turbulent length scales.

The 2D dam break case was used to ascertain the influence of mesh size in the definition of free-surface position and aeration zone. The magnitude of air-entrainment term does not suffer much variation with the grid size, which let us believe that the new concept for wave's amplitude also improved the model on its independence of mesh size. The free-surface position is in contrast, much more sensible to the grid size and consequently a responsible to the accuracy of the aeration zone.

In the case of the 3D plunging jet, the free-surface shape was plotted using different mesh refinements and alpha values. The mesh refinement is shown to significantly affect the definition of the air cavities. The radial liquid velocity in the fully developed zone of the jet was found to be in reasonable agreement with analytical solution found on the literature. The term E_g for bubble formation reaches its maximum value in the intersection between the free-surface and the jet interface. This result is in agreement with visual descriptions of the air-entrainment process found in the literature. The term was successfully adapted to run within VOF based models and to be independent of user-calibration, by setting the free-surface wave's amplitude to be equal to the radius of the turbulent length scales. The results shown here prove that we might be optimistic about the applicability of this new concept, however, some other test cases are needed to validate the data as well as the conclusion of the air-entrainment model to compare the values of transported air.

9

Flow Self-aeration Using a Sub-grid Volume-of-Fluid Model

Abstract: The accurate prediction of self-aerated flow is not always easy to obtain particularly if the computational performance is the main concern. Two-fluid formulation is suitable to simulate in a fine mesh the dispersed air in a continuous water phase (e.g. bubbly flows) whereas the interface tracking methods are used for sharp interfaces when two continuous and contiguous phases are presented (e.g. free-surface flows). Several approaches have emerged to combine both methods, however all found a gap in the transition between resolved and unresolved scales of air at the interface. Including a source term that predicts the self-aeration process is viewed as a promising step to overcome such difficulty. In this work we use a VOF formulation to detect the air/water interface and a advection-diffusion equation connected to a source of air at the free-surface to simulate the dispersed bubble phase. One-way coupling and two-way coupling versions of this model are test along with sensitivity tests to show the accuracy of the new source term that does not require calibration. The location of the aeration is analysed and investigated. Results are obtained in terms of free-surface flow depths, air-concentration profiles and velocity fields and compared to experimental data acquired in a scaled stepped spillway model with good agreement.

9.1 Introduction

Flow self-aeration is a phenomena by which the air entrains naturally in form of bubbles into the water. In nature this process can be found in waterfalls, turbulent rivers or coastal waves, with significant importance to the equilibrium oxygen/carbon dioxide in the water. In industrial processes, the aeration is rather forced by impinging water jets to increase the amount of oxygen and treat waste water. The flow self-aeration has also implications in engineering design as the case of spillways where the entrained air may cause problems of cavitation and unsigned increments of flow depth; or in ship hydrodynamics, due to its implication for stealth capabilities, drag reduction and ship customization.

Numerical prediction of flow self-aeration has attained crescent attention in last years, however it is still an ambitious goal for most solvers and numerical codes. The main concern is the need for a sufficient fine mesh to solve the small length scales as free-surface fluctuations, surface tension forces and physical processes of bubble formation, breakup, coalescence and collision (order of millimetres and microns), and simultaneously the large length scales of turbulence from the mean flow structure (order of metres). In case of air-entrainment modelling, DNS and LES are not feasible due to the large number of cells involved to simulate the smallest scales. In Deshpande et al. (2012), the simulation of the finer mesh took 2 734 CPU hours to compute 1 s from the 14 s ran in total. By using RAS the smallest scales are here approximated instead of solved, which reduces the number of cells and thus its ability to describe air-entrainment.

To detect the free-surface position, interface capturing methods as VOF or LS are consistently used. Together with a single set of RANS equations, these methods introduce an advection equation to predict the shape and interface position, either by an indicator constant or a function. Qu et al. (2011) compared the LS method with a mixture model to simulate the case of a liquid water jet plunging in a pool. Jet instabilities and deformations, and maximum velocities at jet centre-line were better detected by the interface capturing LS method. As expected, air-concentration values were underestimated, specially the definition of the peak value in both models.

Due to the difficulty of solving air-entrainment process and the range of scales, different approaches have been tested. One of the first attempts is the model of Cerne et al. (2001) where VOF interface tracking was blended with a two-fluid model formulation. In zones where just one fluid is present or the interface is clearly defined, the two-fluid formulation is turned into a single set of RANS equations together with the VOF method for free-surface detection. A criterion based on the local dispersion of the interface is used to switch between the two formulations, unfortunately with a strong dependence on the value of this threshold. To overcome this dependency, Yan and Che (2010) introduced a unified solution

framework by ensuring the conservation of three fluid-phases, namely continuous water and air phase and dispersed gas. A special treatment called "volume fraction redistribution" is used to deal with the cells containing both small and large length scale interfaces. The VOF model is activated if the continuous air phase fills completely the volume of the cell. In remaining cases, the two-phase model is used to solve the local characteristics of the fluids (continuous water and dispersed air). Volume fraction conservation of the continuous water phase and dispersed air phase was not guaranteed when the three phases were present. Hänsch et al. (2012) extended the inhomogeneous MUSIG presented in *ANSYS CFX* by adding a continuous gas phase in order to solve simultaneously dispersed and continuous gas phases. The transition between dispersed to continuous gas regions was assured by the "clustering method" that works as an additional interfacial force to Eulerian multifield framework. The solutions were verified in a case of plunging jets and 2D dam break case (Hänsch et al., 2014). Wardle and Weller (2013) introduced in OpenFOAM® an hybrid formulation given by the combination of an Eulerian multifluid framework with VOF method using a dynamic switching in the interface sharpening term. Solver capability was tested in various examples including liquid-liquid-air simulations in which a sharp interface is maintained between each liquid and air, whereas liquid-liquid iterations were done using the dispersed phase formulation. Shonibare and Wardle (2015) extended their hybrid model to deal with variable bubble size using the reduced population balance method and applied it to a vertical plunging jet. The authors support the need of a sub-grid model to enforce transition between resolved and unresolved scales of air.

By simulating the mean flow and predicting the air-entrainment in the small scales with a sub-grid model, the gain in computational speed and the numerically correct entrained air values overcomes the loss of accuracy in the description of the entrainment process. One of the first attempts was introduced in *FLOW-3D* by assuming entrainment of air when turbulent kinetic energy per unit volume was larger than disturbance kinetic energy per unit volume (Hirt, 2003). This increments a certain volume of air which is further dragged into the flow. Moraga et al. (2008) proposed a bubble source term based on bubble size probability density function that is activated when the downward liquid velocity is superior to 0.22 m/s at the free-surface region. Sensitivity analysis are performed to the parameters that compose this sub-grid model in a case of a breaking wave. Excellent correlation between accuracy and computational expense was found, however the authors assumed that robustness might be achieved if the air-entrainment region correlates with high turbulence intensity and high turbulent dissipation. Ma et al. (2010) extended the previous work, by substituting the source term for air-entrainment through the one suggested by Sene (1988) and applied it to the case of a vertical plunging jet. Based on the entrainment process described by Sene (1988) and Ervine and Falvey (1987), Ma et al.

(2011b) reformulated the source term to deal with the turbulence intensity. The accuracy of this source was proved in vertical plunging jets (Ma et al., 2011b), around a ship (Ma et al., 2011c), and an hydraulic jump (Ma et al., 2011d). Shi et al. (2010) formulated the breaking wave-induced air bubble entrainment by connecting the shear production at the air-water interface and the bubble number intensity with a certain bubble size spectra. Bubble advection velocity is calculated as sum of mean flow velocity and bubble-slip velocity.

In this work we aim to develop a state-of-art air-entrainment model that can be applied in cases of large continuous phase flows. The code is integrated in the open-source code OpenFOAM®. Section §9.2 presents the two-fluid model and the sub-grid air entrainment model made in this study. A new source term for air-entrainment that does not require calibration. The validation case is present in Section §9.3 along with the computational detail in Section §9.4. Section §9.5 presents the results of predicted flow depth, void fraction profiles and velocity field and compared with the available experimental data. Section §9.6 discusses the results. Section §9.7 discloses the main findings of this work.

9.2 Mathematical formulation of the air-entrainment model

The present model aims to describe a time-averaging solution for air-concentration values, attained from self-aeration of the flow, using a sub-grid scale approach within a VOF model. The section starts by exhibiting the time-averaging equations of fluid mechanics, the interface tracking methodology between two fluids and turbulence closure presented in the *interFoam* solver of OpenFOAM®. The self-aeration model is explained as well as the physical and theoretical assumptions used to deduce it.

9.2.1 General concepts

9.2.1.1 Mean flow equations

Practical simulations of turbulent isothermal flow are solved using the RANS equations for mass and momentum conservation. For a Newtonian and incompressible fluid the RANS equations can be written in their conservative form as

$$\nabla \cdot \bar{\mathbf{u}} = 0 \quad (9.1a)$$

$$\frac{\partial \rho \bar{\mathbf{u}}}{\partial t} + \nabla \cdot (\rho \bar{\mathbf{u}} \bar{\mathbf{u}}) = -\nabla p^* - \mathbf{g} \cdot \mathbf{x} \nabla \rho + \nabla \cdot \boldsymbol{\tau} + \mathbf{f} \quad (9.1b)$$

where, $\bar{\mathbf{u}} = (\bar{u}, \bar{v}, \bar{w})$ is the mean velocity vector written in Cartesian coordinates, ρ is the fluid density, p^* is the pressure resulting by removing the hydrostatic component to total pressure, \mathbf{g} the acceleration due to gravity, $\mathbf{x} = (x, y, z)$ are the Cartesian coordinates, τ is the combined turbulent and viscous stress tensor and \mathbf{f} is the representation of any additional momentum exchange force.

Assuming incompressible flow, the viscous stress tensor is simplified to

$$\nabla \cdot \tau = \nabla \cdot (\mu_{Eff} \nabla \bar{\mathbf{u}}) + \nabla \cdot (\mu_{Eff} (\nabla \bar{\mathbf{u}})^T) \quad (9.2)$$

where $\mu_{Eff} = \mu + \mu_t$ stands for effective viscosity, given by the sum of molecular (μ) and turbulent viscosity (μ_t).

9.2.1.2 VOF model

In VOF model, the system (9.1) is solved for two immiscible fluids by sharing the same velocity field, whereas the interface is tracked by an indicator scalar α ranging from 0 to 1, depending on which portion of the cell is filled with fluid 1. In other words, by giving to fluid 1 the properties of liquid water (l) and to fluid 2 the properties of gaseous air (g), this means that cells with $\alpha_l = 1$ will be filled with water whereas $\alpha_l = 0$ will come up as air phase. Cells with intermediate values are interfacial cells. The distribution and transport of the scalar α , also known as volume fraction, is modelled by the advection equation similar to the originally proposed by Hirt and Nichols (1981),

$$\frac{\partial \alpha_l}{\partial t} + \nabla \cdot (\alpha_l \bar{\mathbf{u}}) + \nabla \cdot [\bar{\mathbf{u}}_c \alpha_l (1 - \alpha_l)] = 0 \quad (9.3)$$

The difference to the original VOF lies on the inclusion of a compression term (Weller, 2008) (third term of Eq. (9.3)), used to confine the interface into a small region of space by applying a compression velocity $\bar{\mathbf{u}}_c$ given by

$$\bar{\mathbf{u}}_c = C_\alpha |\bar{\mathbf{u}}| \frac{\nabla \alpha_l}{|\nabla \alpha_l|} \quad (9.4)$$

The factor $\alpha_l(1 - \alpha_l)$ ensures that the compressive term is calculated just at the interfacial cells of the domain. C_α is a binary coefficient that activates ($C_\alpha = 1$) or deactivates ($C_\alpha = 0$) the interface compression term. The factor $\nabla \alpha_l / |\nabla \alpha_l|$ returns the normal to the interface calculated on the gradient of α , and it is used to orientate the magnitude of the velocity $|\bar{\mathbf{u}}|$.

The influence of the phase fraction and the fluids interface on the momentum equation (9.1b) is taken through the addition of a volumetric surface force function, explicitly

estimated by the Continuum Surface Force model (Brackbill et al., 1991)

$$\mathbf{f} = \mathbf{f}_\sigma = \sigma \kappa \nabla \alpha_l \quad (9.5)$$

where σ is the surface tension coefficient ($\sigma = 0.072 \text{ kg.s}^{-2}$ for water at $25^\circ C$) and $\kappa = \nabla \cdot (\nabla \alpha_l / |\nabla \alpha_l|)$ is the surface curvature.

9.2.1.3 Turbulence model

Turbulence plays an important role on self aeration of flow field. In this work it is modelled by the SST $k - \omega$ proposed by Menter (1993), where k is the turbulent kinetic energy and ω is the characteristic frequency for turbulence. This model takes advantage of the accuracy and robustness of $k - \omega$ model in the near-wall zone, whereas the fully turbulent region is simulated with a high-Reynolds-number formulation of $k - \varepsilon$ model. The two additional equations for k and ω are solved using following form

$$\frac{\partial \rho k}{\partial t} + \nabla \cdot (\rho k \bar{\mathbf{u}}) = \nabla \cdot (\Gamma_k \nabla k) + P_k - Y_k \quad (9.6a)$$

$$\frac{\partial \rho \omega}{\partial t} + \nabla \cdot (\rho \omega \bar{\mathbf{u}}) = \nabla \cdot (\Gamma_\omega \nabla \omega) + P_\omega - Y_\omega + D_\omega \quad (9.6b)$$

where Γ_k and Γ_ω represent the effective diffusivity of k and ω . P_k is the generation of turbulence kinetic energy due to the mean velocity gradients and P_ω the production of ω , whereas Y_k and Y_ω are their respective dissipation. D_ω is the cross-diffusion term that arises from the transformation of $k - \epsilon$ theory into $k - \omega$ model by substituting $\varepsilon = kw$. The dynamic eddy viscosity, μ_t is given by

$$\mu_t = \frac{a_1 \rho k}{\max[a_1 \omega, b_1 \mathbf{S} F_2]} , \quad a_1 = 0.31 , \quad b_1 = 1.0 \quad (9.7)$$

where $\mathbf{S} = \sqrt{2S_{ij}S_{ij}}$ and F_2 is a blending function. More detailed description about this model can be found in Menter (1993). Model constants are set to the standard values.

9.2.2 Mass conservation of dispersed gas

In the absence of bubble coalescence and dissolution, the mass conservation of dispersed gas moving with velocity $\bar{\mathbf{u}}_g$ can be derived from general transport equation

$$\frac{\partial \alpha_g}{\partial t} + \nabla \cdot (\bar{\mathbf{u}}_g \alpha_g) - \nabla \cdot (\Gamma_{\alpha_g} \nabla \alpha_g) = S_g \quad (9.8)$$

where Γ_{α_g} is the diffusivity tensor of α_g and S_g is the source of air at the free-surface,

further explained in §9.2.3. In this work we use two approaches to calculate the dispersed air velocity. The simplest way involves assuming the velocity of the dispersed gas $\bar{\mathbf{u}}_g$ as equal to the liquid velocity $\bar{\mathbf{u}}_l$ (9.9a). In this case, bubbles do not influence the dynamics of water phase. The second approach consists in considering $\bar{\mathbf{u}}_g$ as a sum of the mean flow velocity $\bar{\mathbf{u}}_l$ and the relative velocity between water and air $\bar{\mathbf{u}}_r$ (9.9b).

$$\bar{\mathbf{u}}_g = \bar{\mathbf{u}}_l \quad (9.9a)$$

$$\bar{\mathbf{u}}_g = \bar{\mathbf{u}}_l + \bar{\mathbf{u}}_r \quad (9.9b)$$

The velocity $\bar{\mathbf{u}}_r$ is calculated according to Clift et al. (1978) formula,

$$\bar{\mathbf{u}}_r = \begin{cases} -4474r_b^{1.357}\hat{\mathbf{g}} & \text{if } 0 < r_b \leq 7 \times 10^{-4} \\ -0.23\hat{\mathbf{g}} & \text{if } 7 \times 10^{-4} < r_b \leq 5.1 \times 10^{-3} \\ -4.202r_b^{0.547}\hat{\mathbf{g}} & \text{if } r_b > 5.1 \times 10^{-3} \end{cases} \quad (9.10)$$

where r_b is the characteristic bubble radius and $\hat{\mathbf{g}}$ is the normalised gravity vector.

9.2.3 Source of air at the free-surface

9.2.3.1 Volumetric source term

The self aeration of the flow can be developed at the free-surface when two requests are satisfied: (1) the inward velocity at the water free-surface reaches some critical value, and (2) the turbulent characteristics at interface are successful on the development of surface waves, that during their breakage, may trap air and carry it down into the water body. In case of air-water flows it was demonstrated that air entrainment can occur for inward velocities higher than 0.8 ms^{-1} (Ervine et al., 1980), however if they are smaller than 4 to 6 ms^{-1} , most air may result from the appearance of rough free-surface formed by the turbulent eddies. As suggested in Ma et al. (2011b), the quantity of air crossing the free-surface (q) per unit of surface area per unit of time is given by the change of velocity on the interface normal in a layer distanced by a (Fig. 9.1). The bi-dimensional variable q can be written as

$$q(0) = \bar{\mathbf{u}}_n(0 + a\mathbf{n}) - \bar{\mathbf{u}}_n(0) = a \frac{\partial \bar{\mathbf{u}}_n}{\partial \mathbf{n}}(0) \quad (9.11)$$

When the bubbles located at (1) are moving downward with the same velocity as interface (0) or if the velocity points outwards the flow, $q(0)$ returns zero and no air is

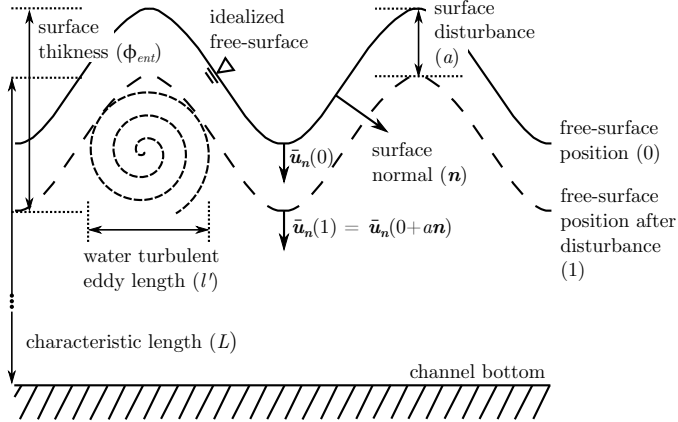


Figure 9.1: Schematic representation of free-surface with definition of physical parameters.

entrained:

$$\langle q(0) \rangle = \begin{cases} q(0) & , q(0) > 0 \\ 0 & , q(0) \leq 0 \end{cases} \quad (9.12)$$

The entrained air should be carried as a volume source over a interface layer that is ϕ_{ent} thick. This thickness is given by $\phi_{ent} = 0.05L$ (Ma et al., 2011b), where L (m) is a characteristic linear dimension (equal to the pipe diameter for pipe flow or the flow depth when dealing with river systems). The tri-dimensional form of the quantity of dispersed air becomes

$$S_g(0) = \frac{a}{\phi_{ent}} \left\langle \frac{\partial \bar{\mathbf{u}}_n}{\partial \mathbf{n}} \right\rangle \delta_{fs} \quad (9.13)$$

where δ_{fs} works as a switching function for the term further described in §9.2.3.2. In our air-entrainment model, as in (Moraga et al., 2008), the aeration is also bounded according to the characteristics of the free-surface. The air starts entraining when the liquid velocity pointing in the vertical direction ($\hat{\mathbf{g}}$) and in the normal to free-surface ($\hat{\mathbf{n}}$) exceeds a critical value (u_c) and generates oscillations capable to increase the turbulence to a certain value k_c . Mathematically these assumptions can be written as:

$$\begin{aligned} \bar{\mathbf{u}}_n \cdot \hat{\mathbf{g}} &> u_c \\ \bar{\mathbf{u}}_n \cdot \hat{\mathbf{n}} &> u_c \\ k &> k_c \end{aligned} \quad (9.14)$$

The constant $u_c = 0.8$ m/s is assumed as the critical inward velocity taken from experimental cases (Ervine et al., 1980) at which the air starts entraining into the flow. To define the critical turbulent kinetic energy k_c , identical works in stepped spillways

show that k at the free-surface has to exceed $k_c = 0.20 \text{ m}^2/\text{s}^2$ to develop the self-aeration (Bombardelli et al., 2010; Hirt, 2003, 2012). This value identifies the level of turbulence needed to overcome surface tension and permit the entrainment of air.

9.2.3.2 Free surface detection

In VOF models, the interfacial structure can only be detected by the change of phase fraction or by its gradient. For a smooth and laminar free-surface, by connecting all the cell centres with phase fraction equal to 0.5, this return a good first guess of the free-surface position. However, for high turbulent flows, that represent the majority of the cases where air-entrainment occurs, due to surface fluctuations and hight turbulent intensity, the free-surface might be given by water volume fraction from 0.5 to 0.1.

To create a switch that activates the source of air S_g at the free-surface, the value 1 must be representative of its effective position. Two different approaches are utilised in this work. Lopes et al. (2016b)(Chapter §8) showed that it is possible to adjust the volume fraction factor to a range within the interval from 0 to 1:

$$\delta_{fs,alpha} = 4\alpha_l(1 - \alpha_l) \quad (9.15)$$

Hänsch et al. (2014) proposed an algebraic equation to predict the free-surface position based on the gradient of α_l volume fraction and a threshold $|\nabla\alpha_l|_{cr}$:

$$\delta_{fs,gradient} = \frac{1}{2} \tanh[\beta \Delta x (|\nabla\alpha_l| - |\nabla\alpha_l|_{cr})] + 0.5 \quad (9.16)$$

The threshold $|\nabla\alpha_l|_{cr}$ is used to define the maximum gradient value in which the free-surface is calculated. By allocating the interface as spreading over a maximum of four cells, as done in (Hänsch et al., 2014), the threshold is given by $|\nabla\alpha_l|_{cr} = 1/(4\Delta x)$, where Δx is the length of an average cell. The hyperbolic tangent transforms the inner difference to the interval [-1,1], depending if the threshold is smaller or higher than the gradient, afterwards transformed to [0,1]. The coefficient β is user-defined, used to enlarge the difference between the gradient and the threshold. Good results were found by using $\beta = 100$.

9.2.3.3 Surface disturbances

As mentioned before, the rate of air-entrainment is dependent on the inward velocity and turbulent intensity, with major effects committed to the second (Ervine et al., 1980). It is essential to take into account the surface roughness contributions to the air-entrainment process, which according to Ervine and Falvey (1987), can be calculated by assuming

the surface disturbances at free-surface (a) as having the same order of magnitude as the radius of the turbulent eddies ($l'/2$) (Fig. 9.1). In Lopes et al. (2016b), the surface disturbances were originally predicted by applying the theoretical concept of turbulent length scales used in CFD for $k-\varepsilon$ and $k-\omega$ turbulent models

$$a_1 = C_\mu^{3/4} \frac{k^{3/2}}{2\varepsilon} \quad \text{or} \quad a_1 = C_\mu^{-1/4} \frac{k^{1/2}}{2\omega} \quad (9.17)$$

were $C_\mu = 0.09$ is a constant from $k - \varepsilon$ turbulence model. Similar approach, was employed in the air-entrainment model of Hirt (2003) by describing the surface waves' amplitude as a function of the turbulent eddies and a constant of proportionality C_a

$$a_2 = C_a C_\mu \left(\frac{3}{2} \right)^{1/2} \frac{k^{3/2}}{\varepsilon} \quad (9.18)$$

In the work of Ma et al. (2011b), by assuming the surface disturbances proportional to the kinetic energy of the turbulent fluctuations we obtain

$$a_3 \approx \frac{u'^2}{2g} = C_a \frac{k}{g} \quad (9.19)$$

where C_a is a calibration factor.

9.2.4 Bubble breakup at free-surface

The transport of gaseous-single-phase needs is completed when bubbles present in the water phase are able to breakup along the free-surface area. Therefore, the dispersed gas phase is turned to continuous when a critical value of water volume fraction ($BBA=\alpha_{l,cr}$) is reached. By default the value of bubble breakup is $BBA=0.1$.

9.2.5 Two-fluid model closure

There are two ways in which this entrainment model may be used. In situations where the volume occupied by the dispersed phase is small ($\alpha_g < 0.1$), the influence of dispersed phase on flow velocities can be neglected and a simple one-way coupling model is sufficient for good and accurate results (Chanson, 1997; Bombardelli et al., 2010). For higher volume fractions ($\alpha_g \geq 0.1$), the volume of entrained air must be taken into account in the calculation of physical properties of the mixture (two-way coupling). In this work, the spatial variation of any physical property (ϕ), such as ρ or μ are weighted on the fluid fraction present in each cell is switched accordantly if a one-way ($b = 0$) or a two-way coupling model ($b = 1$) is requested

$$\phi = \alpha_l \phi_l + (1 - \alpha_l - b\alpha_g) \phi_g \quad (9.20)$$

9.2.6 Solution procedure

The transport equations previously derived requires a numerical model and a computational domain in which, each term of the partial differential equations is subsequently solved. The coupled system of equations is solved sequentially resulting from the discretisation in finite volumes. The overall procedure is summarised in Fig. 9.2.

9.3 Description of the experimental facility

Experimental data is acquired in a stepped spillways physical model built at the Hydraulic Engineering Section Laboratory of FH Aachen - University of Applied Sciences (Fig. 9.3). The water runs in a closed circuit of water composed by two reservoirs, controlled by a butterfly valve and measured by an inductive flow meter. Between the head tank and the first step exists an approaching channel of 1 m length that guarantees a hydrostatic pressure distribution. The spillway model is composed by 28 steps (S1 to S28) with 0.12 m length \times 0.06 m high \times 0.50 m width, resulting in a total drop height $H = 1.68$ m. The slope is constant and equal to $\varphi = 26.6^\circ$. The unit water discharge is defined to $q_w = 0.07 \text{ m}^2\text{s}^{-1}$, which returns a critical water depth at stepped spillway crest of $h_c = 0.08$ m ($h_c/s = 1.3$). Froude number at inlet is 0.71 and over the steps is ≈ 4.27 . The structural designs here used and flow conditions originate a skimming flow regime with a surface inception point at the 5th step edge, visually detected through the appearance of a white front in the free-surface fluctuations. More details about the installation can be found in (Lopes et al., 2015a; Bung and Valero, 2016).

Numerical flow velocities close to the wall are validated using BIV technique, firstly developed by Ryu et al. (2005). The flow field from step 6 to 13 of SSP05 is individually captured with a high-resolution high-speed camera (HSC) Phantom Miro M120 (sample rate: 700 fps, resolution: 1920 \times 1200 px) equipped with Nikon 50mm f/1.4D AF Lens. The camera is positioned 0.6 m away from the spillway front wall. Each step is illuminated with the same light intensity, achieved by the sequential displacement of two white halogen spotlights on the top of the spillway. Acquisition time is set to 1 s. In order to ensure a sharp image, before each measurement the pump is switched off and the lens are focused to a printed target, positioned 2-5 mm inside the acrylic wall.

BIV technique is applied to this work in order to obtain the flow velocity field, where the bubbles, illuminated by halogen spotlights, are used as tracers. Some loss of accuracy

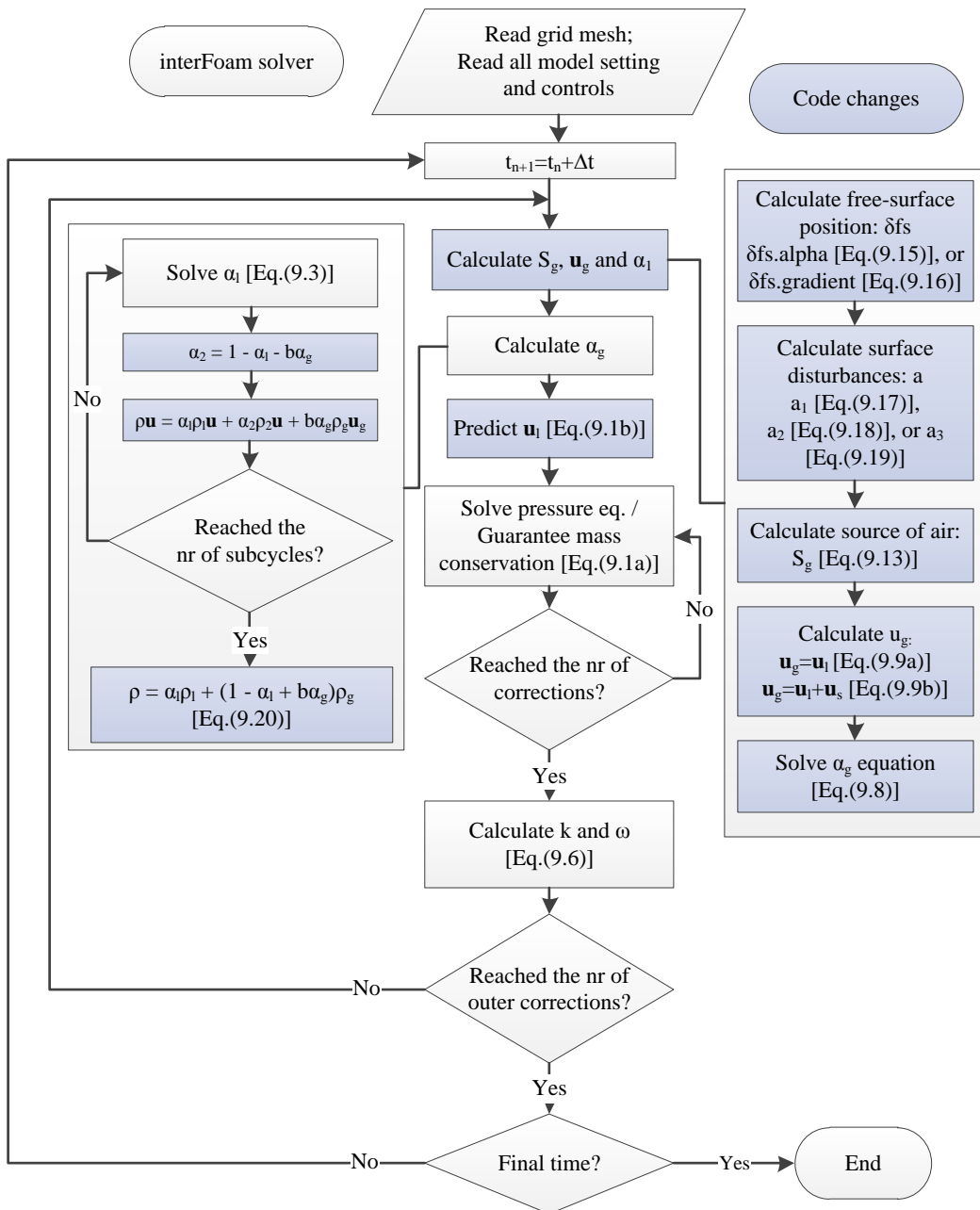


Figure 9.2: Flow chart of the model. Light grey boxes are part of the standard *interFoam* solver. Dark grey boxes are additions to the code made in this work.

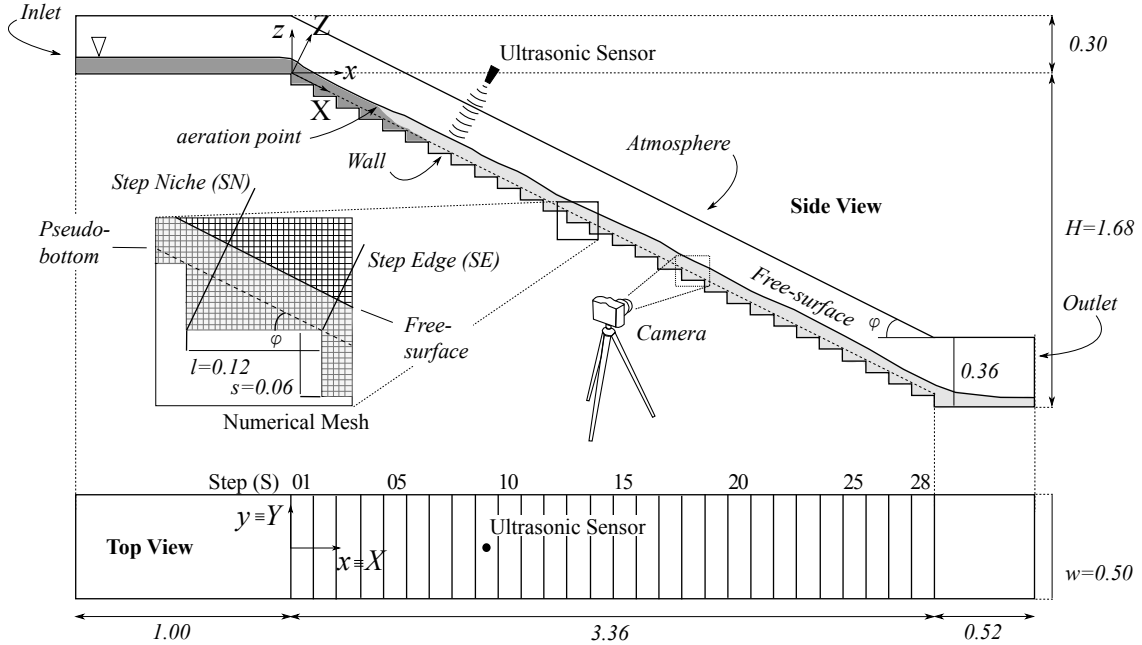


Figure 9.3: Scheme of the experimental installation.

must be taken into account, because bubbles can leave focused planes and distort the resulting velocity field (Leandro et al., 2014a). After some tests about software performance and accuracy, BIV technique is applied using a simple cross-correlation analysis of an interrogation window composed by 96×96 px with 75 % overlap.

9.4 Computational tests

The computational flow conditions and domain are the same as in the experiments (Fig. 9.3). At the inlet of the computational domain we prescribe uniform velocity with a constant flow depth using a Dirichlet BC, whereas pressure is defined by a null Neumann-BC. The initial values for turbulent variables k , ε and μ_t are calculated based on general approximations used in CFD (Versteeg and Malalasekera, 2007, p. 77). Since the flow is supercritical, the outlet-BC is set as free-outflow by defining flow depth and velocity as null Neumann-BC and pressure to hydrostatic. In the model walls, zero velocity is imposed using Dirichlet-BC and walls functions are implemented in the calculation of turbulence. At top of the domain, free exchanges of air and water are allowed by imposing null Neumann-BC for all the variables except for pressure, which is set to zero.

Mesh sensitivity analysis is conducted following the ASME's procedure (Celik et al., 2008) for a simulation with no air model activated. Three uniform and structured meshes: M1, M2 and M3; with cells size 0.005 m, 0.007 m and 0.01 m are used in this study,

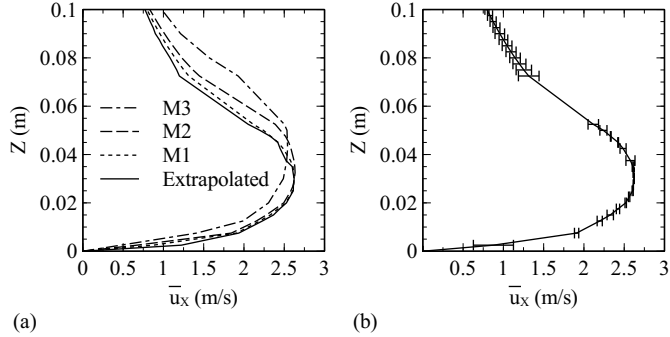


Figure 9.4: Mesh convergence study: (a) X-velocity profiles placed above the 12th step edge; (b) Fine-grid M1 solution with discretisation error bars.

generating a total of 6 528, 2 754 and 816 thousands volumes within the domain. GCI analysis, which measures the percentage of convergence for the finer mesh to a mesh independent solution, is applied over 30 points in X-velocity profile placed above the 12th step edge. Figure 9.4a shows the X-velocity profiles for meshes M1, M2 and M3 and the optimal solution from the application of the convergence procedure. Figure 9.4b presents the velocity profile acquired with the finest mesh together with error bars. The local order of accuracy ranges from 1.6 to 13.0 with a global average of 4.6. Oscillatory convergence occurs at 23% of the 30 points. The convergence achieved in the transition between M3 and M2 (GCI_{M2}) is 8% and the convergence between M2 and M1 (GCI_{M1}) is 5%. For this gain of accuracy and the small errors found in Fig. 9.4b, all subsequent analysis are based upon the results from simulations using mesh M1.

Fifteen simulations divided in nine tests categories are set-up to simulate the different combinations of model settings (Table 9.1). Test T1 has the air-entrainment model inactive. Test T2 and T3 uses the air-entrainment model in which the gas velocity is equal to the mean velocity of the flow. Difference between T2 and T3 is in the free-surface detection factor. Test T4 adds to T3 the two-way coupling system by changing the density of the flow. Test T5 considers the velocity of the gas as sum of the mean flow velocity and relative velocity, and test T6 completes the mass conservation equation of dispersed gas with the diffusivity term. Test T5 is further divided in i, ii, iii and iv to test different calibration coefficients in the calculation of surface disturbances in a_3 (9.19). Coefficient C_{air} is changed to 0.01, 0.02, 0.05 and 0.1 in accordance to Ma et al. (2011b). Test T7 and T8 calculates the surface disturbances by means of a_2 (9.18) and a_1 (9.17), respectively. In the calculation of a_2 , C_{air} is set to 0.5, as recommended by Hirt (2003). Test T8 is further divided in i, ii, iii and iv to test different bubble breakup factors $BBA = 0.1, 0.3, 0.5$ and 0.7. Test T9 differs to T8 in the application of a limiter to S_g .

Table 9.1: Summary of tests and simulation settings used in this work. Gas velocity settings and Diffusivity are explained in §9.2.2. Model closure is explained in §9.2.5. Free-surface detection models (δ_{fs}) are described in §9.2.3.2. Surface disturbances formulas (a) are explained in §9.2.3.3. Bubble breakup settings are explained in §9.2.4. Limiters on S_g are presented in §9.2.3.

Test ID	Air Model	Gas velocity ($\bar{\mathbf{u}}_g$)	Diffusivity	Model closure	δ_{fs}	Surface disturbances (a)	BBA	limiter on S_g
T1	No	-	-	-	-	-	-	
T2	Yes	$\bar{\mathbf{u}}_l$	No	One-way	<i>alpha</i>	$a_3, C_{air} = 0.1$	0.1	No
T3	Yes	$\bar{\mathbf{u}}_l$	No	One-way	<i>grad</i>	$a_3, C_{air} = 0.1$	0.1	No
T4	Yes	$\bar{\mathbf{u}}_l$	No	Two-way	<i>grad</i>	$a_3, C_{air} = 0.1$	0.1	No
T5i	Yes	$\bar{\mathbf{u}}_l + \bar{\mathbf{u}}_r$	No	Two-way	<i>grad</i>	$a_3, C_{air} = 0.1$	0.1	No
T5ii	Yes	$\bar{\mathbf{u}}_l + \bar{\mathbf{u}}_r$	No	Two-way	<i>grad</i>	$a_3, C_{air} = 0.02$	0.1	No
T5iii	Yes	$\bar{\mathbf{u}}_l + \bar{\mathbf{u}}_r$	No	Two-way	<i>grad</i>	$a_3, C_{air} = 0.1$	0.05	No
T5iv	Yes	$\bar{\mathbf{u}}_l + \bar{\mathbf{u}}_r$	No	Two-way	<i>grad</i>	$a_3, C_{air} = 0.1$	0.1	No
T6	Yes	$\bar{\mathbf{u}}_l + \bar{\mathbf{u}}_r$	Yes	Two-way	<i>grad</i>	$a_3, C_{air} = 0.1$	0.1	No
T7	Yes	$\bar{\mathbf{u}}_l + \bar{\mathbf{u}}_r$	No	Two-way	<i>grad</i>	$a_2, C_{air} = 0.5$	0.1	No
T8i	Yes	$\bar{\mathbf{u}}_l + \bar{\mathbf{u}}_r$	No	Two-way	<i>grad</i>	a_1	0.1	No
T8ii	Yes	$\bar{\mathbf{u}}_l + \bar{\mathbf{u}}_r$	No	Two-way	<i>grad</i>	a_1	0.3	No
T8iii	Yes	$\bar{\mathbf{u}}_l + \bar{\mathbf{u}}_r$	No	Two-way	<i>grad</i>	a_1	0.5	No
T8iv	Yes	$\bar{\mathbf{u}}_l + \bar{\mathbf{u}}_r$	No	Two-way	<i>grad</i>	a_1	0.7	No
T9	Yes	$\bar{\mathbf{u}}_l + \bar{\mathbf{u}}_r$	No	Two-way	<i>grad</i>	a_1	0.1	Yes

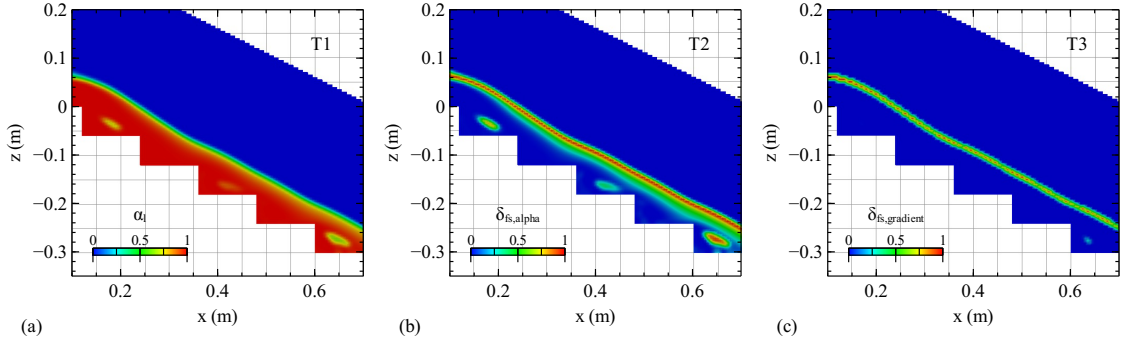


Figure 9.5: Detail of free-surface above steps 1 to 5 using (a) VOF equation (9.3) (test T1), (b) free-surface detection based on α_l values (δ_{fa,α_l}) expressed by equation (9.15) (test T2) and (c) free-surface detection based on the gradient of α_l ($\delta_{fa,gradient}$), given by the algebraic equation (9.16) (test T3). Profiles taken at centre-channel.

9.5 Results

9.5.1 Free-surface detection

Figure 9.5 presents the free-surface detection using the two methods presented in this work, given by equations (9.15) and (9.16). Figure 9.5a shows the volume fraction calculation from VOF model, where 1 indicates the presence of water and 0 the presence of air. Figure 9.5b shows the free-surface represented by δ_{fa,α_l} (9.15). Figure 9.5c presents the free-surface predicted with $\delta_{fa,gradient}$ (9.16).

9.5.2 Influence of surface disturbances formulas and source of air

Figure 9.6 shows the comparison between the mean free-surface disturbances measured with the ultrasonic sensor at each step edge, and the numerical disturbances calculated with the numerical formulas: a_1 (9.17), a_2 (9.18) and a_3 (9.19) presented in section §9.2.3.3. Tests T5-i,ii,iii,iv, T7, T8i and T9 (Table 9.1) are run in this case. The experimental disturbances (Exp) are calculated by averaging the absolute difference between the instantaneous flow depth to the overall mean water depth.

Figure 9.7 presents the free-surface position along the spillway for tests T1, T5iv, T8i and T9 (Table 9.1). Test T1 does not have the air-entrainment model active. Tests T5iv, T8i and T9 are chosen in order to show the free-surface position when the air-entrainment model is activated. Test T9 show the benefit of including limiters on S_g term. Box plots of water depths measured with the ultrasonic sensor are made for comparison in which

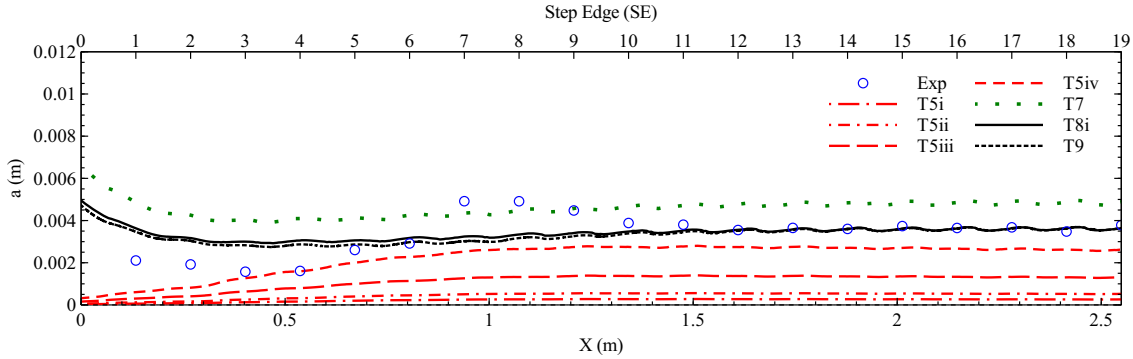


Figure 9.6: Surface disturbances calculated along the stepped spillway for tests: T5 - surface disturbances calculated with a_3 , T7 - surface disturbances calculated with a_2 , and T8i/T9 - surface disturbances calculated with a_1 . Tests T5-i,ii,iii,iv applies respectively the calibration coefficient $C_{ent} = 0.01, 0.02, 0.05$ and 0.1 . Test T9 differs from T8i by applying a limiter to S_g . Dots represent the surface disturbances calculated with the ultrasonic sensor.

Profiles taken at centre-channel.

the band inside the box represents the second quartile around the median and the end of the whiskers represent the 2nd percentile and the 98th percentile.

Figure 9.8 shows the values of S_g calculated on top of the isosurface that connects $\alpha_l = 0.5$. Figure 9.8a outputs the free-surface calculated with the test T8i whereas Fig. 9.8b shows the result of test T9. The difference resides in the fact that in T9 we applied limiters to inward velocity ($u_c = 0.8 \text{ m/s}$) and turbulent at interface $k_c = 0.22 \text{ m}^2/\text{s}^2$ in order to switch S_g [see (9.12)].

9.5.3 Air-concentration profiles

Figure 9.9 shows the air-concentration profiles above step niche 12 for tests T3, T4, T5 and T6 (Table 9.1). Test T3 uses the air-entrainment model in which the gas velocity equals the mean velocity of the flow ($\bar{\mathbf{u}}_g = \bar{\mathbf{u}}_l$). Test T4 adds to T3 the two-way coupling system by changing the density of the flow. Test T5 considers the velocity of the gas as sum of the mean flow velocity and relative velocity ($\bar{\mathbf{u}}_g = \bar{\mathbf{u}}_l + \bar{\mathbf{u}}_r$) in a two-way coupling. Test T6 completes the mass conservation equation of dispersed gas with the diffusivity term. Numerical air-concentration profiles are compared with air volume fraction taken with a dual-tip conductive probe (Bung, 2011a). This comparison is possible because the tests are performed in an identical experimental installation, and under the same inflow conditions.

Figure 9.10 shows the air-concentration profiles above step niche 12 for simulations

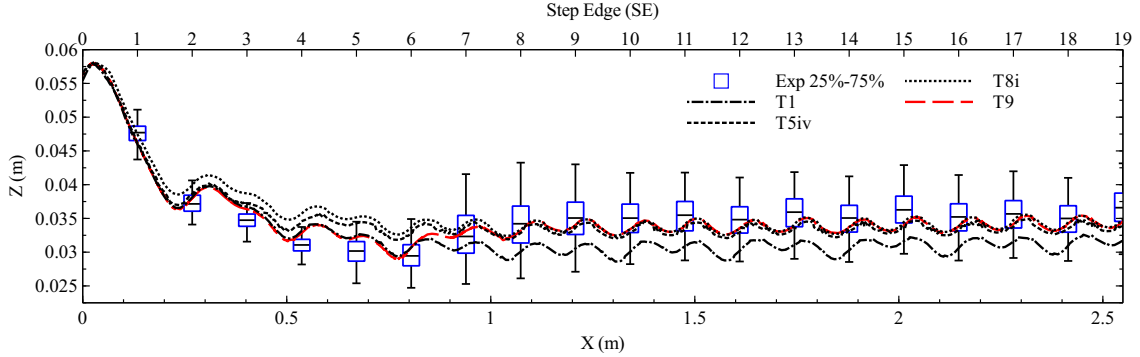


Figure 9.7: Free-surface evolution delimited by $\alpha_l = 0.5$ for tests: T1 - no air model, T5i - surface disturbances calculated with a_3 and $C_{ent} = 0.1$, and T8i/T9 - surface disturbances calculated with a_1 . Test T9 differs from T8i by applying a limiter to S_g . Box plots represent the water depths measured with the ultrasonic sensor at each step edge, in which the whiskers represent the 2nd percentile and the 98th percentile. Profiles taken at centre-channel.

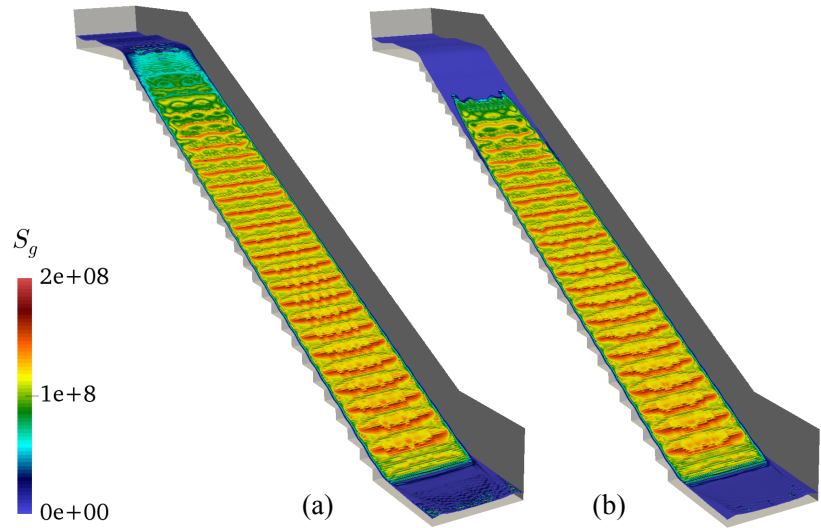


Figure 9.8: 3D view of S_g term calculated at free-surface delimited by $\alpha_l = 0.5$ for tests: (a) T8i - simulation without limiter on S_g and (b) T9 - simulation with limiter on S_g .

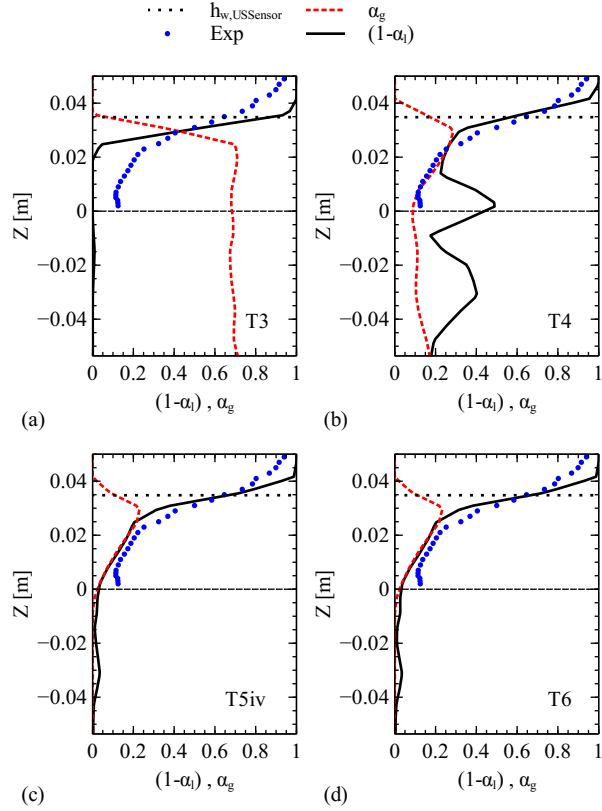


Figure 9.9: Air concentration profiles above step niche 12 for tests: T3 - Gas velocity $\bar{u}_g = \bar{u}_l$, T4 - two-way coupling model and gas velocity $\bar{u}_g = \bar{u}_l$, T5 - two-way coupling model and gas velocity $\bar{u}_g = \bar{u}_l + \bar{u}_r$, and T6 - diffusivity term active. Profiles taken at centre-channel. $Z=0$ corresponds to pseudo-bottom level.

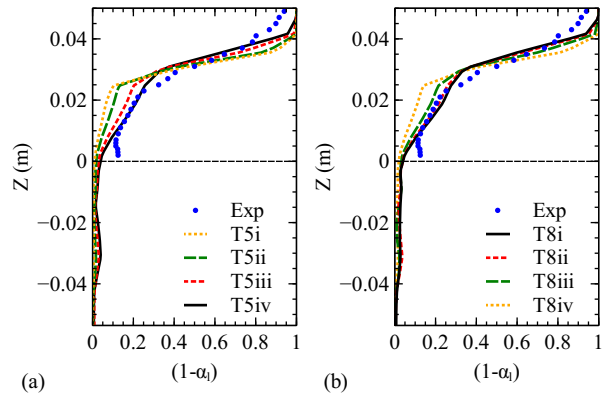


Figure 9.10: Sensibility test of air-concentration profile above step niche 12 for tests: (a) T5-i,ii,iii,iv - changing C_{air} constant in surface disturbances formula a_3 , and (b) T8-i,ii,iii,iv - changing bubble breakup factor at free-surface. Profiles taken at centre-channel. $Z=0$ corresponds to pseudo-bottom position.

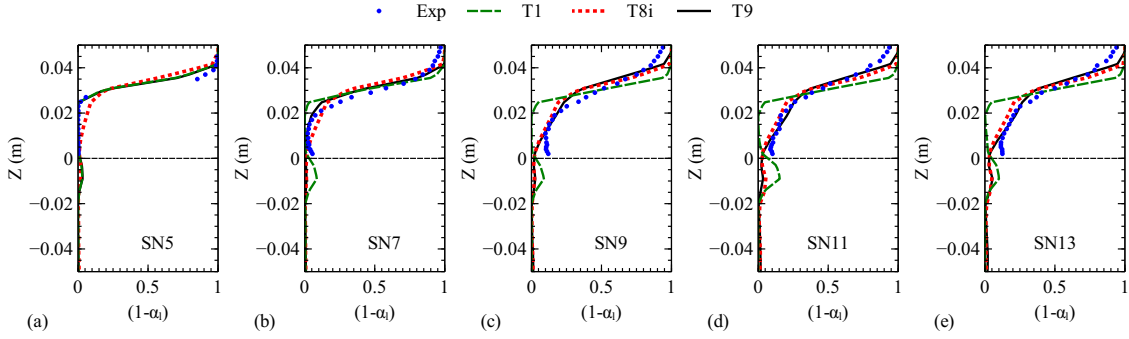


Figure 9.11: Air-concentration profiles at odd SN from 5 to 13 for tests: T1 - no air model, T8i - with air model, and T9 - with air model and limiters on S_g . Numerical results are plotted against experimental air-concentration profiles taken with air-concentration probe. Profiles taken at centre-channel. $Z=0$ corresponds to pseudo-bottom position.

T5-i,ii,iii,iv and T8-i,ii,iii,iv (Table 9.1). Figure 9.10a present a sensibility test of values C_{air} in the surface fluctuations function a_3 (tests T5), whereas Fig. 9.10b presents how the bubble breakup factor at free-surface influences the air-concentration profile (tests T8). As done in Fig. 9.9 the data is plotted against with experimental air-concentrations profiles.

Figure 9.11 shows the air-concentration profiles at odd SN from 5 to 13 for simulations T1, T8i and T9 (Table 9.1). Test T1 is the simple VOF model, T8i uses the air model with surface disturbances calculated by a_1 formula and T9 adds to T8i limiters on S_g term. The numerical data is compared with air-concentration profiles measured with the air-concentration probe. Table 9.2 presents the accuracy of the tests T1, T8i and T9 in comparison to experimental air-concentration profiles measured using BIV technique. NSE (Nash and Sutcliffe, 1970) and Pearson- R^2 (Pearson, 1986) are used to calculate the degree of fit of model output. In both cases, a perfect match of modelled to the measured data is indicated by 100% efficiency.

9.5.4 Flow velocity

Figure 9.12 shows the X-velocity profiles at centre-channel for SN from 5 to 13 and for simulations T1, T8i and T9 (Table 9.1). Test T1 is the simple VOF model, T8i uses the air model with surface disturbances calculated by a_1 formula and T9 adds to T8i limiters on S_g term. Table 9.3 presents the accuracy of the tests T1, T8i and T9 in comparison to experimental velocity profiles measured using BIV technique. NSE (Nash and Sutcliffe, 1970) and Pearson- R^2 (Pearson, 1986) are used to calculate the degree of fit of model output. In both cases, perfect match of modelled to measured data is indicated by 100% efficiency.

Table 9.2: Accuracy of the tests T1, T8i and T9 in comparison to experimental air-concentration profiles measured with an air-concentration probe. NSE and Pearson- R^2 are used to quantitatively describe the accuracy of model outputs. An efficiency of 100% corresponds to a perfect match of modelled air-concentration profiles to the measured data. Bold numbers mark the best of NSE and R^2 for each step niche profile.

Eff. model (%)	Test ID	SN5	SN7	SN9	SN11	SN13
NSE	T1	95.9	96.6	90.3	88.4	84.8
	T8i	91.5	96.6	96.7	97.4	95.9
	T9	96.4	98.1	97.3	98.5	97.5
R^2	T1	98.6	99.2	98.5	97.8	97.9
	T8i	97.0	98.4	99.3	99.5	99.4
	T9	98.8	99.4	99.3	99.6	99.4

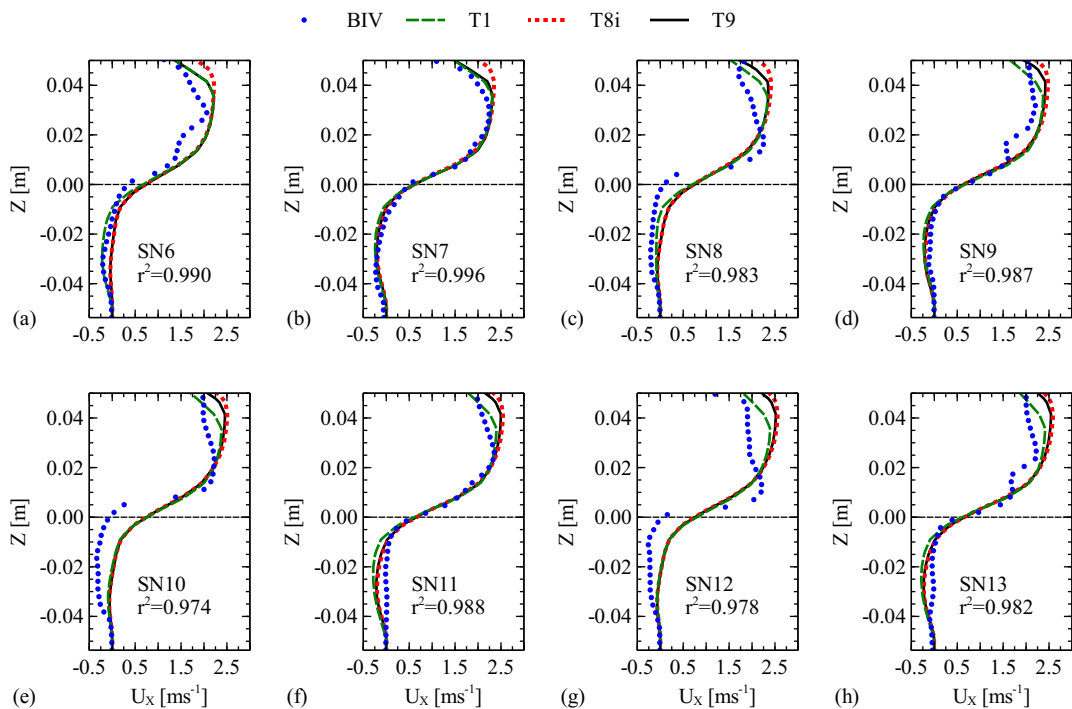


Figure 9.12: X-velocity profiles at SN from 6 to 13 for tests: T1 - no air model, T8i - with air model, and T9 - with air model and limiters on S_g . Numerical results are plotted against data from BIV. Profiles taken at centre-channel. $Z=0$ corresponds to pseudo-bottom position.

Table 9.3: Accuracy of the tests T1, T8i and T9 in comparison to experimental velocity profiles measured using BIV technique. NSE and Pearson- R^2 are used to quantitatively describe the accuracy of model outputs. An efficiency of 100% corresponds to a perfect match of modelled velocity profiles to the measured data. Bold numbers mark the best of NSE and R^2 for each step niche profile.

Eff. model (%)	Test ID	SN6	SN7	SN8	SN9	SN10	SN11	SN12	SN13
NSE	T1	92.6	98.8	93.5	96.0	89.7	97.4	89.6	95.3
	T8i	87.7	95.7	88.6	95.0	87.0	96.6	83.5	91.7
	T9	91.2	98.7	90.6	96.1	88.2	96.8	85.0	92.9
R^2	T1	99.4	99.6	97.6	99.0	97.1	99.6	96.5	99.1
	T8i	99.1	98.7	96.6	99.6	97.0	99.4	95.2	99.1
	T9	98.0	99.6	97.0	99.5	97.1	99.5	95.4	99.1

9.6 Discussion

9.6.1 Free-surface detection

Figure 9.5 presents the free-surface detection using the two methods presented in this work, namely by equations (9.15) and (9.16). On top of step edge 1, the free-surface has laminar characteristics. Therefore, the air-water transition takes place in a short space and the factor in (9.15) can represent accurately the free-surface (Lopes et al., 2016b). After that step, due to the increase of turbulence levels at free-surface and the production of air-water mixtures in the step cavities, $\delta_{fs,alpha}$ returns non-zero values inside the water body. By solving the S_g term on these zones, un-physical production of air inside the cavities is not avoided. On the other hand, by adding a limiter based on the α_l gradient (Figure 9.5c), the method just detects the interface as requested. Nonetheless the latter requires calibration.

9.6.2 Surface disturbances, source of air and free-surface shape

Figure 9.6 shows the values of the surface disturbances calculated with formulas a_1 (9.17), a_2 (9.18) and a_3 (9.19). Experimental surface disturbances are calculated based on the fluctuations of the free-surface around the mean value. The measured surface fluctuations have a slight increase in the transition between step 4 and 5, from which the air starts entraining into the flow. A higher increment is observed after passing step 6. Later in step 10, the surface fluctuations tend to stabilise to $\approx 3.5\text{ mm}$. The formula based on turbulent length scales (a_1) is the best approximation to detect the surface fluctuations in the aeration zone of the stepped spillway. Formulas a_2 and a_3 would further require

calibration of the factor C_{air} to improve results. The shape of the function given by formula a_2 is indeed quite similar to our case. In the absence of information about free-surface fluctuations, the only way to calibrate those factors is by recursively changing the calibration factors.

Fig. 9.7 presents the final free-surface shape. It can be noticed that while the pure VOF model (test T1) is accurate in the characterisation of the free-surface level in the non-aerated zone, the aerated part of the stepped spillway must be described by a model with air-entrainment activated (T5iv, T8 or T9). Differences are mostly found in the flow transition. Once the free-surface disturbances detected by a_3 are small in the non-aerated part of the spillway (Fig. 9.6), we observe a smooth transition between the free-surface coincident to the VOF model and the free-surface in the aerated zone. However, the transition started in step 3, which is not in accordance to the experiments. Test T8i shows high values of surface fluctuations found by a_1 in the non-aerated zone and the free-surface is affected since the beginning of the spillway. Similar situation would happen for T7. Limiters on S_g (T9) block the entrainment through the free-surface when the natural characteristics for aeration are not ideal. Free-surface produced by test T9 is therefore in better agreement. The values of a_1 before step 5 are neglected and the increment of the flow depth is cut-off. This detail can be also confirmed through the analysis of Fig. 9.8, as S_g values in Fig. 9.8b are activated accordingly to what was observed experimentally - the air-entrainment phenomena starts after step 4 in a zone close to the side walls and at step 5 in the centre channel.

9.6.3 Air-concentration and velocity profiles

Figure 9.9 shows the influence in the air-concentration profile on top of step niche 12 by changing the settings in the air-entrainment model. In tests T3 and T4, the velocity of the dispersed gas phase is equal to the velocity of the flow, which means that bubbles have the same velocity as water. In T3 (Fig. 9.9a), the presence of bubbles do not influence the flow velocity. They are viewed as small elements whose volume, mass and density are neglected during the transportation with the water phase. As the bubbles in this case can occupy easily more than 10% of the total volume, this concept of model is in general far from a correct prediction of dispersed air. Its application is limited to the transportation of massless particles or dissolved elements within the water flow. By introducing the density change in test T4 (Fig. 9.9b), the bubbles influence the dynamics of the flow. Therefore, Fig. 9.9b shows a much closer approximation of the air-concentration profile above the pseudo-bottom, in the free-stream part of the flow. Below this zone, once the bubbles are trapped in the vortices formed at steps cavities of the spillway, the ratio of density is not

enough to make the bubbles escape throughout the free-surface. In test T5 (Fig. 9.9c), the dispersed phase has now the influence of a vertical velocity. Although we do not have the experimental air-concentration profile in the step cavity for comparison, the profile above the pseudo-bottom outlines a much similar shape to the given data. To complete the box of tests, in T6 we include the diffusive term to the mass conservation equation of dispersed phase. Despite some small differences found in the step cavity, this term has no influence in the transportation of the bubbles and in the general shape of the air-concentration profile.

Figure 9.10a presents the relationship between the coefficient C_{air} , used in the formula for surface disturbances of the formula a_3 , and the respective air-concentration profile on top of the step niche 12. As showed previously, by changing the coefficient C_{air} , we can increase or decrease the level of surface disturbances and with it the amount of entrained air. As expectable, larger values of C_{air} will push down the air-concentration profile as the amount of entrained air was increased. Figure 9.10b shows the influence of the bubble breakup factor to the air-concentration profile. If the cut-off value of BBA is too high, e.g. BBA=0.7, the bubbles reach the artificial surface much earlier than desired and the air exits the flow. It is recommended to keep this value low and equal to BBA=0.1.

In order to show the overall applicability of this model, Fig. 9.11 shows the air-concentration profiles in the five odd SN, from 5th to 13th step. It is clear that a great improvement was done in the characterisation of the air-concentration when compared test T1 to tests T8i and T9 (Table 9.2). The application of limiters to S_g term (T9) improves the numerical profile to agree the experimental data in steps niches 5 ($NSE_{SN5}=96.4$) and 7 ($NSE_{SN7}=98.1$) more than T1 ($NSE_{SN5}=95.9$; $NSE_{SN7}=96.6$) or T8 ($NSE_{SN5}=91.5$; $NSE_{SN7}=96.6$) (Table 9.2). Small differences are found between T8i and T9 in the accuracy of the profiles in steps 9, 11 and 13.

Figure 9.12 shows the comparison between the velocity profile above SN 6 to 13 measured using BIV technique, with simulation tests T1, T8i and T9. The profiles and analysis of Table 9.3 show a good accuracy of the numerical model in the representation of the velocity profiles. The activation of an air-entrainment model does not change too much the dynamics of the water phase. The profiles given by the simulation with no air-entrainment model (T1) are marginally in better agreement to experimental. Higher differences are visible on the top of the velocity profiles because the model with air-entrainment activated detects a higher flow depth. Nonetheless, it should be noted that BIV underestimates the velocity (Leandro et al., 2014a). Furthermore a closer look to the velocity profiles shows that the agreement level is higher for odd SN (SN7, SN9, SN11 and SN13), which in turn is related to the alternation of flow pattern between adjacent steps observed in (Lopes et al., 2015a).

9.7 Conclusions

The present work presents an air-entrainment model that can be applied in most engineering problems where self-aeration phenomena is presented. It is developed within the open-source code OpenFOAM®. A source term for air-entrainment detection was used to interplay the interface capturing model formulation and the dispersed air phase. This model is applied to solve the flow over a stepped spillway structure.

The following conclusions can be retrieved from this work:

- The free-surface detection formula for high complex flows and to be used in VOF method needs to include a threshold to mitigate the effect of an un-physical production of air inside the flow. It can be captured using the formula $\delta_{fa,gradient}$ (9.16) by Hänsch et al. (2012).
- Different surface fluctuations formulas were tested in this work and their values were tested against experimental data. The a_1 formula by Lopes et al. (2016b)(Chapter §8) shown a good agreement in the fully-aerated zone of the stepped spillway without calibration process.
- Numerical flow-depths along the stepped spillway were validated with the air-entrainment model. It was shown that by switching the air model the flow depths in the fully-aerated zone were coincident to those experimentally measured.
- By including a limiters to inward velocity ($u_c = 0.8 \text{ m/s}$) and turbulent at interface ($k_c = 0.22 \text{ m}^2/\text{s}^2$) in the entrainment source term it is also possible to rectify the transition between the non-aerated and aerated zone of the spillway.
- Air-concentration profiles have improved with the inclusion of the air-model. Velocity fields do not change significantly with the presence of the dispersed air phase.
- Air-entrainment model is needed in detriment of the simple VOF when air-concentration values are significant.

10

Numerical and experimental study of the fundamental flow characteristics of a 3D gully box under drainage

Abstract: Gullies are linking elements of urban drainage systems. Their purpose is to convey the surface runoff to the buried systems under a stated efficiency. While multiple numerical works are focused on the study of the hydraulic behaviour and efficiency, none of them studied the influence of the air. This is due to the lack of a model that simulates the air-entrainment phenomena and consequently the entrapped air. In this work we used experimental data to validate an air-entrainment model which uses a VOF-based method to detect the interface and the SST $k - \omega$ turbulence model. The air is detected in a sub-grid scale, generated by a source term and transported using a slip velocity formulation. Results are shown in terms of free-surface elevation, velocity profiles, turbulent kinetic energy and discharge coefficients. A slight increase of the surface elevation and a better performance of the drainage are found when a small amount of air is present.

10.1 Introduction

Towards an efficient performance of the urban drainage systems, the study of the hydraulic behaviour of their elements is from crucial importance. Gullies, also known as storm inlets are the most common linking-element to convey the water from the surface runoff to the pipe networks with multiple designs and applications (Fig. 10.1a,b,c). In United Kingdom drop manholes can be used in gullies substitution (Fig. 10.1d). Numerous numerical and experimental works can be found in the literature regarding the flow characteristics within pipes networks and in the surface runoff; however, on linking-elements the works are scarce due to the numerous costs to construct such experimental facilities and the difficulty in performing calibration/validation of numerical models. Also, given the worldwide variety on geometrical dimensions of gullies and grate shape, the studies already done tend to have limited applicability.

Djordjević et al. (2013) used the 3D CFD OpenFOAM® code to model a UK-type gully to investigate the interactions between surface flood flow and surcharged pipe flow. Carvalho et al. (2011) used a 2D-V VOF in-house numerical model to simulate a typical Portuguese gully (Fig. 10.1a) under drainage conditions, work that was further extended in Carvalho et al. (2012) to cover both drainage and surcharge conditions using the OpenFOAM® model. An experimental investigation of turbulence characteristics and mean flow properties was made by Romagnoli et al. (2013) for a gully where the flow were coming from the pipes. More detailed work on both drainage and surcharge performance of a gully was made by Leandro et al. (2014b) by means of the characterisation of a 2D middle plane of the gully and a qualitative interpretation of the entrapped air. Martins et al. (2014) conveyed numerical and experimental investigation of a gully under drainage for a wide range on inflows in order to understand the hydraulic performance of this device and investigate the drainage coefficients. Similar work was extended by Lopes et al. (2015b)(Chapter §3) for surcharge conditions. Experimental works on the drainage efficiency also exist for grated inlets (Russo and Gómez, 2011; Sabtu et al., 2016) and continuous transverse gullies (Gómez and Russo, 2009; Lopes et al., 2016a) (Fig. 10.1c).

The presence of air in the urban drainage elements may cause severe damages and considerable operational disruptions (Ramezani et al., 2016), along with reduction of the drainage capacity (Pothof and Clemens, 2010). On the other hand, deficient ventilation of the drainage elements lead to negative pressures and an increase in pool depths of drop manholes (Fig. 10.1d) (Granata et al., 2014b), whereas scarce aeration will diminish the capacity of the sewer to auto-treat the residuals due to the low levels of dissolved oxygen. Furthermore equilibrium of air quantity is needed.

On the basis of the previous results and investigations this work aims to recognize the

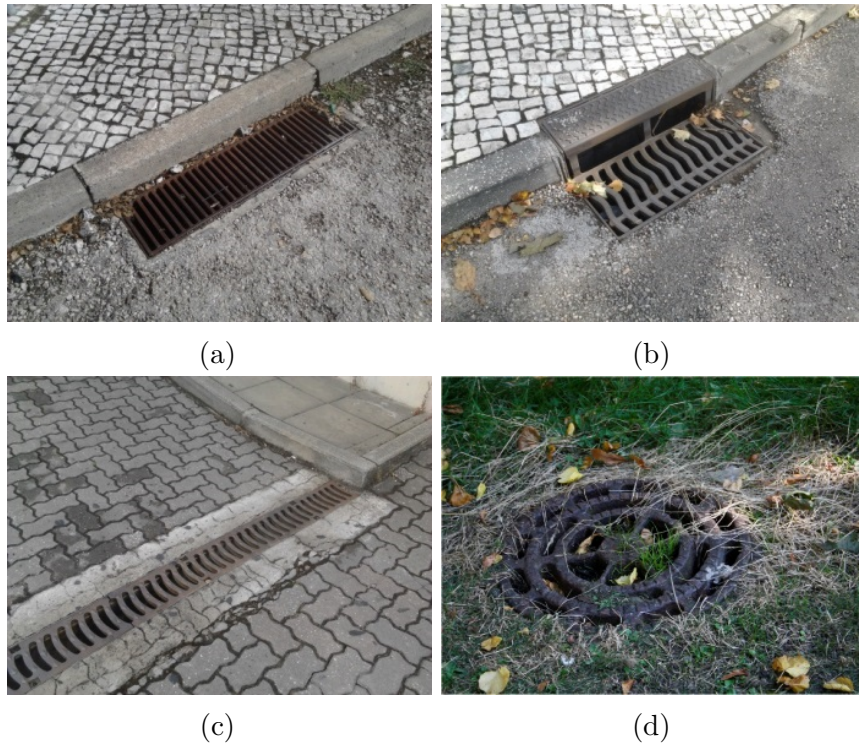


Figure 10.1: Some examples of linking-elements: (a) grated inlet close to a side walk (Coimbra, Portugal), (b) curbside inlet (Coimbra, Portugal), (c) continuous grates placed transversally to the street (Coimbra, Portugal), and (d) grated drop manhole in a park (Sheffield, United Kingdom). Photographs from author.

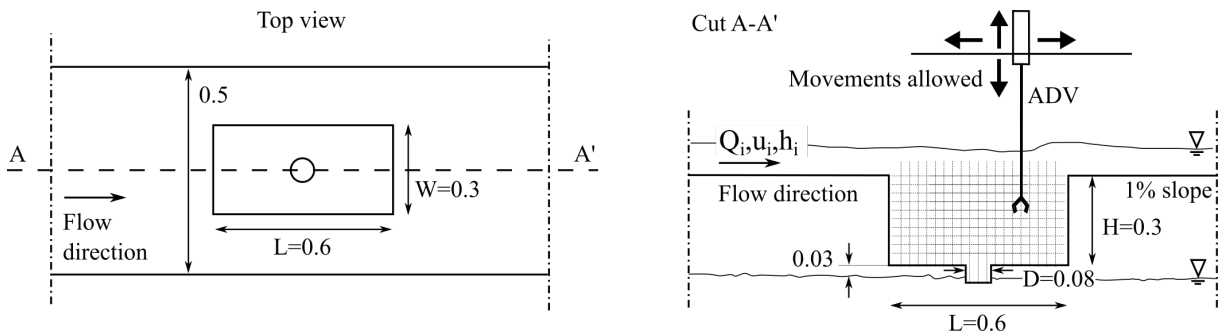


Figure 10.2: Steady-state convergence check for numerical simulations S1 (VOF), S2 (VOF + turbulence) and S3 (VOF + turbulence + air).

influence of the entrapped air within a gully under drainage conditions. A numerical solver implemented in the CFD toolbox OpenFOAM® is used to predict the air-entrainment mechanism at the free-surface and to detect the amount of air that is trapped inside the gully box. The free-surface is calculated using VOF technique and the turbulence statistics with a SST $k - \omega$ turbulence model. Section §10.2 describes the experimental apparatus of a real scale gully box located at the University of Coimbra. Section §10.3 describes the numerical model used amongst the mathematical formulations. Section §10.4 presents the methodology used in this work. Section §10.5 describes and discusses the results. Section §10.6 summarises the work.

10.2 Experimental apparatus

Experimental tests were carried out in a full scale gully box placed in a flume inside a multi-purpose channel at the Hydraulic, Water Resources and Environment Laboratory of the University of Coimbra. Since the experimental results have been published in (Leandro et al., 2014b) solely a brief summary is provided here. The water is pumped from an underground tank to the multi-purpose channel and returned in a closed circuit. The flow is controlled by four butterfly valves, associated to each of the four pumps, and measured by an electromagnetic flow meter. Valves are electronically controlled by a SCADA system. Inside the multi-purpose channel is placed another flume which contains our gully box. This flume has rectangular shape with 1% bottom slope, 8 m long and 0.5 m wide. The gully box has dimensions 0.6 m long (L), 0.3 m deep (H) and 0.3 m wide (W) (Fig. 10.2) and is placed half distance to the flume' side walls. At the bottom of the box, a circular hole with a 0.08 m diameter with an additional pipe of 0.05 m, allows the drainage of the gully.

Flow photographs are captured using a digital Sony Alpha DSLR-A350 camera with

14.2 MP with lens DT18-70 *mm* F3.5–5.6. The camera is fixed in a tripod, distanced in about 2 *m* outwards the channel's side wall. To provide flow illumination, a reflector Photoflex SilverDome NXT with 1000 *W* light is positioned above the gully. A video of the flow is taken using a Panasonic DMC-FS16 (14 MP) in a frame rate of 24 fps. Instantaneous velocities are measured with an ADV probe. The frequency and sampling period are set to 25 *Hz* and 180 *s* respectively.

10.3 Numerical model

10.3.1 General flow equations

The flow in the gully is a complex problem to simulate due to the highly complex three-dimensional rotational flow and the turbulent surface. As such, the solution cannot be achieved using shallow water approaches; but requires a full description of the flow properties just possible with the solution of the Navier-Stokes equations. For an incompressible and isothermal fluid, the mean flow properties can be achieved by the solution of the incompressible Reynolds-Averaged Navier-Stokes equations:

$$\nabla \cdot \bar{\mathbf{u}} = 0 \quad (10.1a)$$

$$\frac{\partial \rho \bar{\mathbf{u}}}{\partial t} + \nabla \cdot (\rho \bar{\mathbf{u}} \bar{\mathbf{u}}) = \mathbf{g} - \nabla p + \nabla \cdot \tau + \mathbf{f} \quad (10.1b)$$

where ρ is the fluid density, $\bar{\mathbf{u}}$ the mean velocity vector, \mathbf{g} the gravitational acceleration, τ the shear stress tensor, p the pressure, \mathbf{f} the surface forces and t the time. The decomposition of the viscous stress term is given by constitutive relation

$$\nabla \cdot \tau = \nabla \cdot (\mu \nabla \bar{\mathbf{u}}) + \nabla \cdot [\mu (\nabla \bar{\mathbf{u}})^T] \quad (10.2)$$

where μ is the dynamic viscosity given by the sum of mean and turbulent dynamic viscosity ($\mu = \bar{\mu} + \mu_t$) admitting Boussinesq hypothesis. In this model, modified pressure (p^*) is used

$$\nabla p^* = \nabla p - \rho \mathbf{g} - \mathbf{g} \cdot \mathbf{x} \nabla \rho \quad (10.3)$$

10.3.2 Free-surface position

The free-surface position is calculated using the interface capturing VOF method. The original VOF, proposed by Hirt and Nichols (1981) is based on the introduction of the

advection equation [Eq. (10.4)]. This equation introduces an indicator function that records the volume fraction of each fluid,

$$\frac{\partial \alpha}{\partial t} + \nabla \cdot (\alpha \bar{\mathbf{u}}) = 0 \quad (10.4)$$

Further, a distinct advection technique is used to control the numerical diffusion of the interface while ensuring boundedness and conservation of the phase fraction (Carvalho et al., 2008; Rider and Kothe, 1997). Many proposals have been done to the initial DAS of Hirt and Nichols (1981), as the geo-reconstruction techniques: SLIC (Noh and Woodward, 1976), PLIC (Youngs, 1984) and isoAdvector (Roenby et al., 2016) and high-resolution compressive schemes: flux-corrected transport, CICSAM (Ubbink and Issa, 1999) and HRIC (Muzaferija et al., 1998). Gopala and van Wachem (2008) and Waclawczyk and Koronowicz (2008) provide a useful comparison between different advection schemes.

The VOF used in this work, and implemented in the OpenFOAM® as *interFoam* solver, has slight modifications to the original VOF. The first is that, a volumetric surface force function (\mathbf{f}_σ), explicitly estimated by the CSF (Brackbill et al., 1991) is added to the momentum equation [Eq. (10.1b)],

$$\mathbf{f} = \mathbf{f}_\sigma = \sigma \kappa \nabla \alpha \quad (10.5)$$

where σ is the surface tension and κ the interface curvature. The physical properties (ϕ) density and viscosity need further to be defined by a weighting of the values for air and water,

$$\phi = \alpha \phi_{water} + (1 - \alpha) \phi_{air} \quad (10.6)$$

Finally in OpenFOAM®, the compression of the interface is achieved by introducing an extra, artificial compression term (Rusche, 2002; Weller, 2008) into the VOF equation [Eq. (10.4)]. This term is given by:

$$\nabla \cdot [\bar{\mathbf{u}}_c \alpha (1 - \alpha)] \quad (10.7)$$

The sub-term $\alpha(1 - \alpha)$ ensures that interface compression is calculated just where the mixture happens and $\bar{\mathbf{u}}_c$ is known as compressive velocity, acting in the perpendicular to the interface. The compression term appears as an artificial contribution to the convection of the phase fraction.

$$\bar{\mathbf{u}}_c = \min[C_\alpha |\bar{\mathbf{u}}|, \max(|\bar{\mathbf{u}}|)] \frac{\nabla \alpha}{|\nabla \alpha|} \quad (10.8)$$

The $\nabla\alpha/|\nabla\alpha|$ term is the interface unit normal vector, which yields the direction of the compressive velocity. The coefficient C_α is an adjustable coefficient (standard $C_\alpha = 1.0$) which determines the magnitude of the compression.

10.3.3 Turbulence closure

Turbulent variables were calculated with the SST $k - \omega$ model (Menter, 1993) which combines the best of two Reynolds-Average Simulation formulations: it takes advantage of the accuracy and robustness of $k - \omega$ model in the near-wall zone, whereas the free-stream region, i.e. the outer part of the boundary layer, is simulated with a high-Reynolds-number formulation of $k - \varepsilon$ model.

10.3.4 Sub-grid air-entrainment model

The air-entrainment model is triggered by solving an additional advection equation for dispersed gas phase.

$$\frac{\partial\alpha_g}{\partial t} + \nabla \cdot (\alpha \bar{\mathbf{u}}_g) = E_g \delta_{fs} \quad (10.9)$$

where δ_{fs} is a switching function that returns the position of the free-surface and $\bar{\mathbf{u}}_g$ is the bubble advection velocity which can be calculated by

$$\bar{\mathbf{u}}_g = \bar{\mathbf{u}} - \bar{u}_r \frac{\mathbf{g}}{|\mathbf{g}|} \quad (10.10)$$

in which \bar{u}_r is the bubble-relative velocity, calculated according to Clift et al. (1978) model:

$$\bar{u}_r = \begin{cases} 4474r_b^{1.357} & \text{if } 0 < r_b \leq 7 \times 10^{-4} \\ 0.23 & \text{if } 7 \times 10^{-4} < r_b \leq 5.1 \times 10^{-3} \\ 4.202r_b^{0.547} & \text{if } r_b > 5.1 \times 10^{-3} \end{cases} \quad (10.11)$$

where r_b is the averaged bubble radius. The source E_g calculates the rate of dispersed gas that penetrates through the free-surface. In this study we adopt the formulation described in the work of Ma et al. (2011b),

$$E_g = \frac{a}{\phi_{ent}} \left\langle \frac{\partial \bar{\mathbf{u}}_{\mathbf{n}}}{\partial \mathbf{n}} \right\rangle \quad (10.12)$$

where $\bar{\mathbf{u}}_{\mathbf{n}}$ is the normal velocity component to the free-surface, a is the amplitude of

the cavities formed at the free-surface, ϕ_{ent} is the interface thickness, given by $\phi_{ent} = 0.05L$, where L is the characteristic linear dimension (equal to the pipe diameter for pipe flows or the water depth in free-surface flows). The symbols $\langle \rangle$ are used to turn the inner parcel to zero if its value is negative. As mentioned in (Lopes et al., 2016b)(Chapter §8), the amplitude of the surface disturbances (a) is considered as having the same order of magnitude as the radius of the turbulent eddies at the free-surface, calculated according to the formulation for the SST $k - \omega$ turbulence model,

$$a = C_\mu^{-1/4} \frac{k^{1/2}}{2\omega} \quad (10.13)$$

where $C_\mu = 0.09$. The transport of gaseous-single-phase is completed when bubbles present in the water phase are able to breakup along the free-surface area. The dispersed gas phase (α_g) is turned to continuous when the volume of the water at each cell is residual. In this work we assumed this residual as $\alpha = 0.1$.

The air-entrainment model is also able to influence the dynamics of the continuous water phase (two-way coupling). This is done by imposing a new conservation law to the volume fractions; guaranteeing the mass conservation for variables α and α_g

$$\alpha_{air} = 1 - (\alpha + \alpha_g) \quad (10.14)$$

In turn, the physical properties (ϕ) of the two-fluid mixture, such as density or viscosity, are weighted in the volume of each fluid

$$\phi = \alpha \phi_{water} + (1 - \alpha - \alpha_g) \phi_{air} \quad (10.15)$$

10.3.5 Mesh, initial and boundary conditions

A regular non-uniform mesh with variable grid sizing space from 0.01 m to 0.04 m is used in this work (Fig. 10.3). The largest cell is placed on top of the domain ($V_{cell} = 64 \text{ cm}^3$) whereas the smallest cell volume is generated inside the gully box ($V_{cell} = 1 \text{ cm}^3$). The mesh is adapted from work of Martins et al. (2014), created with *blockMesh* utility from OpenFOAM®. The initial condition comprehends a column water with the same level and velocity as the inlet.

Five types of BC are applied to this case (Fig. 10.3). The “inlet surface” boundary allows the flow enter the domain by setting Dirichlet-BC whereas the “outlet surface” allows the flow to leave the domain by fixing pressure. The boundary “outlet pipe” has the value of p^* pressure imposed using Dirichlet-BC. The “atmosphere” boundary allows exchanges of air. “Wall” boundary imposes zero velocity using Dirichlet-BC.

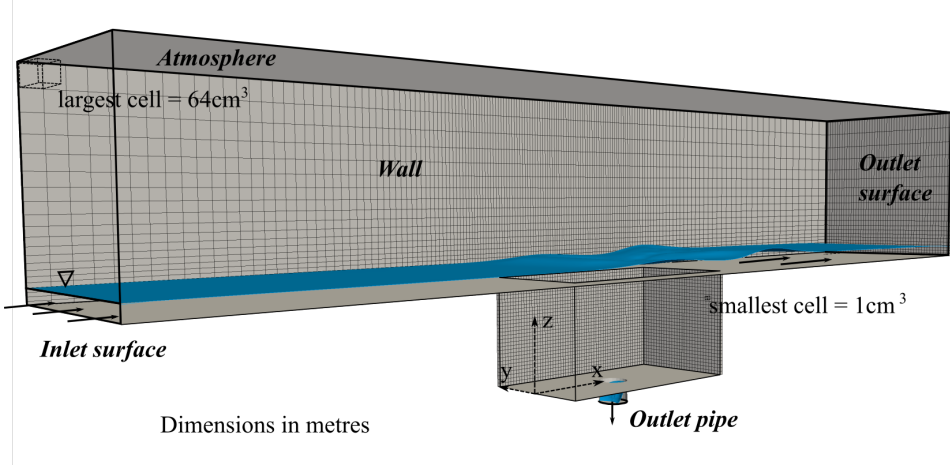


Figure 10.3: Numerical mesh and boundary conditions definition.

10.3.6 Model discretisation and solution methods

The governing equations were discretised in time using the backward Euler method. The gradient terms are discretised using linear interpolation from cell centres to face centres. Different schemes are used to discretise the convective terms. The term $\nabla \cdot (\rho \bar{u} \bar{u})$ of the momentum equation uses Total Variation Diminishing (TVD)-limited form of central-differencing in the “V” (vector-field) version. The “V” schemes are calculated based on the direction of most rapidly changing gradient, resulting in a less accurate but very stable solution. Van Leer scheme is used for $\nabla \cdot (\alpha \bar{u})$ and upwind scheme is used in $\nabla \cdot (\alpha \bar{u}_g)$. For the second convective term of VOF equation [Eq. (10.4)], the so-called *Interface Compression* scheme is used in order to bound the solution of the compressive term between 0 and 1.

In order to ensure boundedness of the phase fraction and avoid interface smearing, the solution of the VOF equation is done with the MULES. In this study, the PISO procedure proposed by Issa (1985) is used for pressure-velocity coupling in transient calculations. The PISO was calculated 3 times in each time step.

10.4 Methodology

10.4.1 Experimental methodology

The discharge tested corresponds to $Q_i = 22 \text{ l/s}$ and $h_i = 0.037 \text{ m}$. For this combination the mean velocity is $u_i = 1.18 \text{ m/s}$ and $Fr = 1.94$ at the free-surface. Unlike the work of Martins et al. (2014), the bottom outlet of the gully is slightly under surcharge to simulate the real conditions of pressurised systems (Fig. 10.2). This surcharge condition was also

experienced in (Leandro et al., 2014b; Páscoa et al., 2013).

The captured video is used to trace the free-surface position using a Computational Vision Model (Roque, 2011). Video records a total of 720 images. Each image is firstly divided in several horizontal sub-domains. Then, image treatment and segmentation techniques are used to trace the two largest lines found in each sub domain. While one of these lines represents the channel bottom, the other detects the free-surface position, and the distances between the lines midpoints correspond to the flow water depths for each sub-domain.

A spatial grid defined with uniform 0.03 m spacing was chosen to measure the velocities (Fig. 10.2). The bottom of the grid is distanced 0.05 m above the base of the gully box, which is well above the minimum (of 0.02 m) required to avoid boundary effects. A total of 171 points were measured. This resolution has shown to be sufficient to characterize the large vortices structures inside the gully box (Leandro et al., 2014b). ADV signal is post-processed in this work by imposing minimum thresholds to two data quality indicators normally associated with acoustic Doppler data: the Correlation (COR) and the SNR. The COR measures the level of similarity between two consecutive pulses of the ADV. The SNR is calculated using the signal amplitude and background noise level. In the present study we used $\text{SNR} > 15$ and $\text{COR} > 70$ as such values are typically recommended by many ADV manufacturers. According to Wahl (2000), samples with $\text{COR} < 70$ can still be used when the signal to noise ratio is high and the flow is relatively turbulent. The presence of spikes in the water velocity time series were detected and deleted by means of the phase-space thresholding method proposed by Goring and Nikora (2002).

10.4.2 Numerical methodology

In total, three different simulations are setup to study the 3D gully under drainage conditions (Table 10.1). Simulation S1 corresponds to the simulation of the gully using VOF technique to calculate the free-surface calculation and RANS equation to model the flow characterization. Simulation S2 includes the SST $k - \omega$ turbulence model to the previous simulation in order to calculate the influence of the turbulence on the mean flow. Simulation S3 adds the air-entrainment model to S2. In order to surpass some numerical instabilities of the air-entrainment model when the water drops into the gully box, S3 was sorely activated on top of S2 when this model has achieved 10 s of total running (see also section 10.5.1).

As referred before, since bottom outlet of the gully is slightly under surcharge, the pressure of this boundary is set to hydrostatic considering a head of 2 cm of water.

Table 10.1: Summary of simulation cases tested in this work.

Simulation ID	Model equations		
	RANS + VOF model	Includes turbulence model	Includes air-entrainment model
S1	Yes	No	No
S2	Yes	Yes	No
S3	Yes	Yes	Yes
CPU Time (s)	103.94	79.19	102.42

10.5 Results and Discussion

10.5.1 Steady-state achievement

The achievement of a steady-state condition in numerical simulations is sensible to initial and boundary conditions, model properties and geometry. In the authors' previous works, it was shown that running the simulation for 15 s is enough to achieve the convergence of the main flow properties (Carvalho et al., 2011; Leandro et al., 2014b; Lopes et al., 2015b; Martins et al., 2014). Figure 10.4 shows that herein, all simulations also converged to the steady state within 15 s of time simulation. In S2 and S3 the volume of water was converged to a much constant and stable value than in S1. However, for the last 5 s, the relative errors to the mean water volume fraction remain smaller than 0.8% for all simulations. The inclusion of the turbulence model preserved more 0.8% of water in the domain when compared with S1. The small collapse of water volume, observed at 10 s in simulation S3 is due to the activation of the air-entrainment model. This suddenly imposed a higher quantity of air inside the domain, which has recovered after 3 s (13 s in the run time).

10.5.2 Free-surface position

Figure 10.5 shows the comparison between numerical and experimental free-surface position. Experimental free-surface is detected using the Computational Vision Model. Mean water level is marked with dots in Fig. 10.5 whereas error bars are used to bound the maximum and minimum values of free-surface elevation. Numerical free-surface is given by isolines of α . Three isolines of $\alpha = 0.1, 0.5$ and 0.9 are plotted, representing respectively the levels free-surface levels in which the fraction of water is 10, 50 and 90 %. A good agreement is found between the numerical and the experimental free-surface in a zone where the free-surface is smooth, i.e. $x < 0.3$ m. The position of the hydraulic jump is also well

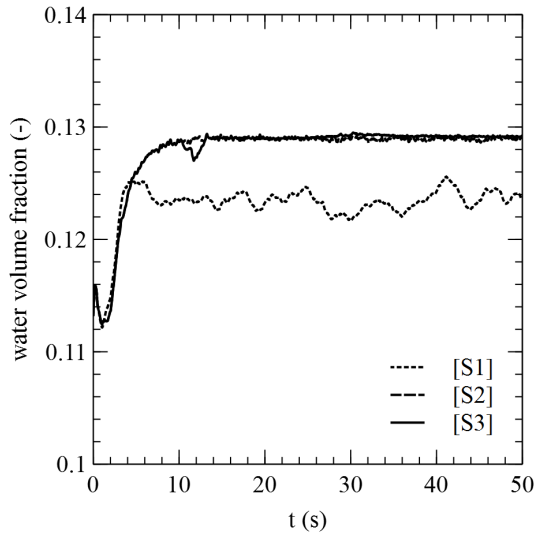


Figure 10.4: Steady-state convergence check for numerical simulations S1 (RANS + VOF), S2 (RANS + VOF + turbulence) and S3 (RANS + VOF + turbulence + air).

detected in all simulations. Using S1, the best approximation of the free-surface elevation is given by $\alpha = 0.1$, whereas for S2 and S3, the free-surface must be set as $\alpha = 0.5$.

10.5.3 Velocity and turbulence

Figure 10.6 presents the time-averaged velocity profiles at centre-channel measured with ADV (Fig. 10.6a) and simulated by S1 (Fig. 10.6b), S2 (Fig. 10.6c) and S3 (Fig. 10.6d). In the experimental profile (Fig. 10.6a), the points measured near the water surface were discarded due to low correlation found in the ADV signal. Pearson's-R2 correlation coefficients are calculated between numerical and experimental, horizontal (\bar{u}_x) and vertical (\bar{u}_z) components of the velocity.

Simulations S2 and S3 present some slight improvements regarding the accuracy of the velocity patterns. Notorious progresses are verified in terms of the velocity along z-axis between S1 and S2/S3, as $R^2_{\bar{u}_z}$ [S1] is 0.9281, whereas $R^2_{\bar{u}_z}$ [S2] and $R^2_{\bar{u}_z}$ [S3] are 0.9426 and 0.9433 respectively. The difference is mostly found on the left side of the gully box where S2 and S3 detects a vertical velocity of $\approx 0.25 \text{ m/s}$, which is in accordance to experimental. The horizontal velocity decreases in its accuracy from S2 to S3. However if we observe the flow pattern it looks quite similar. The Pearson's-R2 coefficients between S2 and S3 agree with the previous assumption as $R^2_{\bar{u}_x}$ [S2-S3]=0.997 and $R^2_{\bar{u}_z}$ [S2-S3]=0.994.

The Turbulent Kinetic Energy (TKE) yields the value of kinetic energy generated by the fluctuation velocity field (\mathbf{u}'),

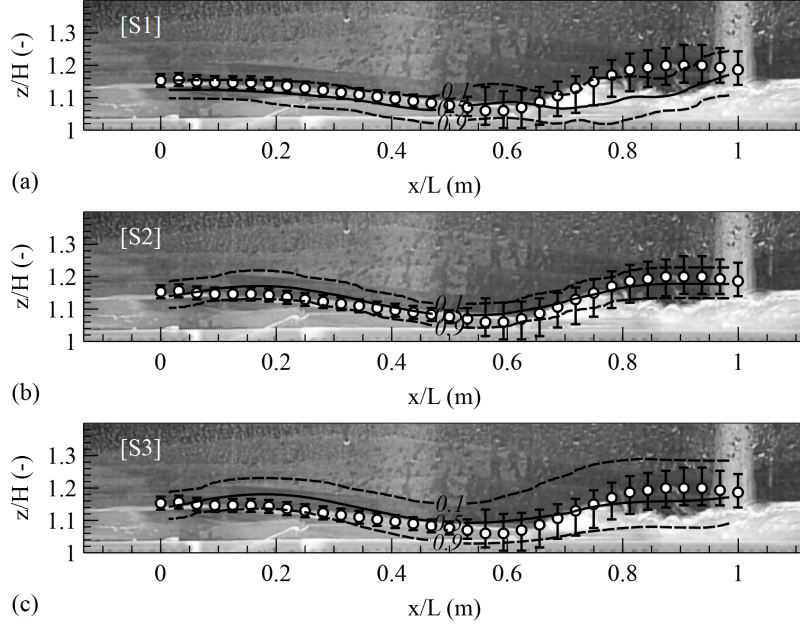


Figure 10.5: Free-surface position detected by $\alpha=0.1, 0.5$ and 0.9 at $y=0$ m for simulations: (a) S1 (RANS + VOF), (b) S2 (RANS + VOF + turbulence) and (c) S3 (RANS + VOF + turbulence + air). Dots mark the experimental free-surface position detected by the Computational Vision Model.

$$k = 0.5(u'_x{}^2 + u'_y{}^2 + u'_z{}^2) \quad (10.16)$$

Figure 10.7 shows the distribution of TKE at the centre-channel measured with ADV (Fig. 10.7a) and simulated using S3 (Fig. 10.7b), which is very similar to S2. We opted by not showing S2 profile as it is similar to S3. In the experimental profile (Fig. 10.7a), zero values of turbulent kinetic energy represent the points that were discarded from the measurement due to low correlation signal.

The overall magnitudes of TKE are in accordance to experimental despite some deviations in the two top corners. On the top-left corner, below the stream that feeds the gully box, the numerical model returns higher values of TKE than in experiments. However, as TKE is mostly generated due to fluid shear, friction or buoyancy, we believe that numerical results are more correct. The incoherent values of experimental TKE may be due to the lower correlation signal of the ADV. On the top-right corner the experimental profile has values of TKE in the order of $0.14 \text{ m}^2/\text{s}^2$. These high values are comprehensive as the flow collides with the top-right corner of the gully and turns down, contributing substantially to the generation of a large eddy inside the structure.

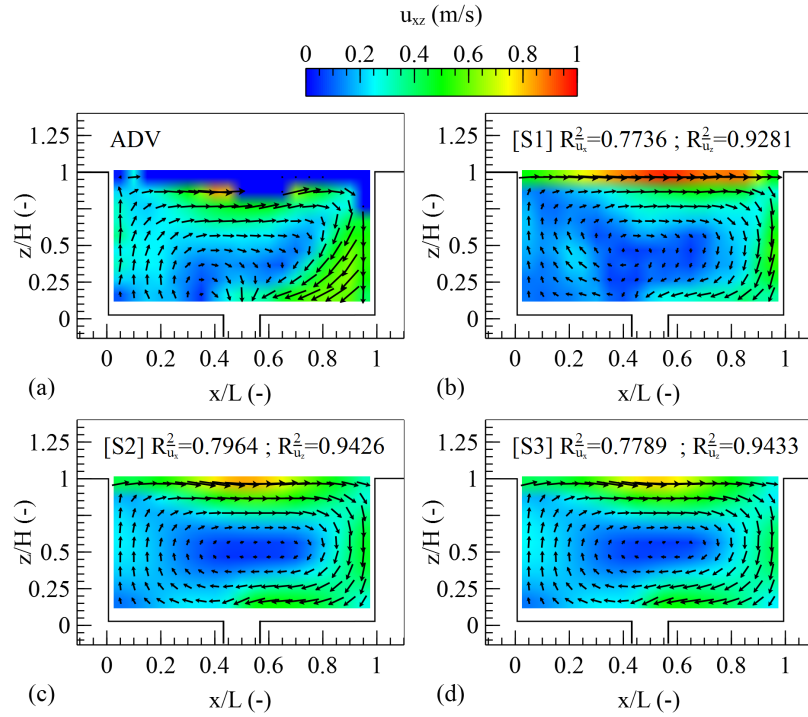


Figure 10.6: Time-averaged velocity fields at centre-plane of the gully: (a) measured with ADV, and simulations (b) S1 (RANS + VOF), (c) S2 (RANS + VOF + turbulence) and (d) S3 (RANS + VOF + turbulence + air). Blue area on top of ADV measurements indicate a zone where the signal correlation was low and no measurements were done.

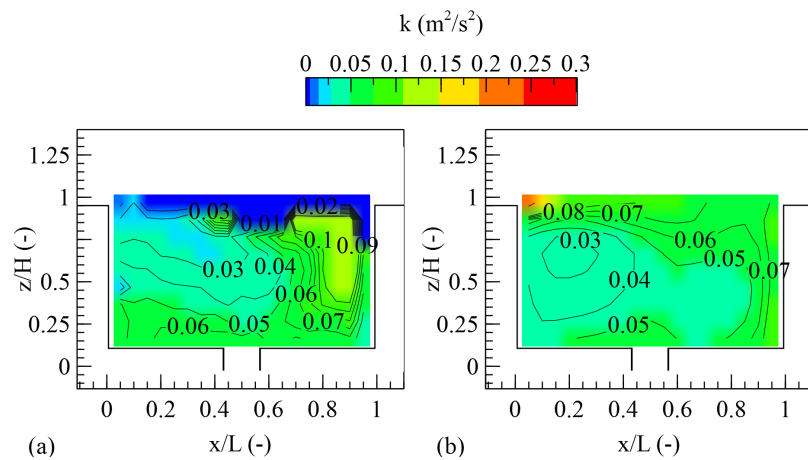


Figure 10.7: Time-averaged turbulent kinetic energy profile at centre-plane of the gully: (a) measured with ADV, and (b) simulation S3 (similar results for S2) (RANS + VOF + turbulence + air).

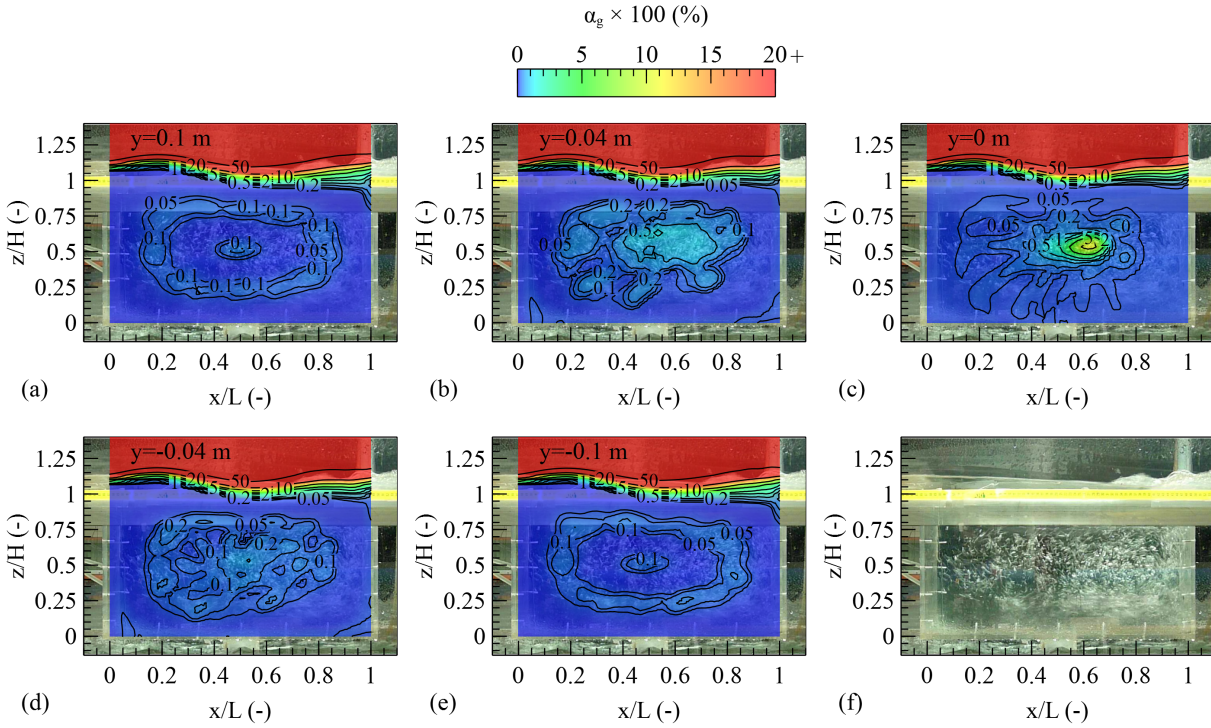


Figure 10.8: Time-averaged air-concentration profiles (45-50s) using simulation S3, at positions (a) $y=0.1$ (back panel), (b) $y=0.04$, (c) $y=0$, (d) $y=-0.04$ and (e) $y=-0.1$ m (front panel). (f) Experimental observation.

10.5.4 Time-averaging of air-concentration profiles

Figure 10.8 presents the time-averaged air-concentration profiles in the time interval 45-50 s using simulation S3. Profiles are taken at $y=-0.1$ (front panel), -0.04, 0, 0.04 and 0.1 m (back panel). Qualitative comparison can be done to the photograph showed in Fig. 10.8f.

The air-profiles at $y=-0.1$ and $y=0.1$ present quite similar features. These profiles are characterised by a large ring of air that occupies almost all the gully and a peak of air-concentration in the centre (maximum of 0.1%). In the positions $y=-0.4$ and $y=0.4$ m, the air-profiles do not show such similarity. Although the profile looks like a stain, their shape is different. Finally, in the middle profile, the air is concentrated at the point (0.62,0.55), where it reached the peak of 5%. This was also the maximum value of air-concentration found in the gully. Although no experimental data is present to compare these values, the given order of magnitude is plausible since the ADV instrument would not give good correlations ($COR>70\%$) when the air-concentration is above 10%.

As the profiles of air are different in y -direction, none of them is representative of the photograph visible in background (Fig. 10.8f). As such, Fig. 10.9 presents the time-averaged air-concentration profiles, integrated over y -axis for every 5 s of simulation. For

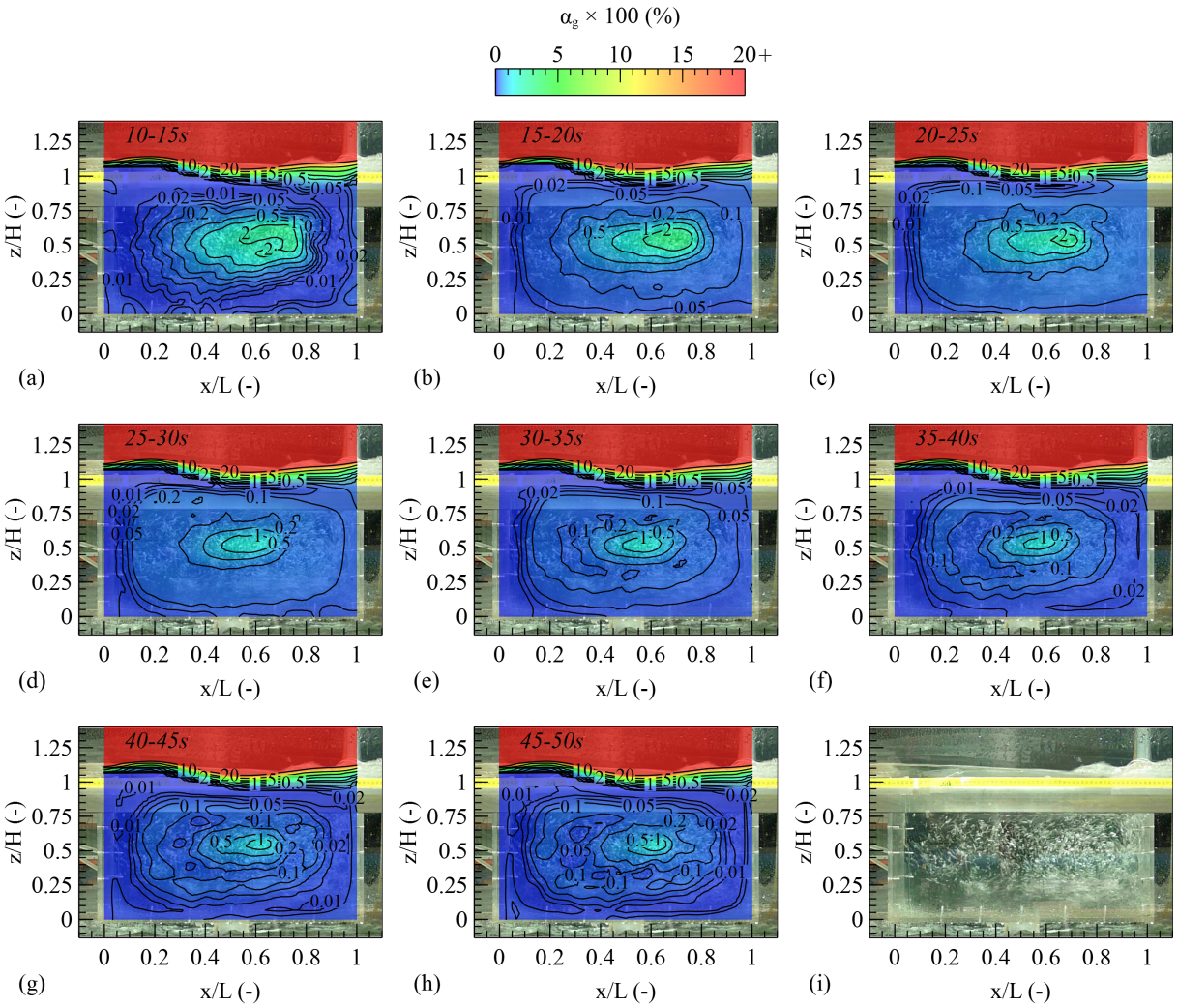


Figure 10.9: Time-averaged air-concentration profiles interpolated over y-axis using simulation S3 in the time intervals: (a) 10-15 s, (b) 15-20 s, (c) 20-25 s, (d) 25-30 s, (e) 30-35 s, (f) 35-40 s, (g) 40-45 s and (h) 45-50 s. (i) Experimental observation.

this integration we used a discrete air-profile every 2 cm in the y-direction. A qualitative comparison can be done to the photograph shown in Fig. 10.9i.

The first aspect that should be highlighted is that this integrated profile is much more understandable in terms of dispersion of air concentration when compared to the single profile showed in Fig. 10.8. A steady state of air-concentration has been achieved after 25 s of simulation, as the further profiles do not change the aspect and the distribution of air within the gully. However, it must be noted that this steady state was achieved 10s after the steady state admitted initially ($t=15s$). In fact, the increment of air volume is diluted in the error assumed for the initial steady state achievement, turning it almost indistinguishable when calculated the total water volume fraction of the domain (Fig. 10.4). Moreover, the

air-entrainment model is just turned on when accomplished 10s of simulation S2, delaying the complete mixture with the water. From 25 s to 30 s of simulation (Fig. 10.9d) the maximum air-concentration value is around 1% in the point that is not centred with the gully but slightly disposed to the right, with coordinates (0.62,0.55). At the left side of the gully no air is found, which is in accordance to the photograph (Fig. 10.9i).

For this flow rate, the hydraulic jump occurring on top of the gully is the only source of air, result that is in line with previous assumptions (Leandro et al., 2014b). This air is further carry down to the gully following the downstream wall. While some bubbles are trapped in the vortex, some bubbles are allowed to escape through the bottom orifice or the free-surface. The latest is likely to happen when the outer part of the vortex reaches the interface. The swirling regime of the vortex is characterised by zero velocity on the centre (Fig. 10.6) and high tangential velocities in the outer part. This is the reason why a large number of bubbles are trapped on its centre, whereas a small percentage is flowing across the entire gully.

10.5.5 Discharge coefficients

Weir and orifice coefficients can be obtained experimentally and numerically as done in (Martins et al., 2014), following the equations

$$Q_w = C_w b_w \sqrt{2gh^3} \quad (10.17)$$

$$Q_o = C_o A \sqrt{2gh} \quad (10.18)$$

where, the subscripts w and o stand for weir and orifice respectively, Q is the discharge flow, A the area, b the width, g the acceleration due to gravity and h the uniform water depth upstream the weir or orifice. Figure 10 presents through lines, the drainage coefficients C_w and C_o according to the power law

$$C_{w,o} = b \times h^c \quad (10.19)$$

where b and c are coefficients given in (Martins et al., 2014). $C_w E$, $C_w N$, $C_o E$ and $C_o N$ are the drainage coefficients for weir and orifice formulated based on the experimental (E) and numerical (N) data. In the experiments and simulations of Martins et al. (2014), the bottom outlet was under atmospheric pressure as the gully had free outflow. In the present work, the pipe outlet is under surcharge; therefore, the drainage coefficients previously formulated cannot be directly compared to our case. Simulations S1*, S2* and S3* uses the same numerical methodology as S1, S2 and S3, excepting the bottom outlet pipe boundary condition that is now a free-outlet boundary. This means that S1* is a copy of

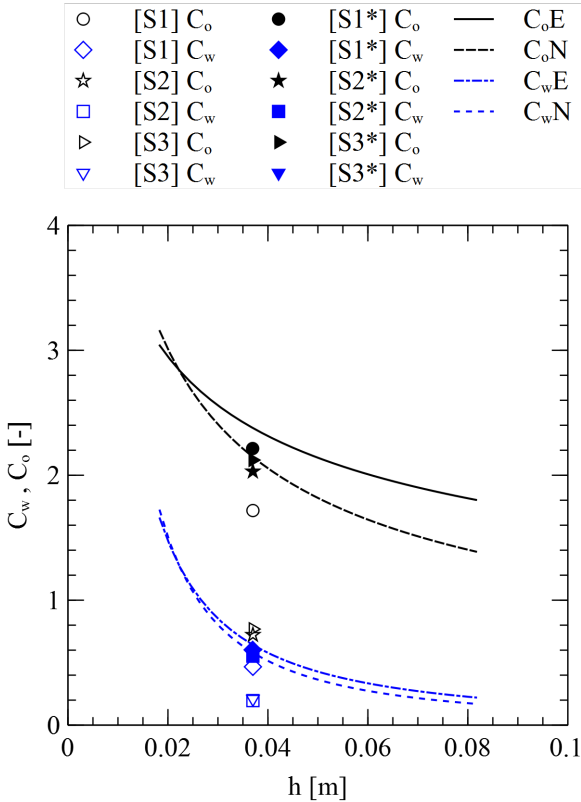


Figure 10.10: Weir (C_w) and orifice (C_o) discharge coefficients for simulations S1, S2 and S3. Lines are the coefficients found by Martins et al. (2014). Asterisks (*) are simulations where the outlet boundary conditions characterise the experiments of Martins et al. (2014).

the simulations performed by Martins et al. (2014).

The drainage coefficient decrease for both weir and orifice formulations when the turbulence and air-entrainment model was activated. The introduction of an air-entrainment formulation still under-predicts C_o when compared to the experimental coefficients C_oE . As such the reason for the underestimated coefficients given by simulations of Martins et al. (2014) cannot be associated to the absence of an air-entrainment model. In the simulations where the gully has a free-outlet (simulations marked with asterisk), the drainage coefficient does not change too much with the inclusion of turbulence or air-entrainment model. In contrast, for the pressurized outlet (simulations without asterisk), it can be noticed a large difference between S1 and S2/S3. As we have seen in section §10.5.3, the velocity fields for S2 and S3 are more accurate than S1, therefore such difference is associated with the inclusion of the turbulence model.

Another relevant aspect we can discuss is the influence of air to the drainage. For this particular case, the amount of air found in the gully box almost does not influence the drainage coefficient, and consequently, the drainage efficiency. The inclusion of air should

decrease the drainage efficiency as the volume occupied by the air would at some point interrupt the quantity of water that passes through the outlet (Pothof and Clemens, 2010; Ramezani et al., 2016). Nevertheless, for S3 and S3* the inclusion of air has increased C_o when compared to S2 and S2*. It could be that while considering the contribution of air, an increasing of momentum may occur as the air within the boundary layer is known as a reducer of the shear stress (Ackers and Priesley, 1985; Chanson, 1993). However, more tests on other discharges are needed to verify this finding.

Imposing pressure on the pipe outlet, the simulations returns the coefficients without asterisks. As expected, the drainage coefficients were reduced. Such reductions are in the order of 22.4% for S1, 64.4% for S2 and 63.8% for S3 in comparison to the coefficients for the simulations with free outlet.

10.6 Conclusions

In this work, a 3D gully structure is simulated using a solver that combines the interface tracking VOF model for free-surface detection, with a sub-grid air-entrainment model to simulate the self-aeration process of the flow, and a SST $k - \omega$ model turbulence model to predict the turbulent statistics.

Following conclusions can be retrieved from this work:

- The air-concentration profiles are in qualitative good agreement when compared to the photographs. Modelled velocity profiles and turbulent kinetic energy are comparable to the ones measured with ADV.
- The numerical accuracy of the velocity patterns were more influenced by the turbulence closure than the air-entrainment model.
- Values of air-concentration do not surpass 6% in the middle profile. Given such low value, it is not surprising that both the velocity profiles and the drainage coefficients do not change with the simulation of air in the gully.
- The increment of pressure on gully's outlet diminishes the drainage coefficient and efficiency. For this specific case, imposing a water level 3 cm below the bottom of the box, we found decrements of about 60% on the drainage.
- For the quantity of air found in the pressurized gully we even observed an increment of drainage efficiency when the air is modelled. Such conclusion might be connected to the reduction of shear stress and the increasing of momentum.

- The free-surface elevations when S1 is applied, is mostly given by the α 's isoline that represent 10% of in each cell water. When either the turbulence model (simulation S2) or the air-entrainment model (simulation S3) is activated, the free surface is well predicted by the isoline of α equals to 0.5.

11

Final Remarks

11.1 Conclusions

The work presented in this Thesis was carried out in order to replicate and analyse the free-surface flow characteristics in hydraulic structures using the VOF model present in the OpenFOAM®, and further enhance the ability of the original solver to deal with the air-entrainment process. This aim is achieved by completing all intermediate objectives defined in section §1.2.

Chapter 2 provides a literature review about free-surface flow modelling, dispersed-continuous phase flow modelling and air-entrainment modelling. VOF and LS are the most common methods when performing free-surface interface capturing (§2.1.3.1). However, when the methodology include dispersed particles in continuous fluids, these no longer hold as the best methodologies and other formulations should be used. Examples of this are the Two-fluid model (§2.2.1), the Algebraic Slip Mixture Model (§2.2.2) and the Euler-Lagrange model (§2.2.3). In the nature, most of the flows combine the two aforementioned situations where at least two continuous phases and dispersed particles are present. A combination of an interface capturing method with continuous-dispersed formulation is needed to simulate such cases. Such models were reviewed in §2.3. For the study of the air-entrainment process more advanced models than previous are needed, normally relying in introduction of a robust and accurate sub-grid model that locates the point of aeration and the rate of air bubbles produced (§2.4). From all the air-entrainment models studied in this Thesis, the results given by the sub-grid model of Ma et al. (2011b) is the most promising, and was, as consequence, used in this work.

A gully under surcharge condition was studied in Chap. 3. ADV measurements were carried out on the vicinity of the jet and image techniques were applied to measure the position of the free-surface. It was observed that this type of flow is characterised by a free-stream water jet placed above the inlet pipe, and that the height of this jet increases along with the sewer overflow. Numerical simulations showed two evident eddies at the gully box, one at each side of the jet. Relations between 'flow height'-'sewer overflow' and 'pressure'-'sewer overflow' were proposed. These relations present a step toward to the correct calibration of the linking elements of the Urban Drainage Models.

A numerical investigation of the drainage efficiency of a continuous transverse gully with grate's slots was performed in Chap. 4. It was shown that the numerical model used is much more efficient in medium and high efficiencies range, which are mostly found in urban drainage systems, than in low efficiencies. A linear relation was found between the flow Froude number and the efficiency of the grate, which was in agreement with experimental measurements.

A scaled manhole was experimentally studied in Chap. 5. Recirculation processes

inside the manhole using the mean velocity profiles were acquired experimentally with an ADV and the respective turbulence analysis. The air concentration values inside the manhole were also measured with an in-house resistive dual-tip probe. Two scenarios were tested: (1) simultaneously flow from the surface to the manhole and flow on the subsurface system and (2) flow only from the surface to the manhole. It was observed that in scenario (1) the presence of the pipe inlet influences the flow pattern inside the manhole. In both configurations, the flow adheres to the manhole wall creating a torus shaped recirculating pattern with velocity vectors pointing downwards near the wall and upwards near the centre of the manhole.

A numerical methodology to replicate the free-surface was developed in Chap. 6 by comparing the modelled free-surface, obtained by a Volume-of-Fluid based model, with the flow depths measured with three ultrasonic sensors in a stepped spillway. It was found that there is no global volume fraction isoline that predicts the overall shape of free-surface, contrary to what is assumed when using the constant $\alpha = 0.5$. Isoline of $\alpha = 0.7$ should be assumed in the non-aerated zone, whereas $\alpha = 0.5$ is just applicable when free-surface is non aerated. It was shown that the experimental measurements of flow depths using an ultrasonic sensor allowed the definition of the different flow regions over a stepped spillway.

Chapter 7 investigates the alternating skimming flow regime. This regime was observed by widening the spillway from 0.3 m to 0.5 m. A mass and momentum exchange is caused by the presence of cross waves in the transversal direction of the spillway. The water depth is higher in the intersection of these cross waves, forming a skimming flow-type 2 (SK2) regime. In the non-intersections, a SK1 regime is formed. Consecutive SK1 and SK2 regimes originate the seesaw pattern of water depths observed in the longitudinal direction of the spillway. The presence of an alternating skimming flow is more evident at step cavities than in the free-stream flow. This work also showed that the centre-channel measurements may be insufficient for full regime definition.

In Chap. 8, together with the investigation of the influence of mesh size to the quality of the interface representation using a VOF based model, a reformulated term was used to calculate the bubble formation at the free-surface. Two cases were studied: a 2D dam break and a 3D plunging jet. The magnitude of air-entrainment term does not suffer much variation with the grid size, which let us to believe that the new concept for wave's amplitude also improved the model on its independence of the mesh size. In contrast, the free-surface position is much more sensible to the grid size. In case of 3D plunging jet, it was observed that the mesh refinement is preponderant to the definition of the air cavities and consequently the correct prediction of the aeration point.

Chapter 9 presented the developed air-entrainment model. One-way and two-way coupling versions of this model are test along with sensitivity tests to show the accuracy

of the new source term that does not require calibration. The model is tested in the case of a stepped spillway (same case study presented in Chap. 6 and Chap. 7). It was shown that numerical air-concentration profiles were improved when the air-entrainment model was switched on. Same has happened with the flow depths in the fully-aerated zone. The transition between the non-aerated and aerated zone of the spillway in terms of flow depths and aeration was improved with the inclusion of limiters to free-surface inward velocity and turbulence at interface. In this chapter was possible to verify that water velocity fields do not change significantly with the presence of the dispersed air phase.

Chapter 10 presented the complete characterisation of the flow into a gully, achieved by the inclusion of the air-entrainment model developed in Chap. 9. The air-concentration profiles were found to be in qualitative good agreement when compared to the photographs. The numerical accuracy of the velocity patterns were more influenced by the turbulence closure than the air-entrainment model. For the quantity of air found in the gully (maximum of 6%) it was observed an increment of drainage efficiency when the air is modelled.

11.2 Research question

In §1.1 a question was presented to be discussed and analysed in this Thesis: "Is it possible to adapt a 3D CFD open-source model, which uses VOF method to detect the free-surface position, to compute the air-entrainment process in hydraulic structures?"

This research question was answered through the development of an air-entrainment model which combines the interface tracking VOF model, with a sub-grid air-entrainment model to simulate the self-aeration process of the flow. This Thesis provided an insight on the assessment of quality of VOF based model to predict the free-surface position and the flow physics. Simulations using the *interFoam* solver from open-source OpenFOAM® toolbox showed that VOF model is a very robust and reliable solution when applied to a gully and a stepped spillway. The gully was study both in drainage and surcharge condition. The appearance of an unclassified alternating skimming flow regime is replicated and described in the stepped spillway.

The air-entrainment is solved by adding an extra transport equation to solve the dispersed phase, where the motion is calculated according to slip velocity formulation. The amount of air created at the free-surface is calculated by a source term that requires no calibration factor. The quality of this new solver is tested in the solution of the flow physics in a gully and a stepped spillway with very accurate results. The new solver is published in the open-source code OpenFOAM®.

11.3 Future work

Further research may include:

- Inclusion of effects of drag, lift, turbulent dispersion and virtual mass to the momentum exchange force between dispersed air and continuous water;
- Improvement of the bubble breakup system;
- Inclusion of the bubble size function to permit different bubble diameters in same domain;
- Implementation of Level-Set function for more precise detection of the free-surface position.

References

- Abramovic, G. (1963). *The Theory of Turbulent Jets*. MIT Press.
- Ackers, P. and Priesley, S. J. (1985). Self-aerated flow down a chute spillway. In *Proceedings of 2nd International Conference on the Hydraulics of Floods and Flood Control*, pages 1–16, Cambridge, England. British Hydraulics Research Association, Fluid Engineering.
- Afshar, N. R., Asawa, G. L., and Raju, K. G. R. (1994). Air concentration distribution in self-aerated flows. *Journal of Hydraulic Research*, 32(4):623–631, [doi:10.1080/00221686.1994.9728359](https://doi.org/10.1080/00221686.1994.9728359).
- Albadawi, A., Donoghue, D., Robinson, A., Murray, D., and Delauré, Y. (2013). Influence of surface tension implementation in Volume of Fluid and coupled Volume of Fluid with Level Set methods for bubble growth and detachment. *International Journal of Multiphase Flow*, 53:11–28, [doi:10.1016/j.ijmultiphaseflow.2013.01.005](https://doi.org/10.1016/j.ijmultiphaseflow.2013.01.005).
- Amador, A. (2005). *Comportamiento Hidráulico de los Aliviaderos Escalonados en Presas de Hormigón Compactado*. Phd thesis (in spanish), UPC, Barcelona, Spain.
- Amador, A., Sánchez-Juny, M., Dolz, J., F.Sánchez-Tembleque, and Puertas, J. (2004). Velocity and pressure field in skimming flow in stepped spillways. In F. Yazdandoost and J. Attari Edition, editor, *Intl Conf. on Hydraulics of Dams and River Structures*, pages 179–285. Balkema Publ., The Netherlands.
- Ashgriz, N. and Poo, J. Y. (1991). FLAIR: Flux line-segment model for advection and interface reconstruction. *Journal of Computational Physics*, 93(2):449–468, [doi:10.1016/0021-9991\(91\)90194-P](https://doi.org/10.1016/0021-9991(91)90194-P).
- Batchelor, G. K. (1967). *An Introduction to Fluid Dynamics*. Cambridge University Press.
- Baylar, A. and Emiroglu, M. E. (2014). An Experimental Study of Air Entrainment and Oxygen Transfer at a Water Jet from a Nozzle with Air Holes. *Water Environment Research*, 76(3):231–237.

Begum, S., Rasul, M. G., Brown, R. J., Subaschandar, N., and Thomas, P. (2011). An Experimental and Computational Investigation of Performance of Green Gully for Reusing Stormwater. *Journal of Water Resuse and Desalination*, 1(2):99–112, doi:10.2166/wrd.2011.010.

Bennett, P. R., Stovin, V. R., and Guymer, I. (2011). Improved CFD Simulation Approaches for Manhole Mixing Investigations. In *12th International Conference on Urban Drainage (ICUD12)*. IWA Publishing, London, UK.

Berberović, E., van Hinsberg, N. P., Jakirlić, S., Roisman, I., and Tropea, C. (2009). Drop impact onto a liquid layer of finite thickness: Dynamics of the cavity evolution. *Physical Review E*, 79(3):1–15, doi:10.1103/PhysRevE.79.036306.

Biń, A. K. (1993). Gas entrainment by plunging liquid jets. *Chemical Engineering Science*, 48(21):3585–3630, doi:10.1016/0009-2509(93)81019-R.

Boes, R. M. and Hager, W. H. (2003). Two-Phase Flow Characteristics of Stepped Spillways. *Journal of Hydraulic Engineering*, 129(9):661–670, doi:10.1061/(ASCE)0733-9429(2003)129:9(661).

Bombardelli, F. A., Hirt, C. W., and García, M. H. (2001). Computations of Curved Free Surface Water Flow on Spiral Concentrations. *Journal of Hydraulic Engineering*, 127(7):629–631, doi:10.1061/(ASCE)0733-9429(1999)125:11(1126).

Bombardelli, F. A., Meireles, I., and Matos, J. (2010). Laboratory measurements and multi-block numerical simulations of the mean flow and turbulence in the non-aerated skimming flow region of steep stepped spillways. *Environmental Fluid Mechanics*, 11(3):263–288, doi:10.1007/s10652-010-9188-6.

Borges, J. E., Pereira, N. H. C., Matos, J., and Frizell, K. H. (2010). Performance of a combined three-hole conductivity probe for void fraction and velocity measurement in air–water flows. *Experiments in Fluids*, 48(1):17–31, doi:10.1007/s00348-009-0699-1.

Bormann, K. (1968). *Der Abfluss in Schussrinnen unter Berücksichtigung der Luftaufnahme [Chute flow under consideration of air entrainment]*. Phd thesis (in german), Technische Hochschule München, Germany.

Boussinesq, J. (1877). Essai sur la théorie des eaux courantes. *Mémoires présentés par divers savants à l'Académie des Sciences*, 23(1):1–680.

- Brackbill, J. U., Kothe, D. B., and Zemach, C. (1991). A continuum method for modeling surface tension. *Journal of Computational Physics*, 100:335–354, [doi:10.1016/0021-9991\(92\)90240-Y](https://doi.org/10.1016/0021-9991(92)90240-Y).
- Bung, D. B. (2011a). Developing flow in skimming flow regime on embankment stepped spillways. *Journal of Hydraulic Research*, 49(5):639–648, [doi:10.1080/00221686.2011.584372](https://doi.org/10.1080/00221686.2011.584372).
- Bung, D. B. (2011b). Non-intrusive measuring of air-water flow properties in self-aerated stepped spillway flow. In *Proceeding of 34th WCIAFERE: 33rd HWRS and 10th CHWE*, number 2005, pages 1–8.
- Bung, D. B. (2013). Non-intrusive detection of air – water surface roughness in self-aerated chute flows. *Journal of Hydraulic Research*, 51(3):322–329, [doi:10.1080/00221686.2013.777373](https://doi.org/10.1080/00221686.2013.777373).
- Bung, D. B. and Valero, D. (2016). Optical flow estimation in aerated flows. *Journal of Hydraulic Research*, [doi:10.1080/00221686.2016.1173600](https://doi.org/10.1080/00221686.2016.1173600).
- Bureau of Reclamation (2015). Cavitation Damage Induced Failure of Spillways. In *Best Practices and Risk Methodology*, chapter VI-3, pages VI-3–1–16. Washington DC.
- Cain, P. and Wood, I. R. (1981). Measurements of Self-Aerated Flow on a Spillway. *Journal of the Hydraulics Division*, 107(11):1425–1444, [doi:10.1061/\(ASCE\)0733-9429\(1983\)109:1\(145\)](https://doi.org/10.1061/(ASCE)0733-9429(1983)109:1(145)).
- Carvalho, R. F. (2002). *Acções Hidrodinâmicas em Estruturas Hidráulicas: Modelação Computacional no Ressalto Hidráulico*. Phd thesis (in portuguese), Universidade de Coimbra, Portugal.
- Carvalho, R. F. and Amador, A. T. (2009). Physical And Numerical Investigation of the Skimming Flow Over a Stepped Spillway. In Zhang, C. and Tang, H., editors, *Advances in Water Resources and Hydraulic Engineering*, chapter Vol.V, pages 1767–1772. Springer Berlin Heidelberg, Hohai, China.
- Carvalho, R. F., Leandro, J., Martins, R., Abreu, J. M., and de Lima, J. M. L. P. (2011). 2DV numerical modelling of different flows occurring in gullies. In *12th International Conference on Urban Drainage (12ICUD)*, September 11-16, 2011, Porto Alegre/RS, Brazil. IWA Publishing, London, UK.

Carvalho, R. F., Leandro, J., Martins, R., and Lopes, P. (2012). Numerical study of the flow behaviour in a gully. In *4th IAHR International Symposium on Hydraulic Structures*, February 9-11, 2012, Porto, Portugal. APRH Publishing, Lisbon, Portugal.

Carvalho, R. F., Lemos, C. M., and Ramos, C. M. (2008). Numerical computation of the flow in hydraulic jump stilling basins. *Journal of Hydraulic Research*, 46(6):739–752, [doi:10.3826/jhr.2008.2726](https://doi.org/10.3826/jhr.2008.2726).

Carvalho, R. F. and Martins, R. (2009). Stepped Spillway with Hydraulic Jumps : Application of a Numerical Model to a Scale Model of a Conceptual Prototype. *J. Hydraulic Engineering, ASCE*, (July):615–619, [doi:10.1061/\(ASCE\)HY.1943-7900.0000042](https://doi.org/10.1061/(ASCE)HY.1943-7900.0000042).

Celik, I. B., Ghia, U., Roache, P. J., and Freitas, C. J. (2008). Procedure for Estimation and Reporting of Uncertainty Due to Discretization in CFD Applications. *Journal of Fluids Engineering*, 130(7), [doi:10.1115/1.2960953](https://doi.org/10.1115/1.2960953).

Cerne, G., Petelin, S., and Tiselj, I. (2001). Coupling of the Interface Tracking and the Two-Fluid Models for the Simulation of Incompressible Two-Phase Flow. *Journal of Computational Physics*, 171(2):776–804, [doi:10.1006/jcph.2001.6810](https://doi.org/10.1006/jcph.2001.6810).

Chanson, H. (1988). *Study of Air Entrainment and Aeration Devices on Spillway Model*. PhD thesis, Department of Civil Engineering, University of Canterbury, Christchurch, New Zealand.

Chanson, H. (1993). Self-Aerated Flows on Chutes and Spillways. *Journal of Hydraulic Engineering*, 119(2):220–243, [doi:10.1061/\(ASCE\)0733-9429\(1993\)119:2\(220\)](https://doi.org/10.1061/(ASCE)0733-9429(1993)119:2(220)).

Chanson, H. (1997). *Air Bubble Entrainment In Free-Surface Turbulent Shear Flows*. London, UK: Academic Press.

Chanson, H. (2001). Hydraulic design of stepped spillways and downstream energy dissipators. *Dam Engineering*, 11(4):205–242.

Chanson, H. (2002a). Air-Water Flow Measurements with Intrusive , Phase-Detection Probes : Can We Improve Their Interpretation? *Journal of Hydraulic Engineering*, 128(3):252–255, [doi:10.1061/\(ASCE\)0733-9429\(2002\)128:3\(252\)](https://doi.org/10.1061/(ASCE)0733-9429(2002)128:3(252)).

Chanson, H. (2002b). *The hydraulics of stepped chutes and spillway*. CRC Press, Inc.

Chanson, H. (2007). Bubbly flow structure in hydraulic jump. *European Journal of Mechanics - B/Fluids*, 26(3):367–384, [doi:10.1016/j.euromechflu.2006.08.001](https://doi.org/10.1016/j.euromechflu.2006.08.001).

- Chanson, H., Aoki, S., and Hoque, A. (2004). Physical modelling and similitude of air bubble entrainment at vertical circular plunging jets. *Chemical Engineering Science*, 59(4):747–754, **doi:10.1016/j.ces.2003.11.016**.
- Chanson, H. and Brattberg, T. (2000). Experimental study of the air-water shear flow in a hydraulic jump. *International Journal of Multiphase Flow*, 26:583–607, **doi:10.1016/S0301-9322(99)00016-6**.
- Chanson, H. and Manasseh, R. (2003). Air Entrainment Processes in a Circular Plunging Jet: Void-Fraction and Acoustic Measurements. *Journal of Fluids Engineering*, 125(5):910–921, **doi:10.1115/1.1595672**.
- Chanson, H. and Toombes, L. (2002). Air-water flows down stepped chutes: turbulence and flow. *International Journal of Multiphase Flow*, 28(11):1737–1761, **doi:10.1016/S0301-9322(02)00089-7**.
- Cheng, X., Chen, Y., and Luo, L. (2006). Numerical simulation of air-water two-phase flow over stepped spillways. *Science in China Series E: Technological Sciences*, 49(6):674–684, **doi:10.1007/s10288-006-2029-2**.
- Clift, R., Grace, J. R., and Weber, M. E. (1978). *Bubbles, Drops and Particles*. Academic Press Inc., New York, USA.
- Comport, B. C., Cox, A. L., and Thornton, C. I. (2012). Performance Assessment of Grate Inlets For Highway Median Drainage. Technical report, The Urban Drainage and Flood Control District, USA.
- Comport, B. C. and Thornton, C. I. (2009). Hydraulic Efficiency of Grate and Curb Inlets for Urban Storm Drainage. Technical report, The Urban Drainage and Flood Control District, USA.
- Cummings, P. D. and Chanson, H. (1997a). Air Entrainment in the Developing Flow Region of Plunging Jets - Part 1: Theoretical Development. *Journal of Fluids Engineering*, 119:597–602, **doi:10.1115/1.2819286**.
- Cummings, P. D. and Chanson, H. (1997b). Air Entrainment in the Developing Flow Region of Plunging Jets - Part 2: Experimental. *Journal of Fluid Mechanics*, 119(3):603–608, **doi:10.1115/1.2819287**.
- Daly, B. J. (1969). A technique for including surface tension effects in hydrodynamic calculations. *Journal of Computational Physics*, 4(1):97–117, **doi:10.1016/0021-9991(69)90042-4**.

Damián, S. M. and Nigro, N. M. (2010). Comparison of Single Phase Laminar And Large Eddy Simulation (LES) Solvers Using The OpenFOAM Suite. *Asociación Argentina de Mecánica Computacional*, XXIX:3721–3740.

Deardorff, J. W. (1970). A numerical study of three-dimensional turbulent channel flow at large Reynolds numbers. *Journal of Fluid Mechanics*, 41(2):453–480, [doi:10.1017/S0022112070000691](https://doi.org/10.1017/S0022112070000691).

DeLapp, W. W. (1947). *The High Velocity Flow of Water in a Small Rectangular Channel*. Phd thesis, University of Minnesota, USA.

Deshpande, S. S., Trujillo, M. F., Wu, X., and Chahine, G. (2012). Computational and experimental characterization of a liquid jet plunging into a quiescent pool at shallow inclination. *International Journal of Heat and Fluid Flow*, 34:1–14, [doi:10.1016/j.ijheatfluidflow.2012.01.011](https://doi.org/10.1016/j.ijheatfluidflow.2012.01.011).

Djordjević, S., Prodanović, D., Maksimović, C., Ivetić, M., and Savić, D. (2005). SIPSON-simulation of interaction between pipe flow and surface overland flow in networks. *Water Science and Technology*, 52(5):275–283.

Djordjević, S., Saul, A. J., Tabor, G. R., Blanksby, J., Galambos, I., Sabtu, N., and Sailor, G. (2013). Experimental and numerical investigation of interactions between above and below ground drainage systems. *Water Science and Technology*, 67(3):535–42, [doi:10.2166/wst.2012.570](https://doi.org/10.2166/wst.2012.570).

Drew, D. A. and Passman, S. L. (1998). *Theory of Multicomponents Fluids*. Springer, New York, USA.

Ervine, D. A. and Falvey, H. T. (1987). Behaviour of turbulent water jets in the atmosphere and in plunge pools. *Ice Proceedings*, 83(1):295–314, [doi:10.1680/iicep.1987.353](https://doi.org/10.1680/iicep.1987.353).

Ervine, D. A., McKeogh, E., and Elsayy, E. M. (1980). Effect of turbulence intensity on the rate of air entrainment by plunging water jets. *Proceedings of Inst Civil Engineers, Part2*, 69:425–445.

Evans, G. M., Jameson, G. J., and Rielly, C. D. (1996). Free jet expansion and gas entrainment characteristics of a plunging liquid jet. *Experimental Thermal and Fluid Science*, 12(2):142–149, [doi:10.1016/0894-1777\(95\)00095-X](https://doi.org/10.1016/0894-1777(95)00095-X).

Falvey, H. T. (1980a). Air-water flow in hydraulic structures. Technical report, Engineering Monograph No. 41.

- Falvey, H. T. (1980b). Cavitation in Chutes and Spillways. Technical report, Engineering Monograph No. 42.
- Felder, S. and Chanson, H. (2009). Turbulence , dynamic similarity and scale effects in high-velocity free-surface flows above a stepped chute. *Experiments in Fluids*, 47(1):1–18, doi:10.1007/s00348-009-0628-3.
- Felder, S. and Chanson, H. (2011a). Air–water flow properties in step cavity down a stepped chute. *International Journal of Multiphase Flow*, 37(7):732–745, doi:10.1016/j.ijmultiphaseflow.2011.02.009.
- Felder, S. and Chanson, H. (2011b). Energy Dissipation down a Stepped Spillway with Non-Uniform Step Heights. *Journal of Hydraulic Engineering*, 137(11):1543–1548, doi:10.1061/(ASCE)HY.1943-7900.0000455.
- Felder, S. and Chanson, H. (2014). Air–water flows and free-surface profiles on a non-uniform stepped chute. *Journal of Hydraulic Research*, 52(2):253–263, doi:10.1080/00221686.2013.841780.
- Felder, S. and Chanson, H. (2015a). Closure to "Aeration , Flow Instabilities , and Residual Energy on Pooled Stepped Spillways of Embankment Dams" by Stefan Felder and Hubert Chanson. *Journal of Irrigation and Drainage Engineering*, 141(2):07014039, doi:10.1061/(ASCE)IR.1943-4774.0000627.
- Felder, S. and Chanson, H. (2015b). Phase-detection probe measurements in high-velocity free-surface flows including a discussion of key sampling parameters. *Experimental Thermal and Fluid Science*, 61(February):66–78, doi:10.1016/j.expthermflusci.2014.10.009.
- FHWA (1984). Drainage of Highway Pavements - HEC12. Technical report, U.S. Department of Transportation, USA.
- FHWA (2001). Urban Drainage Design Manual - HEC22. Technical report, U.S. Department of Transportation, USA.
- Fluent Inc. (2006). *Fluent 6.3 - User's guide*. Fluent Inc.
- Galambos, I. (2012). *Improved Understanding of Performance of Local Controls Linking the above and below Ground Components of Urban Flood Flows*. Phd thesis, University of Exeter, UK.

Gomes, J. F. (2006). *Campo de pressões : condições de incipiência à cavitação em vertedouros em degraus com declividade 1V:0,75H*. Phd thesis (in portuguese), Universidade Federal do Rio Grande do Sul. Instituto de Pesquisas Hidráulicas. Programa de Pós-Graduação em Recursos Hídricos e Saneamento Ambiental.

Gómez, M. and Russo, B. (2009). Hydraulic Efficiency of Continuous Transverse Grates for Paved Areas. *Journal of Irrigation and Drainage Engineering*, 135(2):225–230, doi:10.1061/(ASCE)0733-9437(2009)135:2(225).

Gong, Y. and Tanner, F. X. (2009). Comparison of RANS and LES Models in the Laminar Limit for a Flow Over a Backward-Facing Step Using OpenFOAM. In *19th International Multidimensional Engine Modeling Users Group Meeting at the SAE Congress*, April 19 2009, Detroit, Michigan. Engine Research Center at the University of Wisconsin System, USA.

Gonzalez, C. A. (2005). *An Experimental Study of Free-surface Aeration on Embankment Stepped Chutes*. Phd thesis, Faculty of Engineering, Physical Sciences and Architecture, The University of Queensland Brisbane, Australia.

Gonzalez, C. A., Takahashi, M., and Chanson, H. (2006). Flow resistance and design guidelines for embankment stepped chutes. In Berga, L., Buil, J., Bofill, E., De Cea, J., Perez, J. A., Mañueco, G., Polimon, J., Soriano, A., and Yagüe, J., editors, *International Symposium on Dams in the Societies of the 21st Century, 22nd International Congress on Large Dams (ICOLD)*, Barcelona, Spain, 18 June 2006.

Gonzalez, C. A., Takahashi, M., and Chanson, H. (2008). An experimental study of effects of step roughness in skimming flows on stepped chutes. *Journal of Hydraulic Research*, 46(1):24–35, doi:10.1080/00221686.2008.9521937.

Gopala, V. R. and van Wachem, B. G. M. (2008). Volume of fluid methods for immiscible-fluid and free-surface flows. *Chemical Engineering Journal*, 141(1-3):204–221, doi:10.1016/j.cej.2007.12.035.

Goring, D. G. and Nikora, V. I. (2002). Despiking Acoustic Doppler Velocimeter Data. *Journal of Hydraulic Engineering*, 128(1):117–126, doi:10.1061/(ASCE)0733-9429(2002)128:1(117).

Govender, K., Mocke, G. P., and Alport, M. J. (2002). Video-imaged surf zone wave and roller structures and flow fields. *Journal of Geophysical Research*, 107(C7):3072, doi:10.1029/2000JC000755.

- Granata, F., de Marinis, G., and Gargano, R. (2014a). Air-water flows in circular drop manholes. *Urban Water Journal*, pages 1–11, [doi:10.1080/1573062X.2014.881893](https://doi.org/10.1080/1573062X.2014.881893).
- Granata, F., de Marinis, G., and Gargano, R. (2014b). Flow-improving elements in circular drop manholes. *Journal of Hydraulic Research*, 52(3):347–355, [doi:10.1080/00221686.2013.879745](https://doi.org/10.1080/00221686.2013.879745).
- Gumbel, E. J. (1935). Les valeurs extrêmes des distributions statistiques. *Annales de l'institut Henri Poincaré*, 2(5):115–158.
- Gupta, H., Sorooshian, S., and Yapo, P. (1999). Status of Automatic Calibration for Hydrologic Models: Comparison with Multilevel Expert Calibration. *Journal of Hydrologic Engineering*, 4(2):135–143, [doi:10.1061/\(ASCE\)1084-0699\(1999\)4:2\(135\)](https://doi.org/10.1061/(ASCE)1084-0699(1999)4:2(135)).
- Guymer, I., Dennis, P., O'Brien, R., and Saiyudthong, C. (2005). Diameter and Surcharge Effects on Solute Transport across Surcharged Manholes. *Journal of Hydraulic Engineering*, 131(4):312–321, [doi:10.1061/\(ASCE\)0733-9429\(2005\)131:4\(312\)](https://doi.org/10.1061/(ASCE)0733-9429(2005)131:4(312)).
- Hager, W. H. (1992). *Spillways: Shockwaves and Air Entrainment: Review and Recommendations*. Commission Internationale des Grands Barrages.
- Hager, W. H. and Pfister, M. (2013). Stepped Spillways : Technical Advance from 1900. In *Proceedings of 2013 IAHR World Congress*.
- Hänsch, S., Lucas, D., Höhne, T., and Krepper, E. (2014). Application of a new concept for multi-scale interfacial structures to the dam-break case with an obstacle. *Nuclear Engineering and Design*, 279:171–181, [doi:10.1016/j.nucengdes.2014.02.006](https://doi.org/10.1016/j.nucengdes.2014.02.006).
- Hänsch, S., Lucas, D., Krepper, E., and Höhne, T. (2012). A multi-field two-fluid concept for transitions between different scales of interfacial structures. *International Journal of Multiphase Flow*, 47:171–182, [doi:10.1016/j.ijmultiphaseflow.2012.07.007](https://doi.org/10.1016/j.ijmultiphaseflow.2012.07.007).
- Harlow, F. H. and Welch, J. E. (1965). Numerical Calculation of Time-Dependent Viscous Incompressible Flow of Fluid with Free Surface. *The Physics of Fluids*, 8(12):2182–2189.
- Hirt, C. W. (2003). Modeling Turbulent Entrainment of Air at a Free Surface. Technical report, Flow Science Report FSI-03-TN61, USA.
- Hirt, C. W. (2012). Modeling Turbulent Entrainment of Air at a Free Surface. Technical report, Flow Science Report 01-12, USA.

Hirt, C. W. and Nichols, B. D. (1981). Volume of Fluid (VOF) Method for the Dynamics of Free Boundaries. *Journal of Computational Physics*, 39:201–225, doi:10.1016/0021-9991(81)90145-5.

Höhne, T. and Vallée, C. (2010). Experiments and numerical simulations of horizontal two-phase flow regimes using an interfacial area density model. *Journal of Computational Multiphase Flows*, 2(3):131–143.

Hunt, S. L. and Kadavy, K. C. (2013). Inception Point for Embankment Dam Stepped Spillways. *Journal of Hydraulic Engineering*, 139(2013):60–64, doi:10.1061/(ASCE)HY.1943-7900.0000644.

Hussein, H. J., Capp, S. P., and George, W. K. (1994). Velocity measurements in a hight-Reynolds-number, momentum-conserving, axisymmetric, turbulent jet. *Journal of Fluid Mechanics*, 258(1):31–75, doi:10.1017/S002211209400323X.

Hyman, J. M. (1984). Numerical Methods for Tracking Interfaces. *Physica D: Nonlinear Phenomena*, 12(1-3):396–407, doi:10.1016/0167-2789(84)90544-X.

IPCC (2012). Managing the risks of extreme events and disasters to advance climate change adaptation. Technical report, A Special Report of Working Groups I and II of the Intergovernmental Panel on Climate Change, Cambridge University Press, Cambridge, UK, and New York, NY, USA.

Ishii, M. (1975). *Thermo-fluid dynamic theory of two-phase flow*. Eyrolles, Paris, France.

Issa, R. I. (1985). Solution of the implicitly discretised fluid flow equations by operator-splitting. *Journal of Computational Physics*, 62(1):40–65, doi:10.1016/0021-9991(86)90099-9.

Jarman, D. S., Faram, M. G., Butler, D., Tabor, G. R., Stovin, V. R., Burt, D., and Throp, E. (2008). Computational fluid dynamics as a tool for urban drainage system analysis : A review of applications and best practice. In *11th International Conference on Urban Drainage*, pages 1–10, Edinburgh, Scotland, UK.

Jasak, H. (1996). *Error Analysis and Estimation for the Finite Volume Method with Applications to Fluid Flows*. PhD thesis, Imperial College, London, UK.

Keller, R. J., Lai, K. K., and Wood, I. R. (1974). Developing region in self-aerated flows. *Journal of the Hydraulics Division*, 100(4):553–568.

- Kendil, F. Z., Salah, A. B., and Mataoui, A. (2010). Assessment of three turbulence model performances in predicting water jet flow plunging into a liquid pool. *Nuclear Technology and Radiation Protection*, 25(1):13–22, [doi:10.2298/NTRP1001013Z](https://doi.org/10.2298/NTRP1001013Z).
- Kiger, K. T. and Duncan, J. H. (2012). Air-Entrainment Mechanisms in Plunging Jets and Breaking Waves. *Annual Review of Fluid Mechanics*, 44(1):563–596, [doi:10.1146/annurev-fluid-122109-160724](https://doi.org/10.1146/annurev-fluid-122109-160724).
- Kolmogorov, A. N. (1962). A refinement of previous hypotheses concerning the local structure of turbulence in a viscous incompressible fluid at high Reynolds number. *Journal of Fluid Mechanics*, 13:82–85, [doi:10.1017/S0022112062000518](https://doi.org/10.1017/S0022112062000518).
- Kositgittiwong, D., Chinnarasri, C., and J., P. Y. (2012). Numerical simulation of flow velocity profiles along a stepped spillway. *Proceedings of the Institution of Mechanical Engineers, Part E: Journal of Process Mechanical Engineering*, 0(0), [doi:10.1177/0954408912472172](https://doi.org/10.1177/0954408912472172).
- Lamb, O. P. and Killen, J. M. (1950). An Electrical Method for Measuring Air Concentration in Flowing Air-Water Mixtures. Technical report, St. Anthony Falls Hydraulic Laboratory, University of Minnesota, USA.
- Launder, B. E. and Spalding, D. B. (1974). The numerical computation of turbulent flows. *Computer Methods in Applied Mechanics and Engineering*, 3(2):269–289, [doi:10.1016/0045-7825\(74\)90029-2](https://doi.org/10.1016/0045-7825(74)90029-2).
- Leandro, J., Bung, D. B., and Carvalho, R. F. (2014a). Measuring void fraction and velocity fields of a stepped spillway for skimming flow using non-intrusive methods. *Experiments in Fluids*, 55(5), [doi:10.1007/s00348-014-1732-6](https://doi.org/10.1007/s00348-014-1732-6).
- Leandro, J., Carvalho, R. F., Chachereau, Y., and Chanson, H. (2012). Estimating void fraction in a hydraulic jump by measurements of pixel intensity. *Experiments in Fluids*, 52:1307–1318, [doi:10.1007/s00348-011-1257-1](https://doi.org/10.1007/s00348-011-1257-1).
- Leandro, J., Chen, A., Djordjević, S., and Savić, D. A. (2009). Comparison of 1D/1D and 1D/2D Coupled (Sewer/Surface) Hydraulic Models for Urban Flood Simulation. *Journal of Hydraulic Engineering*, 135(6):495–504, [doi:10.1061/\(ASCE\)HY.1943-7900.0000037](https://doi.org/10.1061/(ASCE)HY.1943-7900.0000037).
- Leandro, J., Lopes, P., Carvalho, R., Páscoa, P., Martins, R., and Romagnoli, M. (2014b). Numerical and experimental characterization of the 2D vertical average-velocity plane at the centre-profile and qualitative air entrainment inside a gully for drainage and reverse flow. *Computers & Fluids*, 102:52–61, [doi:10.1016/j.compfluid.2014.05.032](https://doi.org/10.1016/j.compfluid.2014.05.032).

Leandro, J., Schumann, A., and Pfister, A. (2016). A step towards considering the spatial heterogeneity of urban key features in urban hydrology flood modelling. *Journal of Hydrology*, 535:356–365, [doi:10.1016/j.jhydrol.2016.01.060](https://doi.org/10.1016/j.jhydrol.2016.01.060).

Lee, H. and Rhee, S. H. (2015). A dynamic interface compression method for VOF simulations of high-speed planing watercraft. *Journal of Mechanical Science and Technology*, 29(5):1849–1857, [doi:10.1007/s12206-015-0405-6](https://doi.org/10.1007/s12206-015-0405-6).

Lemos, C. M. (1992). Wave Breaking - A Numerical Study. In Brebbia and Orszag, S. A., editors, *Lecture Notes in Engineering*. Springer-Verlag vol. 71.

Leonard, B. P. (1988). Simple high-accuracy resolution program for convective modelling of discontinuities. *International Journal for Numerical Methods in Fluids*, 8:1291–1318, [doi:10.1002/fld.1650081013](https://doi.org/10.1002/fld.1650081013).

Lopes, P. (2013). *Free-surface flow interface and air-entrainment modelling using Open-FOAM*. Phd thesis project, University of Coimbra, Coimbra, Portugal.

Lopes, P., Bung, D. B., Leandro, J., and Carvalho, R. F. (2015a). The effect of cross-waves in physical stepped spillway models. In *36th IAHR World Congress 2015*.

Lopes, P., Leandro, J., Carvalho, R., Páscoa, P., and Martins, R. (2015b). Numerical and experimental investigation of a gully under surcharge conditions. *Urban Water Journal*, 12(6):468–476, [doi:10.1080/1573062X.2013.831916](https://doi.org/10.1080/1573062X.2013.831916).

Lopes, P., Leandro, J., Carvalho, R. F., and Martins, R. (2012). Hydraulic behaviour of a gully under surcharge conditions. September 4-6, 2012, Belgrade, Serbia. Faculty of Civil Engineering, University of Belgrade. USB flash drives. ISBN 978-86-7518-156-9.

Lopes, P., Leandro, J., Carvalho, R. F., Russo, B., and Gómez, M. (2016a). Assessment of a VOF Model Ability to Reproduce the Efficiency of a Continuous Transverse Gully with Grate. *Journal of Irrigation and Drainage Engineering*, [doi:10.1061/\(ASCE\)IR.1943-4774.0001058](https://doi.org/10.1061/(ASCE)IR.1943-4774.0001058).

Lopes, P., Tabor, G., Carvalho, R. F., and Leandro, J. (2016b). Explicit calculation of natural aeration using a Volume-of-Fluid model. *Applied Mathematical Modelling*, 40(17-18):7504–7515, [doi:10.1016/j.apm.2016.03.033](https://doi.org/10.1016/j.apm.2016.03.033).

López, J., Hernández, J., Gómez, P., and Faura, F. (2004). A volume of fluid method based on multidimensional advection and spline interface reconstruction. *Journal of Computational Physics*, 195(2):718–742, [doi:10.1016/j.jcp.2003.10.030](https://doi.org/10.1016/j.jcp.2003.10.030).

- Lubbers, C. L. and Clemens, F. (2005). Air and gas pockets in sewerage pressure mains. *Water Science and Technology*, 52(3):37–44, [doi:10.2166/wst.2006.769](https://doi.org/10.2166/wst.2006.769).
- Lubbers, C. L. and Clemens, F. (2006). Breakdown of air pockets in downwardly inclined sewerage pressure mains. *Water Science and Technology*, 54(11-12):233–240.
- Lubin, P., Vincent, S., Abadie, S., and Caltagirone, J.-P. (2006). Three-dimensional Large Eddy Simulation of air entrainment under plunging breaking waves. *Coastal Engineering*, 53(8):631–655, [doi:10.1016/j.coastaleng.2006.01.001](https://doi.org/10.1016/j.coastaleng.2006.01.001).
- Ma, G., Shi, F., and Kirby, J. T. (2011a). A polydisperse two-fluid model for surf zone bubble simulation. *Journal of Geophysical Research*, 116:1–21, [doi:10.1029/2010JC006667](https://doi.org/10.1029/2010JC006667).
- Ma, J., Oberai, A. A., Drew, D. A., Lahey, R. T., and Hyman, M. C. (2011b). A Comprehensive Sub-Grid Air Entrainment Model for RaNS Modeling of Free-Surface Bubbly Flows. *The Journal of Computational Multiphase Flows*, 3(1):41–56, [doi:10.1260/1757-482X.3.1.41](https://doi.org/10.1260/1757-482X.3.1.41).
- Ma, J., Oberai, A. A., Drew, D. A., Lahey, R. T., and Moraga, F. J. (2010). A quantitative sub-grid air entrainment model for bubbly flows – plunging jets. *Computers & Fluids*, 39(1):77–86, [doi:10.1016/j.compfluid.2009.07.004](https://doi.org/10.1016/j.compfluid.2009.07.004).
- Ma, J., Oberai, A. A., Hyman, M. C., Drew, D. A., and Lahey, R. T. (2011c). Two-fluid modeling of bubbly flows around surface ships using a phenomenological subgrid air entrainment model. *Computers & Fluids*, 52(1):50–57, [doi:10.1016/j.compfluid.2011.08.015](https://doi.org/10.1016/j.compfluid.2011.08.015).
- Ma, J., Oberai, A. A., Lahey, R. T., and Drew, D. A. (2011d). Modeling Air Entrainment and Transport in a Hydraulic Jump using Two-Fluid RANS and DES Turbulence Models. *Heat and Mass Transfer*, 47(8):911–919.
- Maiwald, A. and Schwarze, R. (2011). Numerical analysis of flow-induced gas entrainment in roll coating. *Applied Mathematical Modelling*, 35(7):3516–3526, [doi:10.1016/j.apm.2011.01.004](https://doi.org/10.1016/j.apm.2011.01.004).
- Marschall, H. and Hinrichsen, O. (2013). Numerical simulation of multi-scale two-phase flows using a Hybrid Interface-Resolving Two-Fluid Model (HIRES-TFM). *Journal of chemical engineering of Japan*, 46(8):517–523, [doi:10.1252/jcej.12we074](https://doi.org/10.1252/jcej.12we074).
- Martins, R., Carvalho, R. F., Leandro, J., Lopes, P., and Roque, J. (2012). Estudo do Comportamento Hidráulico de um Sumidouro em Modelo Numérico OpenFOAM™. In *11º Congresso da Água*, Porto, Portugal.

- Martins, R., Leandro, J., and Carvalho, R. F. (2014). Characterization of the hydraulic performance of a gully under drainage conditions. *Water Science & Technology*, 69(12):2423–2430, [doi:10.2166/wst.2014.168](https://doi.org/10.2166/wst.2014.168).
- Matos, J. (1999). *Emulsionamento de ar e dissipação de energia do escoamento em descarregadores em degraus*. Phd thesis (in portuguese), Instituto Superior Técnico de Lisboa, Lisbon, Portugal.
- Matos, J., Frizell, K., André, S., and Frizell, K. (2002). On the Performance of Velocity Measurement Techniques in Air-Water Flows. In *Proceedings of Hydraulic Measurements and Experimental Methods Specialty Conference (HMEM) 2002*.
- McDonough, J. M. (2007). *Introductory lectures on turbulence - Physics, Mathematics and Modeling*. University of Kentucky, USA.
- McKeogh, E. J. (1978). *A Study of Air Entrainment Using Plunging Water Jets*. Phd thesis, Queen's University of Belfast, UK.
- McKeogh, E. J. and Ervine, D. A. (1981). Air entrainment rate and diffusion pattern of plunging liquid jets. *Chemical Engineering Science*, 36(7):1161–1172, [doi:10.1016/0009-2509\(81\)85064-6](https://doi.org/10.1016/0009-2509(81)85064-6).
- Meireles, I. and Matos, J. (2009). Skimming Flow in the Nonaerated Region of Stepped Spillways over Embankment Dams. *Journal of Hydraulic Engineering*, 135(8):685–689, [doi:10.1061/\(ASCE\)HY.1943-7900.0000047](https://doi.org/10.1061/(ASCE)HY.1943-7900.0000047).
- Meireles, I., Renna, F., Matos, J., and Bombardelli, F. (2012). Skimming, Nonaerated Flow on Stepped Spillways over Roller Compacted Concrete Dams. *Journal of Hydraulic Engineering*, 138:870–877, [doi:10.1061/\(ASCE\)HY.1943-7900.0000591](https://doi.org/10.1061/(ASCE)HY.1943-7900.0000591).
- Menter, F. (1993). Zonal two-equation $k-\omega$ turbulence model for aerodynamic flows. In *AIAA 24th Fluid Dynamics Conference*, Orlando, Florida, USA.
- Moraga, F., Carrica, P., Drew, D., and Lahey, R. (2008). A sub-grid air entrainment model for breaking bow waves and naval surface ships. *Computers & Fluids*, 37(3):281–298, [doi:10.1016/j.compfluid.2007.06.003](https://doi.org/10.1016/j.compfluid.2007.06.003).
- Moriasi, D. N., Arnold, J. G., Liew, M. W. V., Bingner, R. L., Harmel, R. D., and Veith, T. L. (2007). Model Evaluation Guidelines for Systematic Quantification of Accuracy in Watershed Simulations. *American Society of Agricultural and Biological Engineers*, 50(3):885–900.

- Mossa, M. and Tolve, U. (1998). Flow visualization in bubbly two-phase hydraulic jump. *Journal of Fluids Engineering*, 120(1):160–165, [doi:10.1115/1.2819641](https://doi.org/10.1115/1.2819641).
- Murzyn, F. and Chanson, H. (2008). Experimental assessment of scale effects affecting two-phase flow properties in hydraulic jumps. *Experiments in Fluids*, 45(3):513–521, [doi:10.1007/s00348-008-0494-4](https://doi.org/10.1007/s00348-008-0494-4).
- Muzaferija, S., Peric, M., Sames, P., and Schelin, T. (1998). A two-fluid navier-stokes solver to simulate water entry. In *Proc. Twenty-Second Symposium on Naval Hydrodynamics*.
- Nagash, B. W. (1994). Void fraction measurement techniques for gas- liquid bubbly flows in closed conduits: a literature review. *Proceedings of hydraulic engineering conference, ASCE, Buffalo*, pages 278–288.
- Nash, J. E. and Sutcliffe, J. V. (1970). River flow forecasting through conceptual models part I — A discussion of principles. *Journal of Hydrology*, 10(3):282–290, [doi:10.1016/0022-1694\(70\)90255-6](https://doi.org/10.1016/0022-1694(70)90255-6).
- NFCO (1998). *Catalog*.
- Nikseresht, A. H., Talebbeydokhti, N., and Rezaei, M. J. (2013). Numerical simulation of two-phase flow on step-pool spillways. *Scientia Iranica*, 20(2):222–230, [doi:10.1016/j.scient.2012.11.013](https://doi.org/10.1016/j.scient.2012.11.013).
- Noh, W. F. and Woodward, P. (1976). SLIC (Simple Line Interface Calculation). In Vooren, A. I. and Zandbergen, P. J., editors, *Proceedings of the Fifth International Conference on Numerical Methods in Fluid Dynamics June 28 – July 2*, volume 59 of *Lecture Notes in Physics*, Berlin, Heidelberg. Springer Berlin Heidelberg.
- Ohtsu, I., Yasuda, Y., and Takahashi, M. (2004). Flow Characteristics of Skimming Flows in Stepped Channels. *Journal of Hydraulic Engineering*, 130(9):860–869, [doi:10.1061/\(ASCE\)0733-9429\(2004\)130:9\(860\)](https://doi.org/10.1061/(ASCE)0733-9429(2004)130:9(860)).
- OpenFOAM (2014). *OpenFOAM v.2.3.0 - The Open Source CFD Toolbox - User Guide*. OpenCFD.
- Osher, S. and Sethian, J. (1988). Fronts propagating with curvature-dependent speed: Algorithms based on Hamilton-Jacobi formulations. *Journal of Computational Physics*, 79(1):12–49, [doi:10.1016/0021-9991\(88\)90002-2](https://doi.org/10.1016/0021-9991(88)90002-2).
- Páscoa, P., Leandro, J., and Carvalho, R. F. (2013). Characterization of the flow in a gully: average velocity and air entrainment. In *International Workshop on Hydraulic Design of*

- Low-Head Structures (IWLHS 2013)*, pages 141–148, Aachen, Germany. Bundesanstalt für Wasserbau (BAW), Karlsruhe, Germany.
- Pearson, K. (1986). Mathematical Contributions to the Theory of Evolution. III. Regression, Heredity and Panmixia. *Philosophical Transactions of the Royal Society of London*, 187:253–318, [doi:10.1098/rsta.1896.0007](https://doi.org/10.1098/rsta.1896.0007).
- Pegram, G. G. S., Officer, A. K., and Mottram, S. R. (1999). Hydraulics of Skimming Flow on Modeled Stepped Spillways. *Journal of Hydraulic Engineering*, 125(5):500–510, [doi:10.1061/\(ASCE\)0733-9429\(1999\)125:5\(500\)](https://doi.org/10.1061/(ASCE)0733-9429(1999)125:5(500)).
- Pfister, M. and Chanson, H. (2012). Scale effects in physical hydraulic engineering models. *Journal of Hydraulic Research*, 50(2):244–246, [doi:10.1080/00221686.2012.654671](https://doi.org/10.1080/00221686.2012.654671).
- Pfister, M. and Hager, W. H. (2011). Self-entrainment of air on stepped spillways. *International Journal of Multiphase Flow*, 37(2):99–107, [doi:10.1016/j.ijmultiphaseflow.2010.10.007](https://doi.org/10.1016/j.ijmultiphaseflow.2010.10.007).
- Pilliod, J. E. and Puckett, E. G. (2004). Second-order accurate volume-of-fluid algorithms for tracking material interfaces. *Journal of Computational Physics*, 199(2):465–502, [doi:10.1016/j.jcp.2003.12.023](https://doi.org/10.1016/j.jcp.2003.12.023).
- Piro, D. J. and Maki, K. J. (2013). An adaptive interface compression method for water entry and exit. Technical report, Technical Report, University of Michigan, USA.
- Pope, S. B. (2000). *Turbulent flows*. Cambridge University Press.
- Pothof, I. and Clemens, F. (2010). On elongated air pockets in downward sloping pipes. *Journal of Hydraulic Research*, 48(4):499–503, [doi:10.1080/00221686.2010.491651](https://doi.org/10.1080/00221686.2010.491651).
- Qu, X., Khezzar, L., Danciu, D., Labois, M., and Lakehal, D. (2011). Characterization of plunging liquid jets: A combined experimental and numerical investigation. *International Journal of Multiphase Flow*, 37(7):722–731, [doi:10.1016/j.ijmultiphaseflow.2011.02.006](https://doi.org/10.1016/j.ijmultiphaseflow.2011.02.006).
- Raees, F., der Heul, D. R. V., and Vuik, C. (2011). Evaluation of the interface-capturing algorithm of OpenFOAM for the simulation of incompressible immiscible two-phase flow. Technical report, Deft University of Technology, The Netherlands, Deft, The Netherlands.
- Rahimzadeh, H., Maghsoodi, R., Sarkardeh, H., and Tavakkol, S. (2012). Simulating Flow Over Circular Spillways by Using Different Turbulence Models. *Engineering Applications of Computational Fluid Mechanics*, 6(1):100–109, [doi:10.1080/19942060.2012.11015406](https://doi.org/10.1080/19942060.2012.11015406).

- Rajaratnam, N. (1962). An experimental study of air entrainment characteristics of the hydraulic jump. *Journal of The Institution of Engineers (India)*, 42(7):247–273.
- Rajaratnam, N. (1976). *Turbulent Jets*. Elsevier Scientific Publishing Company.
- Ramezani, L., Karney, B., and Malekpour, A. (2016). Encouraging Effective Air Management in Water Pipelines : A Critical Review. *Journal of Water Resources Planning and Management*, pages 1–11, doi:10.1061/(ASCE)WR.1943-5452.0000695.
- Resch, F. J. and Leutheusser, H. J. (1972). Reynolds stress measurements in hydraulic jumps. *Journal of Hydraulic Research*, 10(4):409–430, doi:10.1080/00221687209500033.
- Resch, F. J., Leutheusser, H. J., and Alemum, S. (1974). Bubbly two-phase flow in hydraulic jump. *Journal of Hydraulic Division*, 100(1):137–149.
- RGSPPDADAR (1995). *Regulamento Geral dos Sistemas Públicos e Prediais de Distribuição de Água e Drenagem de Águas Residuais*. Decreto Regulamentar 23/95 de 23 de Agosto - Diário da República Portuguesa- I Série-B.
- Rice, C. E. and Kadavy, K. C. (1996). Model Study of a Roller Compacted Concrete Stepped Spillway. *Journal of Hydraulic Engineering*, 122(6):292–297, doi:10.1061/(ASCE)0733-9429(1996)122:6(292).
- Richardson, L. F. (1922). *Weather Prediction by Numerical Process*. Cambridge, The University press.
- Rider, W. J. and Kothe, D. B. (1997). Reconstructing Volume Tracking. *Journal of Computational Physics*, 141(2):112–152, doi:10.1006/jcph.1998.5906.
- Roenby, J., Bredmose, H., and Jasak, H. (2016). A Computational Method for Sharp Interface Advection. *Royal Society*.
- Romagnoli, M., Carvalho, R. F., and Leandro, J. (2013). Turbulence characterization in a gully with reverse flow. *Journal of Hydraulic Engineering-ASCE*, 139(7):736–744, doi:10.1061/(ASCE)HY.1943-7900.0000737.
- Roque, J. M. (2011). *Medição de alturas de água usando visão computacional num modelo Simulink®*. Msc thesis, University of Coimbra, Coimbra, Portugal (in Portuguese).
- Rubinato, M., Shucksmith, J., Saul, A. J., and Shepherd, W. (2013). Comparison between InfoWorks hydraulic results and a physical model of an urban drainage system. *Water Science & Technology*, 68(2):372–379, doi:10.2166/wst.2013.254.

- Rusche, H. (2002). *Computational Fluid Dynamics of Dispersed Two-Phase Flows at High Phase Fractions*. PhD thesis, Imperial College of London, London, UK.
- Russo, B. and Gómez, M. (2011). Methodology to estimate hydraulic efficiency of drain inlets. *Proceedings of the ICE - Water Management*, 164(WM2):81–90, [doi:10.1680/wama.900070](https://doi.org/10.1680/wama.900070).
- Russo, B., Gómez, M., and Tellez, J. (2013). Methodology to Estimate the Hydraulic Efficiency of Nontested Continuous Transverse Grates. *Journal of Irrigation and Drainage Engineering*, 139(10):864–871, [doi:10.1061/\(ASCE\)IR.1943-4774.0000625](https://doi.org/10.1061/(ASCE)IR.1943-4774.0000625).
- Ryu, Y., Chang, K.-A., and Lim, H.-J. (2005). Use of bubble image velocimetry for measurement of plunging wave impinging on structure and associated greenwater. *Measurement Science and Technology*, 16:1945–1953, [doi:10.1088/0957-0233/16/10/009](https://doi.org/10.1088/0957-0233/16/10/009).
- Sabtu, N., Saul, A. J., and Sailor, G. (2016). Hydraulic Interaction of a Gully System. *American Scientific Research Journal for Engineering, Technology, and Sciences*, 21(1):202–209.
- Salome (2011). SALOME 6 Platform Download.
- Sene, K. J. (1988). Air entrainment by plunging jets. *Chemical Engineering Science*, 43(10):2615–2623.
- Sethian, J. A. (1998). Fast marching methods. *SIAM Review*, 41:199–235.
- Shi, F., Kirby, J. T., and Ma, G. (2010). Modeling quiescent phase transport of air bubbles induced by breaking waves. *Ocean Modelling*, 35(1-2):105–117, [doi:10.1016/j.ocemod.2010.07.002](https://doi.org/10.1016/j.ocemod.2010.07.002).
- Shonibare, O. Y. and Wardle, K. E. (2015). Numerical Investigation of Vertical Plunging Jet Using a Hybrid Multifluid – VOF Multiphase CFD Solver. *International Journal of Chemical Engineering*, 2015(Article ID 925639):14, [doi:10.1155/2015/925639](https://doi.org/10.1155/2015/925639).
- Simões, A., Schuls, H., Porto, R., and Gulliver, J. (2013). Free-surface Profiles and Turbulence Characteristics in Skimming Flows along Stepped Chutes. *Journal of Water Resource and Hydraulic Engineering*, 2(1):1–12.
- Smagorinsky, J. (1963). General Circulation Experiments with the Primitive Equations. *Weather Review*, 91(3):99–164, [doi:10.1126/science.27.693.594](https://doi.org/10.1126/science.27.693.594).
- Spaliviero, F. and May, R. W. P. (1998). Spacing of road gullies. Hydraulic performance of BS EN 124 gully gratings. Technical report, HR Wallingford, UK.

- Stovin, V. R., Guymer, I., and Lau, S. D. (2008). Approaches to validating a 3D CFD manhole model. In *11th International Conference on Urban Drainage (11ICUD)*. IAHR/IWA.
- Straub, L. G. and Anderson, A. G. (1958). Experiments on self-aerated flow in open channels. *Journal of the Hydraulics Division*, 84(7):1–35.
- Štrubelj, L. and Tiselj, I. (2011). Two-fluid model with interface sharpening. *International Journal for Numerical Methods in Engineering*, 85:575–590, [doi:10.1002/nme.2978](https://doi.org/10.1002/nme.2978).
- Štrubelj, L., Tiselj, I., and Mavko, B. (2009). Simulations of free surface flows with implementation of surface tension and interface sharpening in the two-fluid model. *International Journal of Heat and Fluid Flow*, 30(4):741–750, [doi:10.1016/j.ijheatfluidflow.2009.02.009](https://doi.org/10.1016/j.ijheatfluidflow.2009.02.009).
- Sussman, M. and Puckett, E. G. (2000). A Coupled Level Set and Volume-of-Fluid Method for Computing 3D and Axisymmetric Incompressible Two-Phase Flows. *Journal of Computational Physics*, 162(2):301–337, [doi:10.1006/jcph.2000.6537](https://doi.org/10.1006/jcph.2000.6537).
- Tabbara, M., Chatila, J., and Awwad, R. (2005). Computational simulation of flow over stepped spillways. *Computers & Structures*, 83(27):2215–2224, [doi:10.1016/j.compstruc.2005.04.005](https://doi.org/10.1016/j.compstruc.2005.04.005).
- Tabor, G. (2010). OpenFOAM: An Exeter Perspective. Lisbon, Portugal, 14-17 June 2010.
- Turan, C., Politano, M. S., Carrica, P. M., and Weber, L. (2007). Water entrainment due to spillway surface jets. *International Journal of Computational Fluid Dynamics*, 21(3-4):137–153, [doi:10.1080/10618560701525954](https://doi.org/10.1080/10618560701525954).
- Ubbink, O. (1997). *Numerical prediction of two fluid systems with sharp interfaces*. Phd thesis, Imperial College of Science, London, UK.
- Ubbink, O. and Issa, R. (1999). A Method for Capturing Sharp Fluid Interfaces on Arbitrary Meshes. *Journal of Computational Physics*, 153(1):26–50, [doi:10.1006/jcph.1999.6276](https://doi.org/10.1006/jcph.1999.6276).
- Valero, D. and Bung, D. B. (2016). Development of the interfacial air layer in the non-aerated region of high-velocity spillway flows. Instabilities growth, entrapped air and influence on the self-aeration onset. *International Journal of Multiphase Flow*, 84:66–74, [doi:10.1016/j.ijmultiphaseflow.2016.04.012](https://doi.org/10.1016/j.ijmultiphaseflow.2016.04.012).
- Valero, D. and García-Bartual, R. (2016). Calibration of an Air Entrainment Model for CFD Spillway Applications. In Gourbesville, P., Cunge, J. A., and Caignaert, G., editors, *Advances in Hydroinformatics*, pages 571–582. Springer Singapore.

- Van der Pijl, S. (2005). *Computation of Bubbly Flows with a Mass-Conserving Level-Set Method*. Phd thesis, Delft University of Technology, The Netherlands.
- Verloop, W. C. (1995). The inertial coupling force. *International Journal of Multiphase Flow*, 21:929 – 933.
- Versteeg, H. K. and Malalasekera, W. (1995). *An Introduction to Computational Fluid Dynamics - The Finite Volume Method*. Pearson Education.
- Versteeg, H. K. and Malalasekera, W. (2007). *An Introduction to Computational Fluid Dynamics - The Finite Volume Method*. Pearson Education, 2nd edition.
- Viparelli, M. (1953). The flow in the flume with 1:1 slope. In *International Association for Hydraulic Research, Joint Conference, Minneapolis, Minnesota*, pages 415–423.
- Volkart, P. (1980). Self-aerated Flow in Steep, Partially Filled Pipes. *Journal of the Hydraulics Division*, 108(9):1029–1046.
- Waclawczyk, T. and Koronowicz, T. (2008). Comparison of CICSAM and HRIC high-resolution schemes for interface capturing. *Journal of Theoretical and Applied Mechanics*, 46(2):325–345.
- Wahl, T. L. (2000). Analyzing ADV Data Using WinADV. In *Joint Conference on Water Resources Engineering and Water Resources Planning & Management*, pages 1–10, Minneapolis, Minnesota.
- Wahl, T. L. (2003). Discussion of “Despiking Acoustic Doppler Velocimeter Data” by Derek G. Goring and Vladimir I. Nikora. *Journal of Hydraulic Engineering*, 129(6):484–487, [doi:10.1061/\(ASCE\)0733-9429\(2003\)129:6\(484\)](https://doi.org/10.1061/(ASCE)0733-9429(2003)129:6(484)).
- Wang, H. and Chanson, H. (2015). Air entrainment and turbulent fluctuations in hydraulic jumps. *Urban Water Journal*, 12(6):1–17, [doi:10.1080/1573062X.2013.847464](https://doi.org/10.1080/1573062X.2013.847464).
- Wardle, K. E. and Weller, H. G. (2013). Hybrid Multiphase CFD Solver for Coupled Dispersed / Segregated Flows in Liquid-Liquid Extraction. *International Journal of Chemical Engineering*, Article ID 128936, page 13, [doi:10.1155/2013/128936](https://doi.org/10.1155/2013/128936).
- WEF & ASCE (1992). *Design and Construction of Urban Stormwater Management Systems*. Manual of Practice No.: 77. American Society of Civil Engineers, New York, USA.
- Weibull, W. (1951). A Statistical Distribution Function of Wide Applicability. *Journal of Applied Mechanics*, 18(3):293–297.

- Weller, H. (2008). A New Approach to VOF-based Interface Capturing Methods for Incompressible and Compressible Flows. *Report TR/HGW/04, OpenCFD Ltd., USA*.
- Wilcox, D. C. (1993). *Turbulence Modeling for CFD*. DCW Industries, Inc.
- Willmott, C. J. (1981). On the validation of models. *Physical Geography*, 2(2):184–194, doi:10.1080/02723646.1981.10642213.
- Witt, A., Gulliver, J., and Shen, L. (2015). Simulating air entrainment and vortex dynamics in a hydraulic jump. *International Journal of Multiphase Flow*, doi:10.1016/j.ijmultiphaseflow.2015.02.012.
- Wood, I. R. (1991). *Air entrainment in free-surface flows*. IAHR Hydraulic Structures Design Manual Nr.4, Hydraulic Designs Considerations. A. A. Balkema, Rotterdam, The Netherlands.
- Wood, I. R., Ackers, P., and Loveless, J. (1983). General method for critical point os spillways. *Journal of Hydraulic Engineering*, 109(2):308–312, doi:10.1061/(ASCE)0733-9429(1983)109:2(308).
- Yan, K. and Che, D. (2010). A coupled model for simulation of the gas – liquid two-phase flow with complex flow patterns. *International Journal of Multiphase Flow*, 36(4):333–348, doi:10.1016/j.ijmultiphaseflow.2009.11.007.
- Yasuda, Y. and Chanson, H. (2003). Micro- and macro-scopic study of two-phase flow on a stepped chute. In *Proceedings of the 30th IAHR Biennial Congress*, volume vol. D, pages 695–702, Thessaloniki, Greece.
- Yeoh, G. H. and Tu, J. (2010). *Computational Techniques for Multi-Phase Flows*. Elsevier Ltd.
- Young, P. C. (2002). Advances in real-time flood forecasting. *Philosophical Transactions of the Royal Society of London*, 360(1976):1433–1450, doi:10.1098/rsta.2002.1008.
- Youngs, D. L. (1984). An Interface Tracking Method for a 3D Eulerian Hydrodynamics Code. Technical report, Report n. 44/92/35, AWRE Design Mathematics Division, UK.

A

Publications

The content of this thesis have partially been published or submitted for peer-reviewing process in International Journals and Proceedings of International Conferences. A full list of papers submitted during this thesis, from a time period starting from September 2012 and in which Pedro Lopes is an author or co-author are presented herein:

Publication in international journals:

- Leandro, J., **Lopes, P.**, Carvalho, R. F., Páscoa, P., Martins, R., & Romagnoli, M. (2014). Numerical and experimental characterization of the 2D vertical average-velocity plane at the centre-profile and qualitative air entrainment inside a gully for drainage and reverse flow. *Computers & Fluids*, 102, 52–61.
<http://doi.org/10.1016/j.compfluid.2014.05.032>.
- **Lopes, P.**, Leandro, J., Carvalho, R. F., Páscoa, P., & Martins, R. (2015). Numerical and experimental investigation of a gully under surcharge conditions. *Urban Water Journal*, 12(6), 468–476. <http://doi.org/10.1080/1573062X.2013.831916>.
- **Lopes, P.**, Tabor, G., Carvalho, R. F., and Leandro, J. (2016). Explicit calculation of natural aeration using a Volume-of-Fluid model. *Applied Mathematical Modelling*, 40(17-18), 7504–7515. <http://doi.org/10.1016/j.apm.2016.03.033>.
- **Lopes, P.**, Leandro, J., Carvalho, R. F., Russo, B., and Gómez, M. (2016). Assessment of a VOF Model Ability to Reproduce the Efficiency of a Continuous Transverse Gully with Grate. *Journal of Irrigation and Drainage Engineering*. [http://doi.org/10.1061/\(ASCE\)IR.1943-4774.0001058](http://doi.org/10.1061/(ASCE)IR.1943-4774.0001058).
- **Lopes, P.**, Leandro, J., Carvalho, R. F. and Bung, D. B. (2016). Alternating skimming flow over a stepped spillway, *Environmental Fluid Mechanics*.
<http://doi.org/10.1007/s10652-016-9484-x>. (in press)
- **Lopes, P.**, Leandro, J. and Carvalho, R. F. (2016). Numerical procedure for free-surface detection using a Volume-of-Fluid model. (submitted, under review)
- **Lopes, P.**, Leandro, J. and Carvalho, R. F. (2016). Flow self-aeration using a sub-grid Volume-of-Fluid model. (submitted, under review).
- **Lopes, P.**, Carvalho, R. F. and Leandro, J. (2016). Numerical study of the fundamental flow characteristics of a 3D gully box under flooding drainage. (submitted).

Publications in proceedings of international conferences and workshops:

- **Lopes, P.**, Leandro, J., Carvalho, R. F. and Martins, R. (2012). Hydraulic behaviour of a gully under surcharge conditions. In 9th International Conference on Urban Drainage Modelling (9UDM) (pp. 1–9). September 4-6, 2012, Belgrade, Serbia: Faculty of Civil Engineering, University of Belgrade. USB flash drives. ISBN 978-86-7518-156-9.
- Carvalho, R., Páscoa, P., Leandro, J., Abreu, J., **Lopes, P.**, Quinteiro, R. and Lima, J. L. M. P. de. (2013). Experimental investigation of the linking element gully - drop manhole. In Proceedings of 35th IAHR World Congress 2013. Chengdu, China.
- **Lopes, P.**, Shucksmith, J., Leandro, J., Carvalho, R. F. and Rubinato, M. (2014). Air-entrainment characterization and velocities profiles in a scaled circular manhole. In 13th International Conference on Urban Drainage. Sarawak, Malaysia.
- **Lopes, P.**, Tabor, G., Carvalho, R. F. and Leandro, J. (2015). Modelling air-entrainment in circular, 3D plunging jet using the OpenFOAM CFD toolbox. In Advances in Numerical Modelling of Hydrodynamics workshop.
- Buhler, P., Leandro, J., Bung, D. B., **Lopes, P.** and Carvalho, R. F. (2015). Measuring void fraction of a stepped spillway with non-intrusive methods using different image resolutions. In R. F. Carvalho & S. Pagliara (Eds.), 2nd International Workshop on Hydraulic Structures: Data Validation (pp. 41–48).
- **Lopes, P.**, Bung, D. B., Leandro, J. and Carvalho, R. F. (2015). The effect of cross-waves in physical stepped spillway models. In 36th IAHR World Congress 2015.
- Beg, Md. N. A., Carvalho, R. F., Leandro, J., **Lopes, P.** and Cartaxo, L. (2016). Investigation of the Flow Field inside a Drainage System: Gully – Pipe – Manhole. 6th IAHR International Junior Researcher and Engineer Workshop on Hydraulic Structures (IJREWHS) 2016.
- **Lopes, P.**, Leandro, J., Carvalho, R. F. and Tabor, G. (2016). “Development of a Sub-grid Model for Self-aeration.” OpenFOAM Workshop 11, Guimarães, Portugal.
- Beg, Md. N. A., Carvalho, R. F., **Lopes, P.**, Leandro, J. and Melo, N. (2016). “Numerical Investigation of the Flow Field inside a Manhole-Pipe Drainage System.” 6th International Symposium on Hydraulic Structures, B. Crookston & B. Tullis, ed., Hydraulic Structures and Water System Management, Portland, Oregon, USA.

B

Workflow

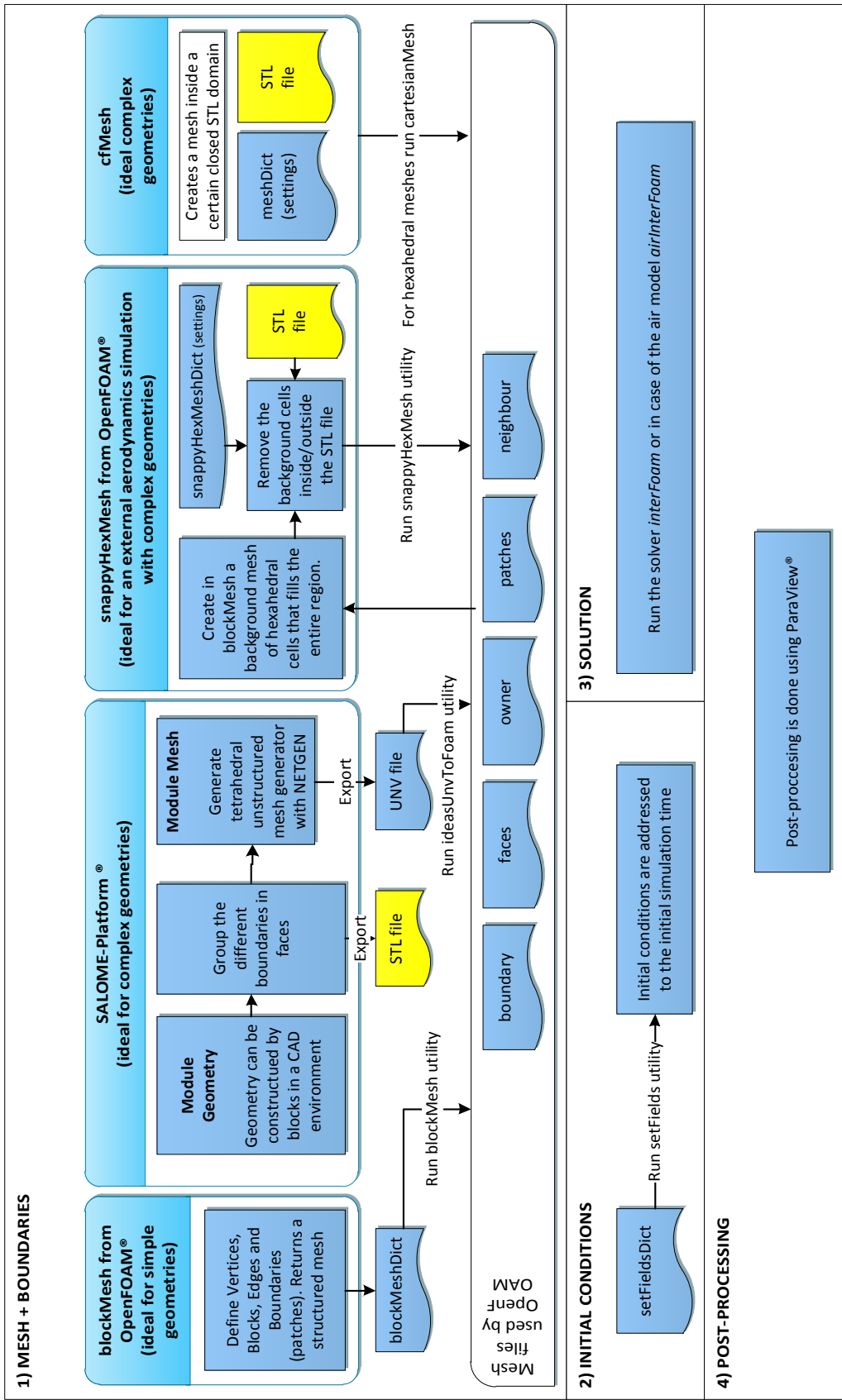


Figure B.1: Workflow for any case setup used in this Thesis.

